UNIVERSITÉ DE STRASBOURG

ÉCOLE DOCTORALE DE PHYSIQUE ET CHIMIE PHYSIQUE (ED 182)

Institut Charles Sadron (ICS) – CNRS-UPR22

THÈSE présentée par :

Manon JOUANLANNE

Soutenance prévue le : **15 Décembre 2023**

pour obtenir le grade de : **Docteur de l'université de Strasbourg**

Discipline/ Spécialité : **Physique**

Architectures of foam-fibre assemblies: from liquid systems to polymeric hierarchical materials

Architectures d'assemblages mousse-fibres : des systèmes liquides aux matériaux polymères hiérarchiques

THÈSE supervisée par :

Mr FARAGO Jean	Professeur, ICS, Université de Strasbourg
Mme HOURLIER-FARGETTE Aurélie	Chargée de Recherches CNRS, ICS, Université de Strasbourg

RAPPORTEURS :

Mme LE MERRER Marie	Chargée de Recherches CNRS, ILM, Université de Lyon
Mr RAUFASTE Christophe	Professeur, INPHYNI, Université Côte d'Azur

---

EXAMINATEURS :

Mr COX Simon	Professeur, Dpt de Mathématiques, Université d'Aberystwyth
Mr CHARITAT Thierry	Professeur, ICS, Université de Strasbourg

Acknowledgments

Cette thèse est le résultat d'un travail mené au cours de trois années de recherche au sein de l'Institut Charles Sadron à Strasbourg, France. Elle a impliqué de nombreuses personnes sans qui ces travaux n'auraient pas été possibles et j'aimerais ici tous vous remercier.

Tout d'abord, je tiens à remercier mes encadrants. Aurélie, pour m'avoir donné envie de me lancer dans l'aventure d'une thèse, la confiance que tu m'as témoignée dès le début ainsi que pour ta supervision. Je te suis reconnaissante d'avoir partagé avec moi ta philosophie et ta rigueur en matière de recherche scientifique mais aussi de m'avoir fait grandir en me permettant de sortir de ma zone de confort avec la participation à de nombreuses conférences internationales. Jean, merci également pour ta supervision et pour avoir transmis avec passion tes connaissances lors de nos nombreuses discussions. Mention très spéciale pour la conférence à Las Vegas qui restera certainement dans les annales.

Mes sincères remerciements vont également aux membres du jury qui ont accepté d'évaluer cette thèse. Je suis honorée et reconnaissante à Christophe Raufaste et Marie Le Merrer pour l'intérêt qu'ils ont porté à ce travail et pour avoir accepté d'en être les rapporteurs. I am grateful to Simon Cox for his venue in Strasbourg for my defense, and for the interest he took in my work. Merci beaucoup à Thierry Charitat d'avoir présidé ce jury, ainsi que pour toutes nos interactions à l'Institut. Je tiens également à remercier Pierre Muller et Camille Duprat pour leurs précieux conseils à mi-parcours.

Je tiens à remercier chaleureusement Christian pour m'avoir permis de construire mon projet professionnel toujours en considérant mes passions et cela depuis le début de mes études.

Un grand merci à Wiebke pour son regard extérieur, son aide constante mais surtout pour m'avoir présentée à l'équipe des Foamies qui ont rendu ces trois années incroyables. Je pense à mes amis Imene et Friedrich sans qui ces trois années n'auraient pas été possibles ; mais aussi à Guillaume, Luca, Benjamin, Jonathan, Martin, Stéphane, François, Katja, Seb, Rajam et Vipin. Merci pour tout ! Merci à Marina, Thierry et toute l'équipe MIM pour m'avoir aussi bien accueillie. Je tiens aussi à remercier mes étudiants Le Quan Ngo et Pierre Guichard pour avoir débroussaillé certaines questions que nous nous posions. Je tiens à exprimer ma reconnaissance à Damien, Leandro, Christophe Lambour et François Courtier pour nos différents échanges et votre aide dans la réalisation des expériences, ainsi qu'à l'équipe PECMAT pour le prêt de matériel.

Un million de mercis à Antoine pour avoir réalisé tous ces scans au tomo mais surtout pour ton aide, nos nombreuses discussions et ton soutien.

Plus généralement, je tiens à remercier toutes les personnes de l'Institut qui ont contribué à la bonne ambiance de travail et avec qui j'ai eu plaisir à partager un café ou une partie de baby...

Enfin, je tiens à remercier ma famille pour leurs encouragements et leur soutien sans faille. Merci à Thomas pour sa patience et son soutien au quotidien. Merci à ma belle-famille et merci à mes amis d'être là.

Introduction

Solid foams are versatile materials, widely used in everyday applications (automotive, packaging, sports products, insulation or tissue engineering). Generally produced from the solidification of liquid foams, their architectures are linked to the structures of these liquid precursors, which are themselves dictated by strict physical laws [1]. New techniques have recently been developed to produce solid foams from liquid foams with controlled bubble sizes and densities [2]. Despite these innovations and the growing size of the industrial foam market (estimated at 14.5 megatonnes in 2021 [3]), there is still a lack of methods for controlling and customising the geometry and topology of foams (shape, size and connection of bubbles). For these reasons, the aim of this PhD thesis is to work on new ways of fabricating innovative foam-fibre structures. The integration of fibres in the liquid state aims to modify the structure of foams in a self-assembling manner, i.e. by allowing the bubbles and fibres to organise themselves spontaneously before the solidification stage.

The preparation of these foam-fibre systems raises important fundamental questions: how can foam structures be modified by the introduction of fibres, and what are the important fibre parameters that allow these modifications to be controlled?

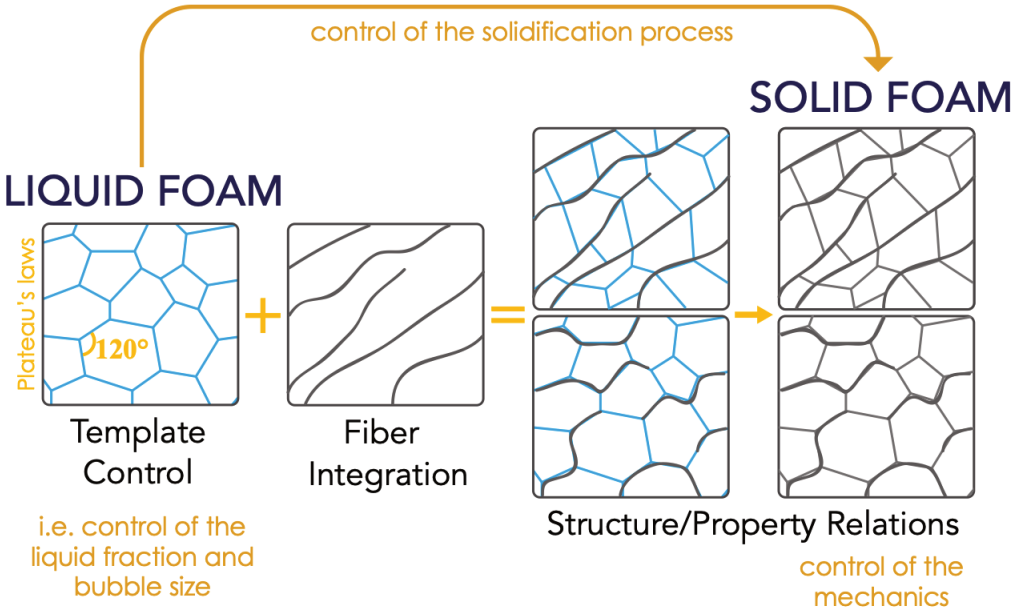


Figure 0.1 – Overview of the approach: A deeper knowledge of the interactions between fibres and a liquid foam that has the ability to solidify will serve as the foundation for self-assembling solid foams with unique structure and mechanical characteristics.

To obtain controllable architectures and improve the properties of foams, we want to explore both theoretically and experimentally the concept of adding fibres inside a liquid foam, that can solidify, in order to modify its topology and geometry in a controlled way before solidification.

To convert liquid precursors into solid foams, an understanding of the mechanisms involved in liquid foams is first important to tune and control the structure of the solid foam. For this reason, the Chapter 1 introduces the general concepts of foams: From the parameters that define their architectures under various conditions to the events that cause their destabilisation. We then present the challenges involved in the use of the liquid foam templating technique, i.e. the process to convert liquid precursors into solid foams, that is mainly employed in Chapters 3, 4 and 5. This first introductive chapter is concluded by generalities on the structural and mechanical properties of solid foams, along with a description of the various imaging tools used during this work to characterise foams.

With the basic knowledge acquired on liquid foams, we then looked at the development of a better understanding of the mechanisms involved in fibre-enriched liquid foams. In Chapter 2, we developed a quasi-2D system based on an ordered model foam and a ribbon that illustrates in a simplified way what could happen in a 3D foam-fibre system. In this chapter, we provide an experimental and theoretical framework that quantifies the equilibrium shape of the ribbon inserted in an ordered liquid foam and highlight the importance of the bending rigidity of the ribbon.

The following step in this PhD work is to go towards 3D complex foams containing fibres, with a formulation allowing a solidification step, to build polymeric solid hierarchical materials. In Chapter 3, we used the liquid foam templating technique to produce hydrogel foams of alginate. We highlighted the importance of the initial liquid properties, the solidification kinetics and the involved foam timescales. To find the right system for its application in Chapter 5, a rheological characterisation protocol for the foam's constituent material was first implemented, along with a study of the foam's temporal evolution according to the formulation used, using X-Ray tomography.

Improvements of the liquid foam templating technique were then made in Chapter 4 to produce polyurethane foams, which have the advantage of being able to be removed from the container (compared with alginate systems) and then used for various characterisations (structural and mechanical). The focus was given on the protocol for obtaining homogeneous foams with controlled bubble size, density and flexibility.

Chapter 5 is more exploratory. Both alginate and polyurethane foams (produced with the protocols described in Chapters 3 and 4) were used to create foam-fibre systems. Arrays of ordered rigid fibres were made to study the self-organisation of the foams left to settle and solidify inside. For both systems (alginate and polyurethane), we developed a protocol for studying the tomographic images using the software supplied with the tomograph, but also using a home-made Matlab® programme that allows the extraction of the foam structure. We were thus able to show that the foams could self-organise into a highly ordered state between the fibres, in the specific cases where the average bubble sizes were close to the typical distance between the fibres. Finally, the very first in situ mechanical tests (i.e. with X-ray imaging at each step of deformation) were carried out

on polyurethane foam systems containing rigid fibres, highlighting collective effects of the fibres in those systems, and building a foundation for further mechanical characterisations of foam-fibre architectures.

Contents

Acknowledgments 1

Introduction 3

Remerciements 3

1 Foam Fundamentals 1
- 1.1 Liquid foams . . . 2
  - 1.1.1 Generalities . . . 2
  - 1.1.2 Typical foam structures . . . 3
  - 1.1.3 Confined foams . . . 5
- 1.2 Towards solid structures: Liquid foam templating . . . 6
  - 1.2.1 Challenges of liquid foam templating . . . 7
    - 1.2.1.1 Drainage . . . 7
    - 1.2.1.2 Foaming process . . . 8
  - 1.2.2 The resulting solid foam structure . . . 9
- 1.3 Properties of cellular materials . . . 10
  - 1.3.1 Mechanical behaviour of solid foams via compression tests . . . 11
  - 1.3.2 Bending- VS Stretch-dominated structures . . . 14
- 1.4 Foam characterisation . . . 15
  - 1.4.1 State of the art: Structural characterisation of foams . . . 15
  - 1.4.2 X-ray microtomography . . . 16
    - 1.4.2.1 X-ray tomography principles . . . 16
    - 1.4.2.2 3D image reconstruction: Filtered back projection . . . 17
    - 1.4.2.3 Foam analysis from VG Studio software . . . 18
    - 1.4.2.4 Limitations of the VG Studio software . . . 20
    - 1.4.2.5 Dual scaffold analysis . . . 20

2 Elastocapillary deformation of thin elastic ribbons in 2D foam columns 27
- 2.1 State of the art: Elastocapillarity of slender structures . . . 28
- 2.2 Materials and methods . . . 29
  - 2.2.1 Formulation of the soap solution . . . 29
  - 2.2.2 Elastic ribbons . . . 29
  - 2.2.3 Experimental setup . . . 30
  - 2.2.4 Characterisation . . . 32
- 2.3 Results . . . 33

2.3.1 Deflexion measurements . . . 33
2.3.2 Equilibrium shapes . . . 34
2.3.3 Theoretical interpretation . . . 35
2.3.4 Application to bubble-based forming . . . 38
2.4 Influence of gravity . . . 39
2.4.1 Experimental modifications . . . 40
2.4.2 Theoretical modifications . . . 40
2.4.3 Results . . . 42
2.5 Conclusion . . . 43

From liquid to solid foam-fibre systems **45**

3 Alginate foams **47**
3.1 Context . . . 48
3.2 Materials and Methods . . . 49
3.2.1 Preparation of solutions . . . 49
3.2.2 Rheological characterisation . . . 50
3.2.3 Foam generation . . . 51
3.2.4 Foam drainage characterisation via optical imaging . . . 51
3.2.5 X-ray microtomography characterisation . . . 52
3.3 Results and Discussion . . . 53
3.3.1 Tuning the initial liquid properties . . . 53
3.3.2 Tuning the gelation time . . . 54
3.3.3 Drainage and gelation kinetics . . . 55
3.3.4 Control over the hydrogel foam structure . . . 58
3.4 Conclusion . . . 62

4 Polyurethane foams **65**
4.1 Context . . . 66
4.1.1 Chemical generalities . . . 66
4.1.2 Flexible polyurethane formulation . . . 67
4.1.3 Chemical foaming vs microfluidics . . . 67
4.2 PU foam preparation via chemical foaming . . . 68
4.2.1 Materials . . . 68
4.2.2 Foaming process improvements . . . 69
4.2.3 Formulation improvements . . . 70
4.2.4 Fibre introduction . . . 72
4.2.5 Conclusion . . . 73
4.3 PU foam preparation via bubbling through nozzles . . . 74
4.3.1 Formulation . . . 74
4.3.1.1 Tuning the initial viscosity . . . 75
4.3.1.2 Tuning the mechanical properties . . . 75
4.3.2 Experimental setup . . . 78
4.3.2.1 Mixing process . . . 78
4.3.2.2 Foam production . . . 79
4.3.2.3 Tuning the bubble size . . . 79
4.3.2.4 Experimental challenges . . . 80
4.3.3 Foam superimposition: A new method to control foam structure . 81

4.3.3.1 Formulation . . . 81
4.3.3.2 Experimental setup . . . 81
4.3.3.3 Tuning the foam density . . . 82
4.3.4 Conclusion . . . 85

5 Foam-Fibre systems 87
5.1 State of the art . . . 88
5.1.1 Elastocapillarity: collective effects . . . 88
5.1.2 Fibres and liquid foams . . . 89
5.1.3 Fibres and solid foams . . . 90
5.1.3.1 Structure modification in solid foam-fibre composites . . . 90
5.1.3.2 Mechanical behaviour of solid foam-fibre composites . . . 91
5.2 Materials and Methods . . . 92
5.2.1 Ordered nylon fibres . . . 92
5.2.2 Alginate foam-fibre systems . . . 93
5.2.3 Polyurethane foam-fibre systems using the foam superimposition protocol . . . 93
5.3 Results . . . 94
5.3.1 Reference foams without fibre . . . 94
5.3.1.1 Foam analysis from VG-Studio software . . . 94
5.3.1.2 Dual "scaffold" analysis . . . 98
5.3.2 Foam-fibre systems . . . 101
5.3.2.1 Fibres surrounded by foam . . . 101
5.3.2.2 Visual inspection of the foam-fibre systems . . . 102
5.3.2.3 Foam-fibre system analysis from VG-Studio software . . . 108
5.3.2.4 Dual "scaffold" analysis . . . 111
5.3.3 In-situ compression . . . 114
5.4 Conclusion . . . 117

Conclusion and Outlook 119

Résumé de thèse : Architectures d'assemblages mousse-fibres : des systèmes liquides aux matériaux polymères hiérarchiques 125
Introduction . . . 125
1 Modèle aqueux quasi-2D . . . 126
2 Fabrication de mousses solides à partir d'un précurseur liquide . . . 127
2.1 Protocole de moussage . . . 128
2.2 Résultats : mousses d'alginate . . . 129
2.3 Résultats : mousses de polyuréthane . . . 131
3 Système mousse - fibres . . . 132
3.1 Dispersion aléatoire de fibres . . . 132
3.2 Fibres rigides ordonnées . . . 133
Conclusion . . . 134

Appendices 137
1 Impact of the threshold on the bubble size measurement via VG Studio software . . . 137
2 Additional information on the strut network extraction . . . 138

3 Fitting parameters of the Cross model used on the rheological results . . . 140
4 Simulation of the plateau storage moduli for different GDL concentration 141
5 Struts position in the alginate foams using sequential tomography scans . 141
6 Limit of the foam superimposition method for high catalyst concentration in polyurethan foams 142
7 Dual scaffold analysis: Orders of the vertices 142
8 Steinhardt analysis 143

Bibliography **147**

Chapter 1

Foam Fundamentals

A foam is a structure formed by gas bubbles trapped in a continuous phase of material (liquid or solid). How do we go from a well known spherical bubble to the complex polyhedral foam structure?

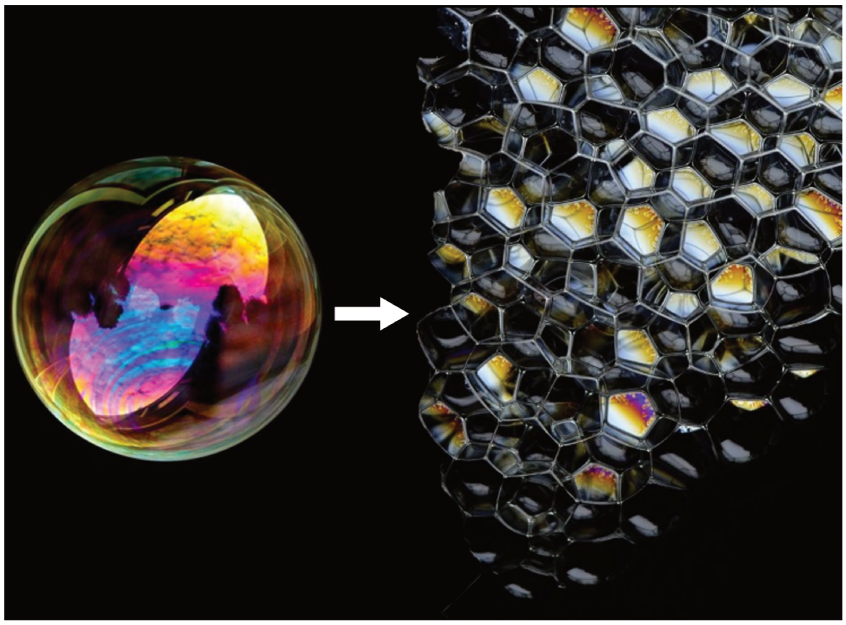


Figure 1.1 – From a spherical bubble to the complex polyhedral foam structure. Credits: [4] and Wiebke Drenckhan.

In this section, we answer this question and introduce general concepts on foams to provide the context of this PhD work. The parameters that define the liquid foams are first explained. The structures of liquid foams under different conditions are then described, as well as the phenomena that lead to foam destabilisation. Focus is then given to *liquid foam templating*, i.e. the method of creating solid foams from liquid precursors that is mainly used in this work. Its challenges are described, in terms of foam fabrication (foaming process, viscosity, destabilisation) that determine the foam structures (bubble size, density, connectivity). Finally, the mechanical and structural characterisations of solid foams are discussed.

Contents

1.1 Liquid foams 2
1.1.1 Generalities 2
1.1.2 Typical foam structures 3
1.1.3 Confined foams 5
1.2 Towards solid structures: Liquid foam templating 6
1.2.1 Challenges of liquid foam templating 7
1.2.2 The resulting solid foam structure 9
1.3 Properties of cellular materials 10
1.3.1 Mechanical behaviour of solid foams via compression tests . . . 11
1.3.2 Bending- VS Stretch-dominated structures 14
1.4 Foam characterisation 15
1.4.1 State of the art: Structural characterisation of foams 15
1.4.2 X-ray microtomography 16

1.1 Liquid foams

A foam is defined as an assembly of air bubbles in a continuous matrix, and is referred to as "liquid foam" if the continuous phase is liquid. Studying the structure of liquid foams is important in the context of our work because it will dictate the structure of solid foams produced by solidification of a liquid foam (Section 1.2).

1.1.1 Generalities

A bubble is a quantity of gas trapped in a thin layer of liquid. The spherical shape of an isolated bubble (Fig. 1.1 left) is that of a minimal surface area, resulting from the minimisation of the total energy, E, of the interfaces between the gas phase and the liquid phase. The total energy is given by $E = 2\gamma A$, where γ is the surface tension and A the interfacial area [5]. The surface tension γ is defined as the energy required to produce an interface of a unit area [6]. Surface tension can be reduced by using surfactants. These are amphiphilic molecules, which have the property of orienting themselves along interfaces [7].

If the number of bubbles is increased and they are brought into close contact, a cohesive foam is formed. The structures of liquid foams are complex and dictated by many parameters such as the bubble size, their dispersity and the liquid fraction.

The *dispersity* is the ratio of the standard deviation to the mean bubble diameter distribution. A foam with a dispersity of less than 5 % is described as monodisperse, while a foam with a dispersity of more than 5 % is polydisperse [8].

The *liquid fraction*, ϕ_ℓ, is the quantity of liquid contained in a foam as $\phi_\ell = V_\ell/V_f$ (with V_ℓ the liquid volume in the foam of volume V_f) and defines the local foam geometry (i.e. the way the bubbles aggregate on each other) [9]. The foams can therefore be classified into two categories: the high-density foam (often called “wet” foam) for a liquid fraction $\phi_\ell > 0.05$ and the low-density foam (or “dry” foam) with a lower liquid fraction: $\phi_\ell < 0.05$. The high-density and low-density foam structures will be described in Section

1.1.2 below. The notion of foam disappears when the liquid fraction is too high and exceeds a critical value ϕ_c, which differs according to the foam dispersity (Fig. 1.2). This transition at ϕ_c is reffered as the "jamming transition" [10].

Once produced, liquid foams evolve over time for several reasons: *Evaporation*, which can accelerate the destabilisation of the outer bubbles in contact with air. *Drainage*, caused by gravity which forces the liquid inside the foam to flow downwards, leading to the thinning of the foam from top to bottom (described in more detail in Section 1.2.1.1) [11]. *Coarsening*, which is the result of the pressure difference between the bubbles: the gas diffuses through the films from the small to the large bubbles, causing the bubble size and its dispersity to increase over time. *Coalescence*, which is the breaking of the thin film between two bubbles [12].

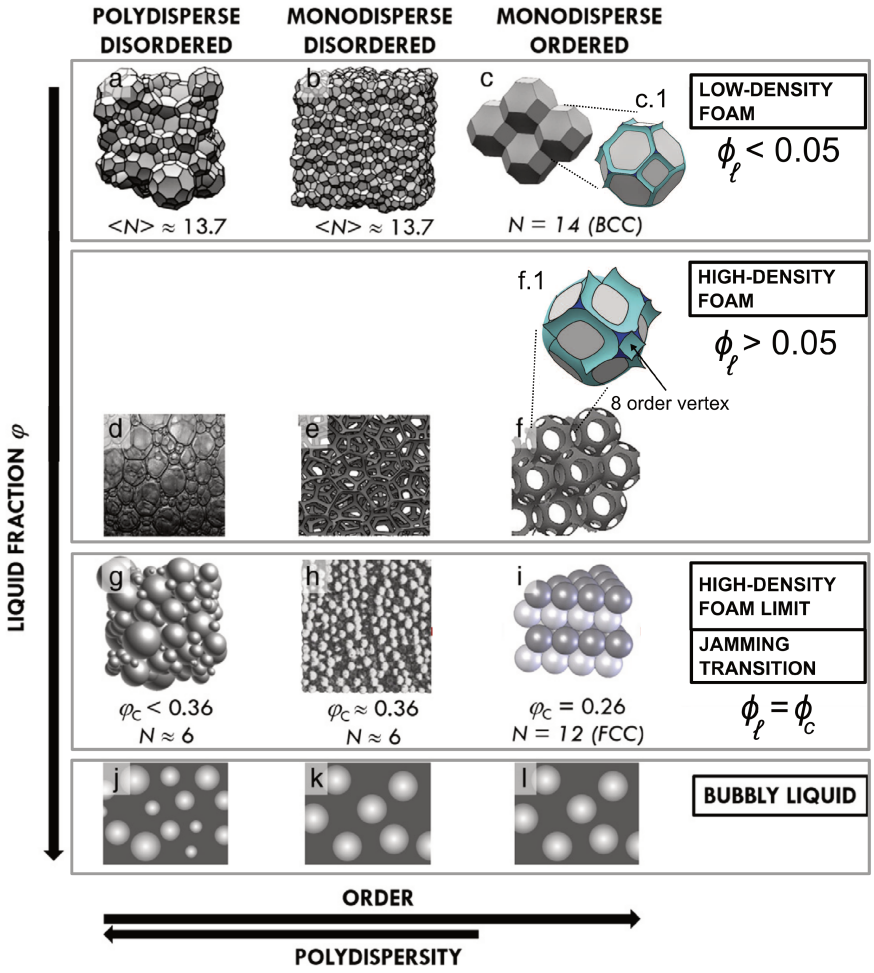


Figure 1.2 – Foam structures as a function of the dispersity, order and liquid fraction. Adapted from [10].

1.1.2 Typical foam structures

Figure 1.2 is adapted from the article of Drenckhan et al. [10] and presents the different foam structures as a function of the dispersity, order and liquid fraction.

Low density foam

At low density ($\phi_\ell \leq 0.05$), the liquid foams follow the so called Plateau's laws [1], which states that:

1. When two bubbles suspended in air come into contact, they spontaneously change their shape in order to share an interface and thus reduce the total interfacial area. This created film is smooth and has a constant mean curvature (Fig. 1.3 1).
2. When three bubbles come into contact, three films are created and meet at an angle of 120° two by two and form a Plateau border (Fig. 1.3 2).
3. When four bubbles come into contact, four Plateau border meet at an angle of 109,5° two by two and form a vertex (Fig. 1.3 3).

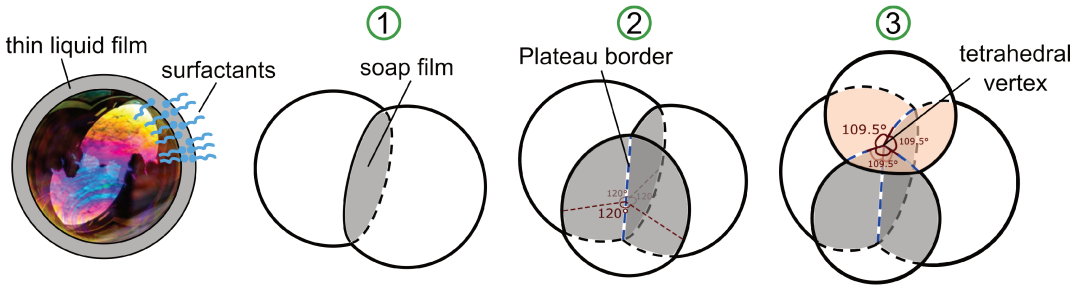


Figure 1.3 – Plateau's laws represented from two to four suspended bubbles, which set the structure of foams.

If we repeat these Plateau's laws with an infinity of bubbles, we find the tetrahedral structures of foams: the bubbles are polyhedral and well faceted (Fig. 1.1 right and 1.2 a,b,c).

These rules describe the local shape of a low-density foam, in particular the angles between the films (120°) and the Plateau borders (109.5°) but, as explained above, the dispersity and order have also a strong influence on the foam structure. As shown in Figure 1.2a-b, polydisperse foams show an alternation of large and small bubbles, leading to an average number of neighbours $< N >$ around 13.7. The same number appears in monodisperse foams when they are disordered. Figure 1.2c shows the so-called *Kelvin structure*, which can be achieved for dry monodisperse foam structure. It is composed of cells of equal units: truncated octahedrons made up of 14 faces (6 squares and 8 hexagons), which cristallise in body-centered cubic (bcc) configuration. In 1887, Lord Kelvin declared this structure to be the most efficient foam structure in terms of minimising energy and interfaces [13]. However, in 1993, Weaire et al. [14], theoretically discovered a new structure, the Weaire-Phelan structure (composed of an arrangement of two types of bubble shapes), which proved to be at 0.18 % more efficient partition of space than the Kelvin structure, but we will not go into the details of this Weaire-Phelan structure as it is outside the scope of this PhD work.

How to obtain the Kelvin structure experimentally?

In the last few decades, several experiments have been used to create foam samples with a Kelvin structure. Rosa et al. [15] showed that layers of bubbles can be reorganised

into a Kelvin structure by changing the distance between a liquid interface and a glass plate that confines the bubbles. Another method consists in confining monodisperse bubbles at the top of a pyramidal container: by modifying the angle of this pyramid, the bubbles crystallises spontaneously into a face-centered cubic (fcc), hexagonal close packed (hcp) or Kelvin structure [16]. In addition, the transition from an fcc structure to a Kelvin structure can also be obtained with the decrease of the liquid fraction of the foam by applying osmotic pressure [17] or using columns a few centimetres high [18, 19, 20].

High density foam

At high density ($\phi_\ell > 0.05$), the bubbles are spherical and perfectly surrounded by liquid (Fig. 1.2a). Plateau's laws do not apply to these high-density foams.

The foam structure therefore depends on how the bubbles are packed, which can be considered as a packing of spheres. For monodisperse foams, we can observe a close-packed structure for $\phi_c = 0.26$ (Fig. 1.2i) and a randomly packed structure at $\phi_c = 0.36$ (Fig. 1.2h). Note that the critical liquid fraction decreases when the polydispersity increases, as the smaller bubbles can fill the "voids" between the larger bubbles (Fig. 1.2g) [10].

Moreover, Figure 1.2f.1 shows a perfectly ordered high-density foam (with $\phi_\ell = 0.05$) which is composed of rhombic dodecahedrons (with 12 rhombus faces) and has 8 order vertices (i.e. 8 struts are connected to the same vertex, as described in Section 1.4.2.5 below)[21]. These cells look like a denser Kelvin structure (Fig. 1.2f) but as if the square faces of the Kelvin cell were closed with matter, forming 8 order vertices.

1.1.3 Confined foams

Foams are complex structures which depend on many parameters that we discussed previously. That is why many work are based on simplified foam systems with well-controlled configurations, including the confinement of bubbles into narrow tubes [22]. When we confine equal-volume bubbles inside a tube, they always rearrange themselves following the geometries and topologies dictated by Plateau's laws [1]. Complex ordered structures are then obtained which depend on the ratio between the dimensions of the tube and the volume of the bubbles. Some of the most classic examples are shown in Figure 1.4a for the case of cylindrical tubes in which the bubbles form different ordered structures by reducing the bubble volume. These kind of experiments were already used to study specific foam structure [23, 24, 25] or investigate their drainage [20].

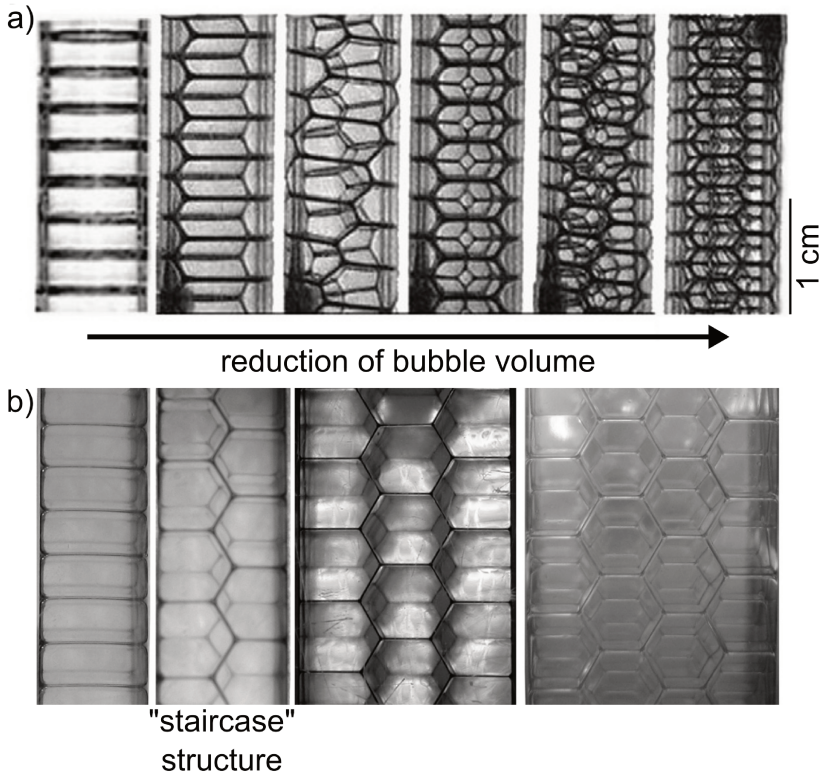


Figure 1.4 – Ordered foam structures in a) cylindrical tubes (from [22]) and b) square cross-section tube (from [18]).

To investigate ordered structures even further, some researchers have confined monodisperse bubbles inside a square cross-section tube [18, 26]. The different possible arrangements proved to be governed by the confinement ratio of the bubbles inside the column (Fig. 1.4b). For our model system, to study elasto-capillary interactions between a foam and an intruder (Chapter 2), we selected the so-called *staircase* structure that offers an invariance by translation along the axis perpendicular to the tube, providing a quasi-2D model system with a well-defined ordered structure.

1.2 Towards solid structures: Liquid foam templating

New approaches to produce solid foams from liquid precursors have recently been developed, known as *liquid foam templating* [2]. The principle is to produce a stable liquid foam from a monomer or polymer solution and then to solidify the continuous phase. The structure of the resulting solid foam is determined by the liquid foam characteristics (Section 1.1).

To obtain solid foams with the same structures as their liquid templates, the bubbles need enough time after generation to reach an equilibrium before solidification but the solidification time need to be short enough to avoid destabilisation. The key parameters are the initial liquid properties (such as the viscosity), the foaming process, the solidification kinetics and the involved foam timescales (drainage, foam ageing, evaporation).

1.2.1 Challenges of liquid foam templating

1.2.1.1 Drainage

Under the effect of capillary forces and gravity, the liquid contained inside the foam drains, firstly, from the films into the Plateau borders. It is a negligible contribution because of the very small quantity of liquid involved, the liquid is therefore mainly inside the Plateau borders and drains from the top to the bottom of the foam. The downward flow of liquid reduces the density of the foam as a function of the foam height and the liquid accumulates at the base of the container. A density gradient can then be observed, as shown in Figure 1.5a. For many studies, the control of the liquid fraction can be important, especially to create homogeneous solid foam via the liquid foam templating methods. Several experimental tricks have already been proposed to counterbalance this density gradient.

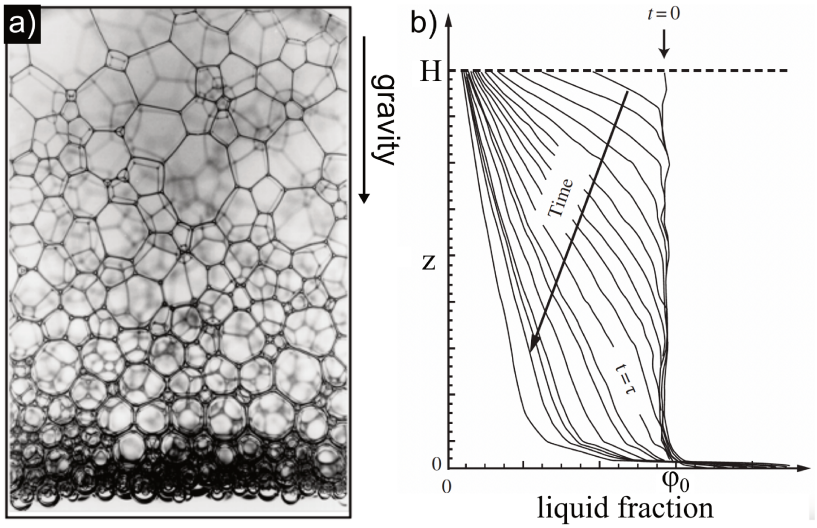


Figure 1.5 – a) Picture of a liquid foam subjected to gravity. Taken from [11] b) Vertical profiles of liquid fraction as a function of time measured by electrical conductivity. Taken from [12].

Dealing with the drainage to obtain high-density foam structure

One of the simplest way is to add a continuous flow of liquid at the top of the foam. This method is known as *forced drainage* and results in a high-density foam structure which is constant as long as the liquid is flowing [27]. Another method is to work in microgravity (used in very few experiments because it requires more resources: finances, contacts, scheduling), where the gravitational drainage is essentially turned off, as done by Vandewalle et al. [28] and Barret et al. [29]: bringing foams, respectively, aboard the International Space Station (ISS) or parabolic flights.

An alternative is to use capillary effects which result in liquid rising into the foam when in contact with a liquid surface. The liquid can then rise in the Plateau borders on a height H, given by: $H \sim l_c^2/d$ with d the average bubble diameter and l_c the capillary length of the liquid phase, such as $l_c = \sqrt{\gamma/\rho_l g}$ (where γ is the surface tension of the liquid phase of the foam, ρ_l the liquid density and g the acceleration due to gravity) [9]. For typical surfactant aqueous solutions, $l_c \approx 1.6$ mm [30]. In other words, by reducing

the bubble size (around 100 μm for example) we can obtain stable high-density foam with several bubble layers.

It is therefore possible to produce a high-density foam structure using a solidifying liquid material with controllable kinetics in such experimental devices.

Dealing with the drainage to obtain low-density foam structures

One useful parameter for characterising drainage in a liquid foam is the drainage time, which can be estimated by:

$$\tau_D \approx \frac{\eta}{(1-\phi)^{\alpha} d\rho g} \tag{1.2.1}$$

with η the viscosity of the foaming solution, d the average bubble diameter, ϕ the liquid fraction and α (with $0.6 < \alpha < 1$) a dimensionless constant depending on the "mobility" of the liquid-gas interfaces [12].

If we take a liquid foam of height H_0 and high liquid fraction ϕ_0, the liquid will flow downward due to gravity, the Plateau border size will slim down from the top to the bottom of the foam (Fig. 1.5a). The profiles of the liquid fraction as a function of the foam height and time can then be plotted, as shown in Figure 1.5b. In the initial state, $t = 0$, the foam is dense and homogeneous and becomes less and less dense and homogeneous as it drains. At $t = \tau$, the drainage front reaches the bottom of the foam [12].

Thus, by controlling the solidification time, it is possible to stop the drainage and therefore solidify the foam at a given density. Either by waiting for the foam to reach a very low liquid fraction and then solidifying rapidly, or by studying only the bottom of the foam, for example, to obtain a homogeneous sample with a higher density. Moreover, the choice of the material is important because this drainage time also depends on the initial viscosity of the foaming solution.

1.2.1.2 Foaming process

All foaming techniques consist in generating bubbles within a liquid. We can differentiate foaming techniques by the way we insert the gas into the liquid and inject the energy needed to create bubbles. There are two global mechanisms of foaming that can be use with the liquid foam templating technique: *physical* and *chemical foaming* (Table 1.1). The idea behind the liquid foam templating method is to use a solidifying liquid or a liquid that can solidify under the effect of an external stimulus (temperature, UV for example).

Global mechanisms	Sub-mechanisms	Examples
Physical foaming	Mechanical foaming	Bubbling (through nozzle, porous media), shaking, rotor-stator, mixers, double syringe technique
	Phase transition	Extrusion
Chemical foaming	Chemical reaction	Polyurethane foaming

Table 1.1 – Classification of different foaming techniques that can be used with liquid foam templating [31].

The techniques used during this PhD work are detailed below.

Chemical foaming

This technique creates foams by releasing gas following a chemical reaction. A well known example is polyurethane foaming (described in more details in Chapter 4): foams are prepared by mixing component A (isocyanate) and component B (a mixture of polyol, catalyst, surfactant and water) at room temperature. After a series of chemical reactions, carbon dioxide is formed and then released. With this technique, the obtained foams are totally polydisperse and bubbles sizes are typically of a few hundreds of micrometers.

Mechanical foaming

The principles of the mechanical foaming is to entrain air at the surface of the blended liquid to create large bubbles. Then, large bubbles are broken under the continuous shearing action. As the bubbles break, the gas fraction increases and the average bubble size decreases over time. With this technique, polydisperse foams are obtained with bubbles size ranging from some tens of micrometers to a few millimeters [31].

Mechanical foaming: Bubbling through a nozzle

With the bubbling through nozzle method, gas is blown through one or more nozzles into a stationary foaming liquid. When a bubble forms at the nozzle, buoyancy force is counterbalanced by surface tension forces and the bubble remains attached to the nozzle until its volume reaches a critical value. The bubble is then accelerated upwards and detaches [32]. This method has already been studied experimentally [33, 34, 35] and theoretically [36] in order to obtain an adequate prediction of bubble size. Many parameters can be used to control and adjust bubble size to create obtain a customised foams: The gas pressure, the surface tension and viscosity of the liquid, the dimensions and the shape of the nozzle, the wetting conditions, the density of the gas and liquid and the bubbling regime (quasi-static, dynamic or turbulent) [37, 32].

1.2.2 The resulting solid foam structure

If the liquid foam is sufficiently stable and well-controlled, the resulting solid foam structure will be identical to that of its liquid precursor, but some vocabulary changes

when passing to solidified foams: We saw in Section 1.1 that the key parameters are the bubble size, dispersity and liquid fraction. The solid foam are also characterised by the bubble size distribution and their dispersity, but in some cases, the terms *cells or pores* are used instead of *bubbles* and the *liquid fraction* is no longer used in solid systems, we keep the notion of *relative density* (Section 1.3). In terms of Plateau's laws, which dictated the low-density liquid foam, once solidified we use *struts* instead of Plateau borders. Systematic research into solid foams produced using the liquid foam templating method also focus on *cell connectivity*. Liquid foams are *closed-cell* foams because a thin film separates two bubbles, but by controlling drainage and solidification, *open-cell* foams can be obtained where only the network of struts and vertices remains.

1.3 Properties of cellular materials

Solid foams are part of the *solid cellular materials* category and have enabled researchers and manufacturers to explore a new range of materials by reducing the relative density of existing systems (Fig. 1.6). For example, low density foams allow lightweight materials to be designed with adjustable mechanical, thermal, acoustic and electrical properties, by an appropriate choice of the constituent material.

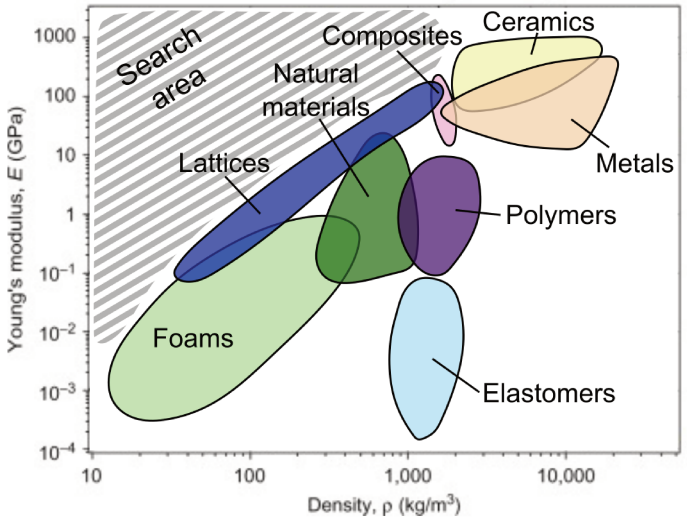


Figure 1.6 – Young modulus-density diagram for different material categories. Updated in 2010. Adapted from [38].

By knowing the parameters that control the mechanical properties of cellular materials, improvements can be made upstream in the choice of foaming process, formulation and solidification kinetics in order to tune the mechanics of the foams. L.J. Gibson and M.F. Ashby [39], specialists in materials engineering and mechanical behaviour of cellular materials, give the three main factors which dominate the properties of cellular solids:

- The material in which the foam is made
- The cell topology and shape
- The relative density

The combination of these properties allows foam to achieve applications that cannot be reached with bulk solid materials.

Influence of the material in which the foam is made

Solid foams have the advantage of being able to be formed by different foaming processes (Section 1.2) in many materials already known in bulk: polymers, metals or ceramics (Fig. 1.6). The use of these materials give foams unique properties [39], for example, the use of an elastomeric matrix can result in a very low density material able to accept very large deformations (70 % and more), whereas metallic or ceramic foams are characterised by high density and rigidity. On the other hand, ceramics have a brittle behaviour but interesting thermal properties.

Influence of relative density and cell topology and shape

Solid foams are physically characterised by their relative density, ρ_{foam}/ρ_s, where ρ_{foam} is the density of the foam and ρ_s that of the solid of which it is made [39]. It corresponds exactly to the liquid fraction, respectively, in liquid foam (Section 1.1).

The equation which links the relative density to the strut length and thickness depends on the cell connectivity (open-cells or closed cells) of the foam (Section 1.2.2) and on the dimensions (2D or 3D), as shown in Table 1.2 with the example of 2D Honeycombs, 3D open- and closed-cell foams:

	2D Honeycombs	**3D open-cell foams**	**3D closed-cell foams**
Relative density ρ_{foam}/ρ_s	$C_1\frac{t}{L}$	$C_{12}(\frac{t}{L})^2$	$C_3\frac{t}{L}$

Table 1.2 – Theoretical equations of relative densities with L the strut length, t the strut thickness ($t << L$) and C_s are numerical constants which depend on the cell shape [39].

1.3.1 Mechanical behaviour of solid foams via compression tests

Foams are often characterised mechanically via compression tests, as done in the context of our work in Chapter 5 (Fig. 1.7).

A force F is applied to the top surface S of a foam sample, resulting in a displacement Δl from an initial height l_0 to a height l such as $\Delta l = l_0 - l$. As shown in Figure 1.8, we can therefore plot the normal stress σ, defined as

$$\sigma = \frac{F}{S} \tag{1.3.1}$$

as a function of the strain ϵ, defined as

$$\epsilon = \frac{\Delta l}{l_0} \text{ [39].} \tag{1.3.2}$$

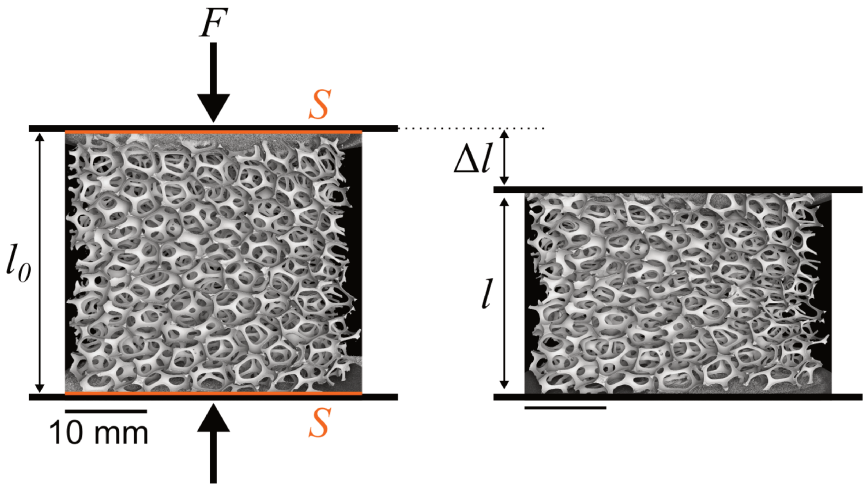


Figure 1.7 – Compression test on a polyurethane foam from Chapter 5 with the main parameters highlighted.

First of all, a linear elastic domain appears (highlighted by a blue box in Figure 1.8): the foam structure (struts and walls) begins to bend elastically, i.e. it returns to its initial state when the stress is removed. The slope of this linear elastic part defines the elastic modulus Y. Note that despite Y is proportional to the Young modulus of the constituent material of the foam, it is usually considerably smaller as the materials are essentially subjected to bending, even in the linear regime of the stress-strain curve (Fig. 1.7). Elastic modulus is a quantitative measure of a material's stiffness, which depends on the nature of the polymer (elastomeric, plastic, brittle) and the morphology of the foam [39].

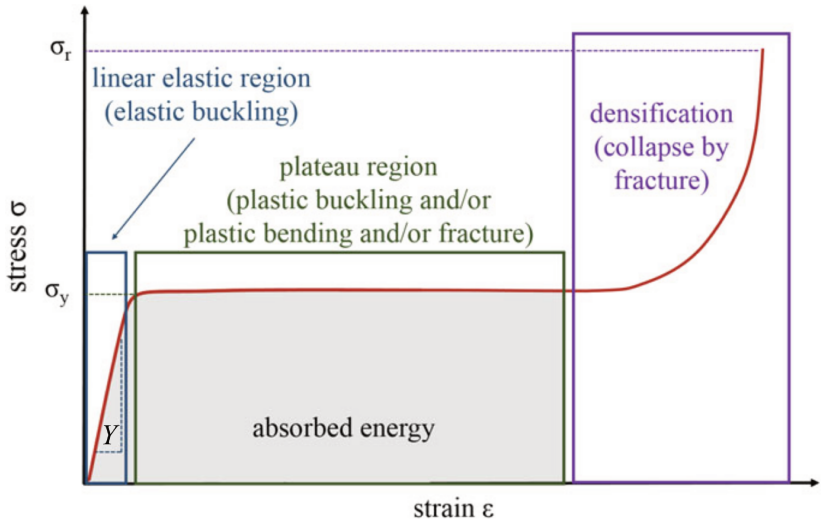


Figure 1.8 – Typical stress-strain curve of an elastomeric foam tested in compression. The three characteristic domains are highligted: the linear elastic, plateau and densification regions. Reproduced from [40].

With the same example than above, Table 1.3 lists the elastic modulus for different dimensions (2D or 3D) and cell connectivity.

	2D Honeycombs	3D open-cell foams	3D closed-cell foams
Relative elastic modulus $\frac{Y_{foam}}{Y_s}$	$C_4\frac{\rho_{foam}}{\rho_s}$	$C_5(\frac{\rho_{foam}}{\rho_s})^2$	$C_6\Phi_v^2(\frac{\rho_{foam}}{\rho_s})^2 + C_6'(1-\Phi_v)(\frac{\rho_{foam}}{\rho_s})$

Table 1.3 – Theoretical equations of relative elastic modulus of a foam Y_{foam}, with Φ_v the fraction of solid material distributed within the foam structure and C_s numerical constants which depend on the cell shape. For fully open-cell foams, there is no wall so we can assume $\Phi_v = 1$ [39].

Stress reaches a plateau at a fixed value known as the yield stress σ_y, as soon as the elastic limit is reached. The deformations turn irreversible and are no longer elastic. In the plateau region (highlighted by a green box in Figure 1.8), the cells collapse locally, at a point of weakness of the foam: Bubbles deform irreversibly layer by layer at almost constant stress. The area below the stress-strain curve in the linear elastic and plateau regions is equal to the energy absorbed by the foam, i.e. the energy required to crack the material. This provides a numerical indicator of the toughness of the foam [39].

When two opposite sides of the cells begin to touch, foam deformation reach what is known as the densification domain (highlighted by a purple box in Figure 1.8), resulting in a significant increase in stress. The strength of the material, or its resistance to fracture, can be here quantified by the maximum stress, also known as the stress at rupture σ_r [39].

Moreover, the response of the foam to compression tests and then the shape of the stress-strain curve can differ according to the morphology of the foam (density, dispersity, connectivity) and the nature of the material in which the foam is made [39].

Based on computer simulations of two-dimensional foams from [41], Figures 1.9a, b, and c show the qualitative variations in the stress-strain curve of a polymer foam when its morphology is changed. We can see in Figure 1.9a that the higher the relative density, the higher the elastic modulus and the yield stress. In fact, when we increase the relative density, we increase the amount of material in the foam structure. The mechanical response of the foam is therefore closer to the mechanical properties of the material constituting the foam. In terms of cell dispersity, a foam (made from the same material and at constant density) reacts in the same way in the elastic domain, regardless of its dispersity. A disordered polydisperse or monodisperse foam reaches the densification domain sooner than an ordered monodisperse foam [41].

As explained above, the material of which foam is made also influences the mechanical properties of a foam. Figures 1.9d, e, and f show typical stress-strain curves for different materials. When the compressive load is applied beyond the elastic limit, the cell edges buckle for a elastomeric foam (Fig. 1.9d), yield plastically for foams made of ductile materials (Fig. 1.9e) or fracture if the foam is made with a brittle material (Fig. 1.9f) [39].

In addition, the shape of the cells have a great influence on the mechanical behaviour. When the shape of the cells has no preferred direction, the properties are isotropic. On the other hand, if the cells are elongated or flattened, anisotropy is induced, resulting in different mechanical behaviour depending on the direction in which the test is performed [39].

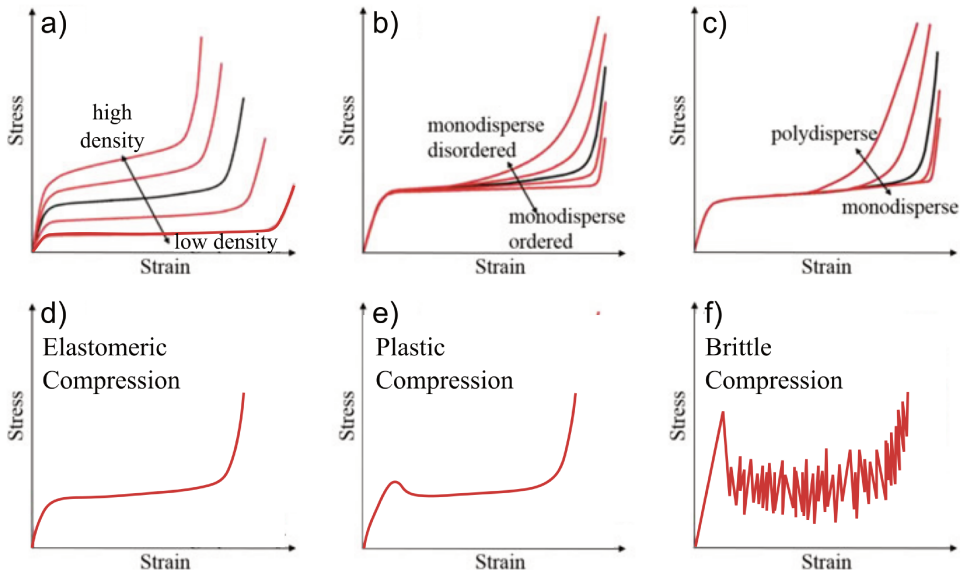


Figure 1.9 – Influence of a) the porosity, b) the order, c) the polydispersity and d-f) the material in which the foam is made on the shape of the stress-strain curve of a two-dimensional foam. Adapted from [39, 41].

1.3.2 Bending- VS Stretch-dominated structures

If rigidity is the key word, foams are not the best candidates, as shown in Figure 1.6: their struts tend to bend under load, which makes them interesting for energy absorption applications, but not for supporting a load. Foams are classified as bending-dominated structures because a foam is a cellular material obtained by self-assembly according to Plateau's laws, which means that their strut connectivity is low (i.e. the number of struts that meet at the vertices) [39].

Foams compete with lattice structures, which are also porous architectured materials based on the repetition of a unit cell. This structure is well known in 3D printing. Their geometry has much more strut connectivity than that of foams, which puts them in the category of stretch-dominated structures. When loaded, parts of these structures stretch rather than bend, making them stiffer and more suitable for lightweight and load-carrying applications.

Fleck et al. [38] showed that the elastic modulus for ideal stretch-dominated structures is proportional to the relative density while the modulus of ideal bending-dominated structures is proportional to the density squared. At a given density, the rigidity of the foams is then lower compared to that of the lattice structures. Moreover, in the previous sections, we compared the density and elastic modulus for open- and closed-cell foams because they are in different category. Indeed, open-cell foams tend to have a bending dominated behaviour while closed-cell foams tend to have a stretch dominated behaviour. The difference is caused by the relative amount of material in the struts and the walls [39]. In addition, Berger et al. [42] studied four closed- and two open-cell geometries (Fig. 1.10a-f). It has been shown that cubic + octet foam material can maximize stiffness-dominated performance, reduce energy storage in dynamic systems, and minimize the weight of the material. They explained how periodic foams with ordered unit cells (i.e. the closed-cell analogue of lattice structures) are capable of reaching the

highest elastic modulus. It is what the graph shows in Figure 1.10g): cubic foam or cubic + octet foam geometries have the largest modulus.

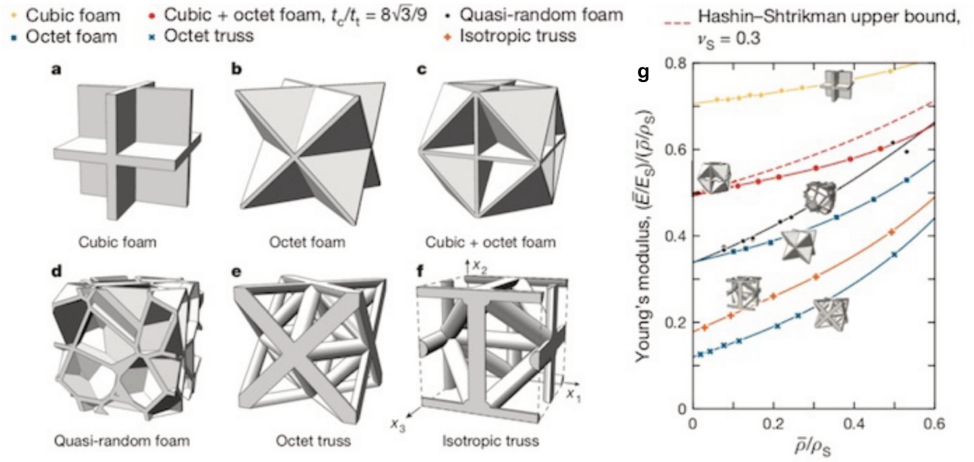


Figure 1.10 – a)-f) Six material geometries characterised in g) with the Young modulus as a fonction of their relative density. Taken from [42].

In contrast to lattice structures, which are often 3D printed, foams have the advantage of being mechanically self-assembled. The inclusion of fibres in foams lead to architectured materials with new structures approaching the mechanical properties of stretch-dominated structures.

1.4 Foam characterisation

After a brief state of the art of the structural characterisation of foams, this section describes the various tools used to structurally characterise foams with or without fibres. We briefly present the principles of X-ray microtomography and the parameters that are important to control when characterising foams. We focus on the *foam/powder analysis* tool provided by VG Studio MAX 2023.1 software, available at the X-ray microtomography platform. We explain the limited number of physical parameters it allows to measure at the foam scale and discuss the shortcomings of this software for the analysis of our samples. We then present a Matlab programme based on the strut network extraction, developed by Jean Farago.

1.4.1 State of the art: Structural characterisation of foams

Foams are complex architectures that are difficult to characterise because of their hierarchical structure (films, struts, vertices, as shown in the Section 1.1). Some experiments on foams still rely on direct visual observation: the first known study was carried out by E.B. Matzke in 1945 [43]. Using a microscope, he observed nearly 5000 bubbles of a liquid foam and counted the number of faces and struts that make up each bubble. He also looked at the shape of each bubble and checked Plateau's laws. When liquid foams are squeezed between two glass plates, the system remains in a simplified quasi-2D system. This other method facilitates the study of their structure and, for example, of their temporal evolution [9, 12].

For solid foams, the most common method is to slice the foam into thin strips and then study them under an optical microscope. As an example, the work of T.C. Cotgreave et al. shows microscopy images of a slice of a sample of 1.5 ± 5 mm thick of a polyurethane foam reinforced with chopped glass fibres [44].

In this thesis, we focus on X-ray tomography techniques both for liquid and solid foams, a characterisation technique already widely used for the in-situ study of foams [45, 46], with the advantage of being non-destructive in the case of solid foams (Section 1.4.2 for more details). For liquid foams, the main experimental challenge is foam stability. This is why the formulation is often meticulously chosen to improve stability. This is a challenge that we had to adress in our study described in Chapter 2.

For the statistical study of solid foam structures using tomographic images, we can cite in particular the work of K. Mader et al. [47]. They were interested in the polydispersity of the foam's bubbles, its homogeneity and even its potential anisotropy resulting from the internal stresses developed during solidification. In addition, thanks to the tomographic data, the traditional measurement of the foam mass density (or quantities equivalent to the volume fraction of the material) as a global characteristic is now supplemented with a very precise evaluation of the mean bubble size and standard deviation, the sphericity of the bubbles and the resulting anisotropies, for example. In this way, all the information now available from X-ray tomography is useful not only for checking the homogeneity and reproducibility of the foams, but also for finely characterising and comparing samples, particularly when solid inclusions are incorporated [48]. To our knowledge, the pioneering work in this direction is probably that of by Montminy et al [49, 50], who wrote a software making the extraction of the strut network, and allowing specific statistical measurement on it. In [50], for a few thousand struts, they calculated the angle formed between two struts at a common vertex and the number of edges per face from a tomography of commercial polyurethane foam. In the following sections, we will present in more details the X-ray tomography techniques as well as the foam analysis that we developed and performed on our samples.

1.4.2 X-ray microtomography

X-ray tomography is a non-destructive imaging method in which 2D radiographs are stacked to reconstruct a 3D object. X-radiations were discovered by the physicist Wilhelm C. Röntgen in 1895 [51]. It was only in the 90s that X-ray tomography was developed in other economic sectors than medicine: For new product development, process control, non-invasive metrology, material performance prediction and failure analysis. Later, with industry and military demands, performance in terms of resolution improved. Resolution can now reach the scale of 1-10 μm and is known as X-ray microtomograph [52].

At the Charles Sadron Institute, we use an X-ray microtomograph EasyTom 150/160 from RX Solutions, XAct software to generate stacks of radiographs, which are then imported into VG Studio MAX 2023.1 software to reconstruct 3D structures.

1.4.2.1 X-ray tomography principles

As shown in Figure 1.11a, the sample is placed between a X-ray source and a detector. A monochromatic X-ray beam penetrates through the sample to the detector, which records a series of 2D projections of the object (radiographs). X-ray absorption depends on the thickness, density and chemical composition of the material. On these radiographs,

the contrast between each sample element is therefore given by the different levels of X-ray absorption of the material. During a measurement, the sample is rotated, allowing images of the object to be obtained at different angular positions. One 2D projection is obtained for each angular position. The recorded projections are then stacked to reconstruct the volume of the sample, using the filtered back projection method (Section 1.4.2.2). The final result is a 3D gray-scale image that we can browse using 2D slices (Fig. 1.11b). The elementary cubic element of these images is called a voxel (pixel in 2D) and its size gives the precision of the resolution. An "adequate" resolution is chosen as a function of the ratio between the source/sample and the source/detector lengths, as well as the size of the sample. For example, in this Ph.D work, for a cubic sample of 35 $\pm$ 5 mm width, the resolution is 25 microns. This can be reduced to 0.7 μm for a sample of a few millimetres. The maximum size of the radiographs is 1920 x 1536 pixels, which in fact corresponds to the dimensions of the detector. To obtain a "good" resolution, at least three voxels are required across the thickness of an object. If this ratio is not respected, as it is often the case for the thickness of the films separating two bubbles, smaller than the voxel size, the software will not be able to detect those thin structures (Fig. 1.11b).

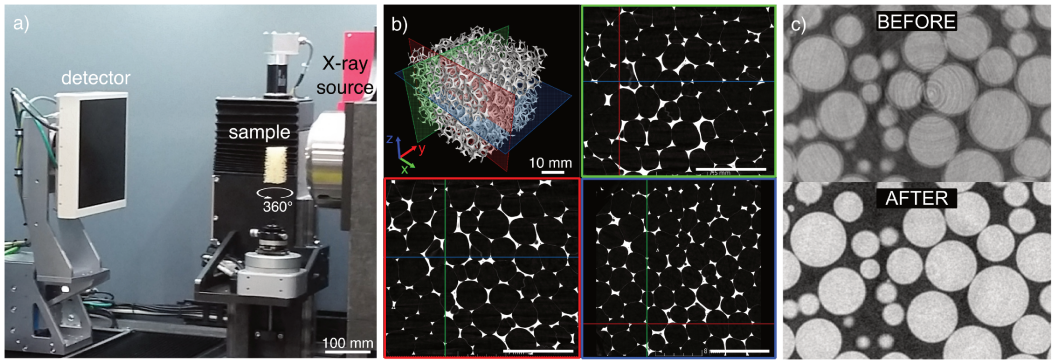


Figure 1.11 – X-ray tomography principles: a) Picture of the X-ray microtomograph at the ICS, including the X-ray source, sample and detector. b) 3D-view of a foam and its three slices corresponding to the x, y and z axis. Note that only the struts are visible in the image because the film thickness is smaller than the voxel size. c) Example of ring artefact correction (credits: RX Solutions).

1.4.2.2 3D image reconstruction: Filtered back projection

The resulting 2D projections are given in grey scale. In order to define the maximum and minimum values of this scale, black and white calibrations must first be carried out. A black calibration is used to remove background noise from 2D and later 3D images. This calibration takes place with the generator switched off, so that the low pixel values are recorded. Then, white calibration allows a uniform response from each pixel. With the generator switched on, "defective" pixels are detected and corrected by replacing them with the average value of neighbouring pixels. The images are then rescaled according to these new extreme pixel values.

The 3D reconstruction of images corresponds to the sum of the grey levels of each pixel. The X-Act software then recalculates the numerical values of the grey levels voxel by voxel to reconstruct a 3D image. If there are any defects (sample movements, X-ray beam artefacts), the software applies filters to correct the images or realign the 2D projections.

This method is known as filtered back projection.

The main filters used on the images from all the experiments in this PhD work correct:

- the focal spot movement: correction of the images for potential movements of the source and the sample. At the end of each measurement, 32 images are taken at different angular positions and then compared with the initial images. If there is a difference between the two, the software can correct it.
- the geometry defect: realignment of the image stacks if they have shifted from one to the other.
- the ring artefact: correction of the circular artefact centred on the axis of rotation, due to the non-linear response of the detector (Fig. 1.11c).

A last filter is also used to reduce background noise: the Butterworth filter.

1.4.2.3 Foam analysis from VG Studio software

In the case of foam, the phase-segmentation of the image (i.e. the distinction between matter and gas) is then initiated by hand to ensure that all the material is taken into account, i.e. which voxel is gas and which one is material, using a cursor on a histogram evaluation in VG Studio. It is very useful for the segmentation of a multi-phase object (i.e. the distinction between the material constituting the foam and any other intruders/objects), but possible only if the contrast between the different parts is sufficient. In the case of alginate samples (Chapter 3), for example, the foams could not be removed from the container, so its walls are visible in the images (Fig. 1.12a). The VG Studio software then automatically counts them as part of the foam. Yet another segmentation must then be carried out by hand to remove the walls from the images. For a foam-fibre system (Chapter 5), it is possible to separate the fibres from the foam to plot their coordinates on a new graph (Fig. 1.12b) or simply to visualise only the fibres (Fig. 1.12c), which can be used, for example, to see the deformation of the fibres in the foam during the in-situ compression described in Section 5.3.3.

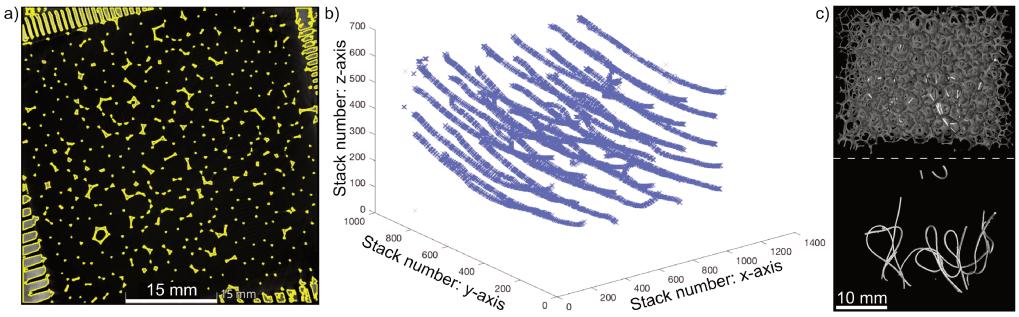


Figure 1.12 – Tomographic image segmentation: a) 2D slice of a foam in a container. In yellow, the detection of the material boundary carried out automatically by the VG Studio software. b) Coordinates x, y and z of the fibres extracted from tomographic slices of a foam-fibre system and plotted using Matlab. Credits: Pierre Guichard's internship. c) Top: 3D-reconstruction of a foam-fibre system; Bottom: 3D-reconstruction of the fibres only.

A *foam/powder analysis* tool is provided by VG Studio to measure several physical parameters at the foam scale, such as the bubble size (volume, equivalent diameter),

structure thickness, sphericity, porosity and the bubble orientation.

To measure the bubble size, the software uses the value of the equivalent diameter, defined as the diameter of a sphere that has the same volume as the bubble. To determine the structure thickness, VG Studio inscribes spheres inside the struts and vertices and measures their diameter, it will then count the number of voxels in each sphere and give a histogram showing the thickness distributions (number of voxels counted for each thickness). Sphericity is measured by calculating the ratio *(surface of a sphere of same volume)/(surface of the bubble)*. Porosity is the volume of the whole sample (matter and gas) minus the volume of the material. For the orientation of the bubbles, the software gives the norm of the principal, medium and least pronounced axis, calculated from a Principal Component Analysis [53].

To illustrate the realisation of these measurements, Figure 1.13 shows the various steps of the characterisation and the measurements made using VG Studio software. For foams in Chapters 3, 4 and 5, tomograms were performed on the zone at the bottom of the foam (i.e. the future location of the fibres), highlighted with a dotted line in Figure 1.13a. With the tomograms, the reconstructed 3D image measures approximately 45x45x35 mm (Fig. 1.13b). Figure 1.13c shows the bubble size analysis, where only the bubbles are represented and Figure 1.13d shows the structure thickness analysis, where only the material is coloured. The same colour corresponds respectively to the same bubble diameter or the same thickness (the vertices thus appear in green and the struts in blue). Note that bubbles at the borders of the sample are automatically excluded from the measurements to avoid possible errors due to edge effects. Indeed, as it can be seen in Figure 1.13a, PU foam imprints the shape of the container, and this is also true for alginate foams which are not unmoulded and therefore placed in the tomograph (container included). For both systems, bubbles in contact with the walls are deformed, which is why we excluded these bubbles and struts from the measurements.

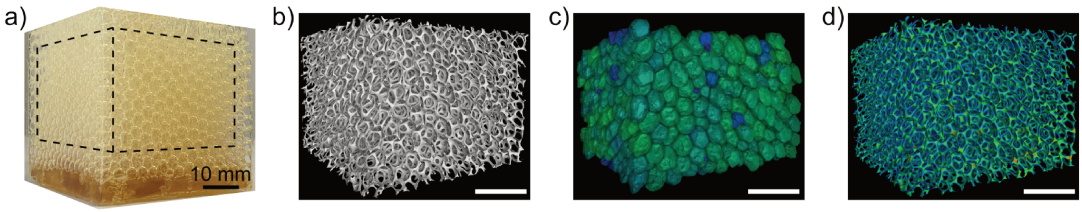


Figure 1.13 – Foam analysis steps: From the sample to the VG Studio software reconstruction and measurements. a) One PU foam sample, prepared following the protocol described in Chapter 4. The entire sample is placed in the tomograph, the dashed lines define the scan zone. Resolution: 25 μm. b) 3D reconstruction of this PU foam with VG Studio software, all PU parts highlighted in grey. c) Bubble size analysis. Only the bubble volumes are represented: identical colours correspond to identical bubble volumes. d) Structure thickness analysis. The material is coloured: vertices are in green and struts in blue. Note that bubbles at the sample borders are automatically excluded from the measurements. Scale bars: 10 mm.

This foam analysis tool can also be used to analyse the sample locally, at the scale of a strut (Chapter 3) or at different foam heights (Chapter 5). Local analysis can be performed by defining regions of interest (ROIs) with VG Studio, to focus on smaller volumes of the sample and carry out specific measurements.

1.4.2.4 Limitations of the VG Studio software

Despite the robustness of this software, it has certain limitations that can lead to errors in various measurements. The strut thickness measurements suffer from higher approximations when measured by the software within the whole sample than what could be measured by looking manually at each strut thickness (in that case, the error would be of the order of 1 or 2 voxels). Moreover, if the software is not able to detect films between bubbles, because the criteria for a good resolution have not been met (Section 1.4.2.1), it can artificially create edges between them (Fig. 1.14a) which induce errors in the volume measurements. We have also detected some inconsistency in the sphericity and porosity measurements. As explained in the Section 1.4.2.1, a threshold controls the segmentation of the bubbles. In the use of the *foam/powder analysis* tool, we also need to determine the sensibility threshold. If it is inadequate, the software can divide one bubble into multiple bubbles (Fig. 1.14b) or merge multiple bubbles into one single bubble (Fig. 1.14c). In some cases, compromises have to be made (in particular on the choice of resolution and threshold) and kept for each experiment so that they can be compared with each other. Some examples of the impact of the sensibility threshold are described in Appendix 1.

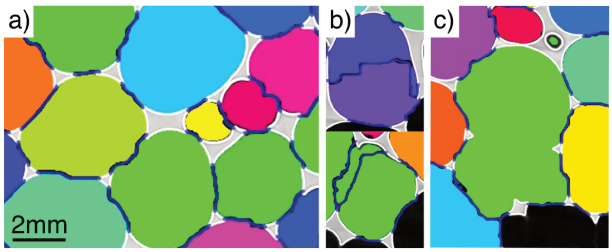


Figure 1.14 – 2D images of a polyurethane foam without fibre from the VG Studio software: a) Focus on a few bubbles where the blue lines correspond to the artificial edges created. In this case, the software has created this edges correctly, i.e. they are connected on both sides to a vertex and separate two bubbles; b) Second example where the sensibility threshold is set too low: Bubbles can be segmented by the software. Artificial edges can be created from defect present on some strut. c) Third example where the sensibility threshold is set too high: Bubbles can be merged by the software. Edges can be removed.

The software provides sufficient elements to carry out a global and statistical study of the geometrical characteristics of the bubbles and the foam structure. These statistics extracted from the VG Studio software are useful to check the homogeneity and reproducibility of the generated foams, with or without fibres. However, to perform in-depth analysis as well as local measurements, we started developing our own analysis tools, described in the following paragraphs.

1.4.2.5 Dual scaffold analysis

Characterising foams only by the size of the bubbles and the thickness of the structure would miss a significant information, namely the fact that foams, with their struts and vertices, form a scaffold or network. It is therefore possible to carry out a dual and complementary analysis to that proposed by the VG Studio software, by extracting the topological network of struts and analysing its structure. For this purpose, a home-made extractor of strut network has been written by Jean Farago, in Matlab, allowing specific

statistical measurements. The programme, called `FoamTopologyExtraction.m` will be made available in a public repository. It was inspired by the work of Montminy et al. [49, 50]. Their software (from [49, 50]) only runs on obsolete versions of Windows and as their code is not available, the rewriting has been done from scratch, using Matlab's image processing toolbox.

All the steps involved in extracting the strut network are summarised in the Figure 1.16 and illustrated in the Appendix 2.

The first steps are to read the stack of 2D greyscale images provided by the VG Studio software, subtract the background and binarise them; the foam scaffold is then skeletonised (Fig. 1.15).

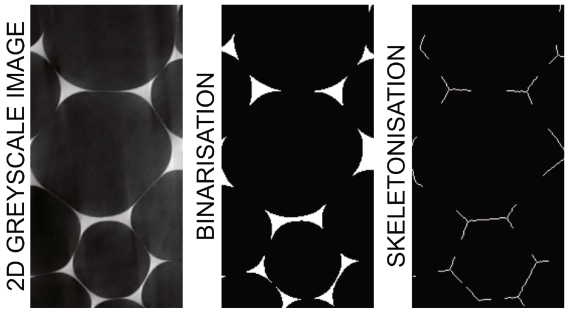


Figure 1.15 – Initial steps of foam network skeletonisation from 2D tomographic images.

To simplify the reading, we call a n-order vertex, $O(n)$, a vertex with n struts connected to it. As a reminder, equilibrated foams exhibit tetrahedral structures (Section 1.1.2), meaning that in principle four struts are always expected to be connected to a vertex. This vertex is therefore of order 4, $O(4)$. In addition, each strut is connected to two vertices on both sides. In fact, there always remains a minor proportion of defects, characterised by an order other than 4. This reflects the fundamentally metastable nature of foams. For the rest of the network extraction procedure, we need to distinguish between the defects potentially created by the programme during steps 4 to 6 (Fig. 1.16) and those that are real. The defects present in the extracted skeleton can be:

- vertices of order other than 4,
- isolated struts: a strut connected only to one vertex,
- loops: a strut connected twice to the same vertex,
- redundancies: two vertices connected directly by distinct struts,
- spurious vertices: a $O(2)$ vertex which divides a strut in two,
- trailing shoots: a $O(1)$ vertex.

FoamTopologyExtraction.m

1. Reading of a stack of `.gif` images.
2. Background substraction and binarisation (Fig. 1.15).
3. 3D skeletonisation with the Matlab command `bwskel`.
4. Removal of isolated struts, $O(1)$ and $O(2)$ vertices.
5. First extraction of vertices and struts, using the Matlab commands `bwmorph3(.,'branchpoints')` and `bwconncomp(.)`.

   The skeletonisation algorithm produces bunches of vertices, particularly when microbubbles are trapped in the vertices. These bunches are visible in the probability density function (PDF) of the strut lengths ℓ_s, with the presence of a peak at small ℓ_s indicating an unphysical excess of very small strut lengths (Fig. 2.2: solid blue line) and, as an example, they are represented in the Figure 2.3 in the Appendix 2.
6. Using the PDF(ℓ_s) to define an arbitrary distance G (also called gluing parameter) between two vertices in order to remove bunches of vertices. Vertices closer than G are glued together. The final vertex being the center of mass of all the glued-together vertices. Figure 2.2 shows the resulting PDF(ℓ_s) for different pixel values of G.
7. Cleaning up defects such as loops, redundancies, spurious vertices and trailing shoots. Note that this step is repeated until none of the four types of defect remain. This looping is necessary because the removing of one type of defect can generate others of a different type.
8. At the location of the vertex clusters, a certain number of $O(3)$ vertices remain. They must be removed, without destroying any real $O(3)$ vertices. A "conservative" point of view is adopted with two constraints: (i) Only pairs of $O(3)$ vertices closer than 1.5 G - 2 G are considered (a somewhat arbitrary upper limit); (ii) Only isolated $O(3)$ vertex pairs are glued together, i.e. when a $O(3)$ vertex are connected to only one other $O(3)$ vertex.

   The step 8 can generate some defects listed in point 7.
9. Repeating step 7 until there are no more defects.

Figure 1.16 – Summary of the steps involved in extracting the strut network. A vertex with n struts connected to it is called n-order vertex, $O(n)$.

To remove these defects, steps 7 to 9 (Fig. 1.16) must be repeated as many times as necessary. At the end of the process, we save the coordinates (x, y, z) of the remaining vertices and identify the pairs of vertices linked to each strut. Figure 1.17 shows the strut scaffold superimposed on the contours of the foam structure material extracted from the tomographic stack.

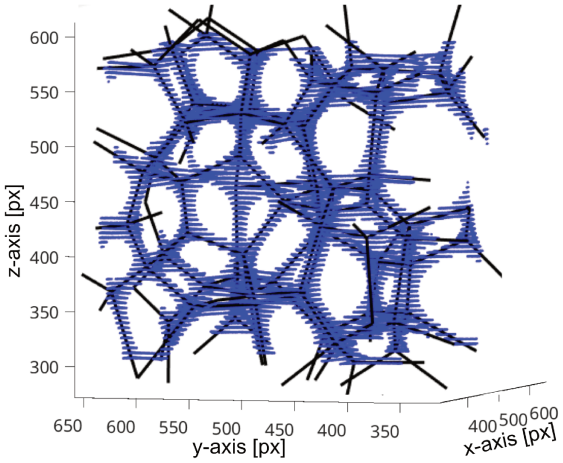


Figure 1.17 – Strut network of an alginate foam without fibres (produced with the protocol described in Chapter 5), with a gluing parameter $G = 20$ voxels and superimposed on the contours of the foam structure material extracted from the tomographic stack. Tomography resolution: 1px = 25 μm.

Once the strut scaffold has been extracted, statistical analyses can be performed. To do this, a second home-made programme has been written in Matlab, called `FoamAnalysis.m` and will be made available in a public repository. Despite the effort made during the scaffold extraction procedure to remove as many spurious $O(3)$ vertices as possible, we note that there are still some $O(3)$ vertices. To support these remarks, we use the example of an alginate foam without fibres, produced with the protocol with the protocole described in Chapter 3 but these observations are true for all the foams produced in Chapter 5. Thus, as shown in Figure 1.18a, for the whole sample of the reference alginate foam (without fibres), the proportion of $O(3)$ vertices is 15 %. After examining the samples, we can see in Figures 1.18b and c that the majority of these $O(3)$ vertices, represented by the black circles, are concentrated on the borders of the samples. As explained in Section 1.4.2.3, the bubbles in contact with the walls of the container in which the foams are made, are deformed. Moreover, the skeletonisation procedure during the numerical extraction of the struts creates artificially numerous $O(3)$ vertices at the boundary of the sample. This is why the presence of $O(3)$ vertices increases at the borders of the sample. We therefore decided to crop the borders of all samples in order to remove the outer vertices. To do this, this second programme allows to virtually cut the sample in horizontal layers (Fig. 1.18b) and radial sublayers (Fig. 1.18c). To help identify a relevant subset, two graphs are produced (Appendix 2), showing the distribution of $O(3)$ horizontally and radially, layer by layer. In Chapter 5, the analyses always consider such cylindrical subsets of samples, chosen to remove outer layers containing spurious $O(3)$ vertices.

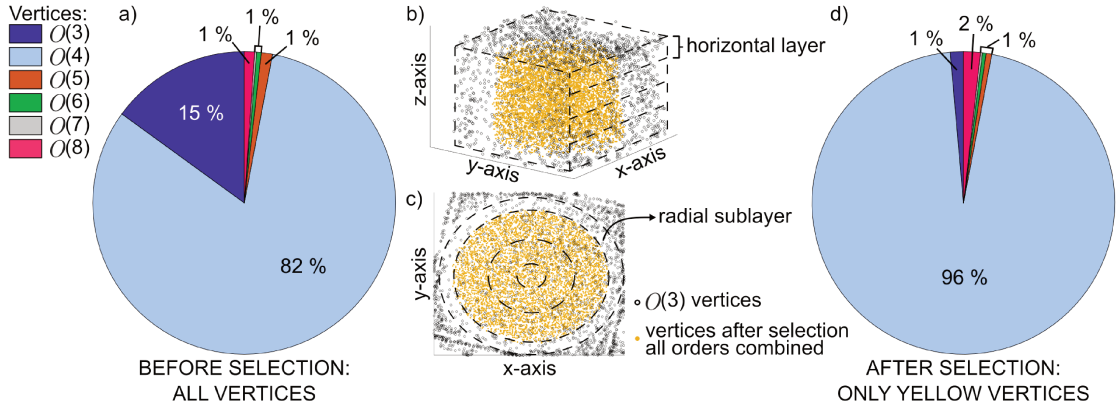


Figure 1.18 – Strut network sampling of an alginate foam without fibres (produced with the protocol described in Chapter 5). Extraction with $G = 20$ voxels. Tomography resolution: 25 μm. a) Proportion of vertex orders over the entire foam, before the sample selection. b) 3D repartition of vertices: in black the $O(3)$ vertices and in yellow the vertices (all orders combined) selected for future analyses. c) Top view of vertex repartition. The dashed lines show possible virtual horizontal or radial cuts in the sample. d) Proportion of vertex orders over the selected sample, highlighted in yellow in b and c.

Figure 1.18d shows the proportion of vertex orders in the selected samples, in yellow in Figure 1.18b and c.

The remaining vertices of order other than 4 are the signatures of materials aggregates that the programme is trying to represent. Figure 1.19 shows some examples of strut networks with vertices of order other than 4, highlighted and superimposed on a stack of 2D images. We can see the complexity of creating this type of network in the case of denser struts. In these cases, it is difficult for the programme to represent aggregates of material by simply alternating circles (representing vertices) and straight lines (struts). These vertices of order other than 4 represent a small percentage. We could consider them as a pair of $O(4)$ vertices or a $O(8)$ vertex and as representative of real defects present in foams.

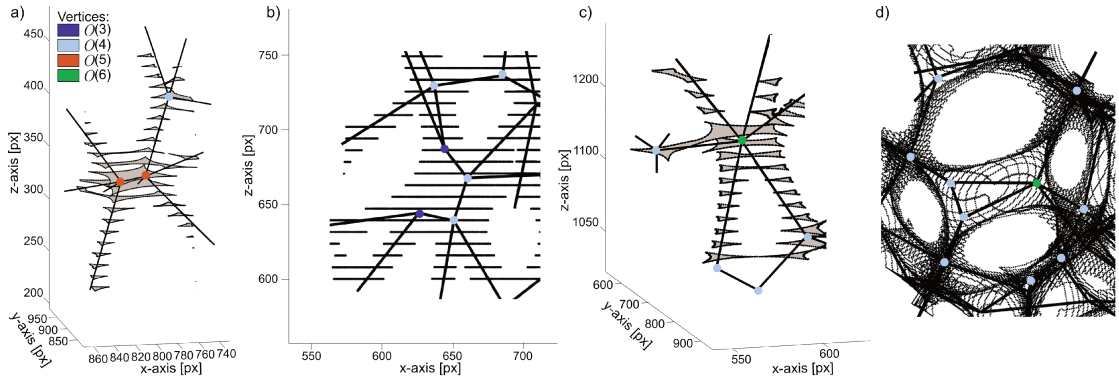


Figure 1.19 – Strut networks superimposed on a stack of 2D tomographic images of a PU foam without fibres (produced with the protocol described in Chapter 5). Extraction with $G = 20$ voxels. Tomography resolution: 25 μm. a) Pair of $O(5)$ vertices in a material aggregate. b) Alternation of $O(3)$ vertices and $O(4)$ vertices by the programme which try to be representative of a material aggregate c) $O(6)$ vertex. d) Top view of a $O(6)$ vertex (in green) on a material aggregate where small bubbles are trapped.

This home-made programme enables to extract the foam scaffolds very accurately. Despite some difficulties in representing the aggregates of material, the program still reflects the metastable nature of foams. In Chapter 5, we will study the order of the vertices, the distribution of the length of the struts and the angles between pairs of struts on foams with and without fibres. It will also enable to describe order in foam-fibre systems, in particular by coupling it with the use of Steinhardt parameters [54, 55].

Chapter 2

Elastocapillary deformation of thin elastic ribbons in 2D foam columns

Contents

2.1 State of the art: Elastocapillarity of slender structures 28
2.2 Materials and methods 29
2.2.1 Formulation of the soap solution 29
2.2.2 Elastic ribbons 29
2.2.3 Experimental setup 30
2.2.4 Characterisation 32
2.3 Results 33
2.3.1 Deflexion measurements 33
2.3.2 Equilibrium shapes 34
2.3.3 Theoretical interpretation 35
2.3.4 Application to bubble-based forming 38
2.4 Influence of gravity 39
2.4.1 Experimental modifications 40
2.4.2 Theoretical modifications 40
2.4.3 Results 42
2.5 Conclusion 43

The first challenge of this PhD work was to understand the key parameters involved in fibre-enriched foams. However, foams are complex structures with precise architectures dictated by Plateau's laws [1]: We needed a model experiment that illustrates in a simplified way what could happen in a fibre-enriched foam. We thus replaced the fibres with a single elastomeric ribbon and the liquid 3D foam with a 2D foam column composed of an ordered assembly of monodisperse soap bubbles (Chapter 1).

First, a short introduction is given on elastocapillarity of slender structures to highlighted the underlying mechanisms that dictate the different shapes of the quasi 2D foam-ribbon system. Then, we provide an experimental and theoretical framework to

quantify such equilibrium shapes, with an excellent agreement between experiments and modeling.

The following content is the basis of the article: **Elastocapillary deformation of thin elastic ribbons in 2D foam columns** by M. Jouanlanne, A. Egelé, D. Favier, W. Drenckhan, J. Farago and A. Hourlier-Fargette, Soft Matter, 2022 [56].

2.1 State of the art: Elastocapillarity of slender structures

Elastocapillarity is a field that focuses on the ability of liquid interfaces to deform elastic objects and vice-versa. As the name suggests, there are two parts in elastocapillarity. On the one side, the capillarity, where the key parameter is the surface tension. On the other side, the elasticity, which comes from the elastic object in contact with the liquid interfaces, where here the important parameters are the geometry of the object and of the interfaces as well as the intrinsic rigidity of the object.

As an example, Figure 2.1a illustrates the model system presented in the work of Bico et al. [57]: First, the two ends of an elastic ribbon are folded on a droplet. The surface tension of the droplet then pulls on the ribbon trying to minimise the interface energy and at the same time the ribbon tries to stay flat in order to minimise the bending energy, which results in an equilibrium shape that depends on the competition between capillarity and elasticity.

Moreover, combination of soft materials and fluids offers a rich physics in which both elasticity and capillarity come into play [57], opening an area of opportunity for novel materials and fabrication strategies in the case of slender elastic structures [58] and of bulk systems [59]. Geometry and size effects play a key role in the control of the shape of slender solids by capillary effects, for which bending dominates over stretching [60]. Some elastocapillary phenomena are already used for microfabrication techniques in the electronic domain [61, 62], as shown in Figure 2.1b where microstructures are self-assembled, but also in soft robotics or drug encapsulation and delivery [63, 64].

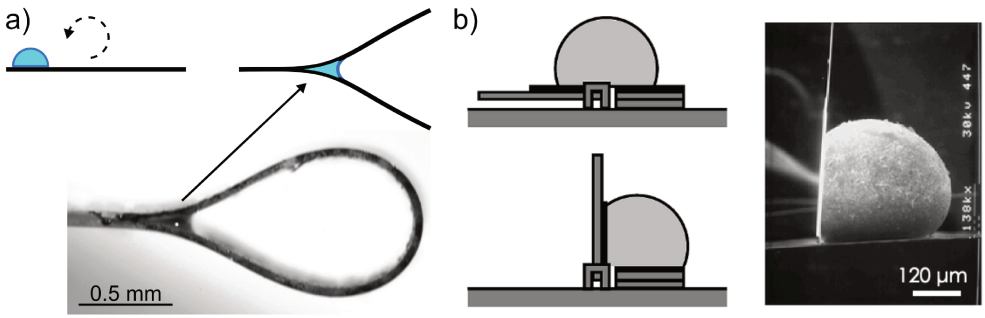


Figure 2.1 – a) "Elastocapillary racket": the two ends of an elastic ribbon are looped onto itself and maintained by a liquid meniscus. Adapted from [57]. b) Microstructure assembled thanks to capillary forces in electronic field. Reproduced from [61].

A limited number of studies on model systems exist in the case of liquid foams but soap bubbles or soap films have already be used to fold thin flexible sheets in the case of "capillary origami" [58] or cellular structures of slender beams [65]. A more detailed analysis of the literature on foam-fibre systems will be presented in Chapter 5.

2.2 Materials and methods

2.2.1 Formulation of the soap solution

The aesthetic properties of liquid foams lead to collaborations between bubble artists and the scientific foam community. These artists were the first to bring up questions such as "How to make the biggest bubble or the most stable film?", but it is only recently that publications sharing these recipes have appeared.

Here are the ingredients that we find most often in the recipes and that we have decided to use:

- **Fairy Liquid:** a commercial detergent from Procter & Gamble bought in a supermarket, that is a mixture of several surfactants. This product is widely used in the foam community because it increases the surface elasticity of interfaces and thus increases the stability of films [66, 67].
- **Jlube:** an industrial lubricant from Jorgensen Labs, which is composed of 25% polyethylene oxide (PEO) and 75 % sucrose. Frazier et al. [66] studied the role of long-chain polymers (PEO or guar) in soap solutions. They showed that adding these polymers provides additional elastic forces that prevent giant bubble films from breaking.
- **Glycerol**: purchased from Sigma - Aldrich in the context of this work. As it is hygroscopic, it helps to reduce evaporation and even allows to reach an equilibrium state where evaporation is compensated by absorbing water [67].

The final formulation that we used in this study comes from the combination of different recipes found in the literature [66] as well as from different discussions with Sebastien Kauffmann[1], a bubble artist who collaborates with our team at the ICS.

We first mix water, 10 g/L industrial PEO lubricant Jlube, 1.5 vol.% Glycerol with a magnetic stirrer for several hours, and 4.5 vol.% Fairy Liquid detergent is added after 24 h. Solutions are used only after an additional 24 h period of rest. The surface tension of this solution, measured using a Kibron tensiometer, is found to be $\gamma = 26.5 \pm 0.5$ mN/m at room temperature.

2.2.2 Elastic ribbons

The elastic ribbons are made of polydimethylsiloxane (PDMS Sylgard 184, from Dow Corning). The elastomer base is first mixed with its crosslinker in proportion 10:1. We then use a Laurell WS-650MZ spin coater to produce 100 x 100 mm films of variable thickness t. Rotational speeds range from 200 to 2000 rpm. PDMS films are then cured in an oven at 60°C for two hours and stored for at least 48 h at room temperature before performing the experiments. Once solidified, the thicknesses t of the films are measured with a Bruker optical profilometer.

The use of the spin coater allows us to obtain film thicknesses from 35 to 359 μm. The Young modulus of PDMS is $E = 1.7 \pm 0.2$ MPa [68] and the Poisson ratio ν is taken as equal to 0.45. To confirm this Young modulus value, we carried out dynamic mechanical analysis (DMA) on three 7 x 30 mm samples cut from a 45 μm thick PDMS

[1] https://www.tricoteriesetcie.com

film (parameters: room temperature, frequency 1 Hz, up to a displacement of 500 μm in the length direction). Figure 2.2a shows the results of the DMA tests, i.e. Young modulus as a function of displacement. The Young modulus value corresponds to the average of the three plateau values taken between 25 and 150 μm displacement and confirms the value reported in the work of Johnston et al. [68].

To cut the ribbon, we use a homemade tool composed of two cutter blades spaced precisely 14.5 mm (Fig. 2.2b). The last step is to hydrophilised both sides of the ribbon via a plasma cleaner treatment (Harrick Plasma) at high intensity for 1 min. Figure 2.2c shows the effect of hydrophilisation. Before this step, the ribbon is hydrophobic as we can see droplets on the ribbon surface; After plasma cleaner treatment the surfaces of the ribbon become charged and hydrophilic. The ribbon is then perfectly wetted by the soap solution, which prevents the bubbles from bursting at its contact.

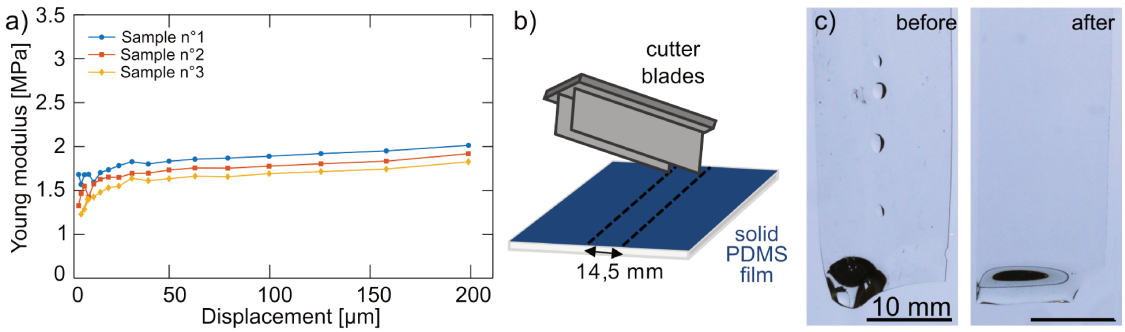


Figure 2.2 – a) Results of the dynamic mechanical analysis carried out on three 7 x 30 mm samples cut from a 45 μm thick PDMS film (parameters: room temperature, frequency 1 Hz, up to a displacement of 500 μm in the length direction). b) Diagram of the homemade tools used to cut the ribbon from the PDMS film. c) Pictures of the ribbon before and after hydrophilisation via plasma cleaner treatment.

2.2.3 Experimental setup

We consider a model system composed of an ordered assembly of monodisperse soap bubbles and an elastomer ribbon. Figure 2.3 shows the experimental setup used to produce the foam-ribbon systems.

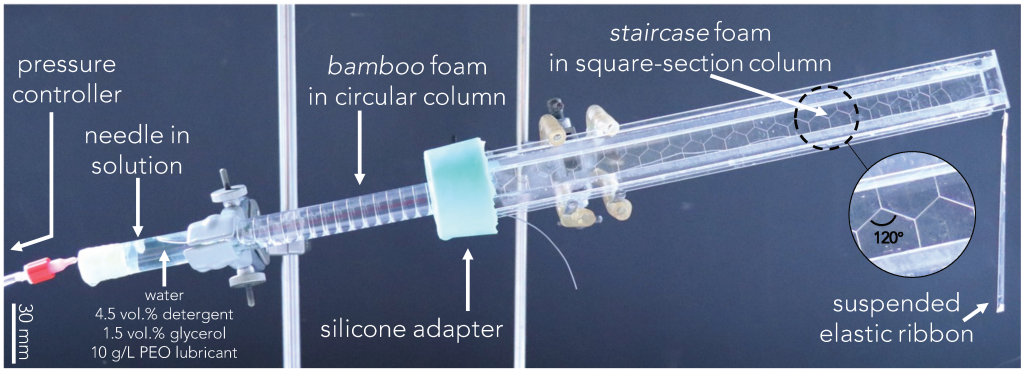


Figure 2.3 – Experimental setup: On the left, the bubble generation: A bamboo foam is made by blowing air through a needle at constant pressure into a soap solution. On the right, the staircase structure: The bamboo foam in the circular tube changes to a staircase structure in the square cross-section column. Note the invariance by translation along the axis perpendicular to the Figure, providing a quasi-2D structure.

Bubble columns are generated in a circular perspex tube (ID 16 mm) connected with a silicone adapter to a PMMA column with a 15 mm square cross-section into which we place a stretched wire at the end of which an elastic ribbon is suspended. The circular tube is sealed on one side with a cork that includes a nozzle (ID 0.61 mm) near the tube wall. The tubes are pre-wetted with clear water and the ribbon with the soap solution to prevent the soap films from breaking. We fill the circular tube with the aqueous detergent solution and tilt it by approximately 10 degrees so that the nozzle opening is just below the air/liquid interface [69].

Air is blown into the solution at a constant pressure (10 mbar) via an Elveflow pressure controller (OB1 MkII), resulting in the formation of a *bamboo structure* [26, 18]. These equally spaced soap films slowly slide upwards through the silicone adapter and into the square section column where the soap films rearrange into a *staircase structure* (Chapter 1), that offers an invariance by translation along the axis perpendicular to the column, providing a quasi-2D model system. The staircase structure presents a central soap film composed of straight sections connected at 120° angles (Fig. 2.3 inset) into which we insert the elastic ribbon (initially suspended at the end of the square section column with a wire that passes through the column, as illustrated at the right of Figure 2.3).

After the staircase structure is produced, we disconnect the square section column from the bubbling setup and introduce the ribbon into the central soap films by carefully pulling on the wire. We close the column on the top side with a silicone plug, leaving the other side open to facilitate the drainage of liquid out of the foam structure for 30 min. The resulting system is stable for another 15 minutes during which shape and position of the ribbon remain fixed. Figure 2.4 shows the time evolution over 75 minutes of a quasi-2D foam/ribbon system. It is important to let the system drain for 30 minutes to allow time for soap liquid to drain, the small stray bubbles to disappear and the ribbon to slide down. The dotted line marks the end of the ribbon at $T = 0$ min. We notice that at $T = 30$ min, the bottom of the ribbon slides below this line evidencing a relaxation dynamics of the ribbon. After this time ($T = 30$ min), the system is stable for 45 minutes, allowing sufficient time for tomograph measurements without motion artefacts.

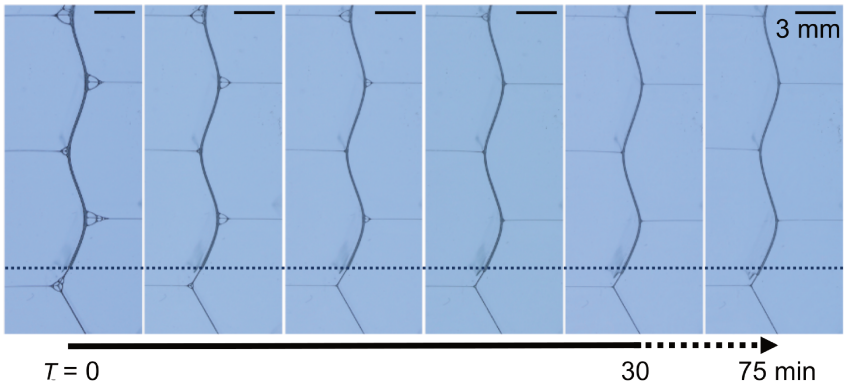


Figure 2.4 – Time evolution over 75 minutes of a quasi-2D foam/ribbon system. The dotted line marks the end of the ribbon at T=0.

2.2.4 Characterisation

The tomographic images are made with resolutions ranging from 12 to 58.8 μm, using the X-ray microtomograph EasyTom 150/160. We focus on slices across the x axis corresponding to the width of the ribbon (Fig. 2.5a). On each slice, we measure the amplitude of the ribbon Δf and the height of the second half-period ℓ (Fig. 2.5b) using a purpose-designed MATLAB code. To account for small deviations from a perfect 2D system, we calculated the average for Δf and ℓ over 100 equally spaced slices along the x axis. We made all our measurements on the second half-period first to avoid edge effects, but also because higher half periods are prone to a flattening due to the weight of lower parts of the ribbon, an effect disregarded in the following theoretical treatment for sake of simplicity but which will be discussed in Section 2.4.

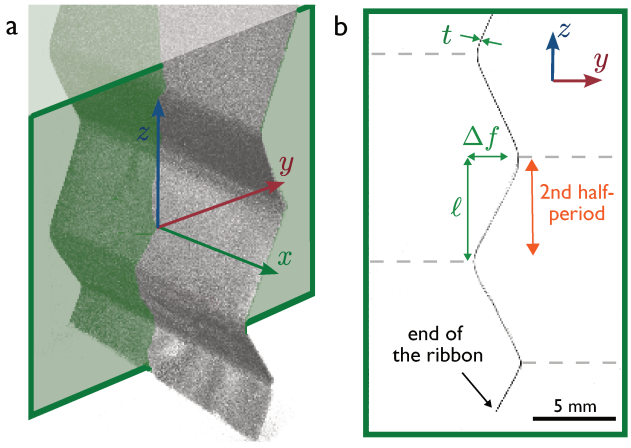


Figure 2.5 – a) 3D-view of the elastomer ribbon in the soap bubble column after 30 minutes of drainage. Note that only the elastic ribbon is visible in the scan, as the soap film thicknesses are smaller than the voxel size. b) Slice perpendicular to the x axis (green color code in (a)), with definition of the measured amplitude Δf and half-period ℓ, highlighting the region of interest (second half-period from the end of the ribbon). Note that the thickness t, mentioned on the figure, is actually measured via an optical profilometer.

2.3 Results

We focus now on the equilibrium shapes of ribbon-foam systems as a function of the competition between elasticity and capillarity. Both experimental and theoretical results are described.

2.3.1 Deflexion measurements

Experimentally, ten different thicknesses of PDMS ribbons, ranging from 35 μm to 359 μm, are introduced into the staircase structure. This represents a variation of the bending rigidity of the ribbons over three orders of magnitude. Among the other parameters in the system, the width and Young modulus of the ribbon, the dimensions of the square section column and the surface tension are kept constant, while the half-period ℓ is measured on each bubble column and comprised between 4.2 ± 0.1 and 6.2 ± 0.2 mm.

We present in Figure 2.6 the dimensionless deformation of PDMS ribbons of thicknesses $T = 35$, 41, 46, 60, 69, 86, 105, 128, 187 and 359 μm as a function of the dimensionless bending rigidity η, defined as

$$\eta = \frac{\alpha}{\gamma \ell^2}, \tag{2.3.1}$$

where α is the bending rigidity per unit width of the ribbon and γ the surface tension. The parameter η compares the elastocapillary length $\sqrt{\alpha/\gamma}$ to the geometrical length ℓ of the problem. For length scales $\ll \sqrt{\alpha/\gamma}$ (resp. $\gg$), the physics is mainly dictated by the rigidity (resp. the capillarity).

For the deformation of the ribbon, we consider the parameter $\sqrt{3}\Delta f/\ell$, which is equal to 1 in the limit case of soft ribbons where the geometry is dictated by Plateau's laws. At large values of η, the deformation of the ribbon is small, and increases when decreasing η. At the limit $\eta \ll 1$, the shape is close to the initial pattern of bubbles, with angles prescribed by Plateau's laws.

Theoretically, we plot in Figure 2.6 the dimensionless amplitude of the ribbon as a function of η, corresponding to Eq. (2.3.12), with values of κ given by Eq. (2.3.11) in the $\eta \gg 1$ limit (rigidity dominated) and Eq. (2.3.14) in the $\eta \ll 1$ limit (capillarity dominated). All equations are developed in Section 2.3.3. We observe an excellent agreement between experiments and theory over the whole range of deformations, showing that the key ingredients chosen and the approximations made in the modeling in the two limit cases are relevant.

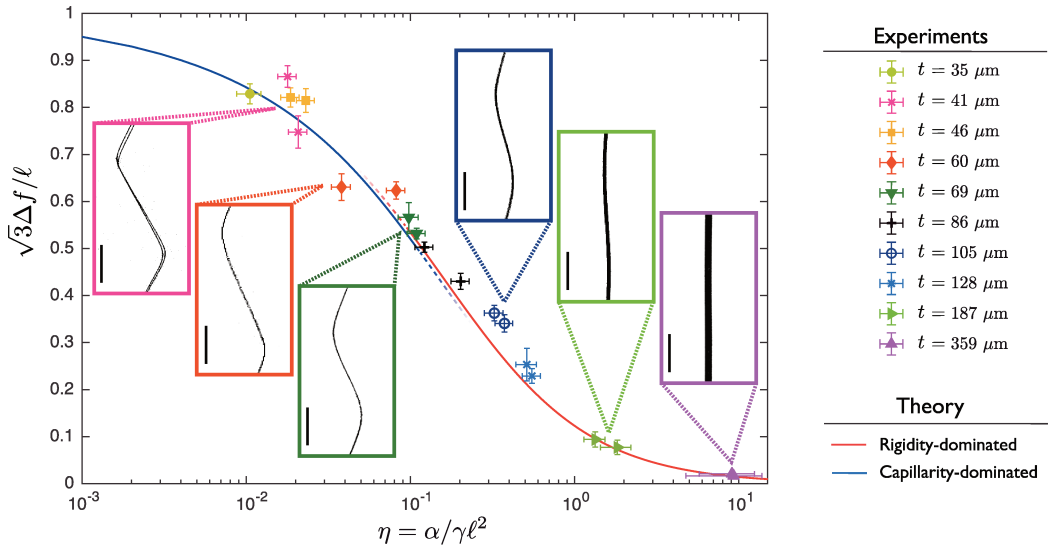


Figure 2.6 – Dimensionless deflexion $\sqrt{3}\Delta f/\ell$ as a function of the parameter $\eta = \alpha/(\gamma\ell^2)$ comparing bending rigidity of the ribbon and capillarity. The left side of the graph corresponds to flexible ribbons, the right side to rigid ribbons. Theoretical prediction for rigidity-dominated case (quadratic order around the *straight ribbon* configuration) and for capillarity-dominated case (quadratic order around the *bubble-only* configuration) are shown with straight lines, respectively in red and blue. Experiments correspond to the second half-period of PDMS ribbons with 10 different thicknesses, resulting in different bending rigidities. Error bars correspond to both systematic uncertainties on α and γ and statistical variation of the parameters Δf and ℓ over 100 slices taken along the x axis, covering the full ribbon width. Insets show X-ray tomographies of corresponding systems (scale bars are 2 mm).

2.3.2 Equilibrium shapes

To go beyond the description of the deformation in terms of amplitudes, we also extract the full profiles, presented in a dimensionless manner in Fig. 2.7, for PDMS ribbons of various thicknesses spanning the range shown in Fig. 2.6.

The full profile of the ribbons is described by Eq. (2.3.10): Fig. 2.7 compares this theoretical prediction to experiments, using the values of Δf and ℓ measured on the profile to establish Figure 2.6, and the value of η measured from profilometry and Young modulus, with no further fitting parameters. Again, our modeling captures well the experimental results, over the whole range of ribbon thicknesses and is described in Section 2.3.3.

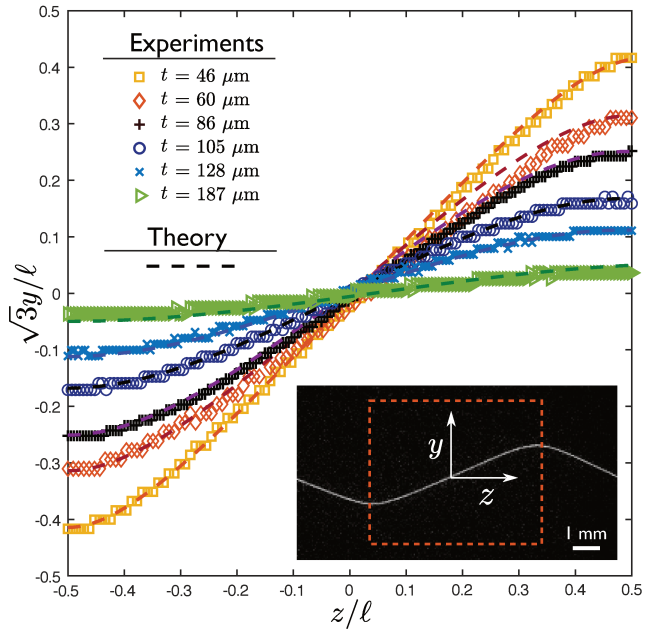


Figure 2.7 – Dimensionless profile of ribbons of different thicknesses t (and thus different bending rigidities), from flexible (yellow squares) to rigid (green triangles) structures. Theoretical shapes are calculated from the values of Δf and ℓ measured on the foam-ribbon system, and of η measured on the ribbon, with no further fitting parameter, using the appropriate model (small deformation around straight line for rigid ribbons, small deformations around the bubble-only case for flexible ribbons). Inset: region of interest considered for those curves, and definition of y and z axis.

2.3.3 Theoretical interpretation

In order to rationalise the results presented in Sections 2.3.1 and 2.3.2, the theoretical modeling, written by Jean Farago, is developed in this section, for both amplitudes and equilibrium shapes of the profiles.

The equilibrium state of the ribbon in the staircase bubble assembly can be obtained by minimising the free energy of the system. The excess free energy (per unit length in the direction transverse to the Figure 2.5b of the system with respect to the situation where only the staircase bubbles are present) is given by

$$\mathcal{F} = \mathcal{E}_{\text{ribbon}} + \Delta\mathcal{E}_\gamma + \Delta F_{\text{gas}}, \tag{2.3.2}$$

where $\mathcal{E}_{\text{ribbon}}$ is the elastic energy per unit width of the ribbon, and $\Delta\mathcal{E}_\gamma$ is the excess interfacial energy per unit width of the liquid films, with respect to the situation without ribbon. Notice that we assume that the ribbon is everywhere in the interior of the liquid films so that the area of the ribbon itself contributes to the liquid interfacial energy. The final term ΔF_{gas} accounts for the free energy cost of the possible contraction/dilation of the gas within the bubbles due to the presence of the ribbon, and is neglected in the following, because the pressure variation within the bubbles modify only minutely their volume.

The actual expression for the elastic term is

$$\mathcal{E}_{\text{ribbon}} = \frac{\alpha}{2}\int C^2 \mathrm{d}s, \tag{2.3.3}$$

where $\alpha = Et^3/12(1-\nu^2)$, and s is the curvilinear abscissa along the ribbon, related to the ribbon profile $f(z)$ by $\mathrm{d}s = \mathrm{d}z\sqrt{1+f'(z)^2}$. The curvature C is given in terms of $f(z)$ by

$$C = \frac{f''(z)}{\sqrt{1+(f'(z))^{3/2}}}. \tag{2.3.4}$$

For a long and uniform ribbon, which zigzags periodically along $N \gg 1$ identical bubbles (we count the bubbles of length 2ℓ only on one side of the ribbon (Fig. 2.5b)), we can write, up to negligible boundary corrections, $\mathcal{E}_{\text{ribbon}} \simeq \frac{N\alpha}{2}\int_{1\text{p}} C^2 \mathrm{d}s$, where $\int_{1\text{p}}(\ldots)$ assumes an integration over one period of the ribbon only.

Making similar assumptions, the second term of the energy in Eq. (2.3.2) is written

$$\Delta\mathcal{E}_\gamma \simeq 2\gamma N\left[\int_{1\text{p}} \mathrm{d}s - \Delta f - \sqrt{3}\ell\right], \tag{2.3.5}$$

where $\Delta f = \max f(z) - \min f(z)$ is the transverse amplitude of the ribbon (Fig. 2.5). Note that (i) the factor 2 corresponds to the two liquid-air interfaces of the liquid films, (ii) the last term of Eq. (2.3.5) comes from the fact that the zero energy reference state is chosen to be the column of bubbles without ribbon for which the interfacial energy per unit width over one period is $2\gamma(\sqrt{3}\ell + w)$ (assuming the square column width and the ribbon width, w, to be equal), and (iii) w does not appear in Eq. (2.3.5) due to the translational invariance of the bubble pattern energy along the y-direction. Moreover, the half length of the bubble ℓ can be considered constant during the minimization process, because the compression/dilation of the gas due to the ribbon is negligible.

We consider now the minimisation process of the free energy : The equilibrium profile $f(z)$ is the one which minimises $\mathcal{F}$ (Eq. (2.3.2)). This minimisation is complex for two reasons. Firstly, since the functional $\mathcal{F}$ is not quadratic in $f(z)$, we will consider two different quadratic approximations according to the physical properties of the ribbon (flexible and rigid limit cases), to obtain a tractable theory. Secondly, for a long homogeneous ribbon, we anticipate that the equilibrium shape is periodic with N identical oscillations embedded in a deformed network of bubbles. But, in contrast to the total length L of the ribbon, the number N is not a constant of the minimisation procedure, since the deformation of the ribbon reduces the number N of oscillations the ribbon can develop. To tackle this specific difficulty, two equivalent routes can be followed. Lagrange multipliers could be used to account for the total length of the ribbon, the number N being temporarily treated as a constant. Alternatively — and it is the route we follow here —, the explicit relation $L \simeq N\int_{1\text{p}} \mathrm{d}s$ allows to both account for the constancy of the total length of the ribbon and the variation of N. As a result, the unconstrained functional to minimise becomes

$$\mathcal{F}_1 \equiv \frac{\mathcal{F}}{\gamma L} - 2 = \frac{\frac{\alpha}{2\gamma}\int_{1\text{p}} C^2 \mathrm{d}s - 2[\Delta f + \sqrt{3}\ell]}{\int_{1\text{p}} \mathrm{d}s}. \tag{2.3.6}$$

Taking into account the internal mirror symmetry of the expected optimal profile (Fig. 2.3), Eq. (2.3.6) can be rewritten

$$\mathcal{F}_1 = \frac{\alpha}{2\gamma}\frac{\int_0^\ell \sqrt{1+(f')^2}C^2\mathrm{d}z}{\int_0^\ell \sqrt{1+(f')^2}\mathrm{d}z} - \frac{\Delta f + \sqrt{3}\ell}{\int_0^\ell \sqrt{1+(f')^2}\mathrm{d}z}, \tag{2.3.7}$$

with $\Delta f = f(\ell) - f(0)$ if $z = 0$ is taken at the position of a transverse liquid film, such that $f(0) = \min f$ (this value being arbitrary, we choose $f(0) = 0$ in the following). For pure bubbles, i.e. in the limit $\alpha \to 0$, the optimal $f(z)$ given by Eq. (2.3.7) is $f(z) = z/\sqrt{3}$, in accordance with Plateau's laws [1], which prescribe 120° angles between connecting films.

The physics of the problem is governed solely by the dimensionless parameter

$$\eta \equiv \frac{\alpha}{\gamma \ell^2}. \tag{2.3.8}$$

For high values of η, i.e. for stiff ribbons, one expects that $f(z)/\ell \ll 1$ and a second order expansion in f for $\mathcal{F}_1$ is physically relevant. Disregarding irrelevant constants, the quadratic approximation for $\mathcal{F}_1$ for large η reads

$$\mathcal{F}_1 \underset{\eta \gg 1}{\simeq} \frac{\eta \ell}{2} \int_0^\ell (f'')^2 \mathrm{d}z + \frac{\sqrt{3}}{2\ell} \int_0^\ell (f')^2 \mathrm{d}z - \frac{\Delta f}{\ell}. \tag{2.3.9}$$

We write $f(z) = (\Delta f) g(z/\ell)$ so that $g(0) = 0$ and $g(1) = 1$ and consider first the optimisation of the shape g before considering the optimisation of the amplitude Δf. The optimal g is found using standard techniques of Lagrangian mechanics [70, 71]:

$$g_{\mathrm{opt}}(z/\ell) = \frac{\tanh(\kappa) \sinh^2(\kappa z/\ell) - [\frac{1}{2} \sinh(2\kappa z/\ell) - \kappa z/\ell]}{\kappa - \tanh(\kappa)}, \tag{2.3.10}$$

$$\text{with } \kappa \equiv \frac{3^{1/4}}{2\sqrt{\eta}} \simeq \frac{0.658}{\sqrt{\eta}}. \tag{2.3.11}$$

Once g_{opt} is known, Δf is computed as the value minimizing Eq. (2.3.9), which is simply a second order polynomial in $\Delta f/\ell$. One finds

$$\frac{\sqrt{3}\Delta f}{\ell} \underset{\eta \gg 1}{\simeq} 1 - \frac{\tanh \kappa}{\kappa}. \tag{2.3.12}$$

In the $\eta \gg 1$ regime, for which this formula is in principle only relevant, one can write one step further $\sqrt{3}\Delta f/\ell \simeq \kappa^2/3 = \eta^{-1}/[4\sqrt{3}]$, showing that Δf goes to zero as $\propto \alpha^{-1}$ for large α. It is interesting to note that in the opposite range $\eta \to 0$, Eq. (2.3.12), though not supposed to work here, gives however the correct limit $= 1$.

Actually the limit of small α (or small η) is incorrectly described by the previous theory, because one expects here the central zigzag of the bubble pattern to be hardly perturbed by the ribbon, therefore assuming $\Delta f/\ell \ll 1$ is simply incorrect. The correct method is to write $f(z) = z/\sqrt{3} + \xi(z)$ and assume that $\xi/\ell \ll 1$. As $z/\sqrt{3}$ the equation is associated to half of a period of the central line of the bubble network (in absence of the ribbon), one expects that weak values of α induce only minor departures from this pattern. The quadratic approximation of Eq. (2.3.7) in the field $\xi(z)$ can be re-expressed in the field $f(z)$ and reads (up to a constant)

$$\mathcal{F}_1 \underset{\eta \ll 1}{\simeq} \frac{\eta \ell}{2(1 + 3^{-3/4})} \int_0^\ell (f'')^2 \mathrm{d}z + \frac{9}{16\ell} \int_0^\ell (f')^2 \mathrm{d}z - \frac{3\sqrt{3}}{8} \frac{\Delta f}{\ell}. \tag{2.3.13}$$

In this case, the optimal solution is given by formulas very similar to the preceding case. As before, one writes a priori $f(z) = (\Delta f)g(z/\ell)$ and finds respectively for g and $\Delta f/\ell$ the results given in Eq. (2.3.10) and Eq. (2.3.12) with κ replaced by

$$\kappa_< \equiv \frac{3(1+3^{-3/4})^{1/2}}{4\sqrt{2\eta}} \simeq \frac{0.636}{\sqrt{\eta}}. \tag{2.3.14}$$

The two regimes are described by almost the same formulas, differing only by a modest change in the constant appearing in κ, a similarity which is somewhat surprising. It comes from the fact that Eq. (2.3.13), valid in the capillarity-dominated domain, has exactly the same functional structure as (2.3.9), the corresponding potential for the rigidity-dominated one, the only change being a limited renormalization of the prefactors of the different terms. This similar structure leads to the same functional form of the optimal profile, up to a minor change in the constant terms. Notice however that the profile shape given in Eq. (2.3.10) has a considerably different limiting expression for small values of η. For $\eta \gg 1$, one can show that $g_{\rm opt}(z/\ell) \simeq 3(z/\ell)^2 - 2(z/\ell)^3$. For $\eta \ll 1$ however, one has $g_{\rm opt}(z/\ell) \sim z/\ell$, a result expected because the bubble profile must be recovered at $\eta = 0$. Notice that the latter limiting form is not compatible with the boundary conditions $g' = 0$, a discrepancy due the fact that a regularisation of the ribbon profile occurs near $z = 0$ and $z = \ell$ over a length $\sim \ell/\kappa_< \sim \sqrt{\alpha/\gamma}$, i.e. the elastocapillary length. As mentioned above, the elasticity dominates on length scales shorter than $\sqrt{\alpha/\gamma}$, as exemplified here.

2.3.4 Application to bubble-based forming

We saw in Section 2.1 that elastocapillarity can be used to form and auto-assemble microstructures or slender elastic objects. We then wondered if this system could also be used to imprint shapes to materials, by solidifying a UV-curable thin elastic ribbon in the staircase bubble assembly. The idea is to create a PDMS "pocket" (or shell) that we can fill with a UV-curable resin. To strongly bond two PDMS surfaces, plasma activation of surfaces is often used in the microfluidic lab-on-a-chip community [72].

Thus, to create the PDMS pockets, we first prepared two crosslinked PDMS ribbons of 70 ± 5 μm thickness and 14.5 ± 0.1 mm width, following the protocol described in Section 2.2.2. We then treated one side of each PDMS ribbon with the plasma cleaner for 2 minutes at high intensity in order to activate their surfaces. A mask protected a rectangular part (8 x 100 mm) from the plasma, located at the middle of the ribbons. We put the two activated surfaces in contact, apply a light pressure by hand for 2 minutes and place it in the oven for 15 minutes at 60°. Only the edges of the ribbon (not protected by the mask) are glued together, so we obtain a PDMS shell which we fill with NOA 85 (Norland Optical Adhesive), a liquid photopolymer that cures when exposed to UV light. We sealed the whole shell with tape and stuck it on a wire. Following the same protocol as for PDMS ribbons, described in the experimental setup (Section 2.2.3), we slide the NOA-filled PDMS shell inside the staircase structure and place it in a Creality UW-01 curing machine (UV light) during 10 minutes at low rotation speed.

The result is a cured ribbon made of two PDMS layers with a NOA 85 layer in the middle, and shaped according to the characteristic geometries of the bubble-ribbon structure (Fig. 2.8). In the UV-cured state, as NOA 85 Young modulus is almost two

orders of magnitude higher than PDMS, the thin layer of NOA is sufficiently stiff to maintain the wavy shape when the composite ribbon is extracted from the foam. With this simple proof-of-concept experiment, we demonstrate that a liquid foam can be used to shape slender objects, with a resulting corrugation imprinted by the foam and the competition between elasticity and capillarity in such systems.

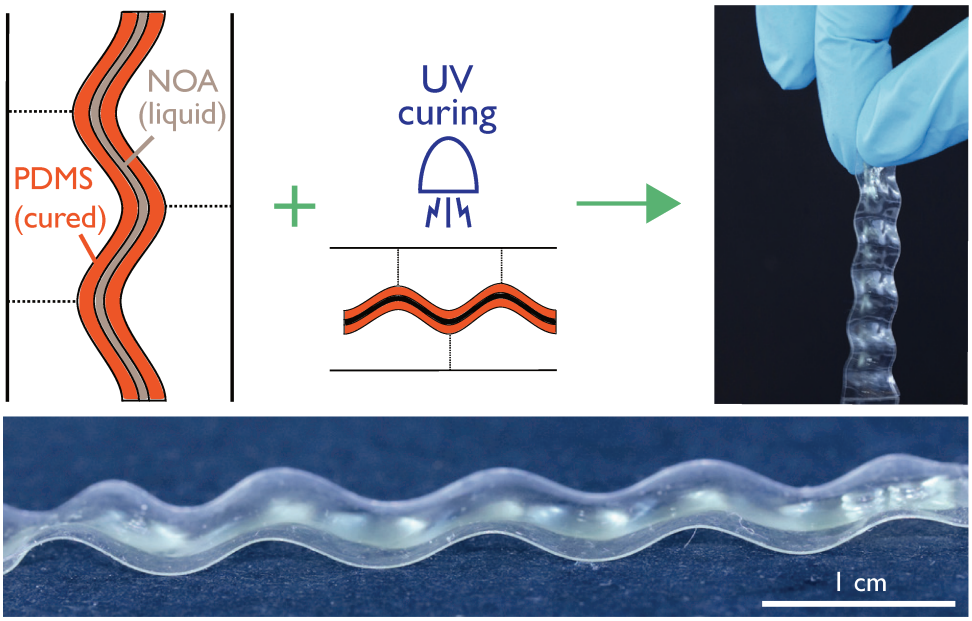


Figure 2.8 – Application of foam-driven ribbon bending to UV-curable composite systems. Bonding of two cured PDMS layers provides an outer shell in which a liquid UV-curable adhesive (NOA) is poured. This composite structure undergoes shaping through insertion inside the bubble column and subsequent UV curing. The resulting solid self-standing structure presents corrugations dictated by the competition between elasticity and capillarity in the uncured system.

2.4 Influence of gravity

As explained in Section 2.2.4, we made all our measurements on the second half-period because we observed that higher half periods are flattened due to the weight of lower parts of the ribbon (Fig. 2.9a). This effect has already been studied, notably by Miller et al. [73] who looked at how natural curvature affects the configuration of a thin elastic rod suspended under its own weight, as when a single strand of hair is suspended under the effect of gravity.

By making a few modifications in our experiments and in the theoretical interpretation, we were able to provide preliminary results on the influence of gravity on the equilibrium forms of the ribbon in the staircase bubble structure.

2.4.1 Experimental modifications

Firstly, we modified the attachment of the ribbon to the wire which helps its insertion into the bubble structure. Six holes of 2 mm were made at the top of the ribbon (Fig. 2.9b) using a biopsy punch in order to remove as much stress as possible from the ribbon. The goal is to keep long ribbons in the same 2D plane along their entire width with no bending in the transverse direction.

The ribbons must be inserted even more gently to avoid disturbing the balance of the bubbles, which could be asymmetrical.

Then, attention must be paid to the positioning of the bottom of the ribbon when it is inserted. Indeed, we noticed that in the extreme case in which the edge of the ribbon is stuck on a horizontal film then the ribbon can be slightly more curved (Fig. 2.9c and d).

Finally, characterisation is carried out with helical X-ray tomography, i.e. the sample is rotated and lowered as it is scanned to obtain a greater image height and therefore several half-periods. Resolution of the X-ray scans is computed between 50 and 90 μm depending on the samples. 30 minutes of draining are always carried out before any characterisation.

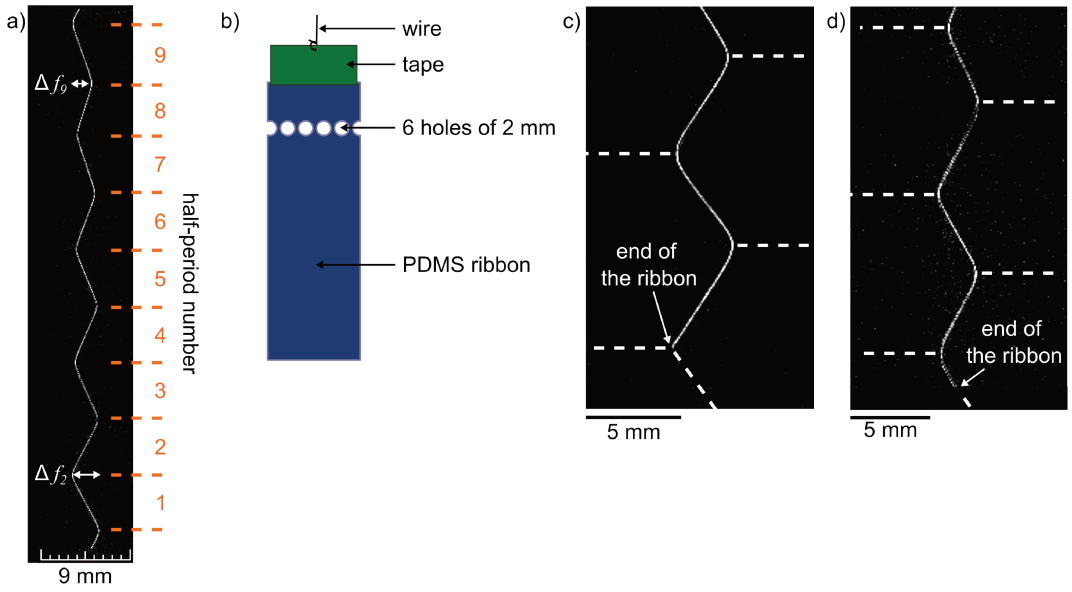


Figure 2.9 – a) 2D image from helical tomography of an elastic ribbon deformed inside the staircase bubble structure. b) Diagram of the modifications made on the ribbon. c)-d) 2D images showing the end of the ribbon, respectively, on a horizontal film and inside a diagonal film.

2.4.2 Theoretical modifications

Based on the theoretical modeling described in Section 2.3.3, the results of the dimensionless deflexion $\sqrt{3}\Delta f/\ell$ as a function of the parameter $\eta = \alpha/(\gamma\ell^2)$ comparing bending rigidity of the ribbon and capillarity for each half-period are calculated here, but some modifications have been made.

Gravity is taken into account in the excess free energy (per transverse unit length) of the system, which is given by

$$\mathcal{F} = \mathcal{E}_{\text{ribbon}} + \mathcal{E}_{\text{gravity}} + \Delta\mathcal{E}_{\gamma} + \Delta F_{\text{gas}}, \tag{2.4.1}$$

where $\mathcal{E}_{\text{ribbon}}$ is the elastic energy per unit width of the ribbon, $\mathcal{E}_{\text{gravity}}$ is the potential energy of gravity of the ribbon and $\Delta\mathcal{E}_{\gamma}$ is the excess interfacial energy per unit width of the liquid films, with respect to the situation without ribbon. ΔF_{gas} is neglected as in the previous case (Section 2.3.3).

The actual expression for the gravity term is

$$\mathcal{E}_{\text{gravity}} = \lambda g \int z(s)\mathrm{d}s, \tag{2.4.2}$$

where λ is the linear mass per unit length, given by $\lambda = \rho t$, with ρ the density and t the thickness of the ribbon.

We can then write

$$\mathcal{F} - 2\gamma L = \frac{\alpha}{2}\int_{1\text{p}} C^2\mathrm{d}s - \lambda g \int z(s)\mathrm{d}s - \gamma \sum_{1/2\ \textit{bubble}\ i} [\sqrt{3}\ell + \Delta f_i]. \tag{2.4.3}$$

with L the length of the ribbon and Δf_i the amplitude of the half-period n°i from the bottom of the ribbon (Fig 2.9a). To simplify the theoretical treatment, the gravitational energy has been approximated to

$$\mathcal{E}_{\text{gravity}} = \sum_{\textit{bubble}\ i} [\lambda g z_{cr,i}], \tag{2.4.4}$$

where $z_{cr,i}$ is the height of the center of the bubble i. This approximation allowed to neglect gravitational effects at the scale of one bubble, which is experimentally relevant.

As before, two limit cases are developed for small and large α, and must be chosen according to the ribbon studied. Then, to plot the curve of the dimensionless deflexion $\sqrt{3}\Delta f/\ell$ as a function of the parameter $\eta = \alpha/(\gamma\ell^2)$, a homemade Matlab script is used for which the parameters to enter are the number of the period (that we want to study), as well as the dimensionless linear mass $\widehat{\lambda} = \frac{\lambda g \ell}{\gamma}$ for the corresponding ribbon studied.

2.4.3 Results

Figure 2.10 shows results of the dimensionless deflexion as a function of the parameter η for different ribbon thicknesses and for each half-period (with half-period numbers defined in Figure 2.9a).

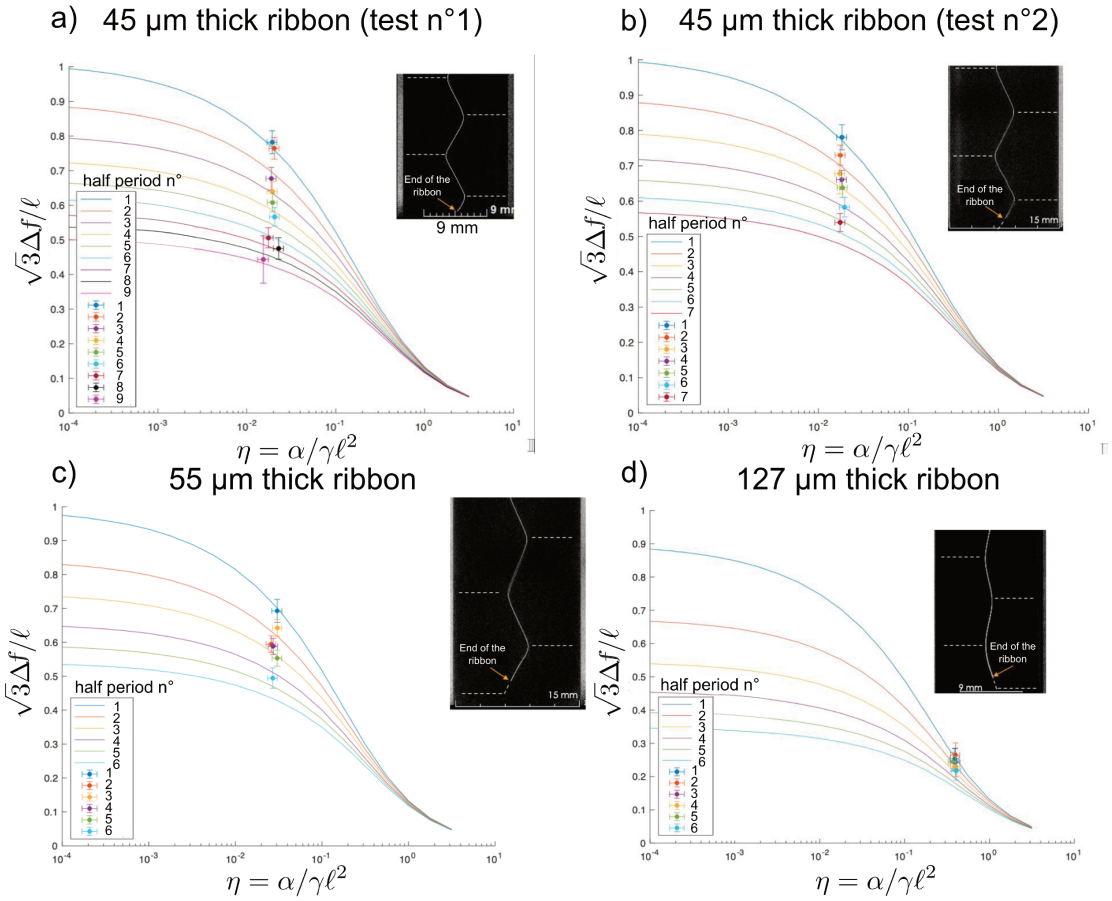


Figure 2.10 – Dimensionless deflexion $\sqrt{3}\Delta f/\ell$ as a function of the parameter $\eta = \alpha/(\gamma\ell^2)$ comparing bending rigidity of the ribbon and capillarity for each half-period of ribbons of thickness a)-b) 45 μm, c) 55 μm and d) 127 μm. Error bars correspond to both systematic uncertainties on α and γ and statistical variation of the parameters Δf and ℓ over 100 slices taken along the x axis, covering the full ribbon width. Insets are images showing the bottom of the ribbon.

Despite some groupings or inversions of certain experimental points, most of the experimental results seem to be consistent with the theoretical curves, all falling within the cluster of curves.

In addition, all the experimental improvements appear to have improved the measurements. Figure 2.11 shows the very first result obtained for a 45 μm thick ribbon before all the improvements, which corresponds to an extreme case. We can see that all the experimental points come out of the cluster of curves. This is mainly due to the fact that, in this case, the ribbon rests on a horizontal film.

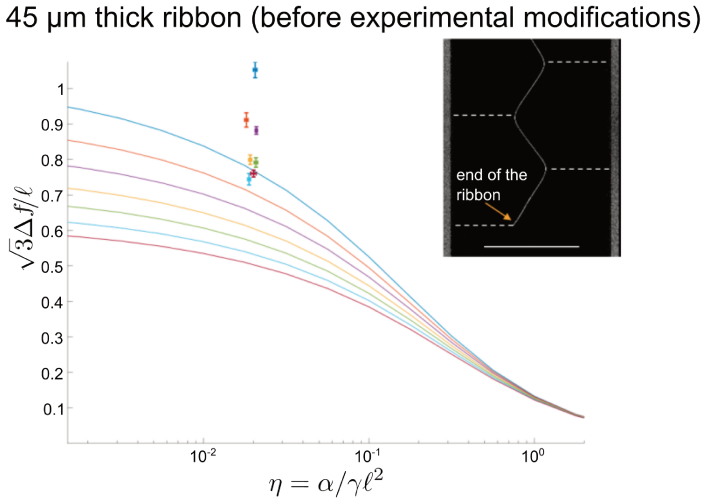


Figure 2.11 – Dimensionless deflexion $\sqrt{3}\Delta f/\ell$ as a function of the parameter $\eta = \alpha/(\gamma\ell^2)$ comparing bending rigidity of the ribbon and capillarity for each half-period of a 45 μm thick ribbon. Error bars correspond to both systematic uncertainties on α and γ and statistical variation of the parameters Δf and ℓ over 100 slices taken along the x axis, covering the full ribbon width. The inset shows a view of the bottom of the ribbon.

2.5 Conclusion

In summary, we have highlighted that the equilibrium geometry of bubble columns can be tuned upon introduction of elastic ribbons, resulting in shapes that differ from classical foam structures dictated by Plateau's laws. We have shown that the resulting geometry of the ribbon-foam system is controlled by the competition between the bending energy of the ribbon and the interfacial energies of the bubble surfaces, as illustrated by the excellent agreement between our experiments and theory for both the amplitude and the full profile of the structures. Liquid foams are excellent model systems for complex cellular structures. Interactions between foams and flexible slender structures also occur in widely used fabrication techniques such as foam-forming of cellulose, as described in Chapter 5. Finally, using a UV-curable system, we have proposed a way to mold materials with characteristic shapes and curves resulting from the elasto-capillary competition.

From liquid to solid foam-fibre systems

The previous study provides a simplified illustration of what could happen in a fibre-enriched foam. The following step in this PhD work is to go towards 3D complex foams with fibres, with formulations allowing a solidification, to build polymeric solid hierarchical materials. The idea behind this strategy is that the incorporation of fibres in the liquid state is aimed at modifying the structure of the foams in a self-assembling manner, i.e. by allowing the bubbles and fibres to organise themselves spontaneously before the solidification. We therefore focused on the fabrication of solid foams from liquid precursors to modify the topology of the foam in the liquid state by introducing fibres and then solidifying this new system. The first step was to find the right formulations and protocols for the fabrication of a model foam without fibres, that allow a certain number of parameters (such as bubble size and liquid fraction) to be controlled. Chapters 3 and 4 focus precisely on this question, before studying the modifications to foam structures induced by fibres, in Chapter 5. We will also discuss the mechanics of such systems, with some preliminary experiments.

In this context, the "ideal" model foam must satisfy the following criteria:

- The foam must have a low relative density for the Plateau's laws to be relevant [1].
- The bubble size must be 5 to 10 times larger than fibre diameter, with the fibres being visible in X-ray tomography, so that the physics of the system, i.e. the interaction of the fibres with the foams, is visible.
- The foam must be sufficiently stable to reach an equilibrium between the fibres (Chapter 5) and not destabilise on contact with them.
- Solidification must be delayed to allow us to foam in a well-defined unique liquid state throughout the whole bubbling step. For the use of bubbling through a nozzle method, we saw in Chapter 1 that the modification of viscosity (by solidification for example) leads to a modification of the size of the bubbles.
- A balance must be found between a too fast solidification time which would prevent the foam to reach equilibrium before solidification (it would give a solidification in an intermediate non-equilibrate state, with non-respect of Plateau's laws) and a too long solidification time which would compromise the stability of the foam.
- The foam must not be brittle and have a linear elastic range, to avoid an excessive complexification of the analysis of mechanical tests on architected materials with

fibres. Indeed, we want to avoid coupling a complex bulk material (i.e with plastic or viscoplastic behaviour) to the mechanics of cellular materials with specific architectures, that is already complex even with linearly elastic materials.

- The foam must not be too flexible to limit the mechanical reinforcement by the fibres themselves. The initial idea is to increase the mechanical properties of foams mainly by modifying their structure.
- The foam must be homogeneous: only 30 mm cubic samples will be characterised and they must be representative of the entire foam.

We studied various systems seeking to satisfy these criteria. Chronologically, the first system studied was polyurethane foams because they have many controllable parameters: the pore size using different foaming techniques, the solidification kinetic and the flexibility of the final foam, which can be modified by the PU formulation. They also have the advantage of being easily removed from the container in which they are produced, so that some mechanical tests can be carried out. We have worked on two manufacturing techniques (both described in Chapter 4): (i) chemical foaming, which is well known and widely used in industrial processes, where the chemical reaction of the two main constituents (polyol and isocyanate) releases CO2 in the presence of water; (ii) mechanical foaming, where bubbles are created directly in the polyurethane mixture through nozzles. There is limited scientific literature about such systems, so we have developed and tested a wide range of parameters to find the right foaming method and polyurethane formulation for the project. As the experiments progressed, we realised that the samples were difficult to reproduce: Either because of the ambient humidity, or because the products were too old, both of which could cause the foam destabilisation.

To overcome these problems and while waiting for new products for polyurethane foams, we have quickly set up a new system based on alginate hydrogel foams, already well known in the laboratory [74] and which have the advantage of dissolving in water and being quick to produce. Unlike polyurethane foams, alginate foams can not be removed from the container (in which they are molded) and tested mechanically, but the gelation of their structures makes them stable for longer time than aqueous foams: they can therefore be characterised by X-rays. This system enabled us to quickly obtain a series of samples with different formulations (Chapter 3) and fibre configurations (Chapter 5).

In the following chapters, we start by a presentation of alginate foams, followed by polyurethane foams, before ending with foam-fibre systems. For both systems, the same foaming process by bubbling through nozzles inside the liquid materials has been investigated and particular attention has been given to ensure that alginate and polyurethane foams without fibres are similar in terms of bubble size and density.

Chapter 3

Alginate foams

Contents

3.1 Context 48
3.2 Materials and Methods 49
3.2.1 Preparation of solutions 49
3.2.2 Rheological characterisation 50
3.2.3 Foam generation 51
3.2.4 Foam drainage characterisation via optical imaging 51
3.2.5 X-ray microtomography characterisation 52
3.3 Results and Discussion 53
3.3.1 Tuning the initial liquid properties 53
3.3.2 Tuning the gelation time 54
3.3.3 Drainage and gelation kinetics 55
3.3.4 Control over the hydrogel foam structure 58
3.4 Conclusion 62

New approaches to produce solid foams from liquid precursors have recently been developed in the literature and are known as *liquid foam templating* [2], to reach a better control over mono/polydispersity, bubble size and density (Chapter 1). To obtain solid foams with the same structures as their liquid templates, the bubbles need enough time after generation to reach an equilibrium before solidification but not too much time to avoid destabilisation. The key parameters to this end are the initial liquid properties (such as the viscosity), the solidification kinetics and the involved foam timescales (drainage, foam ageing, evaporation). In this chapter, we present first the studied system, based on alginate hydrogel foams. After describing the materials and methods used to prepare and characterise the foams, we focus on the impact of gelation kinetics, drainage and how the control of the key parameters listed above can be used to modify the structure of the solidifying foam.

The following content is the basis of the article: **Liquid foam templating of hydrogel foams: a rheological and tomographic characterisation** by M. Jouanlanne, I. Ben-Djemaa, A. Egelé, L. Jacomine, J. Farago, W. Drenckhan and A. Hourlier-Fargette.

3.1 Context

Alginates are polysaccharides extracted from brown seaweed algae (*Phaeophyceae*) and soil bacteria (*Azotobacter vinelandii*) [75]. These polymers are not toxic, do not induce immune responses and are commonly used in food and medicine applications. In the presence of divalent cations, such as Ca^{2+}, the polymer chains rearrange to form a hydrogel. The most common definition of a hydrogel is that it is a cross-linked and water-swollen polymer network produced by the reaction of one or more monomers [76].

There are two types of hydrogel: chemical hydrogels resulting from covalent crosslinks and physical hydrogels resulting from physical bonds (such as ionic bonds, hydrogen bonds) [77]. For this thesis work, we focused solely on physical alginate hydrogels from calcium-crosslinked alginates. As gelation is instantaneous in the presence of Ca^{2+} ions, a direct external contact forms heterogeneous and poorly controllable gels, which is even more accentuated in the form of foam, where diffusion of calcium to the centre of the foam is difficult [78]. For these reasons, the most commonly used gelation method for making hydrogel foams is internal cross-linking [75]. In this method, Ca^{2+} ions are mixed with the alginate solution in an inactive form. The gelation is then initiated by the acidification of the Ca^{2+}-alginate solution. In most cases, acidification is produced using Glucono-δ-lactone (GDL) [75]. Inactive forms of Ca^{2+} include (1) chelating ligands that can be used to "capture" Ca^{2+} ions and protect them from direct contact with the alginate. During acidification, calcium ions are gradually released and cross-link the alginates [79]; (2) Ca^{2+} that can be found in form of solid salts, which are not soluble in water at basic pH but soluble at acidic pH to induce gelation [80].

For the purposes of this work, it is important to control the gelation kinetics. As explained in the intermediate Section *From liquid to solid foam-fibres system*, we need a delayed solidification to produce homogeneous and reproducible foams and to find a balance between too fast and too long solidification.

We therefore decided to use the method with solid Ca^{2+} salts: We precisely used calcium phosphate dibasic ($CaHPO_4$) as a salt, following the protocol suggested by Imene Ben Djemaa [74]. The choice of the formulation was based on the work of Ben Djemaa et al. [74]. They compared several solutions of Ca^{2+}-chelating ligand with solutions of Ca^{2+} salts (at constant alginate and GDL concentrations: 1 wt% for both). Their principal graphs are shown in Figure 3.1 (reproduced with the agreement of authors). We can see in Figure 3.1a that with Ca^{2+}-chelating ligands, gelation occurs slowly, with no plateau storage modules reached after 12 hours for three out of four solutions. Although gelation appears to be delayed and started after about 20 min, gelation is too slow for our application.

Figure 3.1b compares the evolution of the elastic shear modulus over time of two Ca^{2+} salt solutions: calcium carbonate ($CaCO_3$), which is the most frequently used [77, 81] and $CaHPO_4$. The gelation of both Ca^{2+} salt solutions is faster than with the Ca^{2+}-chelating ligand: with a plateau storage moduli reached 2 times faster with $CaCO_3$ and 4 times faster with $CaHPO_4$. In addition, the use of $CaCO_3$ causes alginate gelation to begin immediately after the addition of GDL, whereas gelation with $CaHPO_4$ starts with a delay of around 20 min. Finally, Ben Djemaa et al. [74] explain that formulations which release the most Ca^{2+} result in the strongest gels and it seems that the $CaHPO_4$ salt solution gives the strongest gel, which is interesting in the foam fabrication to obtain free standing samples that do not collapse under their own weight.

All these results allowed us to choose the $CaHPO_4$ formulation for our application because it gives a better control over the gelation kinetics. This means that by controlling the GDL concentration, we can manage the initiation of gelation and thus give ourselves enough time to foam, allow the foam to drain and however gel rapidly before it destabilises.

In the review article by Ben Djemaa et al. [77], the alginate foams produced (regardless of the type of hydrogel or crosslinker, or the foaming technique) often have pore sizes of less than 500 μm. In this chapter, we propose a highly controllable foaming process by bubbling through nozzles inside the alginate solution, which produces hydrogel foams with millimetre-sized bubbles (3-4 mm).

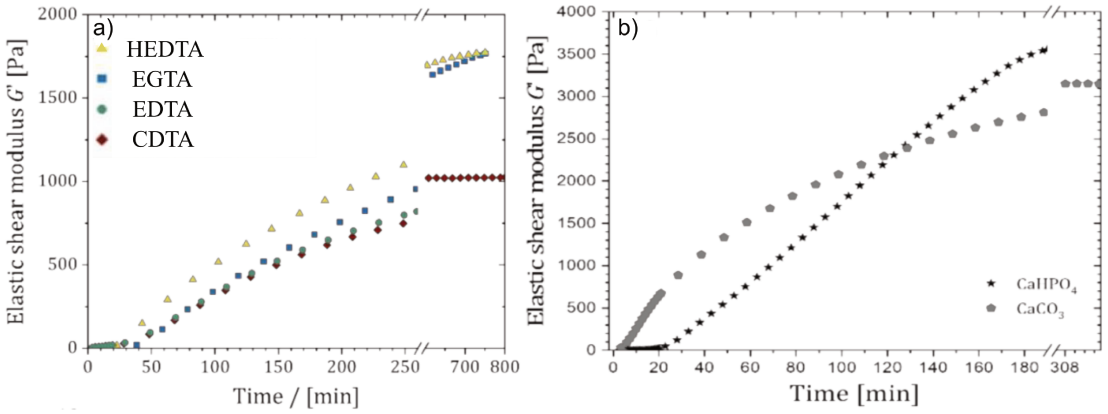


Figure 3.1 – Choice of alginate formulation based on the article by Ben Djemaa et al. [74]. Temporal evolution of the elastic shear modulus G' of gels formed with a) 0.02 M Ca^{2+}-chelating ligand and 1 wt% alginate solutions during acidification with 1 wt% GDL; b) 0.02 M salts ($CaCO_3$ and $CaHPO_4$) and 1 wt% alginate during acidification with 1 wt% GDL. Adapted from [74].

3.2 Materials and Methods

3.2.1 Preparation of solutions

To prepare alginate solutions, 2 wt% of alginic acid sodium salt, low viscosity alginate (LVA - purchased from Alfa Aesar) is solubilised in Milli-Q water under mechanical stirring at 50°C for 30 min. The solution is kept under magnetic stirring and diluted to the desired concentrations (0.5 to 1 wt% of LVA, c_{LVA}) for the different experiments. To ensure reproducibility, this solution is used for one week maximum after preparation. To prepare the gelling solution, we disperse 0.02 M of calcium phosphate dibasic ($CaHPO_4$ – purchased from Sigma-Aldrich) into a 1 wt% solution of LVA using an IKA Ultra-Turrax disperser. We kept this LVA/$CaHPO_4$ ratio constant for all experiments. We then add to this initial solution 2 g of the surfactant Disponil APG 425 (from BASF) per 100 g of solution under gentle stirring to prevent the formation of bubbles for 5 min. D-(+)-Gluconic acid δ-lactone (GDL – from Sigma Aldrich) is finally added to the gelling solution to initiate the gelation by acidification. We consider different concentrations of GDL, from 1 g per 100 g of initial solution to 5 g per 100 g of initial solution, denoted for simplicity as $c_{GDL} = 1$ to 5 wt% in the following. The GDL is first pre-dissolved with 1 g of water, substracted from the total mass of water required, then mixed with the rest for 30 seconds.

3.2.2 Rheological characterisation

As explained in Chapter 1, the initial viscosity of the solution has an impact on the bubble size when the bubbling through nozzles process is used and, in addition, liquid foam templating involves finding a balance between gelation kinetics, foaming time and foam lifetime. Bulk rheology measurements provide both viscosity measurements and gelation kinetics characterisation:

Viscosity measurements: The initial viscosity μ_0 of LVA solutions is measured using the DHR3 rheometer from TA Instruments at 20 °C with the cone-plate geometry (diameter of 60 mm, truncation gap of 28 μm and angle of 1° 00 min 47 s), following the method of Andrieux et al. [82]. The shear rates were varied from 0.1 to 1000 s^{-1}, with acquisition time of 10 points per decade. To avoid evaporation, the sample is covered using a "solvent trap and evaporation blocking" module filled with silicone oil (provided by TA Instruments). For each solution tested, the viscosity value is taken as the zero-shear viscosity measured from the Cross model [83] (the parameters of the Cross model are listed in Appendix 3).

Gelation kinetics: The temporal evolution of LVA solutions gelation is measured using the HR20 rheometer from TA Instruments at 20 °C with the plate-plate geometry (diameter of 40 mm, sandblasted plate, gap of 750 μm, frequency of 1 Hz and an amplitude of 2 %). The solutions were prepared as explained in Section 3.2.1 but due to the small volume of solution required here, the mixing is carried out using a magnetic stirrer. The samples are placed in the rheometer with a pipette, ensuring that there are no bubbles and the "solvent trap and evaporation blocking" module is placed above the sample.

In order to optimise the protocol, different solutions are tested. To be able to differentiate them and choose the best formulation according to the application, the first parameter to study is the gel time (t_g). Winter and Chambon [84] define the gel time as the transition point from the liquid to the solid state, i.e. the time at which the viscosity η tends towards infinity and the elastic modulus G appears measurable (Fig. 3.2a).

The gel time is then taken as the peak of the first derivative of the complex viscosity as a function of time (Fig. 3.2b).

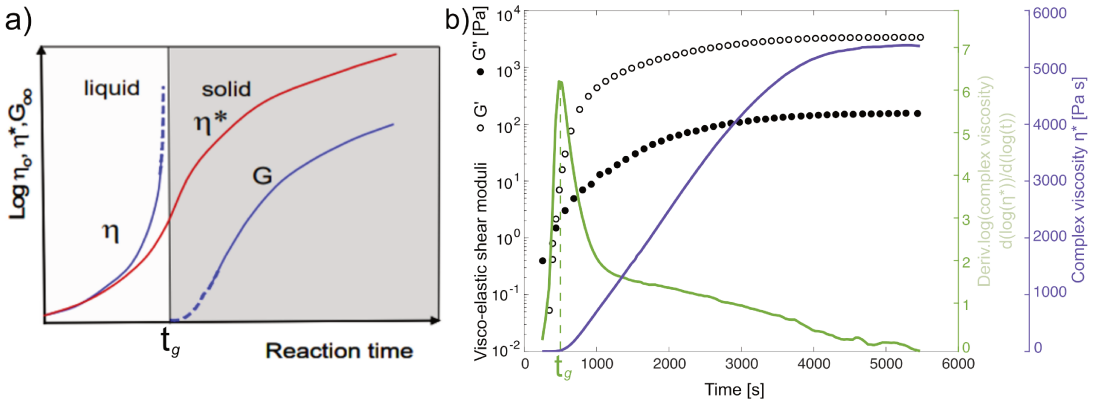


Figure 3.2 – Gel time determination: a) Interpretation of the temporal evolution of viscosity and elastic modulus of a cross-linking polymer. Adapted from [84, 85]. b) Experimental data from a bulk rheology measurement of an LVA formulation (1 wt% LVA, 0.02 M $CaHPO_4$, without surfactant and 1 wt% GDL) prepared following the protocol described in Section 3.2.1. The gel time is determinated using the derivative (in green) of the complex viscosity η^* (in purple).

3.2.3 Foam generation

Figure 3a shows the experimental set-up used to produce LVA foams. First, the foam is generated in a circular perspex tube (ID 25 mm), closed at the bottom. The plug is pierced to allow four nozzles (ID 150 μm) to pass through. To make a waterproof seal, the plug is filled with silicone. Nitrogen is blown through the nozzles into 40 mL of the gelling LVA solution (Section 3.2.1) at a constant pressure (600 mbar) via an Elveflow pressure controller (OB1 MK3+), during 2 minutes. The foam is transferred from the circular tube to a 50 x 50 x 80 mm container using a piece of PVC sheet. The sides of this container are covered with a plastic film to ensure a waterproof seal. The container is then filled to the brim with foam and covered with parafilm in contact with the foam. The resulting system makes it possible to study the drainage over time, with or without gelation of the foam. Moreover, correctly protected, the gelled foam is stable for a sufficient amount of time (almost 2 hours) to be characterised on the X-ray tomograph.

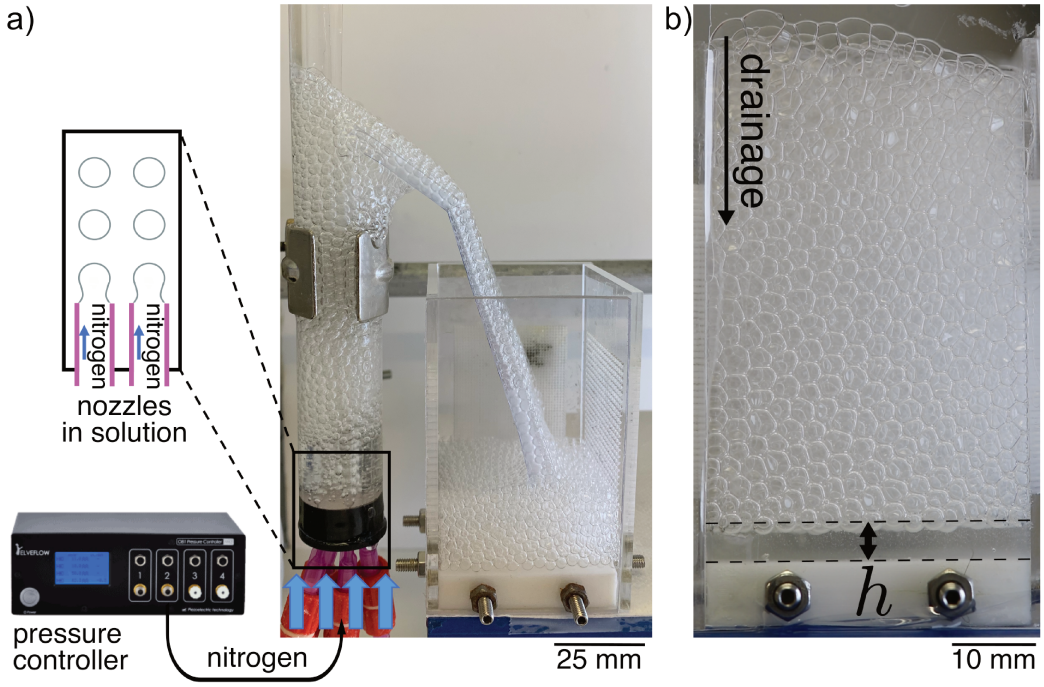


Figure 3.3 – Experimental setup. a) Foam is generated by blowing nitrogen through four nozzles at constant pressure into a gelling LVA solution. It flows down onto a PVC sheet in a square container. b) Picture of the LVA foam on which the drained liquid height h is measured.

3.2.4 Foam drainage characterisation via optical imaging

The foam formed in the container is illuminated from the side by a white light source. A video is recorded at the wall of the container using a Canon EOS 77D camera, with a full-frame resolution of 1920 x 1080 and fitted with an EF 100 mm F/2.8 Canon macro objective lens. These images are first treated to increase brightness and contrast using the free ImageJ software. Then, the evolution of drainage over time is monitored by measuring every minute the height h of the drained liquid at the bottom of the container (Fig. 3b).

3.2.5 X-ray microtomography characterisation

For all experiments, tomograms are launched 20 minutes after the foam fabrication, with a resolution of 25 μm covering a volume of approximately 45 x 45 x 30 mm^3 located at the bottom of the foam (Chapter 1).

First, we use the *foam/powder analysis* tool provided by VG Studio to measure several physical parameters at the scale of the foam, such as the bubble size and the structure thickness (struts and vertices) of the entire sample. For all this study, the sensibility threshold is kept at 20 %. Note that the thickness of the films separating two bubbles are less than 25 μm (the resolution). The software is therefore unable to detect them, which is why the cells are open in Figure 3.4. As explained in Chapter 1, at least three voxels are required over the thickness of an object, which is not the case for the film thickness. However, to measure cell sizes, the software artificially creates films.

It is also interesting to analyse the sample locally, to investigate the drainage at the scale of a strut and to track their thickness over time or at different foam heights. In fact, the density of the sample fluctuates with time and may be lower at the top than at the bottom due to drainage. Local analysis can be performed by defining regions of interest (ROIs) with VG Studio, to focus on smaller volumes of the sample and carry out specific measurements.

In order to track the temporal evolution of drainage in a gelling hydrogel foam, we have carried out a sequence of 15 successive tomograms of 5 minutes each. The total tracking time is 75 min, starting 20 minutes after the foam fabrication. For each 5 min sequence, we obtain a 3D reconstruction on which 4 struts are randomly chosen at different locations. A cubic region of interest (ROI) of 0.7 mm wide is created to contain the centre of a strut (Fig. 3.4). Using the coordinates of the centre of this ROI, we can reproduce this on the successive tomograms (at 20, 30, 40, 55, 80 and 90 min in Figure 3.10) and for the 4 struts. As the structure of the foam changes over time, we need to check that the strut is still contained within the ROI. If this is not the case, the ROI is moved slightly in x, y or z direction.

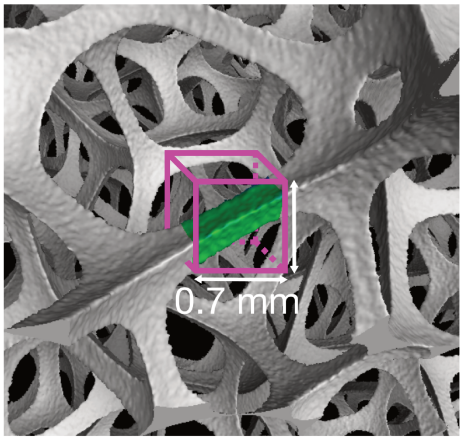


Figure 3.4 – X-ray tomographic analysis. 3D reconstruction of an LVA foam and zoom on a randomly selected strut. A 0.7 mm wide cubic region of interest is created to contain the strut. The thickness of the strut can then be measured using VG Studio software.

3.3 Results and Discussion

In order to use the "liquid foam templating" technique to create solid foams (Chapter 1), we first need to control the initial properties of the liquid, which dictate the initial structure of the liquid foam when using the bubbling through the nozzle process (Chapter 1); and then the solidification kinetics, which have an impact on the foam timescales (drainage) and therefore indirectly on the structure of the solid foam. All the sections below are aimed at understanding these parameters, which define the final structure of the foam.

3.3.1 Tuning the initial liquid properties

The initial viscosity of the liquid is studied because it mainly determines the size of the bubbles (Chapter 1). The variation of the viscosity with the shear rate is measured using rheological characterisation (Section 3.2.2) and is shown in Figure 3.5a for a 1 wt% LVA solution without additives, with 0.02 M $CaHPO_4$ or 0.02 M $CaHPO_4$ + 2 wt% Disponil, compared to a 0.5 wt% LVA solution without additives. As no GDL is added, there is no gelation. First, we see a decrease in viscosity when $CaHPO_4$ is added. This can be explained by the increase in ions when it is added, which changes the LVA chains entanglement [82, 86]. However, the use of the surfactant (Disponil APG 425) does not appear to have a significant effect on viscosity because this surfactant is non-ionic. We notice that all the solutions follow a shear-thinning behaviour according to the Cross model [83], which means that the viscosity η decreases as the shear rate $\dot{\gamma}$ increases (all the fitting parameters of the Cross model are provided in Appendix 3).

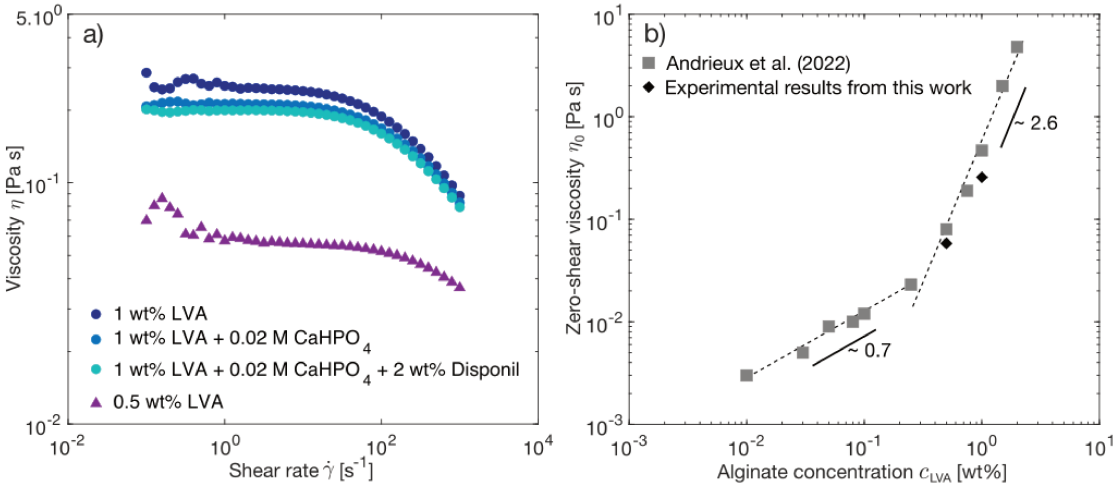


Figure 3.5 – **a)** Viscosity η of different LVA-based solutions as a function of the shear rate $\dot{\gamma}$. **b)** Viscosity η_0 of pure LVA solutions as a function of the LVA concentration c_{LVA}. Comparison of our experimental results (for 1 and 0.5 wt% LVA) with S. Andrieux et al. results in grey [82]. The dashed lines are fits to a power law.

We also use these fits to measure the zero-shear viscosity η_0, corresponding to the plateau value of the curves in Figure 3.5a, only for pure LVA solutions (1 and 0.5 wt% LVA). Figure 3.5b compares the zero-shear viscosity of our experimental results with those from the Andrieux et al. [82] study. We see that the viscosity of pure LVA solutions

increases when increasing LVA concentration. Our results are lower than those of Andrieux et al. [82]. It may be due to a change of operator or LVA batch.

These tests show that the LVA concentration has an impact on the initial viscosity of the solutions. We will see in Section 3.3.4 that this difference in viscosity has indeed an impact on the foam density and the size of the bubbles produced by bubbling through nozzles (Fig. 3.11).

3.3.2 Tuning the gelation time

Liquid foams evolve over time, first flowing and evaporating, then ageing until they break (Chapter 1). Working with solidifying foams makes it possible to stop these phenomena, and controlling solidification allows to "freeze" the foam in a desired intermediate structure.

Figure 3.6 shows the evolution of gel time t_g as a function of GDL concentration c_{GDL} for 1 and 0.5 wt% LVA solutions. The gel time is defined here as to the peak of the first derivative of the complex viscosity as a function of time (Fig. 3.2). We see that the gelation is faster when the GDL concentration is higher. This is because the more GDL, the faster the acidification and therefore the faster the release of calcium ions for cross-linking [87]. We note also that the gel time is smaller for the lowest LVA concentration (0.5 wt%). It can be explained by the fact that with 0.5 wt% of LVA, the solution is less viscous at a given time: K.I. Draget et al. [88] explained that the homogeneity of the gel is obtained by avoiding sedimentation of the calcium salt before gelling. This phenomenon is influenced and controlled by the viscosity and concentration of the LVA, which also influences the initiation and speed of gelation.

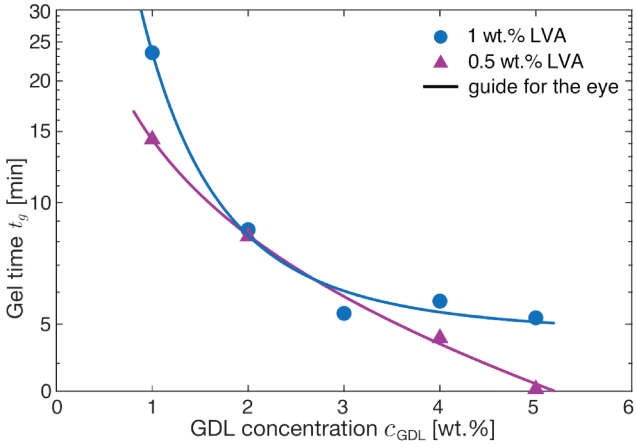


Figure 3.6 – Gel time t_g of LVA solutions (1 and 0.5 wt% LVA, 0.02 M $CaHPO_4$, without surfactant) as a function of time for different GDL concentrations c_{GDL}. The gel point was determined using the first derivative of the complex viscosity. The curves are fits to a power law ($a.x^b + c$).

Figure 3.7a shows the shear elastic modulus as a function of time for LVA solutions (1 wt.% LVA, 0.02 M $CaHPO_4$ and no surfactant to avoid bubbles) containing different GDL concentrations. Again, we see that gelation is faster at higher GDL concentrations because the shear elastic modulus G' reaches a plateau (called the plateau storage moduli) more quickly at high GDL concentrations. We also notice that the value of this plateau decreases

as the GDL concentration increases (Fig. 3.7b). Since the gluconate (Gluc) in the GDL chelates calcium ions and competes with LVA, by also bonding to the calcium released by the $CaHPO_4$ particles, increasing its concentration at a constant LVA concentration leads to an increase in the percentage of Ca-Gluc bonding and therefore a decrease in the percentage of Ca-LVA bonding, which is responsible for the gel's strength at long times (Appendix 4).

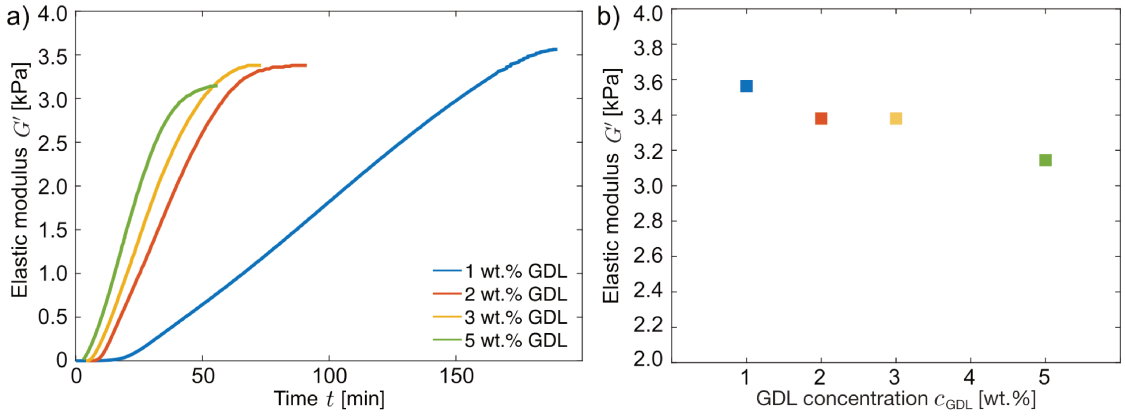


Figure 3.7 – Influence of GDL concentration on the shear elastic modulus: a) Shear elastic modulus G' as a function of time for LVA solutions (1 wt% LVA and 0.02 M $CaHPO_4$, without surfactant) with different GDL concentrations c_{GDL}. b) Plateau moduli G' as a function of c_{GDL} for the formulation presented in a).

These results show that we can have an real impact on the gelation time by modifying the GDL concentration. We will see in Section 3.3.4 that by tuning the gelation time, we can have an impact on the thickness of the foam structure without changing the bubble size, produced by bubbling through nozzles (Fig. 3.13).

3.3.3 Drainage and gelation kinetics

Initial tests were carried out using 5 and 4 % GDL (arbitrary choice) but the resulting foams were too dense and solidification too fast, causing the foam to gel in an intermediate state where 8th order vertices were present in a too high proportion (these vertices are highlighted in red in Figure 3.11b and Figure 3.11b). In this section, we therefore try to reduce the concentration of GDL in order to increase the foam drainage time and achieve the criteria described in the transition Section *From liquid to solid foam-fibre systems.*

Figure 3.8 shows the evolution of the drained liquid height, h, as a function of time for different LVA solutions, with and without gelation. h is measured following the protocol described in Section 3.2.4. All formulation are made with 0.02 M $CaHPO_4$ and 2 wt% Disponil, but for ease of reading, we only specify the LVA and GDL concentrations. First, the drained liquid without gelation is described by the red curve with triangular markers for 1 wt% LVA, and the blue curve with circular markers for 0.5 wt% LVA. We can see that both formulations attain the same drained liquid plateau height, around 11 mm, but this plateau is reached more quickly for 0.5 wt% LVA than for 1 wt%. This can be explained by the fact that with 0.5 wt% LVA, the liquid is less viscous and the foam therefore drains more quickly (Chapter 1).

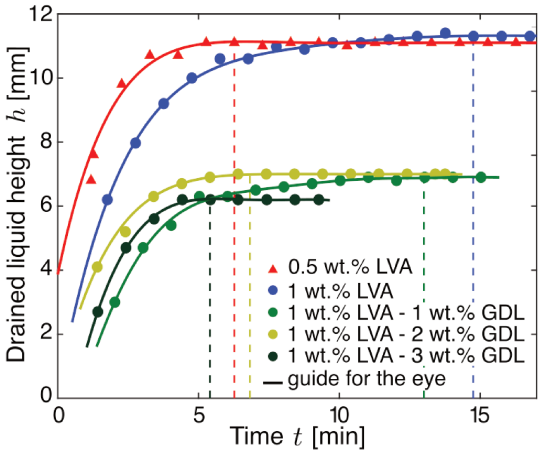


Figure 3.8 – Drained liquid height h as a function of time t for different LVA solutions (1 or 0.5 wt% LVA, 0.02 M $CaHPO_4$ and 2 wt% Disponil) with and without gelation. The GDL concentration is specified in the case of gelation. Dashed lines are a guide for the eye to show, for each formulation, the time at which the height of the drained liquid reaches a plateau. Solid lines are polynomial fits.

Then, the green curves with circular markers represent the results for 1 wt% LVA and different GDL concentrations (1, 2 and 3 wt% GDL). We can see a big difference when the foam is gelled or not. With gelation, the height of the drained liquid plateau is between 6 and 7 mm compared with 11 mm without gelation. It can also be seen that the higher the concentration of GDL, the faster the plateau height is reached. This can be explained by the fact that solidification is faster with a high concentration of GDL, so the foam drains less and remains in an intermediate state. We expect the foam with more GDL to be denser than the other.

To validate this comment, X-ray tomography characterisations are carried out 20 minutes after the foam fabrication with a resolution of 25 μm, in order to measure the structure thickness of the foams for different GDL concentrations. Figure 3.9 shows 2D images from X-ray tomography of LVA foams with 1 wt% LVA and different GDL concentrations (4, 3 and 2 wt%). We note that the foam "moves" for the lowest GDL concentrations. Indeed, in Figures 3.9b and c, we can see at the top of the images (corresponding to the top of the foams) a blur caused by a duplication of the struts and the vertices, which is the sign of motion artefacts which are too large to have been automatically corrected by the VG Studio software (Chapter 1).

Based on the images shown in Figure 3.9, we have investigated why these motion artefacts exist. We have therefore carried out sequences of rapid tomography scans, following the procedure described in Section 3.2.5 in order to study the local evolution of the foam.

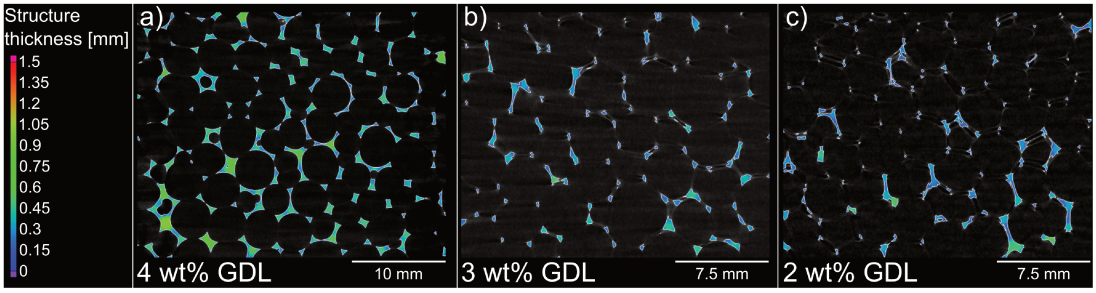


Figure 3.9 – Motion artefact observed in 2D images from X-ray tomography of LVA foams with 1 wt% LVA, 0.02 M $CaHPO_4$, 2 wt% Disponil and a) 4 wt% GDL; b) 3 wt% GDL; c) 2 wt% GDL. Resolution: 25 μm. The colours correspond to the structure thickness measurements taken by the VG Studio software.

Figure 3.10a left shows the evolution of the thickness of four struts taken at random position inside the 3D reconstruction of an LVA foam (1 wt% LVA, 0.02 M $CaHPO_4$, 2 wt% Disponil and 3 wt% GDL) at different times. We can see that their thicknesses decrease with time and seem to stabilise after 40 minutes, which show that the foams are still draining after 20 minutes. This means that as the liquid in the foam flows downwards, h, the liquid height at the bottom of the foam increases (Fig. 3b) and therefore the whole foam rises, which explains the motion artefacts. These observations are in contradiction with the results presented in Figure 3.8 where the foam with 1 wt% LVA and 3 wt% GDL seems to reach a plateau after only 5 min. We have to consider here the resolution used for the two imaging techniques. In Figure 3.10a, between 20 and 40 min, we are talking about a decrease in strut thicknesses of around 50 μm which are not visible with the camera resolution used in Figure 3.8 but sufficient to create motion artefacts in tomography images.

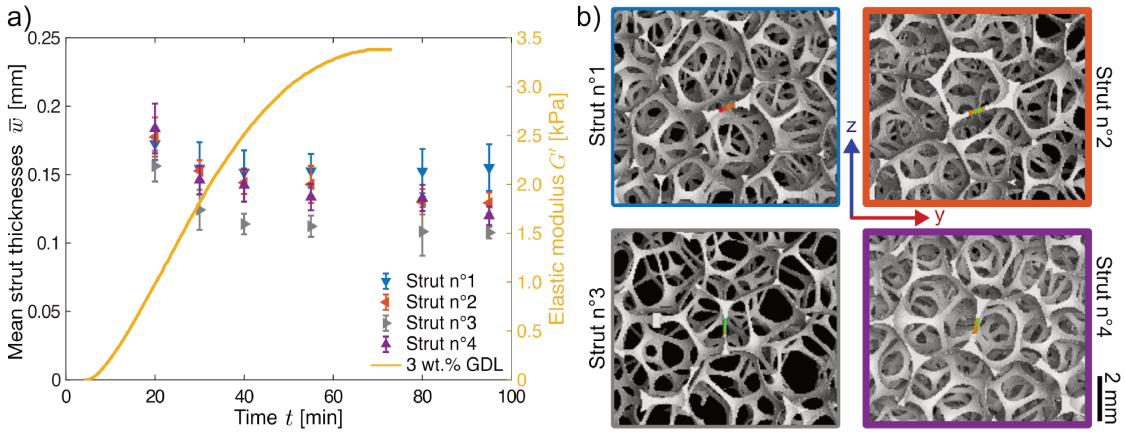


Figure 3.10 – a) Left axis in black: Evolution of the average thicknesses $\bar{w}$ of four different struts over time t. The thickness measurements are made with the VG Studio software and focus on the central part of these struts, contained within a 0.7 mm wide cubic ROI (see Figure 3.4). The struts were randomly selected from X-ray tomographic images of an LVA foam (1 wt% LVA, 0.02 M $CaHPO_4$, 2 wt% Disponil and 3 wt% GDL). The error bars correspond to standard deviations of the strut thickness; Right axis in yellow: shear elastic modulus G' as a function of time t for the same LVA solution (1 wt% LVA, 0.02 M CaHPO4, 3 wt% GDL, without surfactant). b) Zoom on the four struts reconstructed from tomographic images of the LVA foam. Resolution: 25 μm.

The right axis in Figure 3.10a shows in yellow the shear elastic modulus G' as a function of time for the solution with 1 wt% LVA and 3 wt% GDL, measured by rheological tests, which are described in Section 3.3.2. It seems that the foam drains until the material constituting the foam reaches a stiffness between 2.0 and 3.0 kPa. We can make a clear link between the stop of the evolution of the drainage in the foam and the evolution of the shear elastic modulus as a function of time.

We can see from Figure 3.10a that the thicknesses of the four struts are not equal. If we look in more detail at what is happening inside the foam, we remark that the orientation of these struts is also different (Fig. 3.10b). Indeed, it appears that the struts n°3 and 4 (the thinnest) are oriented vertically, unlike the other two. The location coordinates of each strut are listed in Appendix 5.

These results on the foam drainage show that the characterisation tool used (camera or X-ray tomography), its resolution and the time at which the measurements are taken have an importance on the structure of the foam obtained on the images. Indeed, in Figure 3.8 the foam containing 1 wt% LVA and 3 wt% GDL (+ 0.02 M $CaHPO_4$ + 2 wt% Disponil) seems to stop draining at around 6 min, whereas in Figure 3.10a left axis, the foam with an identical formulation seems to stop moving at about 40 min.

3.3.4 Control over the hydrogel foam structure

With all the results given above concerning the adjustment of initial liquid properties, gelation time and drainage in relation to gelation kinetics, we summarise in this section the impact of LVA and GDL concentrations on the resulting LVA foam structure.

All formulations are made with 0.02 M $CaHPO_4$ and 2 wt% Disponil and for ease of reading, we only specify below the LVA and GDL concentrations.

Influence of the alginate concentration on the foam structure

Figure 3.11 shows the foam characteristics (bubble diameters, struts and vertices thicknesses) measured with the VG Studio software (Chapter 1), for two different LVA concentrations (0.75 and 1 wt% LVA, the GDL concentration being kept constant at c_{GDL} = 4 wt%), following the foaming protocol described in Section 3.2.3. All the tomographic characterisations are carried out 20 minutes after the foam fabrication with a resolution of 25 μm and for 20 minutes. First, we can see in Figure 3.11a (left axis) that the diameter of the bubbles is greater when the solution is more concentrated in LVA (Fig. 3.11b bottom). This can be explained by the fact that the viscosity of the solutions increases when the LVA concentration increases (Fig. 3.5a).

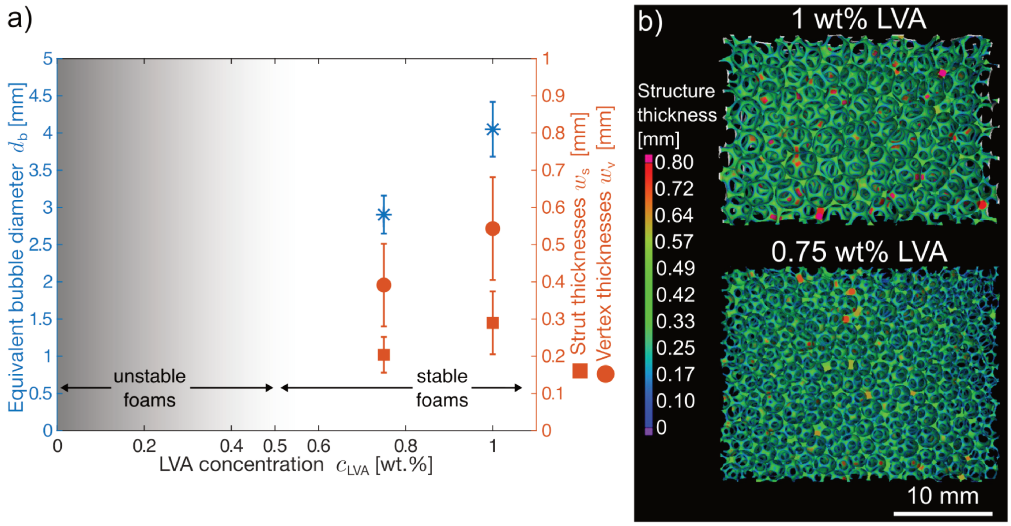


Figure 3.11 – Impact of the LVA concentration: a) Left axis in blue: Equivalent bubble diameters d_b. Right axis in red: Thicknesses of struts w_s and vertices w_v. All results are measured with VG Studio software on LVA foam images for different LVA concentrations c_{LVA} (with 0.02 M $CaHPO_4$ + 2 wt% Disponil + 4 wt% GDL). The error bars correspond to standard deviations of bubble diameters or strut thicknesses, respectively, over the entire sample. A foam containing 0.5 wt% of LVA was tested and found to be unstable. 0.5 wt% of LVA is therefore marked on the graph as the boundary between unstable and stable foams. b) 3D reconstruction of the LVA foams described in a). Tomography is carried out 20 minutes after the foam fabrication with a resolution of 25 μm.

Then, Figure 3.11a (right axis) shows the average thicknesses of the struts and vertices. We can see that for both thicknesses, the foam structure is thinner when the LVA concentration is lower (Fig. 3.11b bottom). This can also be explained by the reduction in viscosity, which allows the foam to drain more. We can note the presence of a greater number of 8 order vertices (Fig. 1.19) when the solution is more concentrated in LVA, perhaps because the liquid has more difficulty to drain (Fig. 3.11b top). When the VG Studio software measures the thicknesses of the material constituting the foam, it does not automatically distinguish the struts from the vertices (Chapter 1). The protocol we used to calculate w_s and w_v from the VG Studio analysis is the following: On the distributions of the structure thickness normalised by the mean structure thickness (Fig. 3.12), we can see two peaks, corresponding to the thickness of (1) the struts; (2) the vertices. The histograms are arbitrarily divided in two to distinguish these two thicknesses. The black dashed line highlights this separation. The average thickness of the struts is then calculated by taking the mean thickness of the left side from the black dashed line. Similarly, the average thickness of the vertices is the mean thickness of the right side from the black dashed line.

A foam containing 0.5 wt% LVA and 4 wt% GDL was also tested, but was found to be unstable. This may be caused by the insufficient quantity of polymer in the less concentrated solution to form a gel strong enough to withstand the stresses provided in a foam.

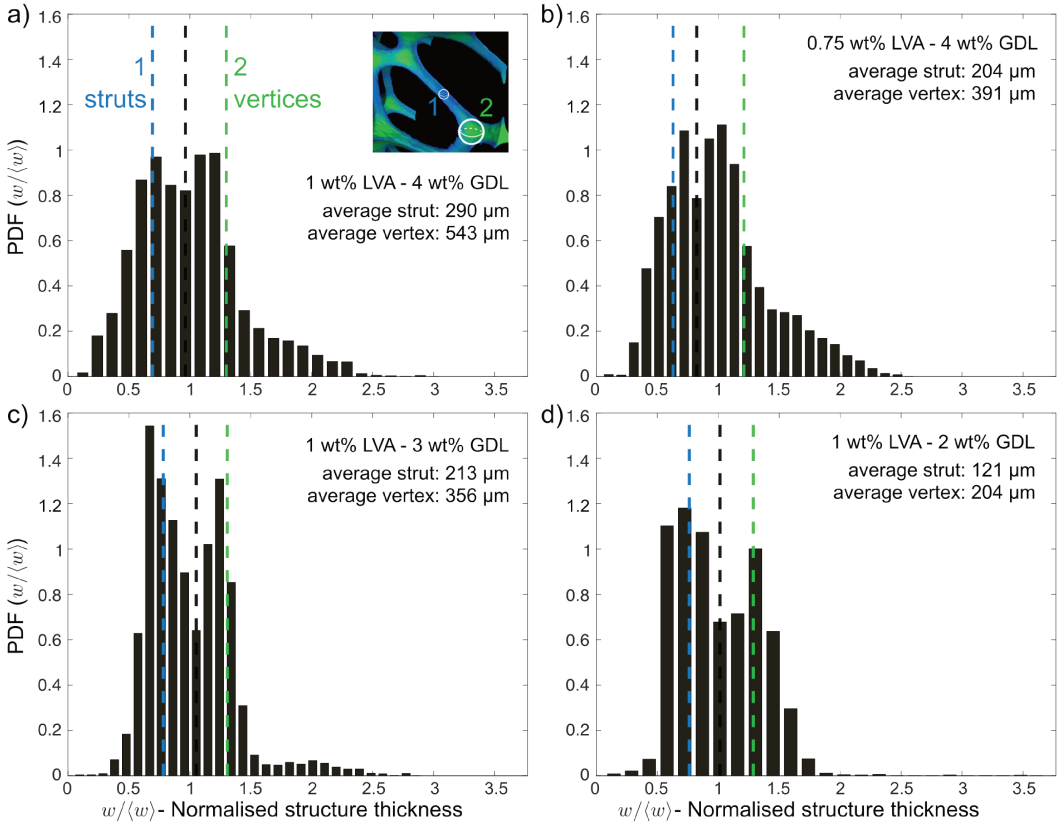


Figure 3.12 – Distribution of the structure thickness normalised by the mean structure thickness for four LVA foams produced following the protocol described in Section 3.2.3, with 0.02 M $CaHPO_4$, 2 wt% Disponil and a) 1 wt% LVA + 4 wt% GDL; b) 0.75 wt% LVA + 4 wt% GDL; c) 1 wt% LVA + 3 wt% GDL; d) 1 wt% LVA + 2 wt% GDL. The inset in a) shows a zoom on a strut to remind the method used to measure thickness using the VG Studio software and to explain the presence of two peaks corresponding to the thickness of (1) the struts; (2) the vertices (Chapter 1). The histograms are arbitrarily divided in two to distinguish these two thicknesses. The black dashed line highlights this separation. The average thickness of the struts is then calculated by taking the mean thickness of the left side from the black dashed line and is highlighted by a blue dashed line. Similarly, the average thickness of the vertices is the mean thickness of the right side from the black dashed line and is highlighted by a green dashed line.

Influence of the GDL concentration on the foam structure

Figure 3.13a shows the impact of the GDL concentration on the foam characteristics (bubble diameter, strut and vertices thicknesses). Three different GDL concentrations are tested (2, 3 and 4 wt%) at constant LVA concentration (1 wt%). The foam characteristics are measured with the VG Studio software (Chapter 1) and the foams are produced following the foaming protocol described in Section 3.2.3. Tomographic characterisation of the LVA foam with 4 wt% GDL is carried out 20 minutes after foam fabrication with a resolution of 25 μm and for 20 minutes. As explained in Section 3.3.3, foams containing 2 and 3 wt% GDL are not sufficiently stable to be characterised in the same way. Therefore, the results described here, for these two formulations, are taken from the first step of sequential rapid tomography scans described in Section 3.3.3. More specifically, this first step corresponds to the scan carried out 20 minutes after foam fabrication at a resolution

of 25 μm and for 5 minutes.

We can see in Figure 3.13a that the GDL concentration has an impact on the thicknesses of the structure. We observe that both thicknesses (struts and vertices) decrease when the solution is less concentrated in GDL (Fig. 3.13b), showing that the longer the solidification time, the longer the foam can drain. This is also reflected by the increase in the relative foam density as the GDL concentration increases.

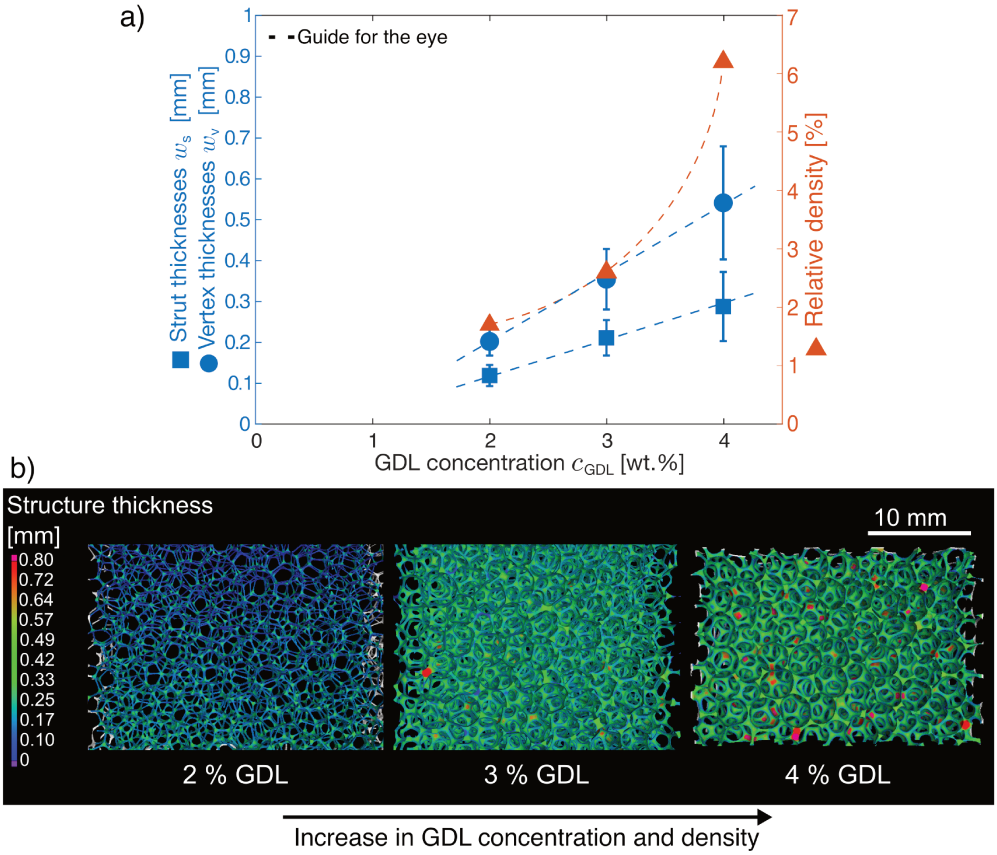


Figure 3.13 – Impact of the GDL concentration: a) Left axis in blue: Thicknesses of struts w_s and vertices w_v. All results are measured with VG Studio software on LVA foam images for different GDL concentrations c_{GDL} (with 1 wt% LVA + 0.02 M $CaHPO_4$ + 2 wt% Disponil). The error bars correspond to standard deviations of bubble diameters or strut thicknesses, respectively, over the entire sample. Right axis in red: Relative density of the corresponding foam. b) 3D reconstruction of the LVA foams described in a). Tomography for foam with 4 wt% GDL is carried out 20 minutes after the foam fabrication for 20 minutes. The two other tomographies are carried out 20 minutes after foam fabrication for 5 minutes. Resolution: 25 μm.

We clearly see that there is a pronounced gradient of thickness for the foam containing 2 wt% GDL (Fig. 3.13b). We can thus question the homogeneity of the samples along the z-axis. We therefore divided the samples in four layers taken at different z positions (Fig. 3.14a). We observe in Figure 3.14b (left axis) that the GDL concentration has no significant impact on the bubble diameters, which vary between 3.6 $\pm$ 0.1 mm and 4 $\pm$ 0.4 mm. In terms of the structure thicknesses, there seem to be a thickness gradient in each sample, regardless of the GDL concentration, with the top of the foam being thinner than the bottom, as a result of drainage. However, it seems that the difference in thickness

between the top and bottom of the foam is larger for foams with a lower concentration of GDL.

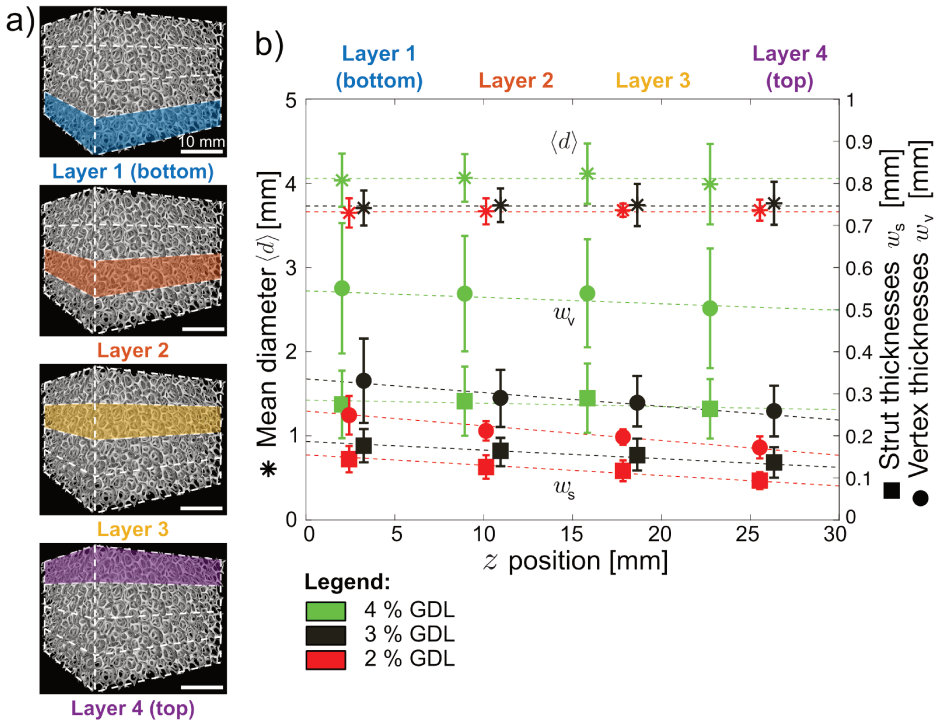


Figure 3.14 – Verification of the sample homogeneity along the z-axis: a) Illustration of the layers positions shown on a Pu foam (from Chapters 4 and 5) with the corresponding layer highlighted in colour. b) Left axis: Mean diameter of the bubbles (star symbols); Right axis: Mean thicknesses of the struts (square symbols) and vertices (circle symbols) as a function of the z-axis for different GDL concentrations (with 1 wt% LVA + 0.02 M $CaHPO_4$ + 2 wt% Disponil). The error bars correspond to the standard deviations of the bubble diameter and the structure thicknesses over the corresponding layer. The dashed lines are guides for the eye.

3.4 Conclusion

This method of producing LVA foams that we developed in this chapter offers a high degree of control over the foam structure. This study shows that the concentration of GDL has an impact on the viscosity of the solutions, but also on the diameter of the bubbles and the thickness of the foam structure. We show that the GDL concentration has an impact on the gelation time and the time at which the final modulus of elasticity is reached. These last two parameters, coupled with the drainage phenomenon, have an impact on the thickness of the foam structure. We have already seen that bubbling through a nozzle gives a high degree of control over the bubble size (Chapter 1), but we demonstrate here that by adding control over the initial properties of the liquid (such as viscosity), solidification kinetics and drainage, we can finely tune the foam structure (bubble size, density, dispersity).

Following the criteria listed in the transition Chapter *From liquid to solid foam-fibre systems*, for the next experiments presented in Chapter 5 below, we decided to use the LVA formulation containing 1 wt% LVA, 0.02 M $CaHPO_4$, 2 wt% Disponil and 3 wt%

GDL. It enables a quick gelation compared with other processes (Section 3.1), while giving time to produce the foam and allowing the system to reach an equilibrium before the solidification begins. Moreover, we believe that with this formulation, we were able to reduce the density of the foam sufficiently by reducing the concentration of GDL, to reduce defects (such as 8th-order vertices) present in large numbers in denser foams (Fig. 3.11b and 3.13b). However, we could not reduce the concentration of GDL any further as this would imply a too important thickness gradient in the structure (Fig 3.13b). The optimised formulation and protocol allow us to obtain reproducible model foams (Fig. 5.11) with which we will study the influence of the fibre integration in Chapter 5.

Chapter 4

Polyurethane foams

Contents

4.1 Context 66
4.1.1 Chemical generalities 66
4.1.2 Flexible polyurethane formulation 67
4.1.3 Chemical foaming vs microfluidics 67
4.2 PU foam preparation via chemical foaming 68
4.2.1 Materials 68
4.2.2 Foaming process improvements 69
4.2.3 Formulation improvements 70
4.2.4 Fibre introduction 72
4.2.5 Conclusion 73
4.3 PU foam preparation via bubbling through nozzles 74
4.3.1 Formulation 74
4.3.2 Experimental setup 78
4.3.3 Foam superimposition: A new method to control foam structure 81
4.3.4 Conclusion 85

Polyurethane (PU) is used here to obtain solid foams that can be removed from the container in which they are prepared and used for various characterisations (structural and mechanical) which is their main advantage compared to alginate systems described in Chapter 3. With PU systems, it is also possible to control the pore size using different foaming techniques (chemical or mechanical), the solidification kinetics and the flexibility of the final solid foam (adjustable by modifying the polyurethane formulation). In this chapter, we first explain the context to show how to obtain a flexible foam and where this project started. We then present a first protocol for the chemical foaming of PU. We finally focus on a new mechanical foaming method developed to improve foam homogeneity and control the physical properties of foams (bubble size, density, flexibility). The formulation of PU foams contains isocyanates, which are CMR components, so all the experiments that follow have been carried out carefully in a fume hood.

The following content is the basis of the article: **Solidification of polyurethane model foams via catalyst drainage from a secondary foam** by M. Jouanlanne, A. Egelé, W. Drenckhan, J. Farago and A. Hourlier-Fargette.

4.1 Context

Polyurethanes are one of the most popular, adaptable and investigated polymeric materials in the world [89]. They were developed by the German research team of Pr Otto Bayer with the idea of finding an alternative to rubber, and led to the creation of the PU industry in 1937 [90]. PU was soon found in the form of coatings, rigid or flexible foams in several fields such as biomedical, construction, automotive and textiles [91].

4.1.1 Chemical generalities

Polyurethane is made by mixing polyols with isocyanates in the presence of a catalyst and other additives (surfactant in the case of foams). Isocyanate (-NCO) groups react with hydroxyl (-OH) groups from the polyol to form urethane (-NHCOO) groups (Fig. 4.1a). Polyols contribute to the flexibility of PU. Depending on the type of polyol, they can provide flexible long segments to produce elastic polymers or hard short segments for rigid polymers. Isocyanates are responsible for the PU reactivity and curing properties. The ratio between isocyanate and polyol ([NCO]:[OH] index) gives the cross-linking density [91, 92]. A [NCO]:[OH] = 100:100 means that there are as many -NCO groups as there are -OH groups.

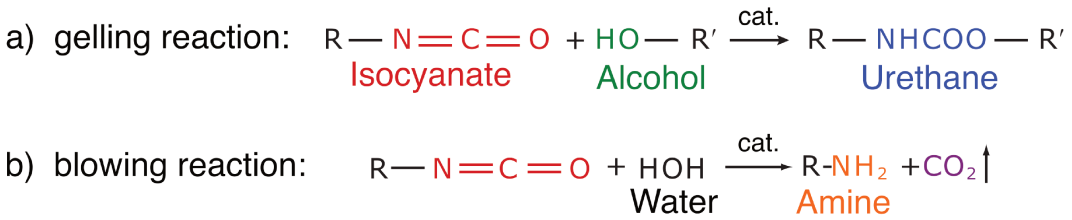


Figure 4.1 – Polyurethane reactions in the context of chemical foaming: a) Hydroxyl groups from polyols react with isocyanate groups to form urethane groups ; b) Water reacts with the isocyanate, producing carbon dioxide at the same time as the first reaction occurs, to obtain a foam [92].

To produce PU foams with the chemical foaming technique (Fig. 4.2), first, the polyol, catalyst, surfactant and water are mixed together because they do not react with each other (mixture A). All these components are then mixed with the mixture B, which contains only the isocyanate, using a mechanical stirrer. Two processes occur at the same time: carbon dioxide is formed when water is added to the formulation (blowing reaction, Fig. 4.1b). Bubbles are created, expand and remain trapped inside the PU mixture, which undergoes a gelling reaction: urethane groups are formed and the polymeric matrix solidifies (Fig. 4.1a) [92]. The catalyst activates and accelerates the reactions. There are different catalysts, some of which facilitate the blowing reaction, others the gelling reaction [93]. Surfactants are indispensable for foam production. They are amphiphilic molecules absorbing at the interface and stabilise films (Chapter 1). There are two types of surfactant: regulating surfactants, which determine the size of the bubbles (in the case

of chemical foaming techniques) and stabilising surfactants, which increase the stability of the foam [91].



Figure 4.2 – Production of polyurethane foam by chemical foaming. Credits: BASF.

4.1.2 Flexible polyurethane formulation

As explained in the transition Section *From liquid to solid foam-fibre systems*, we want to obtain flexible polyurethane foams (non-brittle and with a large linear elastic range) in order to carry out mechanical tests. To achieve this, some key parameters can be controlled to adjust the flexibility of the foam. First, high molecular weight polyols (2000 - 10000 g/mol) are known to be used in the production of flexible foams because they are often linked to long molecule chains. Chain extenders are also available to increase the length of polyol chains but were not used here. The cross-linking density needs to be low to obtain flexible foams, for example by reducing the functionality of the main chemical component but also reducing the [NCO]:[OH] index (i.e. the ratio between hydroxyl and isocyanate groups). In addition, depending on the application, the choice of catalyst (blowing or gelling) and surfactant (regulating or stabilising) may be different [91, 92, 93].

4.1.3 Chemical foaming vs microfluidics

Two protocols (formulation and foaming technique) have already been studied at the ICS: The first protocol was studied by Martin Hamann [94], who used chemical foaming to produce rigid polyurethane foams. The advantage of these foams is their low density (respecting Plateau's laws [1]), their large bubbles and their quick handling, but as mentioned previously, they are too rigid for our application and inhomogeneous. The foam shown in Figure 4.3a was made using the exact protocol and formulation of the work by M. Hamann et al. [95].

The second protocol was developed by Aouatef Testouri [96], who produced flexible polyurethane foams using millifluidics. The millifluidics is the science and technology that manipulates fluids in millimetric channels. Used to produce foam, it is part of the family of mechanical foaming techniques (Section 1.2.1.2). In the work of A. Testouri et al. [97], they were therefore able to inject, foam and mix all the chemicals involved in the formulation of the polyurethane inside a millifluidic chip (Fig. 4.3b). The foams they obtained were highly periodic, with adjustable densities and bubble sizes (Fig. 4.3c). The reproduction of their system was not satisfying because the foams obtained did not meet the criteria described in the transition Section, particularly in terms of the bubble size, which were too small (on a micrometric scale, as illustrated in Figure 4.3c). Moreover, the

polyol used is highly viscous, making it difficult to manage bubbling time, foam stability and solidification time.

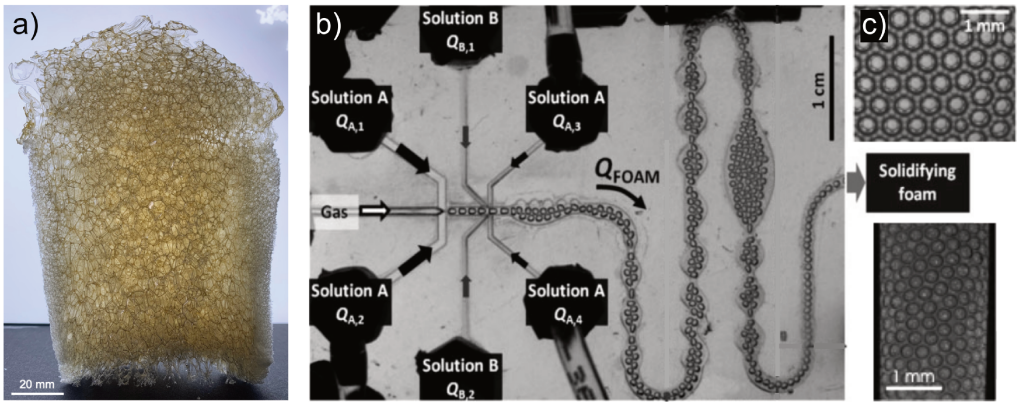


Figure 4.3 – Inspiring literature: a) Rigid polyurethane foam using the protocol from M. Hamann et al. [95] formulation and chemical foaming protocol. b) Millifluidic chip from A. Testouri et al. works [97]. c) Solidifying polyurethane foams produced with this millifluidic device, adapted from [97].

The idea for this thesis is then to combine the two protocols. We have two options:

1. Use M. Hamann et al. [95] protocol to chemically foam A. Testouri et al. [97] formulation by adding water.

2. Use A. Testouri et al. [97] formulation and reduce the polyol viscosity by adding the less viscous polyol from M. Hamann et al. [95] formulation and use mechanical foaming to produce foam (i.e. without water) (Section 1.2.1.2).

In the following sections, we present the materials and methods as well as the results for the two options presented above.

4.2 PU foam preparation via chemical foaming

This section presents the results from the option n°1 described above. Part of the following results come from Le Quan Ngo's internship, which was co-supervised by Aurélie Hourlier-Fargette and myself. Many modifications have been made to the formulation and foaming technique in order to improve the homogeneity, foamability (foam height) and the bubble size distribution of the foams made with the basics of chemical foaming (Fig. 4.2) and A. Testouri et al. [97] formulation. Pictures of characteristic samples of the various modifications made are shown in Figure 4.5. We then present the first experiments on fibres randomly dispersed in PU foams, as well as the results obtained on the characterisation of these foam/fibre systems.

4.2.1 Materials

All experiments have been carried out with a trifunctional polyether polyol Lupranol 2090, an oligomeric form of methylene diphenyldiisocyanate (MDI) Lupranat M20S (both provided by BASF Polyurethanes GmbH), a tertiary-amine based catalyst Jeffcat ZR50

(Huntsmann Corporation) in the blowing catalyst category (Section 4.1.1) and a PDMS-PEO block-co-polymer surfactant (Surf.) Tegostab B8002 (Evonik Industries) in the regulating surfactant category (Section 4.1.1). To increase the size of the bubbles, a physical blowing agent, cyclopentane (CP, $\geqslant$ 95% by BASF), has been added in some of the latest experiments, as in M. Hamann et al. [95] formulation. To facilitate mixing of the fibres with the other components listed above, a low-molecular polyol, tripropylene glycol (TPG, 97% by Sigma Aldrich), has been mixed with Lupranol 2090 to reduce the viscosity of the final mixture (Section 4.3.1.1). In terms of fibres, first tests were conducted with 120 μm diameter fluorocarbon (FC) nylon fibres (Flashmer MagixFluoro) dispersed in a polyurethane foam (Section 4.2.4).

4.2.2 Foaming process improvements

The major improvements in terms of processes have been made in the mixing step. Three different methods were tested, studying their impact on the resulting foams.

The first method is *mixing using the double syringe system* (Fig. 4.4). This is a shear mixing technique, which consists of connecting two luer-lock syringes and mixing the contents of the syringes by a succession of back-and-forth movements. The advantage is that the introduction of gas can be avoided. For the first tests, 5 back-and-forth movements were performed on mixture A, then 3 back-and-forth movements to mix A and B together. The resulting foams were inhomogeneous (Fig. 4.5, Formulation n°2), with big holes and stripes with either stiff brown areas, caused by poorly mixed isocyanate (mixture B), or sticky areas, caused by poorly mixed mixture A. We think that this is caused by a too low number of back-and-forth steps. The high viscosity of the products makes the passage from one syringe to the other too complicated.

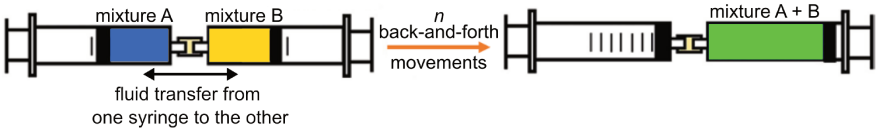


Figure 4.4 – Diagram of the double syringe system for mixing of A (polyol, catalyst, surfactant and water) and B (isocyanate) components.

The second method is *mixing by hand or with a mechanical stirrer* (mech. stirrer). Initially, the mixing was carried out by hand with a glass rod at a speed of $\sim$ 120 rpm (or $\sim$ 2 rotations per second) for $\sim$ 20 seconds, but as manual stirring is very operator-dependent, we have decided to control the speed of rotation using a mechanical stirrer (Fig. 4.2). The speed was set at 200 rpm. The stirrer was immersed in the bottom of the cup containing the foaming mixture and the cup was moved in a circle during stirring to ensure that the stirrer can reach the bottom and walls of the cup. Although reproducibility increased with mechanical stirring, for both techniques the homogeneity of the foams was still not good (Fig. 4.5, Formulation n°5 - 6). One of the possible causes of inhomogeneity is that the stirrer did not reach the bottom and walls of the cup very well.

The third improvement is *the double potting technique* (dbl. pot.) that was set by Le Quan Ngo to solve inhomogeneity problems. It involves using two containers, one for the mixing step and the other for expanding the foam. The mixing step is carried out in a smaller pot, then the foaming liquid is poured into a large cup to leave place for

the expansion of the foam. This technique, combined with mechanical stirring, produces homogeneous and reproducible foams (Fig. 4.5, Formulation n°7 - 8).

4.2.3 Formulation improvements

Table 4.1 lists the major formulation improvements and the foaming process used. For reference, the initial concentrations used in the work of A. Testouri et al. [97] are shown in the first row (Formulation n°0).

Concentrations are calculated with respect to 100 wt% of the A-Component (polyol, catalyst, surfactant and water). The percentage of isocyanate is calculated from the quantity of -NCO required to obtain the [NCO]:[OH] ratio indicated. When water is added, the concentration of the -OH groups increases considerably, which is why the concentration of -NCO varies to achieve the required [NCO]:[OH] ratio.

	A-Component*				B-Component*		Physical Blowing Agent*	
n°	**Polyol [wt%]**	**Catalyst [wt%]**	**Surf. [wt%]**	**Water [wt%]**	**Isocyanate [wt%]**	**[NCO]:[OH] Index**	**CP [wt%]**	**Mixing process**
0	94.95 94.7	0.05 0.3	5	-	6.32 6.34	100:100	-	microfluidics [97]
1	92.9	0.1	5	2	35.8	100:100	-	double-syringe
2	84	1	5	10	154	100:100	-	double-syringe
3	87	1	2	10	30.8	20:100	-	by hand
4	72	1	2	25	75.0	20:100	-	by hand
5	72	1	2	25	75.0	20:100	13.5	by hand
6	72.25	0.75	2	25	75.0	20:100	13.5	mech. stirrer
7	73.25	0.75	1	25	75.0	20:100	13.5	mech. stirrer dbl. pot.
8	71.25 + 2% TPG	0.75	1	25	75.5	20:100	13.5	mech. stirrer dbl. pot.

*percentages calculated with respect to 100 wt% of the A-Component.

Table 4.1 – Evolution of the formulation and the protocol for chemical foaming process in PU foam fabrication.

Starting with A. Testouri et al. [97] formulation (Table 4.1, Formulation n°0), an appropriate concentration of water and catalyst must be found to initiate foaming. We have started with 2 wt% as in M. Hamann et al. [95] formulation but with these chemicals, the mixture did not foam at all (Fig. 4.5, Formulation n°1).

The water concentration was then increased from 2 to 10 wt% and the catalyst concentration to 1 wt%. The resulting foams were inhomogeneous (Fig 4.5, Formulation n°2). Mixing the products using the double syringe was abandoned and the surfactant concentration was reduced to 2 wt%. A reduction in surfactant concentration leads to less stable bubbles, particularly if the concentration is below the critical micellar concentration (i.e. the concentration above which the surface tension does not decrease further when surfactant is added, measured at 1 wt% for Lupranol 2090 [97]) and therefore to more coalescence and larger bubbles.

The [NCO]:[OH] index was then reduced from 100:100 to 20:100, because by reducing the [NCO]:[OH] index, the rigidity of the foam can be reduced (Section 4.1.2). The results showed a nice increase in flexibility but also a decrease in foamability. Figure 4.5, Formulation n°3, shows that the height of the foam was considerably reduced. In fact, by reducing the isocyanate concentration, the reactivity is also reduced and the foamability decreases. This is why the water concentration was increased for the next step.

Water concentration has been varied from 10 to 30 wt%. As expected, bubble size increased, demonstrating the impact of water on chemical foaming (Fig. 4.5, Formulation n°4). The water concentration was then maintained at 25 wt% for the rest of the experiments.

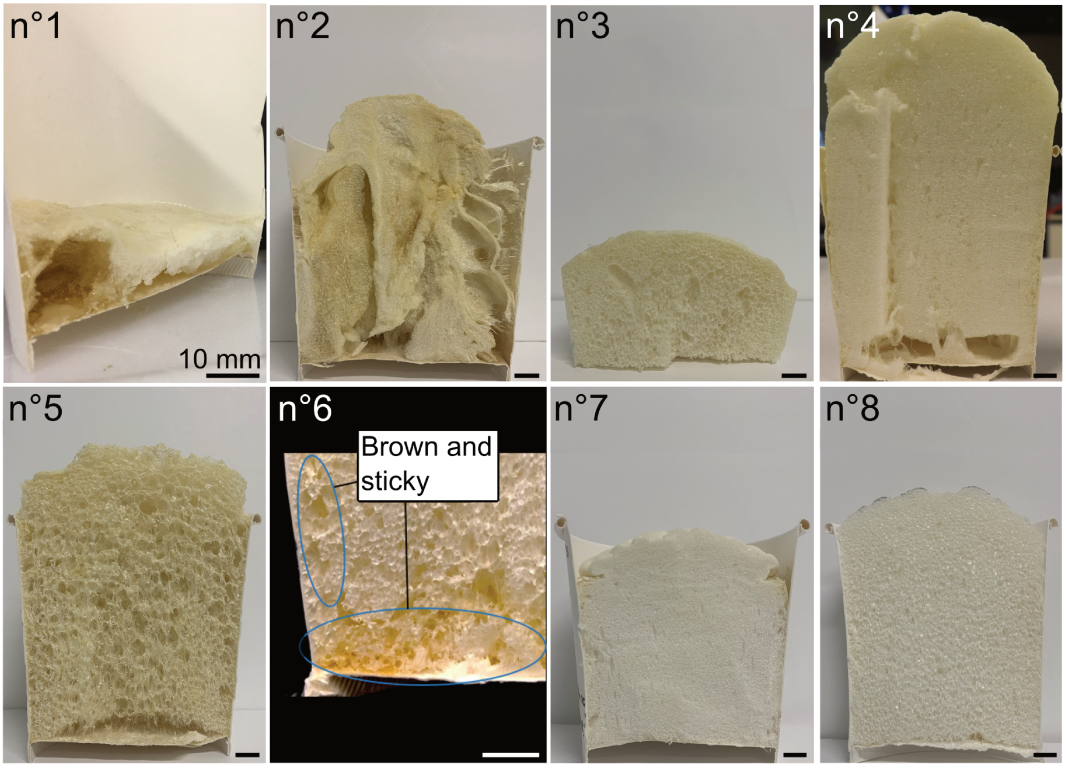


Figure 4.5 – Pictures of the polyurethane foams corresponding to the formulations listed in the Table 4.1, highlighting the defects in the initial formulations and showing how we arrived to the optimized formulation n°7 and its version with a lower viscosity of the liquid precursor n°8. Scale bars: 10 mm.

However, the bubble size was still too small. For this reason, cyclopentane (CP) was added as a physical blowing agent and its concentration was set at 13.5 wt%. This resulted in a significant increase in the bubble size but the bubbles seemed deformed and no longer following the Plateau's laws (Fig. 4.5, Formulation n°5). This may be because the reaction becomes too fast when the CP is added. By reducing the catalyst concentration, the mixing time and the time before the reaction starts can be increased. Tests have been carried out with 0.25, 0.5, 0.75 and 1 wt% catalyst. The results are that 0.25 and 0.5 wt% reduce the height of the foam by half compared with the other two concentrations (from 130 ± 10 mm to 65 ± 5 mm). On the other hand, the 0.75 wt% concentration achieves good foamability while slightly extending the mixing time and the

time before the reaction starts (only 15 seconds, but sufficient in our experiments).

The mixing step is very important to obtain homogeneous foams and Figure 4.5, Formulation n°6, shows that there are still stiff brown zones or sticky zones at the bottom of the foams, even with mechanical stirring. This is why, from here, the double potting technique has been systematically used (Section 4.2.2).

The last step consists in reducing the surfactant concentration to further increase the bubble size. The tests have been carried out with 0.5 and 1 wt% surfactant. The 0.5 wt% concentration shows white drips inside the films and highly deformed cells that do not respect Plateau's laws, which is not the case with the 1 wt% concentration. Formulation n°7 is therefore validated for testing on foam-fibre systems.

4.2.4 Fibre introduction

Chemical foaming can be used to study the impact of randomly dispersed fibres on the foam structure. One of Le Quan Ngo's tasks was to adapt the previous protocol to incorporate the fibres properly. Firstly, 2 wt% TPG is mixed with Lupranol 2090 to reduce the total viscosity of the mixture (Formulation n°8; Section 4.3.1.1 below describes the reduction in viscosity of a two-component mixture).

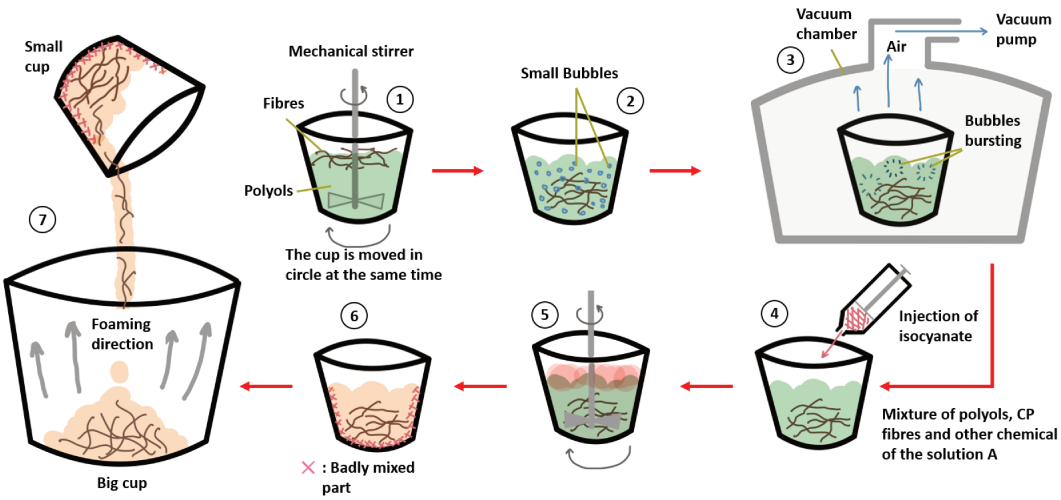


Figure 4.6 – Final protocol of chemical foaming of polyurethane with fibre introduction. Credits: Le Quan Ngo.

Two steps are then added to the protocol to introduce the fibres. First, a premixing step is added to disperse the fibres in the polyols with mechanical stirring (3 x 2 min at 500 rpm). In addition, degassing in a vacuum chamber is necessary to eliminate any small bubbles incorporated during stirring. The end of the protocol remains the same, with the mixing of all the other components (catalyst, surfactant, water, CP and isocyanate) and the double potting technique to keep only the part of the mixture that is well mixed. All these steps are described in Figure 4.6. The obtained foams are homogeneous and the height of the foam is sufficient to obtain a sample which is representative of the entire foam. The bubbles are polydisperse and elongated in the foam rise direction (Fig. 4.5, Formulation n°8). FC nylon fibres with a diameter of 120 μm and a length of 10 mm are incorporated into PU foams following the protocol described in Figure 4.6. Experiments

with longer fibres have also been carried out and the results show that in this system, too long fibres exert too much stress on the bubbles during the foaming process, leading to strong deformation of the bubbles and destabilisation of the foam.

The results for short fibres are shown in Figure 4.7. The PU foam is in grey and the fibres in white. As explained in Section 1.4.2, if the threshold is well defined and the contrast between the different elements is sufficient, the tomography software (VG Studio) can segment the fibres from the foam (Fig. 4.7b). This tool shows here that the fibres are uniformly distributed within the sample and have no preferential direction. It also demonstrates that, as expected, the protocol can be used to make foam-fibre systems with randomly dispersed fibres.

Figure 4.7c is a zoom on a FC nylon fibre surrounded by PU foam. We can see that the FC nylon fibre is not deformed, its slight curvature is due to its original packaging (small rolls). In fact, it is the foam that is deformed. The films surrounding the fibre form 90° angles when in contact with the fibre. This situation corresponds to the rigidity dominated limit case (Chapter 2). Another interesting result is that the FC nylon fibres can be found either inside the Plateau borders or partly in the films.

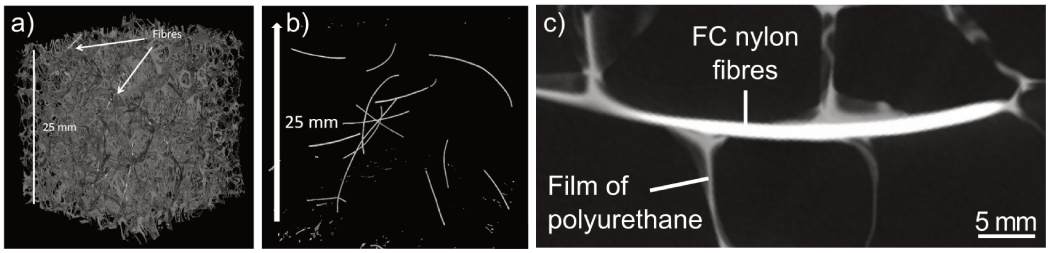


Figure 4.7 – 3D reconstruction from X-ray tomography of a polyurethane foam (Formulation n°8) with randomly dispersed FC nylon fibres (diameter: 120 μm, length: 10 mm), focused on a) the whole cubic sample, b) the segmented fibres. c) Superimposition of three tomographic slices spaced with 20 pixels (resolution: 25 μm). Zoom on a fibre surrounded by PU films. Credits: Le Quan Ngo and Antoine Egelé.

4.2.5 Conclusion

The development of the formulation and the foaming protocol have solved the problems encountered at the beginning: homogeneity, bubble size and fibre dispersion. The improvements are conclusive, as we were able to carry out initial tests integrating the fibres into a satisfying foam structure. We have shown that limiting the length of the fibres is important to preserve the stability of the bubbles, but also that to produce X-ray tomography images, the contrast between the fibres and the foam is important in order to be able to segment them. Results with FC nylon fibres are presented here, but we have also tested the introduction of 11 μm diameter glass fibres (supplied by Saint-Gobain). This latter test has shown that the diameter of the fibres must be large enough compared to the resolution of the tomography. As explained in Section 1.4.2, at least three voxels are needed across the width of an object. To expect a resolution of 3 microns, a 1 cm cube is the maximum sample size that can be treated in one simple X-ray tomography scan, which is too small here to be representative of the foam. However, this chemical foaming method does not give total control over the size and shape of the bubbles. In fact, the bubbles are elongated in the direction of the foam rise. Chemical foaming is

interesting to study the random dispersion of fibres inside foams, but there is also no control over the solidification kinetics. As two chemical reactions take place at the same time, bubbles are created at the same time as the polymer matrix solidifies, sometimes causing the bubbles to deform and no longer respect the Plateau's laws. In terms of mechanics, it seems that the more water we add to increase the quantity of foam, the more brittle it becomes. This study has provided a lot of information on the introduction and choice of fibres. However, because of all drawbacks listed above, we then decided to switch to another system, with a higher level of control via a mechanical foaming and without water to avoid the chemical formation of bubbles.

4.3 PU foam preparation via bubbling through nozzles

Due to the lack of control over the chemical foaming of polyurethane, we decided to adapt the formulation to the same foaming process used to produce alginate foams: bubbling through nozzles, which produces model foams that strongly respect Plateau's laws (Chapter 3). This section presents the second option proposed in section 4.1.3, which is to use A. Testouri et al. [97] formulation and reduce the polyol viscosity by adding the less viscous polyol from M. Hamann et al. [95] formulation and use mechanical foaming to produce foam (i.e. without water) (Section 1.2.1.2). First, we describe the modifications made to the formulation of A. Testouri et al. [97] so that it can be applied to our system. We then show the impact of the mixing of two polyols on the mechanical properties of the material constituting the foam. Finally, we present the protocol that we have developed for producing PU foams by bubbling through nozzles.

4.3.1 Formulation

All experiments are carried out with the same chemicals than in Section 4.2.1: the two polyols Lupranol 2090 (Lup) and TPG, the MDI Lupranat M20S, the catalyst Jeffcat ZR50 and the surfactant Tegostab B8002, but this time without water to avoid chemical foaming. Here, the gas phase is introduced through nozzles to create bubbles. To ensure that no trace of water is present in the mixture, a degasification and drying step for the polyols will be added to the protocol (Section 4.3.2.1).

All the information on chemicals is listed in Table 4.2.

Component	Name	Viscosity [mPa s]	Molecular weight [g/mol]
Polyol	TPG	80	192.25
Polyol	Lupranol 2090	1100	6000
Surfactant	Tegostab B8002	155-235	-
Catalyst	Jeffcat ZR50	500	245
MDI Isocyanate	Lupranat M20S	195	-

Table 4.2 – Summary of chemical components used for the generation of PU foams. Viscosities and molecular weights correspond to those in the suppliers' technical data sheets.

4.3.1.1 Tuning the initial viscosity

Using the same concentrations as in the work of A. Testouri et al. [97] (Table 4.1, Formulation n°0) results in the obtention of inhomogeneous foams. The diameter of the bubbles increases as the viscosity of the mixture increases during solidification. With this formulation, it is even more complicated to control the size of the bubbles and the stability of the foam because the viscosity of the mixture is already high initially. To solve this problem, we add TPG, which is less viscous than Lupranol 2090, to reduce the viscosity of the polyol mixture.

The viscosity of the TPG - Lupranol 2090 mixture, $\eta_{\text{TPG-Lup}}$ can be estimated using the Arrhenius equation [98]:

$$\ln\eta_{\text{TPG-Lup}} = x_{\text{TPG}}\ \ln\eta_{\text{TPG}} + x_{\text{Lup}}\ \ln\eta_{\text{Lup}} \tag{4.3.1}$$

where x_{i} is the mole fraction and η_{i} the viscosity of each component in the mixture.

The concentration of TPG (c_{TPG}, [wt%]) writes:

$$c_{\text{TPG}} = \frac{x_{\text{TPG}} M_{\text{TPG}}}{x_{\text{TPG}} M_{\text{TPG}} + (1 - x_{\text{TPG}}) M_{\text{Lup}}} * 100 \tag{4.3.2}$$

where M_{i} is the molecular weight of each component in the mixture.

Figure 4.8 shows the viscosity of the polyol mixture as a function of the TPG concentration. We can see that even a small amount of TPG can significantly reduce the total viscosity of the mixture. For example, with just 2 wt% of TPG (as in Section 4.2), the viscosity is divided by almost 3.

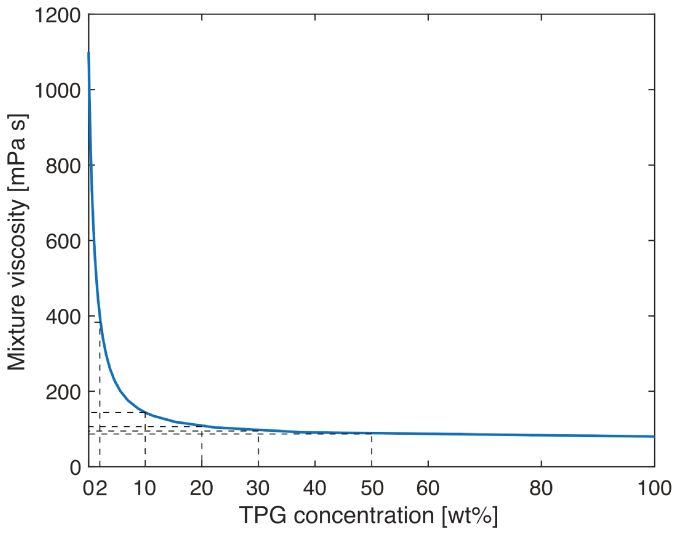


Figure 4.8 – Viscosity of polyol mixture (Lupranol 2090 + TPG) predicted with the Arrhenius equation as a function of TPG concentration.

4.3.1.2 Tuning the mechanical properties

By mixing the two polyols (Lupranol 2090 and TPG), we have complexified the polymer chemistry in our formulation. TPG is a low molecular weight polyol, often used in the production of rigid PU foams due to its short, highly functionalised polymer chains.

Therefore, by mixing TPG with Lupranol 2090, we have mixed short, hard chains with long, flexible ones, thereby modifying the mechanical properties of the final solid PU [92, 99]. As explained in section 4.1.2, the mechanical properties of the polyurethane are also modified by changing the cross-linking density through the [NCO]:[OH] index [92, 93]. In this section, we investigate several formulations with different TPG-Lupranol ratios and [NCO]:[OH] indices in order to find the best formulations that will satisfy our criteria, i.e. flexible and not brittle foams.

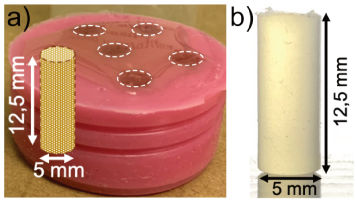


Figure 4.9 – a) Filled silicone mould with six cylindrical PU samples. b) Cylindrical solid PU samples.

As the foam mechanics is linked to the mechanics of the bulk material (Section 1.3), we have carried out a series of experiments to follow the mechanical evolution of the bulk material as a function of TPG concentration and [NCO]:[OH] index. Cylindrical PU bulk samples are made in a homemade silicone mould (Fig. 4.9). The surfactant makes it difficult to degas the mixture before solidification without including bubbles in the samples. For this reason, all cylindrical bulk samples are prepared without surfactant and degassed for 10 minutes in a vacuum chamber.

All compression tests are performed at room temperature (21 ± 1 °C) in an electromechanical testing machine (Instron E3000) at a deformation rate of 0.1 mm/s, up to 25% deformation. The load is measured with a 100 N or 1000 N load cell depending on the samples. From the compression tests, we then obtain force-displacement data which we convert into stress-strain data using the dimensions of the samples.

Table 4.3 lists the different formulations tested.

	Component	**Name**	**Concentrations tested**
A-Component*	Polyol	Lupranol 2090	Base
	Polyol	TPG	2 to 50 wt%
	Surfactant	Tegostab B8002	0 wt%
	Catalyst	Jeffcat ZR50	0.1 wt%
B-Component*	Isocyanate	Lupranat M20S	[NCO]:[OH] index 100:100 to 180:100

*percentages calculated with respect to 100 wt% of the A-Component.

Table 4.3 – Formulation used for mechanical tests of bulk PU samples.

Figure 4.10a demonstrates that the Young modulus of bulk PU materials (with a constant [NCO]:[OH] index at 100:100, blue square symbols) increases with TPG concentration. It also shows that at constant TPG concentration, isocyanate content increases the Young modulus. Figure 4.10b shows the axial compression stress-strain curves for five cylindrical samples with the same formulation (10 wt% TPG and a 100:100 index). The loading and unloading paths superimpose, reflecting the elastic behaviour of the samples. Figure 4.10c shows the results of the same experiment for a different formulation: 30 wt% TPG and a 100:100 index. We observe a large hysteresis loop with residual strain of the unloading paths, reflecting a plastic behaviour. Our empirical

study shows that with a [NCO]:[OH] index greater than 150:100, the mixture rapidly becomes increasingly viscous, probably because the reaction is faster. The more viscous the mixture, the larger the bubbles, so with indices above 150:100, the resulting foams are inhomogeneous with a gradient in bubble size.

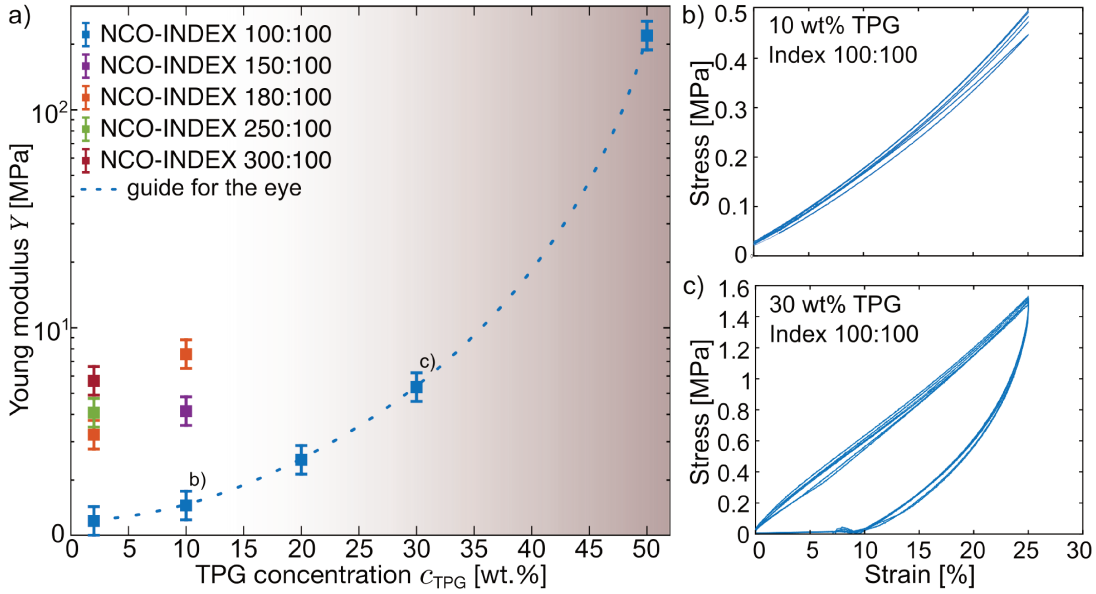


Figure 4.10 – Mechanical characterisation of cylindrical PU bulk samples: a) Young moduli of PU bulk samples as a function of TPG concentration for different [NCO]:[OH] indices. After 20 wt% TPG, the resulting foams exhibit a viscoplastic behaviour (the corresponding zone is highlighted by a grey colour gradient). b) Stress-strain curves for five PU bulk samples with 10 wt% TPG and a 100:100 [NCO]:[OH] index. c) Stress-strain curves for five PU bulk samples with 30 wt% TPG and a 100:100 [NCO]:[OH] index. Formulations are listed in Table 4.3.

To support these results, foams were produced with the same formulations (mixed by hand), following the protocol described in Section 4.3.2.2, with a syringe pump for the bubbling (gas flow rate 1 mL/min). Figure 4.11 shows in a simple way a difference in the stiffness of the foam when a weight of 50g is applied to two samples of respectively 2 and 10 wt% with a constant index of 180:100. The softest one appears to be the one made with 2 wt% TPG and an index of 180:100 (Fig. 4.11a). As expected, as the TPG concentration increases, the foam appears stiffer (Fig. 4.11b). No mechanical tests were carried out on these preliminary foams.

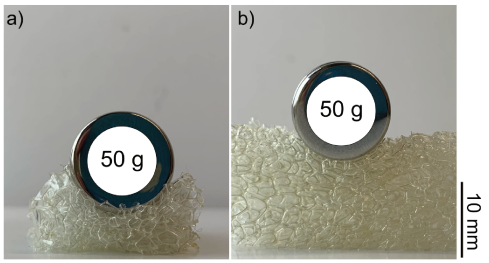


Figure 4.11 – PU foams on which a weight of 50g is applied, with two different formulations: 63 to 71 wt% Lupranol 2090, 5 wt% surfactant, 0.1 wt% catalyst and a) 2 wt% TPG, 180:100 index ; b) 10 wt% TPG, 180:100 index.

In addition, foams with a TPG concentration greater than 20 % exhibit viscoplastic behaviour, which means that the deformation is both dissipative and irreversible and depends on time, temperature and deformation rate. This type of result has already been studied in the literature, where it has been shown that mixing short hard chains of polymers with long flexible chains significantly affects the viscoplasticity of polyurethanes [99, 100].

These results enable us to choose the formulation that would be used for the following experiments. For 2 and 10 wt% of TPG and a [NCO]:[OH] index of 100:100, the PU obtained is too flexible. The long-term objectives of this project are to improve the mechanical properties of the foam by structurally rearranging the foam through the introduction of fibres, which must then be more flexible than the foam to avoid reinforcement by the fibres themselves. We cannot increase the amount of isocyanate too much either, as it accelerates solidification, which reduces the time available to produce foams. On the other hand, adding too much TPG confers a viscoplastic behaviour to the foam, which we want to avoid in order to better understand the influence of the presence of fibres on the mechanics of foam-fibre samples. We therefore have decided to validate the formulation 10 wt% of TPG and [NCO]:[OH] index at 150:100 for the last Section 4.3.3.2 of this chapter, as well as for foam-fibre samples described in Chapter 5.

4.3.2 Experimental setup

4.3.2.1 Mixing process

Before describing the production of foams, it is important to mention the improvements made to the mixing methods for these products. When bubbling through nozzles to produce foams, we want to avoid chemical foaming to occur at the same time. We therefore need a mixing method that does not introduce air bubbles into the mixture, as any traces of water react with the isocyanates and produce CO_2. The methods tested for mixing are the same as those described in Section 4.2.2 for chemical foaming formulations. We have started with the double syringe method but the mixture is inhomogeneous and the resulting foams have sticky areas (polyol in excess) or very hard areas (isocyanate in excess).

The second mixing method tested is hand mixing. First, the polyols are mixed using a glass rod, gently to avoid incorporating air into the mixture, for 1 min. The mixture is then degassed in a vacuum chamber for 10 min. The remaining chemicals (surfactant, catalyst and isocyanate) are then mixed by hand for 1 min. The mixture is then ready for use. This method is convenient but also operator dependent. In addition, when the environment is wetter (rainy weather, for example), chemical foaming occurs.

We then moved on to a more reproducible method and a more robust technique for drying and degassing the products. Unlike mixing products for chemical foaming, we cannot use the mechanical stirrer here because this method incorporates air into the preparation. We therefore use an IKA Ultra-Turrax disperser which, at low speed, does not introduce bubbles into the mixture. This method is divided into three parts: first, the polyols are mixed at speed 2 (around 1000 rpm) for 5 min, then degassed overnight in a vacuum oven (30 °C, -90 kPa). Next, the surfactant and catalyst are added and mixed for 1 min at speed 2. Finally, the isocyanate is added and mixed for 5 min at speed 2.

The mixing technique used for the various experiments presented in this work will be specified each time. Hand mixing was initially used, but during the winter, as the

humidity in the laboratory increased, ultra turrax mixing was introduced.

4.3.2.2 Foam production

Polyurethane foams are produced here using the same foaming technique as for alginate foams, described in Chapter 3. The foam is generated in a homemade 3D-printed square tube (25 mm side), closed at the bottom with a silicone plug which is pierced to allow five nozzles (ID 150 μm) to pass through. Nitrogen is then blown into 18 g of the polyurethane mixture (Table 4.3) at the start of its solidification process.

The first foams are produced by controlling the gas flow rate using a syringe pump (Fig. 4.12a, b), but the first limitation with this method is that the quantity of foam is limited to the volume of the syringe. In addition, the gas flow rate must be slow (1 mL/min), otherwise the foam is not homogeneous (Fig. 4.13a). However, if the flow rate is too slow to produce a sufficient quantity of foam, the viscosity of the mixture changes as it solidifies, leading to the formation of bubbles with diameter increasing with time.

These problems are solved by blowing the gas at a constant pressure using an Elveflow pressure controller (OB1 MK3+). Figures 4.12b and c show the experimental setup and the principle of the foaming process. The pressure controller blows nitrogen in a tank, which then distributes it to 5 nozzles at the same constant pressure. Here, the amount of foam produced depends on the quantity of mixture prepared and poured into the 3D-printed square tube, so there is no gas limit.

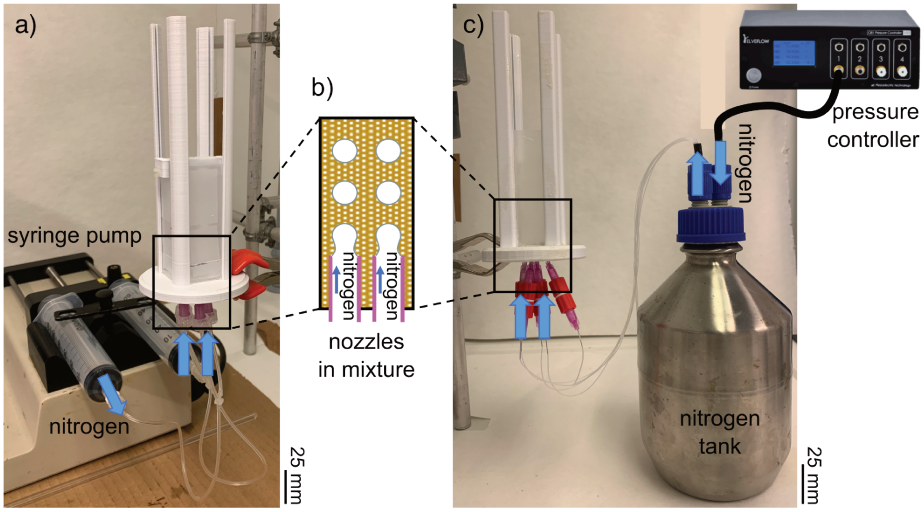


Figure 4.12 – Experimental setup showing a) a first version of the experiment with a syringe pump, b) the bubbling through nozzle principle and c) the final version of the setup with a pressure controller and a nitrogen tank.

4.3.2.3 Tuning the bubble size

As explained in Chapter 1, when bubbling through a nozzle, the size of the bubbles depends on the physical properties of the liquid mixture (viscosity, surface tension, density), the gas (pressure) or the setup (nozzle size and shape, wetting conditions, bubbling regime).

Figures 4.13b, c and d show a quick empirical study of the impact of the nozzle diameter on the bubble size. PU foams are made with the same formulation mixed by

hand (76 wt% Lupranol 2090, 2 wt% TPG, 5 wt% surfactant, 0.1 wt% catalyst and index of 250:100) and bubbling is performed with a syringe pump (gas flow rate of 1 mL/min). In the Figures 4.13b, c and d, from left to right, the diameter of the nozzles increases (ID 150, 250 and 410 μm), as does the equivalent diameter of the bubbles (respectively 3.1 $\pm$ 0.4 mm, 5.0 $\pm$ 0.3 mm and 5.8 $\pm$ 0.2 mm). The surface area of the bubbles is measured using ImageJ from these images and the equivalent diameter corresponds to the diameter of a circle with the same surface area. As the bubbles are in contact with the wall of the tube, the diameters measured are not fully representative of the equivalent bubble diameters (in 3D) of inner bubbles within the sample, but are a good way of comparing the three samples.

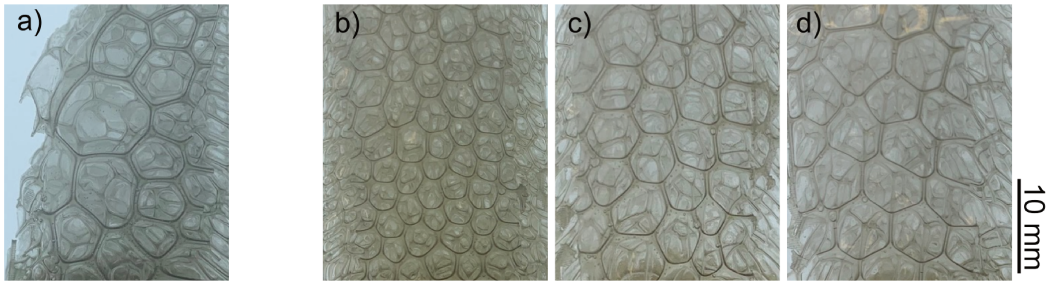


Figure 4.13 – PU foams made with the same formulation (76 wt% Lupranol 2090, 2 wt% TPG, 5 wt% surfactant, 0.1 wt% catalyst and index of 250:100) with a syringe pump at: a) a gas flow rate of 20 mL/min ; and at a gas flow rate of 1 mL/min with nozzle diameters of b) 150 μm ; c) 250 μm ; d) 410 μm.

Similar pre-tests have also been carried out with a fixed nozzle diameter (ID 150 μm) and variable pressure (from 25 to 150 mbar). As the polyurethane was viscous and opaque (see the bottom of the sample in Figure 4.14b), we have not performed quantitative studies. However, we are able to observe that the size of the bubbles increases as the pressure increases, as expected in Chapter 1.

4.3.2.4 Experimental challenges

Bubbling through the nozzle technique is promising to produce monodisperse and homogeneous PU foams. We have, however, encountered problems with the structure of the foams. In fact, as the mixture is more viscous than the alginate solution, PU foams often solidify in an intermediate state, i.e. with a gradient in the strut thickness due to drainage. Figure 4.14a shows a 3D reconstruction of a PU foam where the blue colour corresponds to the thinnest struts ($\leqslant$ 100 μm) and the green colour corresponds to the thickest struts ($\sim$ 300-400 μm). Another problem encountered is the friction of the Plateau borders and films in contact with the tube walls (Fig. 4.14b). As the viscosity of the mixture increases with solidification, the foams adhere to the walls of the tube, deforming the structure (i.e. they do not respect Plateau's laws anymore). This phenomenon can also be caused by the potential chemical foaming that occurs in the bulk puddle formed at the bottom of the container. CO_2 is then released and pushes the centre of the foam upwards, while the foam edges remain stuck to the walls.

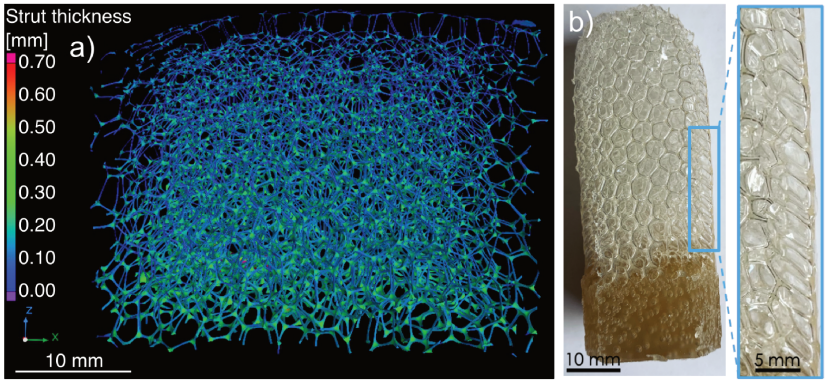


Figure 4.14 – a) 3D reconstruction of a PU foam with strut thickness gradient. b) Picture of a PU foam with border friction. Note also the presence of micro-bubbles wihtin the bulk material at the bottom of the sample.

4.3.3 Foam superimposition: A new method to control foam structure

We have developed a new experimental technique to solve the problems listed in section 4.3.2.4, based on the idea of triggering the solidification of the foam by introducing the catalyst in a second step, via superimposition of a foam with catalyst on a foam without catalyst.

4.3.3.1 Formulation

First, as a reminder, Table 4.4 lists the final formulation used for all experiments in this section and in Chapter 5 (with a catalyst concentration of 0.025 wt% for foam-fibre experiments).

	Component	Name	Concentration
A-Component*	Polyol	Lupranol 2090	84.99 to 84.90 wt%
	Polyol	TPG	10 wt%
	Surfactant	Tegostab B8002	5 wt%
	Catalyst	Jeffcat ZR50	0.0125 to 0.1 wt%
B-Component*	Isocyanate	Lupranat M20S	[NCO]:[OH] index 150:100 28.8 wt%

*percentages calculated with respect to 100 wt% of the A-Component.

Table 4.4 – Formulation used for all experiments in this section to produce foams by bubbling through nozzles.

4.3.3.2 Experimental setup

The foam production that we developed is inspired by the forced drainage explained in Chapter 1. It is based on the protocol described in section 4.3.2.2 with the pressure controller, but here the foam is collected in an outer container. The protocol is almost

identical to the one used for the production of LVA foams (Chapter 3), the main difference being in the control of solidification.

A first foam is produced without catalyst, i.e. with a long solidification time (greater than 24 hours). It is generated in a homemade 3D-printed square tube (25 mm side), closed at the bottom with a silicone plug which is pierced to allow five nozzles (ID 150 μm) to pass through (Fig. 4.12). Nitrogen is blown through the 5 nozzles, into 40 g of the solidifying polyurethane mixture (Table 4.4) at a constant pressure (100 mbar) via an Elveflow pressure controller (OB1 MK3+).

The foam is then transferred from the first tube to the container using a piece of PVC sheet (Fig. 4.15). The walls of this container are covered with a plastic film to ensure a waterproof seal and facilitate removal of the solid foam from the mould. The container is then filled until the middle (approximatively 40 mm height). The foam formed is not touched for approximatively 10 min. This allows this first foam to drain and find its equilibrium.

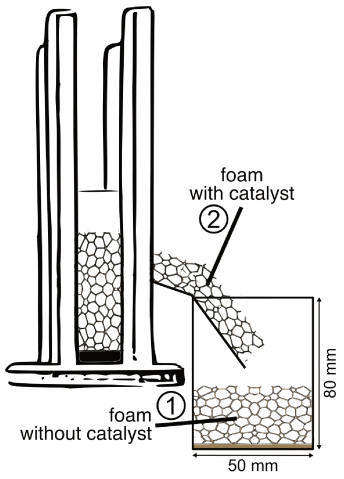


Figure 4.15 – Diagram of the foam superimposition protocol. Step 1: a foam is produced without catalyst to provide it time to find its equilibrium. Step 2: the second foam, with catalyst, flows into the first foam and fixes its structure.

A second foam is produced using the same protocol, but this time with catalyst (solidification time of a few hours), and is then superimposed on the first foam. To ensure homogeneity, the container is moved under the PVC sheet, at the same time as the second foams is deposited on the first one. With this superimposition and under the effect of drainage, the liquid PU contained in this second foam will flow down into the first foam and cure it (Fig. 4.15).

This superimposition of foams is left in the fume hood for at least 24 hours to ensure that all the isocyanates have been consumed. After unmoulding, we cut a 25 $\pm$ 1 mm square cubic sample with a thermocut (Proxxon). The samples are extracted at the bottom corresponding to the first solidified foam, as this is the one that had time to find an equilibrium structure. We weigh each sample on an electronic balance and measure their length, height and width with a calliper, in order to calculate their density. The samples can then be characterised using X-ray tomography.

4.3.3.3 Tuning the foam density

By modifying the concentration of catalyst in the second foam, the latter will drain more or less deeply into the first foam and thus modify the thickness of its structure and the final density of the foam. Figure 4.16a shows the evolution of the structure thickness calculated with the VG Studio software (combining the strut and vertex thicknesses, as they cannot be distinguished for a higher catalyst concentration) and the sample density

as a function of catalyst concentration. We note that the less catalyst there is in the mixture, the longer it drains into the first foam because the solidification is slower. This is reflected by an increase in the structure thickness and therefore in the density of the foam as the catalyst concentration increases. Figure 4.16b illustrates this well with 3D reconstructions of the samples, with the blue colour representing the struts, while the green colour representing the vertices.

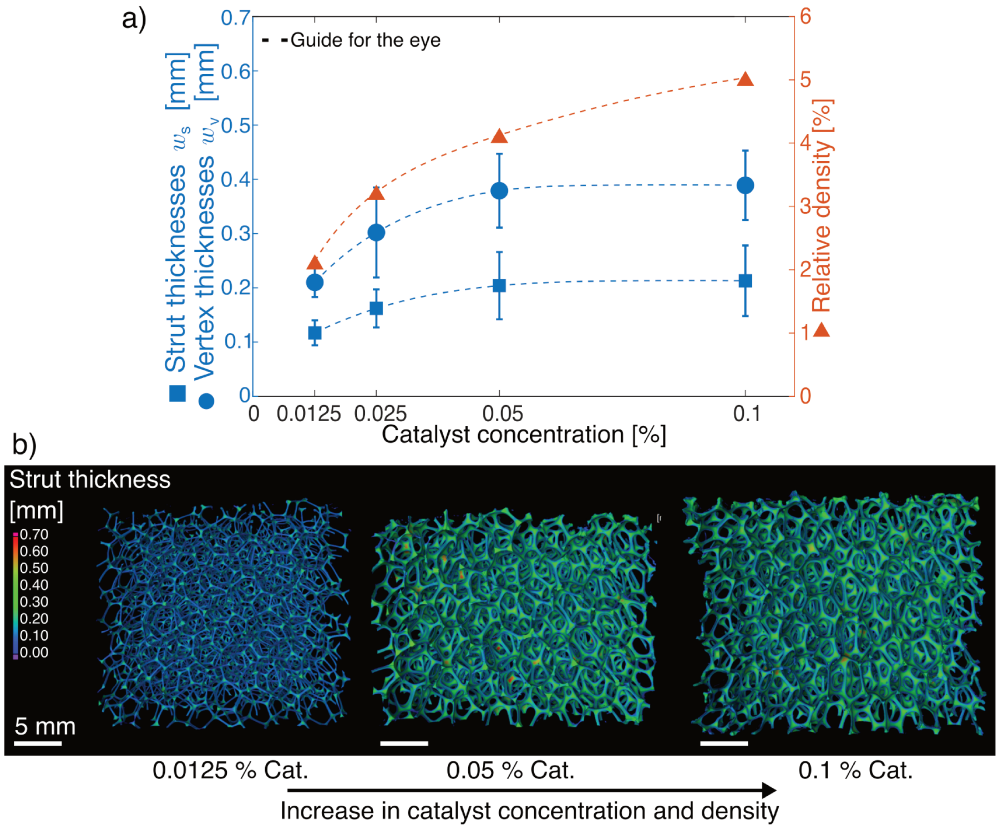


Figure 4.16 – Impact of the catalyst concentration in the second foam on the structure of the first foam: a) Left axis in blue: structure thickness ; Right axis in red: Sample relative density as a function of catalyst concentration. Dashed lines are guides for the eye. b) 3D reconstruction from X-ray tomography of polyurethane foams with different catalyst concentrations.

This foam production method with the superimposition of two foams is complex. The second foam must be uniformly laid on the first foam, but also drain evenly into the first foam. To verify the homogeneity, we divided the samples in four layers taken at different z positions (Fig. 4.17a). We can see in Figure 4.17b (left axis) that the foam superimposition has no significant impact on bubble diameter, showing that the bubble formation protocol is reproducible. In terms of the structure thicknesses, the samples appear homogeneous along the z-axis. Comparing to a "simple and unique" foam (as presented for alginate formulation in Chapter 3, Figure 3.14b), this protocol of superimposing two foams eliminates the effects of thickness gradient caused by the drainage, provided that the parameters are well chosen. The foams are homogeneous and the protocol is reproducible.

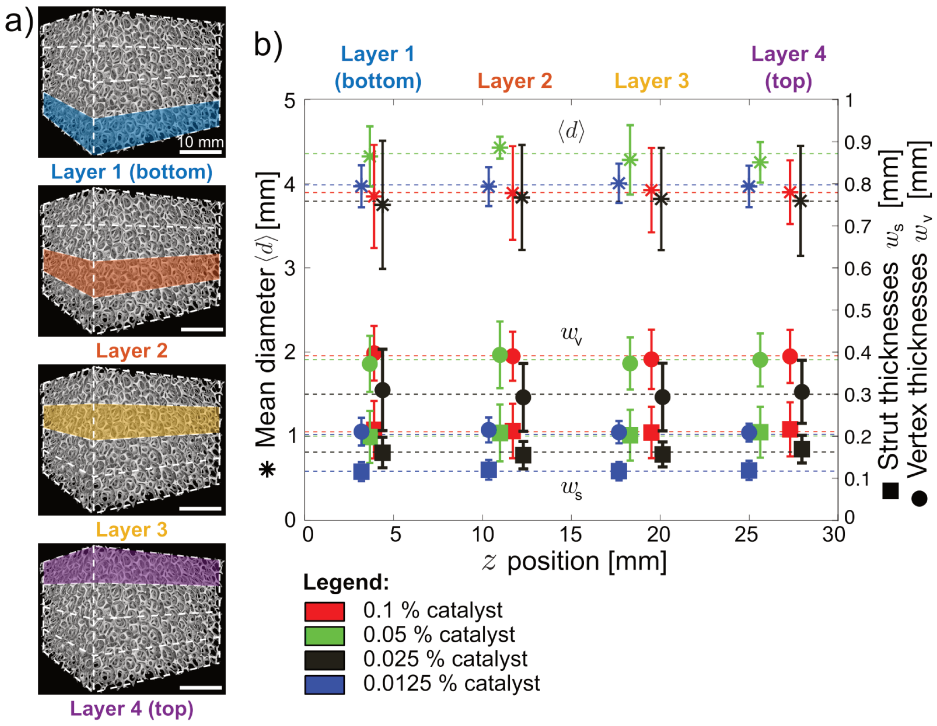


Figure 4.17 – Verification of the sample homogeneity along the z-axis: a) 3D reconstructions of a reference polyurethane foam (with 0.025 % catalyst, from Chapter 5) with the corresponding layer highlighted in colour. b) Left axis: Mean diameter of the bubbles (star symbols); Right axis: Mean thicknesses of the struts (square symbols) and vertices (circle symbols) as a function of the z-axis for different catalyst concentrations. The error bars correspond to the standard deviations of the bubble diameter and the structure thicknesses over the corresponding layer. The dashed line are guides for the eye.

There is a limitation to this method: if the catalyst concentration is too high (0.1 and 0.05 %) and the volume of foam produced too large, the second foam cannot drain down until the bottom of the first foam. The final solid foam is then inhomogeneous, with thin zones that can collapse under the weight of the thicker zones above. This is not clearly visible in Figure 4.17, but the difference in thickness between layer 1 and 2 for foams with 0.1 and 0.05 wt% catalyst is around 5 % (to illustrate this, pictures are presented in Appendix 6). We considered the foam with 0.0125 wt% catalyst as to be "perfect" for our application according to the criteria listed in transition Section *From liquid to solid foam-fibre systems*, but it was too unstable and we only managed to make it once. For these reasons, we have decided to set the catalyst concentration at 0.025 wt% for the rest of the experiments on foam-fibre systems in Chapter 5.

Another point to note is that all the experiments presented in this section were carried out with "old" products (all received in 2021, except for the surfactant, received in 2019). The age of the products undoubtedly has a negative effect on the reproducibility and stability of foams. All the experiments with 0.025 % catalyst concentration, including those for foam-fibre systems were carried out with new products (received in 2023 and used within the year).

4.3.4 Conclusion

This new foam production method, based on the superimposition of two foams, provides a high degree of control over the structure of the resulting solid foam. By adjusting the catalyst concentration, we can make the second foam flow more or less inside the first one and thus control the density of the latter. The mechanical properties of the foam can also be adjusted with the formulation. Furthermore, as explained in Chapter 1, when bubbling through a nozzle, the size of the bubbles is defined by the pressure of the gas, the surface tension and viscosity of the liquid mixture, the size and shape of the nozzles, the wetting conditions, the density of the gas and liquid and the bubbling regime, so that by controlling just one or more of these parameters, we can already control the bubble size and density in foam. Despite the fact that this method is very sensitive to environmental conditions in the laboratory (particularly humidity), the optimised formulation (containing 0.025 % catalyst) and protocol allow us to obtain reproducible model foams with which we will study the influence of the fibre integration in Chapter 5.

Chapter 5

Foam-Fibre systems

Contents

5.1 State of the art 88
5.1.1 Elastocapillarity: collective effects 88
5.1.2 Fibres and liquid foams 89
5.1.3 Fibres and solid foams 90
5.2 Materials and Methods 92
5.2.1 Ordered nylon fibres 92
5.2.2 Alginate foam-fibre systems 93
5.2.3 Polyurethane foam-fibre systems using the foam superimposition protocol 93
5.3 Results 94
5.3.1 Reference foams without fibre 94
5.3.2 Foam-fibre systems 101
5.3.3 In-situ compression 114
5.4 Conclusion 117

Foams are a specific class of mechanically self-assembling systems: bubbles spontaneously aggregate into structures governed by capillarity and Plateau's laws (Chapter 1). We will show in this chapter that, when combined with intruders, foams may become good candidates for the generation of new complex self-assembled solid architectures.

In Chapter 2, we have explored two limit cases (capillarity- and rigidity-dominated) of a quasi-2D liquid foam - elastic ribbon system. In this Chapter 5, we focus on the rigidity-dominated case of 3D solid foam - ordered fibre systems, as we want to start developing our analysis tools on a controllable system. Pre-tests have nevertheless been carried out with elastic silicon fibres in order to explore the capillarity-dominated, as illustrated in Figure 5.1a-c and briefly discussed in the outlook at the end of this manuscript. The notion of self-assembly of fibres (rigid or flexible) in a foam is left aside given the interesting results already obtained with ordered structure and the difficulty of finding a reproducible protocol for homogeneously including the fibres.

After a short state of the art, we focus on the mechanical self assembly of foams able to solidify inside arrays of ordered fibres. Statistical foam analyses are performed with both methods described in Chapter 1, using the VG Studio Software and the home-made extractor of strut network in Matlab. Finally, first results of in-situ compression tests on PU-fibre foams are presented.

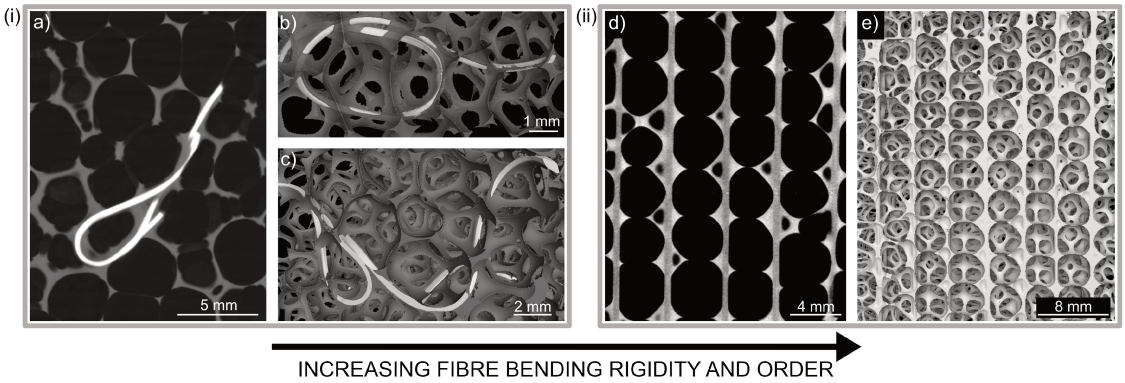


Figure 5.1 – Foam-fibre systems with: (i) **Elastic silicone fibres**, in white, with rectangular cross-sectional dimensions of 300x400 μm, surrounded by PU foam, in grey, (formulation in Table 4.4 (0.1 wt% catalyst) and protocol described in Chapter 4). a) Superimposition of three tomographic slices spaced with 20 pixels. b)-c) 3D reconstruction. (ii) **Ordered nylon fibres** of 500 μm diameter, spaced with 4 mm. d) 2D image of an LVA foam-fibre system (Section 5.2.2). e) 3D reconstruction of a PU foam-fibre system (Section 5.2.3). Tomography resolution: 25 μm.

5.1 State of the art

Research in self-assembly based on elastocapillarity and collective effects is attracting growing interest in the academic and industrial fields, especially for the generation of new architected structures. Here we give some examples of elastocapillarity with collective effects before describing the existing literature on foam-fibre systems. We finally give a brief overview of the solid foams-fibres systems.

5.1.1 Elastocapillarity: collective effects

Chapter 2 described the deformation of a single slender elastic structure caused by capillary forces, but the competition between elasticity and capillarity can also provide a powerful strategy for the collective self-assembly of several structure components. Studies on self-assembled systems based on capillary interactions have started with observations from the daily life, such as the shape of a wet paintbrush [101] or long wet hair [102]. On a micro- or nanoscale, these interactions were initially a challenge particularly in the field of microelectronic devices because they can lead to unwanted deformation or deterioration of micro/nano structures [103]. These fabrication processes are now increasingly used to texture and shape surfaces in applications such as energy transfer, anti-wetting or anti-icing coating, but also optical and acoustic metamaterials [104]. Recently, J. Ha and al. [105] have presented theoretical models demonstrating the dependence of the drain rate on self-assembled hairy bundles by dynamic elastocapillarity (Fig. 5.2a). They also showed the limit cases driven by hydrodynamic (for fast drainage and long fibres) or capillarity (for slow drainage and short fibres). Another recent work [106] demonstrates

how capillarity can be exploited to collectively modify the connectivity and number of nodes, the size and number of cells and thus transform the topology of elastic cellular microstructures with walls initially built on a triangular lattice (Fig. 5.2b). The lattice is immersed in a bath of liquid, which infiltrates and softens the material. Menisci are then formed during evaporation, involving localised capillary forces that stick the edges of the lattice into a new topological structure. Those examples show that the field of elastocapillary morphing of complex structures is promising.

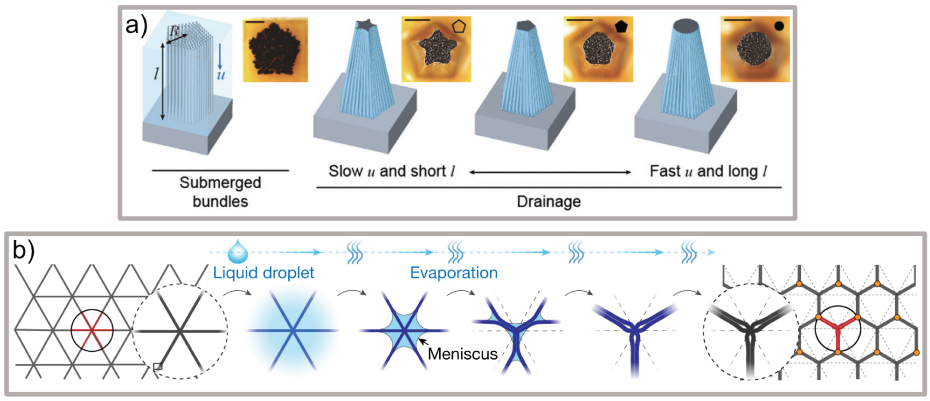


Figure 5.2 – a) Left: immersed bundles with a pentagonal cross-section. Right: three different bundle shapes corresponding to three drainage rates or fibre lengths. Reproduced from [105]. b) Reversible and tunable topological transformation of a triangular cellular microstructure through capillary forces. Reproduced from [106].

5.1.2 Fibres and liquid foams

Liquid foam-fibre systems have already been studied, notably with the development of the foam-forming techniques for the paper industry [107]. Cellulose fibres are dispersed in a solution of water and surfactant, then mechanically foamed. The presence of bubbles evens out and spaces out the cellulose fibres, which tend to stick against the soap films due to capillarity (Fig. 5.3a) [108]. The foam then collapses under the effect of a vacuum, leaving the fibres evenly dispersed in a thin 2D layer which, after drying, forms paper. Using the same technique, S.R. Burke et al. [46] have shown that it is possible to create lightweight 3D cellular materials whose cellulose fibre alignment is induced by capillarity and drainage (Fig. 5.3b). They also demonstrated that the mechanical properties of this type of material can be adjusted by controlling the liquid fraction of the initial liquid foam. When the liquid fraction is increased, the fibres are more aligned with the direction of gravity and the material's compressive modulus seemed to be higher in the direction of the fibre alignement.

Moreover, the study of model experiments is interesting to understand fundamentally what happens when fibres are inserted into a liquid foam. On this subject, D. Whyte et al. [109] have studied the integration of a unique rigid fibre into a simple configuration of liquid soap films (Fig. 5.3c). They found that the central Plateau border length L_0 increases as the thickness of the fibre increases and the contact angles of the films change from 120° to 90°. However, the literature on model experiments of such systems is still limited.

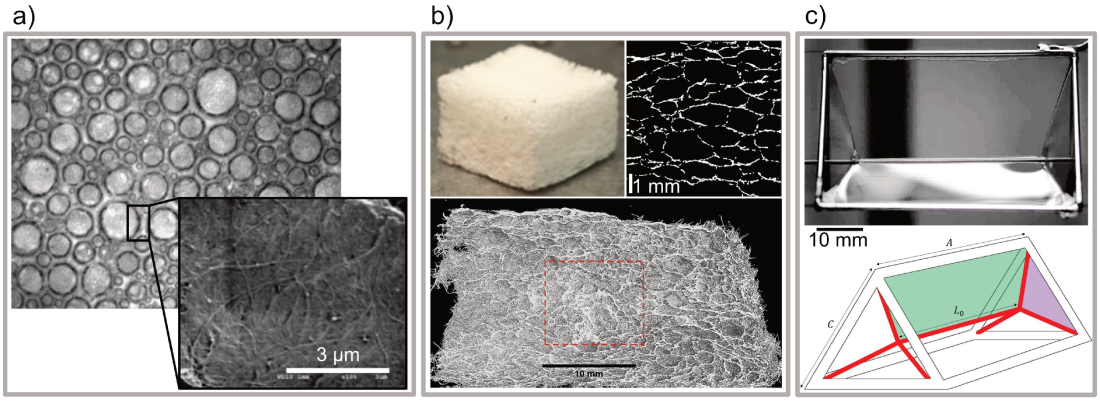


Figure 5.3 – a) Liquid foam-fibre dispersion and zoom on a soap film with fibres stuck to the interface. Reproduced from [108]. b) Picture of a cubic non-woven fibrous sample , 2D slice and 3D reconstruction from X-ray tomography. Reproduced from [46]. c) Picture and diagram of an equilateral triangular prism frame. A cylindrical fibre is introduced into the central Plateau border of length L_0. Reproduced from [109].

5.1.3 Fibres and solid foams

The inclusion of fibres in a bulk matrix is already well-know in the field of composite materials. Assembling at least two materials of different kinds allows to create a new material whose properties are enhanced by the combination of the materials used. The main advantages of these composite materials, which are often cited, are their low volume, mechanical performance, multi-functionality and durability [110]. With the growing interest in lightweight materials, more and more composite materials are emerging, in which the bulk matrix is replaced by a foam. Some recent works show that the solid foam-fibre systems are good candidates for example for thermal, acoustic and mechanical applications [111, 112, 113].

5.1.3.1 Structure modification in solid foam-fibre composites

In the literature, some articles have already shown that the insertion of fibres into foams has an influence on their structure. For example, in the case of chemical foaming, it has been demonstrated that fibres can become precursors of heterogeneous bubble nucleation, resulting in a decrease in the average bubble size [114, 113]. In addition to a decrease in bubble size, Ardanuy et al. [113] have shown that the incorporation of cellulose fibres promoted the formation of characteristic open-cells in an initially closed-cell foam (Chapter 1) based on recycled polypropylene.

PU foams have also been used to create foam-fibre composites. Figure 5.4 shows examples of PU rigid foams reinforced with bundles of glass fibres. Serban et al. [112] observed the alignment of bubbles between two glass fibres (highlighted by two blue arrows in Figure 5.4a), while Cotgreave et al. [44] presented an ordered structure caused by the presence of chopped glass fibres with a local change in angles when the struts are in contact with a fibre.

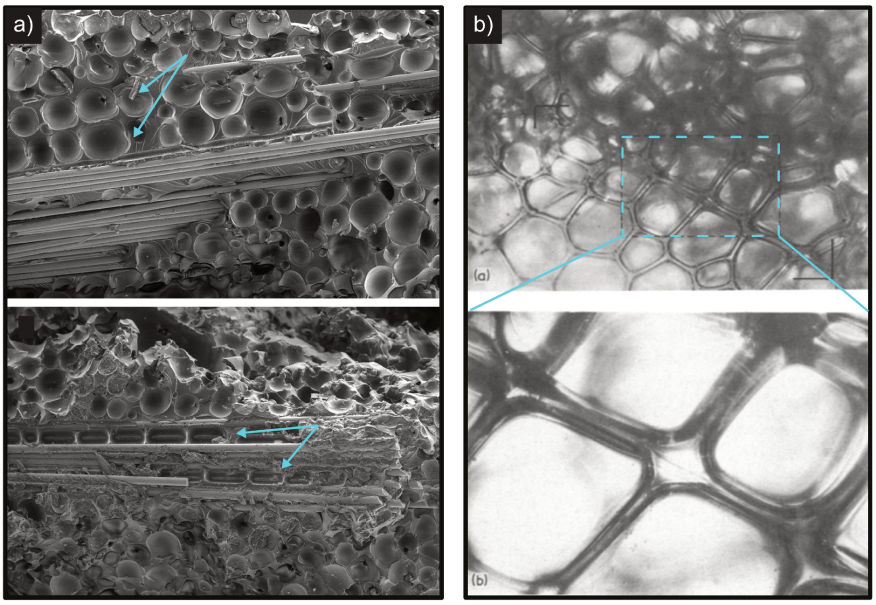


Figure 5.4 – a) SEM images of fracture surfaces of a PU foam reinforced with glass fibre bundles (500x magnification). Blue arrows highlight aligned bubbles. Adapted from [112]. b) Top: Microscopic images of a PU foam containing chopped glass fibres of 13 μm diameter (top); Bottom: Enlargement of the zone surrounded by the dashed rectangle. Adapted from [44].

5.1.3.2 Mechanical behaviour of solid foam-fibre composites

Composite theory suggests that fibres embedded in a weaker bulk matrix improve overall stiffness [115]. When the matrix is replaced by a foam, the resulting system is more complex. Indeed, Hussain et al. [116] observed two fibres configurations: In the first case, the fibres are short (Fig. 5.5 left) and reinforce the cell struts, resulting in the reinforcement of the entire foam, by increasing the Young modulus of the constituent material of the foam (i.e. Y_s according to the mechanical model developed by Gibson and Ashby [39]). In the second case, the fibres are long, i.e. larger than the characteristic bubble size (Fig. 5.5 right). Using the example of PU foams containing dispersed long glass fibres, Hussain et al. [116, 117] showed that the foams are only reinforced if the long fibres are in contact with each other. They refer to a "mechanically percolating network" formed by the fibres.

More recently, there have been only limited advances in the literature in terms of the mechanical reinforcement of foams, indeed, current research is now looking at biobased and renewable alternatives to create materials with similar properties to those already existing [118, 119]. For example, as mentioned in Chapter 4, one way of increasing the rigidity of PU foams is to increase the isocyanate content, but incorporating fibres into foams to reinforce them is a good alternative for reducing the consumption of this non-renewable and toxic component.

To our knowledge, there is no previous study discussing the improvement of the mechanical properties of foams specifically induced by the modification of their topology through the introduction of fibres.

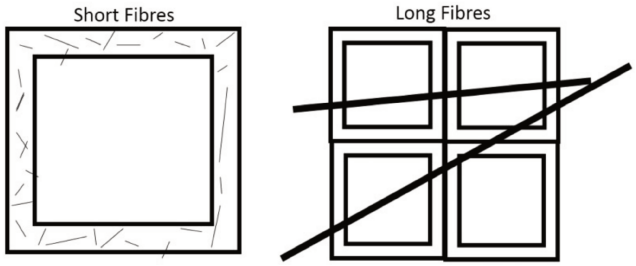


Figure 5.5 – Diagrams of two fibre configurations: Left, short fibres remain inside the struts; Right, long fibres (larger than the bubble size) pass through the bubbles. The images are not to scale and drawn following the Gibson and Ashby model with cubic cells [39]. Figure taken from [116].

5.2 Materials and Methods

5.2.1 Ordered nylon fibres

To investigate the rigidity-dominated case on 3D foam-fibre systems (Chapter 2), we stretched and ordered fluorocarbon (FC) nylon fibres of either 120 μm (Flashmer MagixFluoro) or 500 μm (Savage Gear Regenerator) diameter inside a square container (Fig. 5.6). Several walls of 80x50x3 mm were prepared: some were cut with a laser cutter (Legend 36EXT 75W Epilog Laser) to form holes of 500 μm every 1 mm, while other walls were drilled with holes of 500 μm every 4 mm using a drill press. The walls were then screwed to a 3D-printed base and the fibres were inserted into the holes located 15 mm above the base, on a square surface of 30 mm on each side. To ensure that they are stretched and do not move, the fibres were simply taped to the outside of the container. The containers prepared in this way were then filled with an alginate (LVA) or polyurethane (PU) foam. Figure 5.6a shows 500 μm FC nylon fibres placed every 6 mm and Figure 5.6b shows 120 μm FC nylon fibres placed into a hexagonal pattern. Four different fibre configurations have been tested: a square pattern with 4, 6 or 8 mm between fibres of 500 μm or 120 μm diameter, and a honeycomb pattern with 120 μm fibres (Fig. 5.6c).

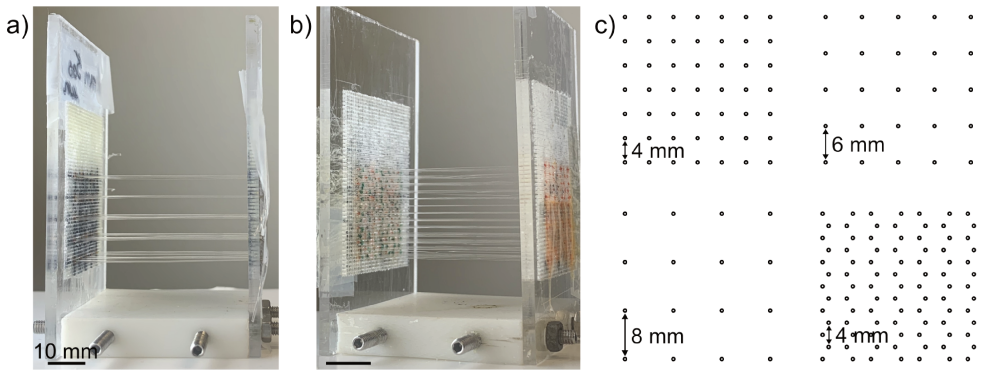


Figure 5.6 – Experimental setup to study the mechanical self-assembly of bubbles in ordered fibre arrays: a) 500 μm FC nylon fibres placed every 6 mm in a square pattern; b) 120 μm FC nylon fibres placed into a honeycomb pattern between the walls of a square container. Two additional plates are then screwed on both sides to close the container. c) Side views of the four fibre configurations investigated in this chapter.

5.2.2 Alginate foam-fibre systems

Alginate (LVA) foams were produced according to the protocol described in (Chapter 3). Table 5.1a recalls the products and concentrations used to produce them. Once produced, each foam was parafilmed to avoid evaporation and placed inside the tomograph enclosure. A 20-minute tomography at 25 μm resolution started 1 hour after the foam production to allow it to drain and equilibrate between the fibres. Figure 3.10 in Chapter 3 shows that the thickness of the struts is stabilised after 1 hour, thus avoiding motion artefacts during tomography. In order to use the foam analysis tool of VG Studio software, the sensibility threshold (Chapter 1) has been set at 20 % for all LVA foams.

After tomography, the LVA foam is destroyed. The container, in which the fibres are still stretched, is then rinsed and a new foam is produced inside by reproducing exactly the same protocol. This is used to test the reproducibility of the system and to carry out a statistical study. Once the experiments with the LVA foams are completed, the container is carefully cleaned and dried in order to use exactly the same fibre configuration with the PU foams.

a) **LVA foam formulation**

Name	**Concentration**
LVA solution:	
Water	99 wt%
LVA	1 wt%
Added to the LVA solution:	
$CaHPO_4$	0.02 M
Disponil	2 wt%
GDL	3 wt%

b) **PU foam formulation**

Component	**Name**	**Concentration**
A-Component*		
Polyol	Lupranol 2090	84.97 wt%
Polyol	TPG	10 wt%
Surfactant	Tegostab B8002	5 wt%
Catalyst	Jeffcat ZR50	0 or 0.025 wt%
B-Component*		
Isocyanate	Lupranat M20S	28.8 wt% [NCO]:[OH] index 150:100

*percentages calculated with respect to 100 wt% of the A-Component.

Table 5.1 – Formulation for a) LVA and b) PU foam production in this Chapter.

5.2.3 Polyurethane foam-fibre systems using the foam superimposition protocol

Polyurethane (PU) foams were produced according to the protocol described in Chapter 4. Two foams were superimposed, the first without catalyst to allow time for the foam to reach equilibrium between the fibres, and the second with 0.025 wt% of catalyst (Table 5.1b). Once the foam has solidified, the fibres are cut from the outside of the container, the sample is unmoulded and placed entirely in the tomograph. A tomography at a resolution of 25 μm is performed on the zone at the bottom of the foam (i.e. the location of the first foam and the fibres). In order to use the foam analysis tool, the

sensibility threshold (Chapter 1) has been set at 35 % for all PU foams.

After the imaging characterisation, we cut a 35 ± 2 mm square cubic sample using a thermocut (Proxxon) and a 3D-printed homemade guide to obtain parallel faces (Fig. 5.7a, b). Mechanical tests are then carried out at 0, 10, 20 and 30 % of deformation inside a compression cell installed in the tomograph in order to follow the in-situ deformation (Fig. 5.7c). The sample is placed in the compression cell and the bottom plate is raised until the first deformation is reached. Then, a 2-hour scan is run at 25 μm resolution. After that, the sample is then compressed further to reach the second deformation, a new scan is run and so on for each deformation rate and sample.

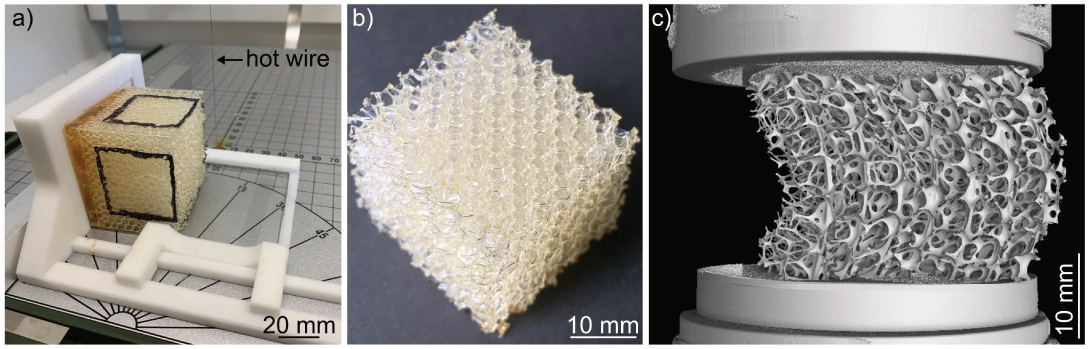


Figure 5.7 – Preparation of the PU samples. a) The sample is cut with a hot wire, highlighted with the black arrow, using an 3D printed guide, in white, to obtain parallel faces. b) Cubic samples (approximatively 30x30x30 mm) c) In-situ compression cell installed in the tomograph with a PU foam-fibre sample (tomographic image. Resolution: 25 μm.)

5.3 Results

5.3.1 Reference foams without fibre

To study the impact of fibres on foam architectures, we need a reproducible protocol to obtain a foam structure that will statistically not change from one experiment to the next. Once the protocols for PU and LVA foams has been optimised, three foams of each type are produced. The analyses of those six foams are presented below, to show statistical parameters on foams without fibres and evaluate robustness and reproducibility of the established protocols.

5.3.1.1 Foam analysis from VG-Studio software

The X-Ray tomography images are analysed with VG-Studio software as a first step. Figure 5.8 shows results of the bubble size analysis. First results are focusing on PU foams. Figure 5.8a presents the probability density function (PDF) of the bubble diameter normalised by the mean bubble diameter, over the whole sample. The inset shows a 3D-reconstructed bubble to remind how the equivalent diameter is measured from a sphere of the same volume (Chapter 1). The histograms are quite similar for the three samples. The distributions, very peaked around their maximum, have a slight positive asymmetry. We note also the presence of small bubbles that may be created by chemical foaming

and trapped in the PU matrix. As a reminder, the water in the mixture reacts with the isocyanates, releasing CO_2 (Chapter 4). Despite rigorous prior degassing, ambient humidity may be sufficient to explain the presence of small bubbles.

Figure 5.8b show the results of bubble size analysis for LVA foams over the whole sample. Results also demonstrate reproducibility. The bubbles have almost all the same mean diameter. In the case of LVA foams, we note that there are no smaller bubbles, which clearly shows that their presence in PU foams may be due to chemical foaming and not because of the bubbling protocol (Chapter 4).

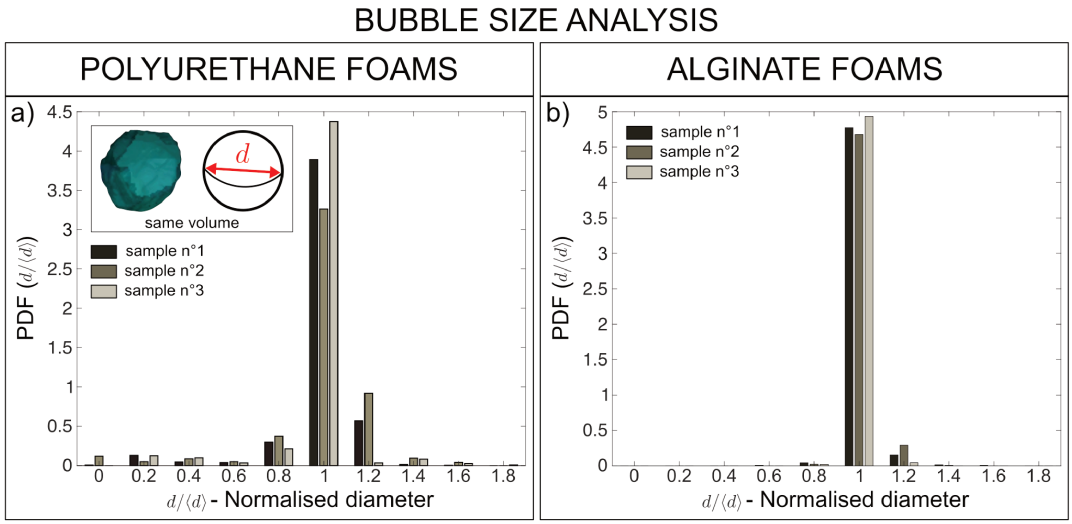


Figure 5.8 – Bubble size analysis of reference foams without fibre: Distribution of the equivalent bubble diameter normalised by the mean bubble diameter for a) three PU foams produced with the protocol described in Chapter 4. The inset shows how the equivalent diameter is measured (Chapter 1); b) three LVA foams produced with the protocol described in Chapter 3.

Figure 5.9 shows the results of the structure thickness analysis for a) PU and b) LVA foams without fibre. The PDF of the structure thickness normalised by the mean thickness is represented for three reference foams. The inset shows a zoom on a strut as a reminder of the method used to measure thickness with the VG Studio software (Chapter 1). For each sample, PU or LVA, the histograms are identical. We can see two peaks, corresponding to the thickness of (1) the struts; (2) the vertices. These results demonstrate good reproducibility of the protocol. Figures 5.8 and 5.9 show the reproducibility of the reference samples in terms of bubble diameter and structure thickness.

To verify the homogeneity of each the sample, we divided the samples in four layers taken at different z positions (Fig. 5.10a). Figures 5.10b and c show the mean bubble diameter and the mean strut and vertex thicknesses for each layer of the reference samples for the LVA and PU formulations (Table 5.1). In terms of bubble diameter (left axis of the graphs), the samples are homogeneous and show good similarity along the four layers on the z axis, for both systems (PU and LVA). In terms of structure thicknesses, for the reference PU foams without fibres, Figure 5.10b (right axis) shows a homogeneity along the z axis, demonstrating once again that the protocol of superimposing two foams is a relevant method for producing homogeneous foams (Section 4.3.3.2). We can however note that the structure thicknesses of the `sample n°1` are slightly lower (less than 25 %) than for the other two samples.

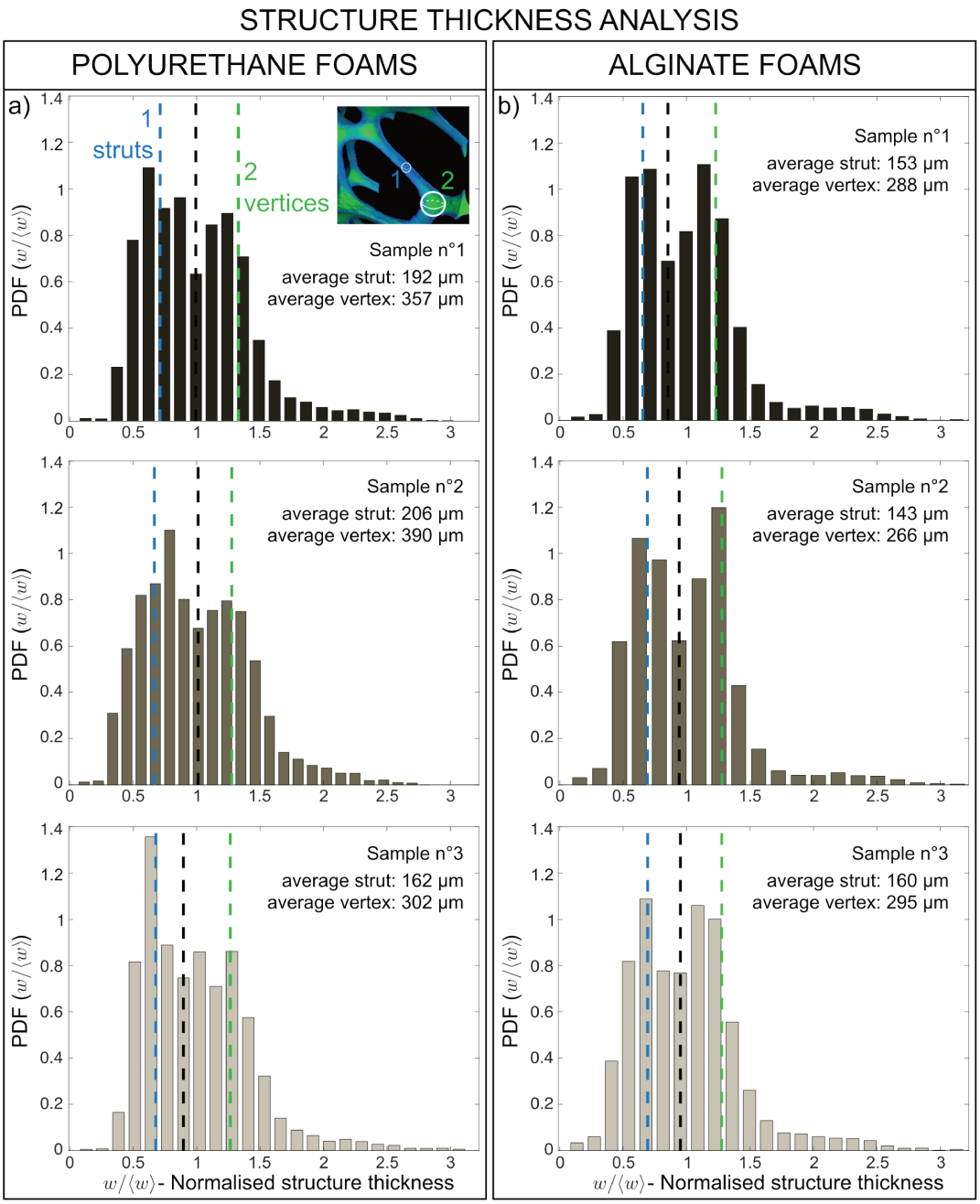


Figure 5.9 – Structure thickness analysis of reference foams without fibre: Distribution of the structure thickness normalised by the mean structure thickness a) for three PU foams; b) for three LVA foams. The inset shows a zoom on a strut to remind the method used to measure thickness using the VG Studio software and to explain the presence of two peaks corresponding to the thickness of (1) the struts; (2) the vertices (Chapter 1). The histograms are arbitrarily divided in two to distinguish these two thicknesses. The black dashed line highlights this separation. The average thickness of the struts is then calculated by taking the mean thickness of the left side from the black dashed line and is highlighted by a blue dashed line. Similarly, the average thickness of the vertices is the mean thickness of the right side from the black dashed line and is highlighted by a green dashed line.

For the reference LVA foams without fibres, Figure 5.10c (right axis) shows a difference of almost 100 μm in the vertex thickness and about 40 μm in the strut thickness between the top and the bottom of the foams, which is again the impact of the drainage on the foam (Chapter 3), as it is not compensated by the superimposition of a second foam as with PU foams (Section 4.3.3.2). We can note that this phenomenon is identical in the three reference LVA foams, demonstrating good reproducibility of the protocol (Section 3.2.3).

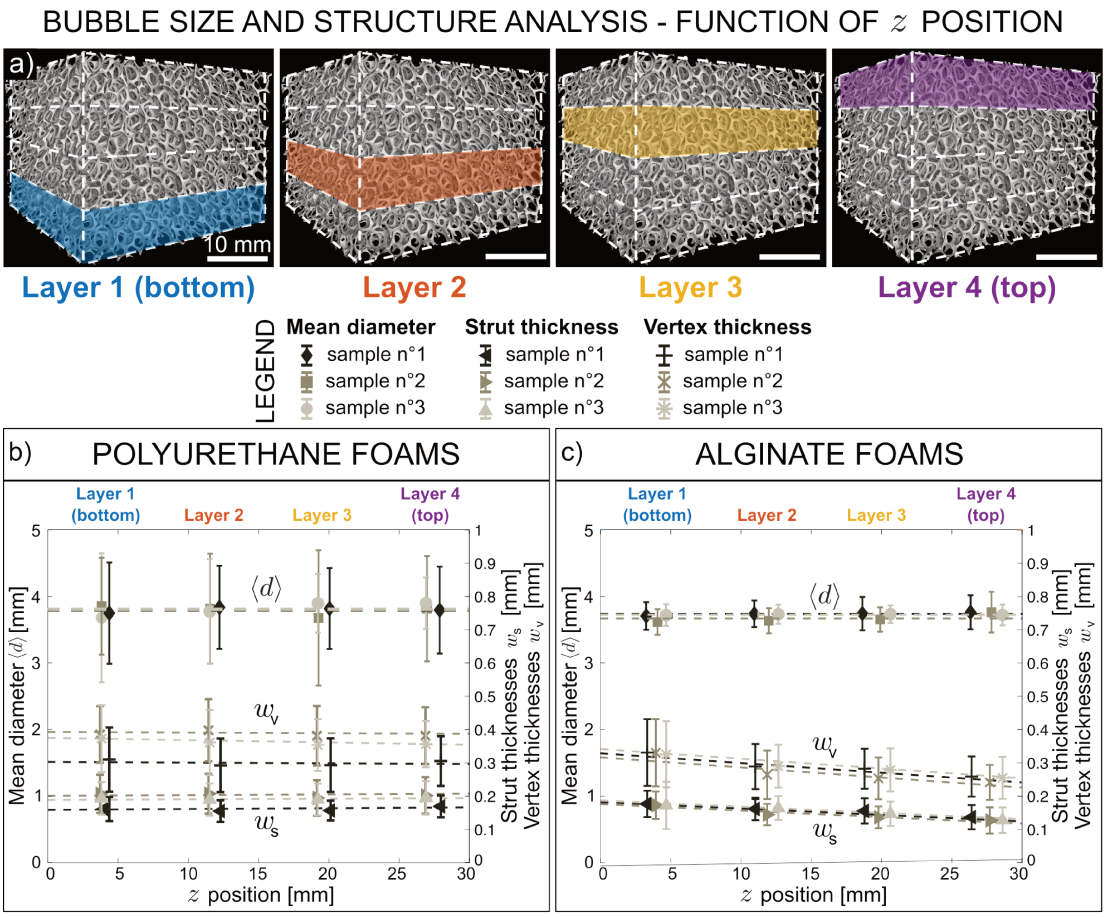


Figure 5.10 – Verification of the sample homogeneity along the z-axis: a) 3D reconstructions of a reference PU foam with the corresponding layer highlighted in colour. b) Mean diameter of the bubbles (left axis) and mean strut and vertex thicknesses (right axis) as a function of the z-axis for three reference PU foams. c) Mean diameter of the bubbles (left axis) and mean strut and vertex thicknesses (right axis) as a function of the z-axis for three reference LVA foams. b)-c) The error bars on the y-axis correspond to the standard deviations of the bubble diameter and the structure thicknesses over the corresponding layer. The dashed line are guides for the eye.

To conclude, Figure 5.11 summarises the results of the bubble size and the structure thickness analyses, comparing PU and LVA foams without fibre. The average bubble diameter is similar (around 3.8 mm) for both systems, the only change being in their standard deviation. It appears that the bubble diameters of the PU foams are more dispersed than those of the LVA foams. Between the two systems, we can see a difference of 50 μm for the average strut thickness and of 100 μm for the average vertex thickness

(corresponding to a 25 % difference). This can be explained by the fact that the LVA foams drain more due to the lower viscosity of the initial solution (Chapter 3) and also by the fact that we superimpose two foams in the PU system (Chapter 4). All these results show that we succeeded in producing foams with almost identical bubble size and structure thickness for two different systems, by adjusting carefully the protocol parameters.

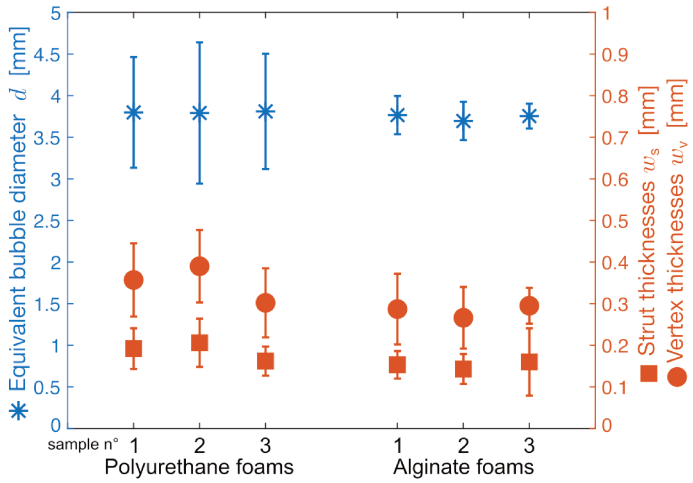


Figure 5.11 – Summary of the result panels from the Figures 5.8 and 5.9, comparing PU and LVA foams. The error bars correspond to the standard deviations, respectively, of the mean bubble diameter and the mean strut and vertex thickness.

5.3.1.2 Dual "scaffold" analysis

The foam analysis tools provided by the VG Studio software are not complete, as they focus mainly on bubble statistics and the geometric characteristics of the struts. In addition, owing to the imperfections of the software (Chapter 1), we find it interesting to supplement the analyses proposed by VG Studio with a strut scaffold analysis using the home-made programmes `FoamTopologyExtraction.m` and `FoamAnalysis.m`, which are briefly described in Chapter 1. Their purpose is to faithfully extract the strut network, i.e. give the vertex positions and the connectivity pairs, from the image stack, and to extract interesting parameters, such as the order of vertices, strut length distributaions, and angles between struts. We show here the various statistical analyses carried out on the reference foams without fibres.

Orders of the vertices

The programme extracts the orders of the vertices, which are found to be predominantly of order 4 (96 % for LVA foams). Diagrams of the vertex orders are shown in Appendix 7 for the PU and LVA reference foams. Note that the vertices of order other than 4 are the signatures of materials aggregates that the programme is trying to represent. As described in Chapter 1, they could be considered as a pair of $O(4)$ or a $O(8)$ vertex and therefore as representative of the real defects present in the foams.

Strut length distribution

The strut length distribution is then investigated for each sample. Figure 5.12 shows the pdf of the strut lengths for the three LVA reference foams (without fibres). We merged the three samples because the three individual pdf were very close to each other, as exemplified by the data shown in table 5.2. In Figure 5.12a, we then compare the strut length distribution of our foams with a curve obtained from the article by Kraynik et al. [120], where different "random monodisperse foams" were considered. We used the so-called random-annealed RSA (RA-RSA) model, because the authors remarked that this model fits extremely well the historic data from Matzke [43].

	LVA Foam 1	LVA Foam 2	LVA Foam 3	Together
Average strut length (mm)	1.373	1.327	1.358	1.354
Standard Deviation (mm)	0.357	0.333	0.343	0.343
Dispersity (%)	6	6	4	-

Table 5.2 – Key parameters to estimate the fluctuations between the three LVA samples. The standard deviation of the three individual averages is 0.02, showing that the fluctuations between samples are negligible.

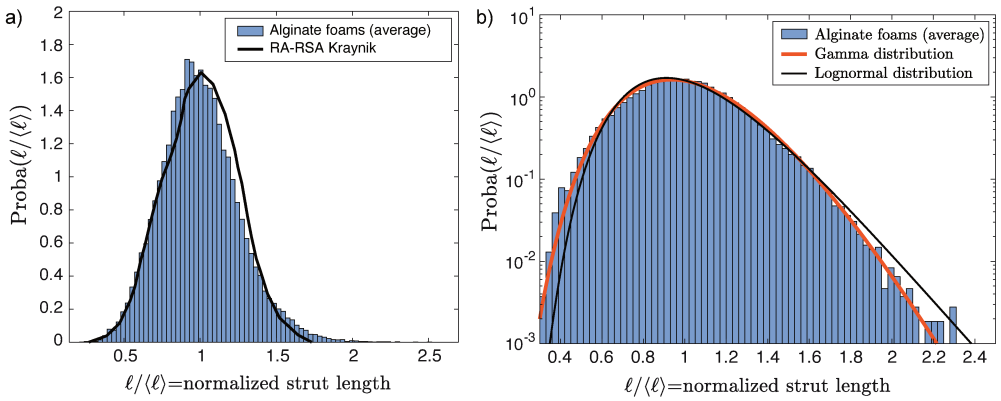


Figure 5.12 – a) Normalised strut length pdf for the LVA reference foams (without fibres). The pdf is created by merging the data from the 3 LVA samples made under identical conditions. Its skewness is 0.45. In black solid : Strut length pdf for a random model of foam by Kraynik *et al.* [120]. b) Fit with a Gamma distribution $p(x) = x^{\alpha-1}\frac{\alpha^\alpha e^{-\alpha x}}{\Gamma(\alpha)}$ with $\alpha = 1/\text{variance} = 15.6$. A Lognormal fit is shown for comparison. Extraction with $G = 20$ voxels following the procedure explained in Chapter 1, from tomographic images with a resolution of 25 μm.

Figure 5.12b, shows a surprisingly good Gamma fit with no adjustable parameter but the variance of the distribution (by construction, the average of the distribution is 1), which sets the parameter $\alpha = \langle\ell\rangle^2/\langle(\ell - \langle\ell\rangle)^2\rangle$. This parameter sets the decreasing rate of the exponential appearing in the definition of the Gamma distribution, i.e.

$$p(x) = x^{\alpha-1}\frac{\alpha^\alpha e^{-\alpha x}}{\Gamma(\alpha)}. \tag{5.3.1}$$

Figure 5.13 shows the normalised strut length distribution of the three PU reference foams (without fibres). We can first see that the samples are reproducible, as the

distributions are fairly identical, and we can see also that the Gamma fits are still quite good.

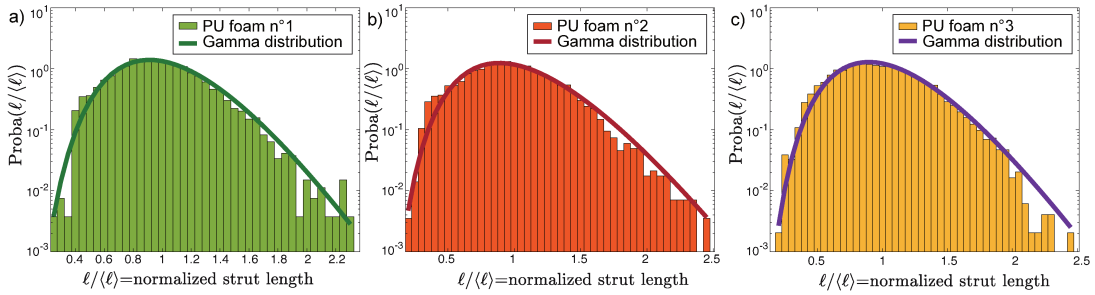


Figure 5.13 – Normalised strut length pdf for PU reference foams (without fibres). Solid lines are Gamma distribution $p(x) = x^{\alpha-1}\frac{\alpha^\alpha e^{-\alpha x}}{\Gamma(\alpha)}$ with α = 1/variance = a) 11.4, b) 8.8 and c) 9.55. Extraction with $G = 20$ voxels following the procedure explained in Chapter 1, from tomographic images with a resolution of 25 μm.

Strut angle distribution

Finally, the programme measures the angles between pairs of struts. Figure 5.14 shows the strut angle distribution for all reference samples (LVA and PU) without fibre. For all foams, we can observe a peak at exactly 109.5 ° corresponding to the typical angle between two struts in the tetrahedral structure of foams, dictated by Plateau's laws [1]. In comparison with the literature, Montminy et al. [50] found angles of 106.7 ± 17.78 ° between a pair of struts in samples of PU foams produced by chemical foaming, showing that our fabrication protocol produces model foams that respect Plateau's laws contrary to those produced by chemical foaming. In addition, our foams without fibre have a narrower distribution than Montminy's [50], with a slight asymmetry similar to their results. These curves show again the very good reproducibility of our protocol.

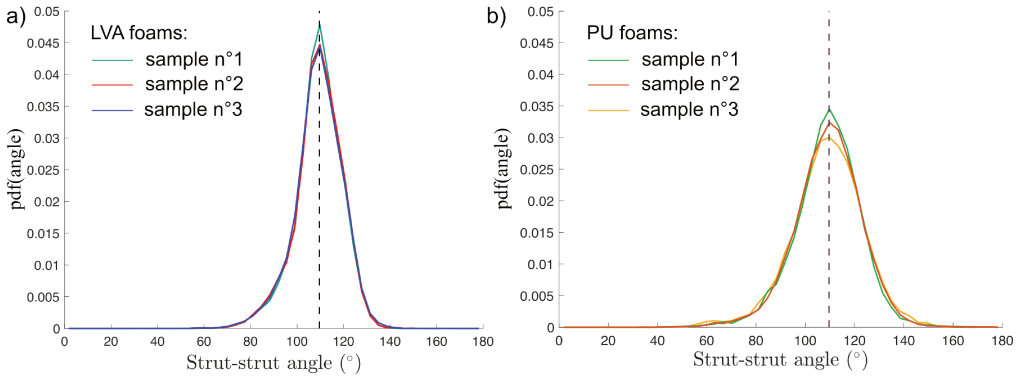


Figure 5.14 – Strut angle distribution for a) three reference LVA samples and b) three reference PU samples (right). The vertical dashed line highlights the angle corresponding to tetrahedral structures, namely 109.5 °. Extraction with $G = 20$ voxels following the procedure explained in Chapter 1, from tomographic images with a resolution of 25 μm.

5.3.2 Foam-fibre systems

PU and LVA foam-fibre systems are prepared following the protocol described in Sections 5.2.2 and 5.2.3 with FC nylon fibres of 120 and 500 μm diameter and 4, 6 or 8 mm spacing between them. All samples are then characterised and studied, firstly by close inspection of the tomographic and photographic images, then using the VG-Studio software and finally using the home-made programme extracting and analysing the strut network with Matlab.

5.3.2.1 Fibres surrounded by foam

The first question to ask when adding fibres into foams is: how do fibres and bubbles interact with each other? Before discussing the structural modifications or deformations, we can first observe the fibre placement within the foam: are they fully immersed inside films, as for cellulose fibres in aqueous foams in the paper industry [108, 46], or restricted to the Plateau borders, as in the work by D. Whyte et al. [109]? For both systems, LVA and PU, the characteristic solidification times are chosen to be long enough to allow the foams to reach an equilibrium state between the fibres. Close examination of the tomographic and photographic images of the PU and LVA foams first shows that a thin layer of material covers the fibres. We have then encountered different scenarios visible in all foam-fibre samples (i.e. for both PU and LVA systems and regardless of fibre diameter).

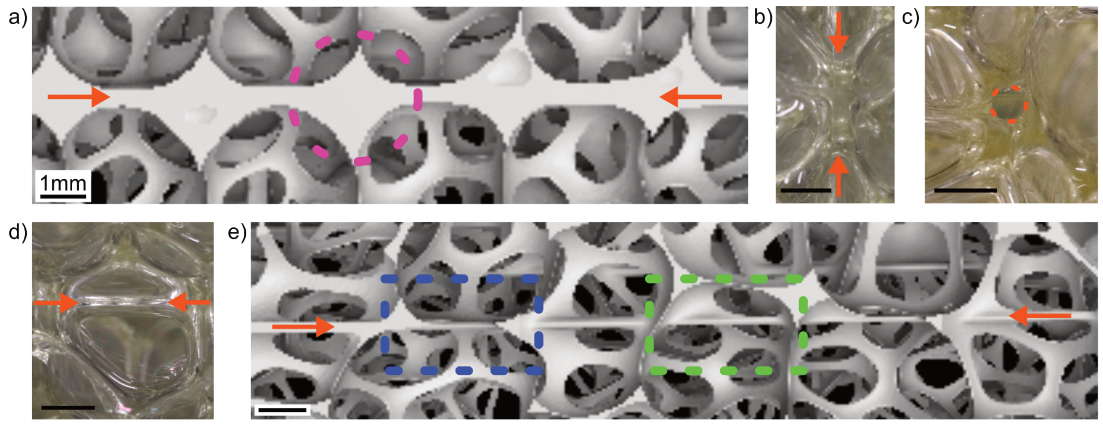


Figure 5.15 – Different experimental observations of fibres surrounded by PU foams (prepared with the protocol described in Section 5.2.3), all fibres are highlighted with orange arrows: a) 3D-reconstruction of a fibre surrounded by bubbles. The image is cut on the middle of a fibre and the pink dashed circle shows a cluster of material retained by the fibre. b) Side view of a fibre inside an aggregate of material to which struts are attached. c) Cross-section of a fibre inside the constitutive material of the foam. The fibre is highlighted with an orange circle. d) Image of a fibre passing through a bubble, dividing a film in two. e) 3D-reconstruction with a blue dashed rectangle showing the fibre that connects bubbles as a strut and a green dashed rectangle showing the fibre that passes through a bubble, dividing a film. All fibres have a 500 μm diameter, except for figure e) which shows fibres of 120 μm. We observed similar configurations for LVA foams. Pictures a and e are tomographic images with a resolution of 25 μm. Pictures b, c, d are taken with a Canon EOS 77D camera fitted with an EF 100 mm F/2.8 Canon macro objective lens.

The fibres (highlighted with orange arrows in Figure 5.15) can:

- retain the material by creating aggregates (circle with pink dashed line in Figure 5.15a) to which struts are attached (Fig. 5.15b, c).
- pass through a face of a bubble. The film will then be deformed because in most cases it remains attached to the fibre, as shown in Figure 5.15d and with the green dashed rectangle in Figure 5.15e.
- pass between two bubbles and become a strut on which films attach (blue dashed rectangle in Figure 5.15e).

5.3.2.2 Visual inspection of the foam-fibre systems

The structure of the PU and LVA foam samples, with and without fibres, is inspected using the tomographic images. This section will be divided according to the spacing between the fibres. The type of foam and the fibre diameters will be specified each time. For ease of reading, we refer to the samples as follows: `Foam Type_Fibre Diameter` (in μm)`_Spacing` (in mm).

The first samples investigated with X-ray tomography have 7x7 FC nylon fibres arranged in a square array with 4 mm between them (Fig. 5.6), respectively following the protocols described in Sections 5.2.2 (LVA) and 5.2.3 (PU). The scanned volume surrounded all the fibres. As explained in Chapter 1, only the struts and vertices are visible in the tomographic images, not the films between two bubbles, due to the resolution chosen.

Figure 5.16 shows transversal (i.e. perpendicular to the fibres) and longitudinal (i.e. parallel to the fibres) sections of 2D and 3D tomographic images, for all samples tested with 4 mm between the fibres. The ordering behaviour of these foam-fibre samples is immediately apparent, especially for the sample `LVA_120_4 n°1` and those with fibres of 500 μm diameter. We can see in the images of the longitudinal sections that the bubbles align themselves between the fibres, regardless of the type of foam and the fibre diameter.

Moreover, the bubbles appear to crystallise spontaneously in a structure similar to the Kelvin-like structure (Chapter 1). Figure 7a shows the well ordered `LVA_120_4 n°1` sample. The fibres are highlighted with red dots. Figure 7b presents a diagram of the Kelvin structure [13] on which the identical faces with Figure 7a have been highlighted with the same colour. These faces are identical but we will see below that other faces are often missing to complete a perfect Kelvin cell. Figure 7c is a 2D view of the bubble stack to help visualise where the fibres pass through the foam.

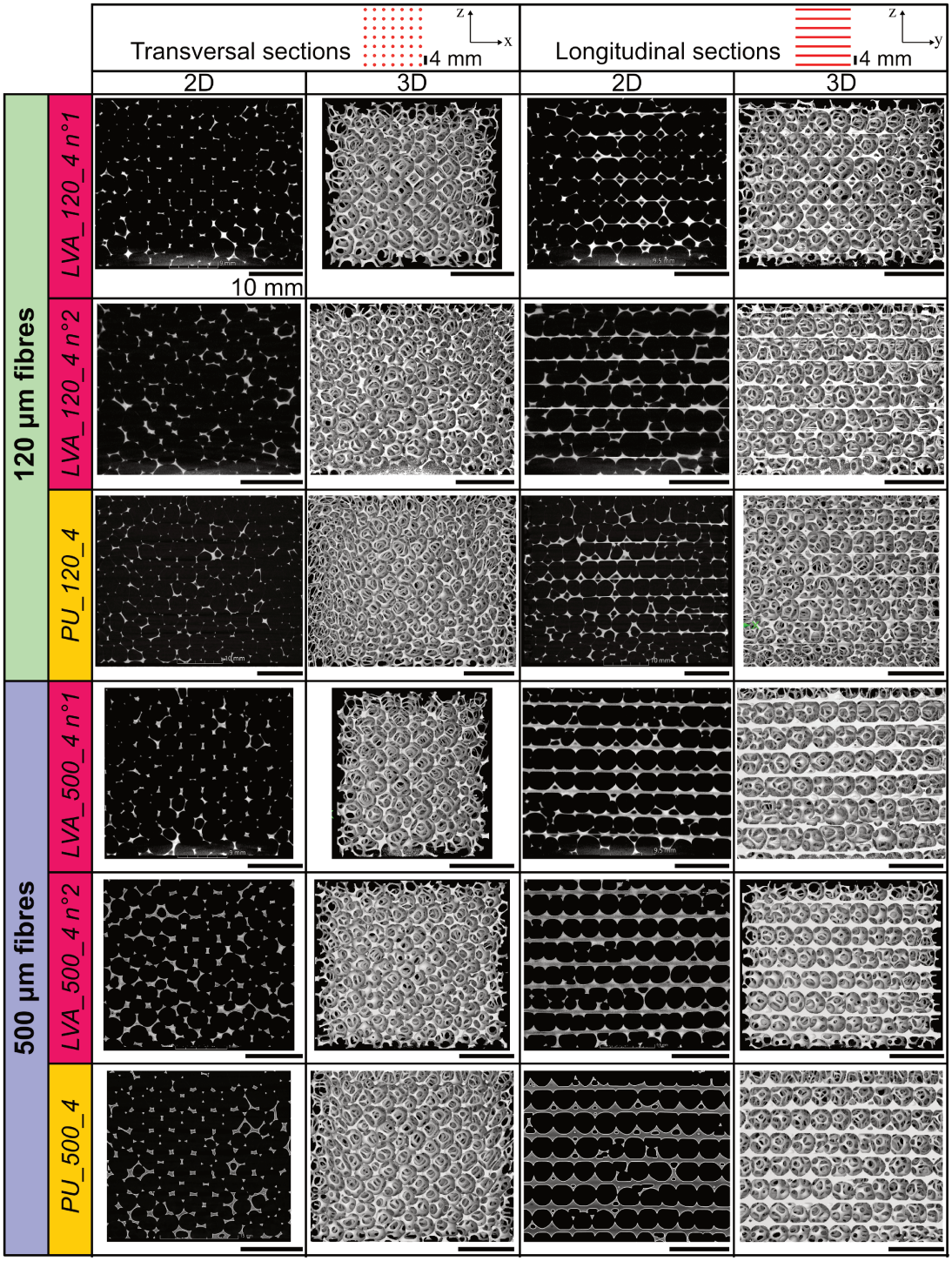


Figure 5.16 – Impact of the presence of fibres in a square array with 4 mm spacing on the foam structure: Transversal (i.e. perpendicular to the fibres) and longitudinal (i.e. parallel to the fibres) sections of 2D and 3D tomographic images, for all samples (LVA and PU foams; Fibres with diameters of 120 and 500 μm). Sample names: `Foam Type_Fibre Diameter` (in μm)`_Spacing` (in mm). Resolution: 25 μm. Scale bar: 10 mm.

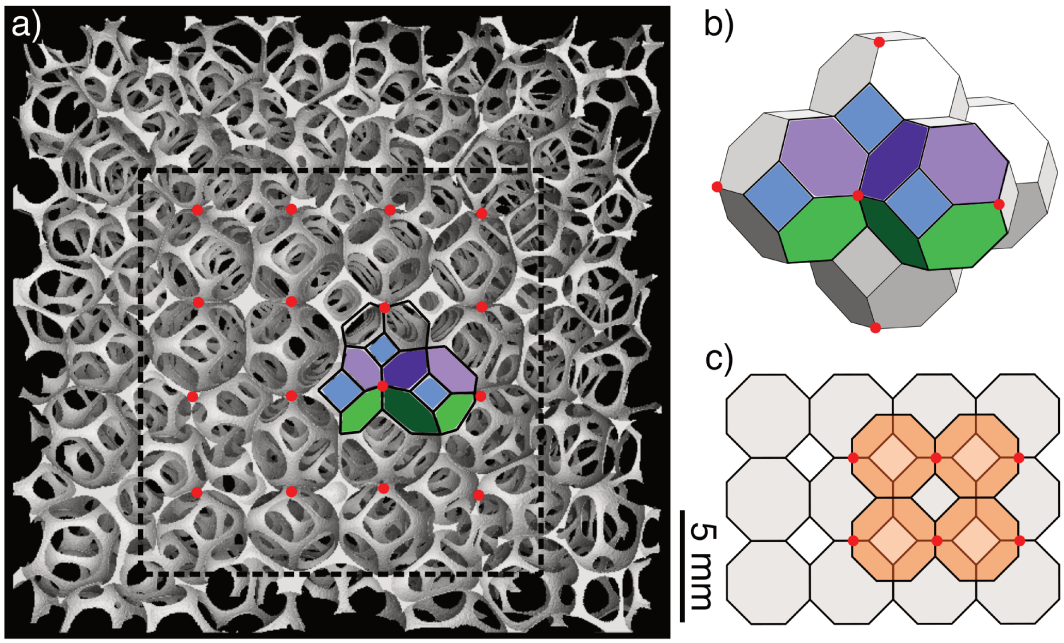


Figure 5.17 – Kelvin-like structures: a) 3D reconstruction of the `LVA_120_4 n°1` sample, using X-ray tomography. Resolution: 25 μm. The fibres, represented by red dots, have a diameter of 120 μm and are spaced by 4 mm for an identical bubble diameter (about 3.6 $\pm$ 0.5 mm, as mentionned in Table 5.3). In the dashed black square, the bubbles are aligned between the fibres and stacked to form a Kelvin-like structure. b) Kelvin structure [13]. The identical faces in a) and b) have been highlighted with the same colour. c) 2D stacking of bubbles to highlight where the fibres (red dots) pass through the foam.

Figure 5.18 shows 3D reconstruction of cells found in the `LVA_120_4 n°1` and `PU_500_4` samples with the fibres highlighted by orange dashed lines or orange circles. As described in Chapter 1, a "perfect" Kelvin cell has 14 faces (8 regular hexagons and 6 squares). Some of these "perfect" Kelvin cells are formed in our foam-fibre systems (Fig. 5.18a `LVA_120_4 n°1` sample), on which we can count 14 faces. Despite the strong visible global ordering of the foam, these "perfect" cells are randomly dispersed in the foam-fibre systems and single (i.e never found in an arrangement of several "perfect" Kelvin cells), regardless of the material of the foam and diameter of the fibres.

In our foam-fibre samples with 4 mm spacing, we observe that the number of faces per bubble is often "lower" (compared to the "perfect" Kelvin cell) due to the presence of fibres and a high liquid fraction located around the fibres. In fact, some faces are replaced with a material aggregate. In the following, we will distinguish a "perfect" Kelvin cell (with 14 well-defined faces) from a Kelvin-like cell in which not all faces are defined.

As an example, we can see in Figure 5.18b `PU_500_4` sample, a Kelvin-like cell which has 3 missing faces, i.e. only 11 faces are well-defined. Comparing to Figures 5.18a.5 and a.6, we can see, in Figures 5.18b.5 and b.6, that the faces appear closed. It should be remembered that due to the tomographic resolution chosen, the films are too thin to be seen. This means that if the faces are seen as closed here, it is because they are thicker at this point thanks to the fibre presence, which can retain the material by creating aggregates, as described in Section 5.3.2.1.

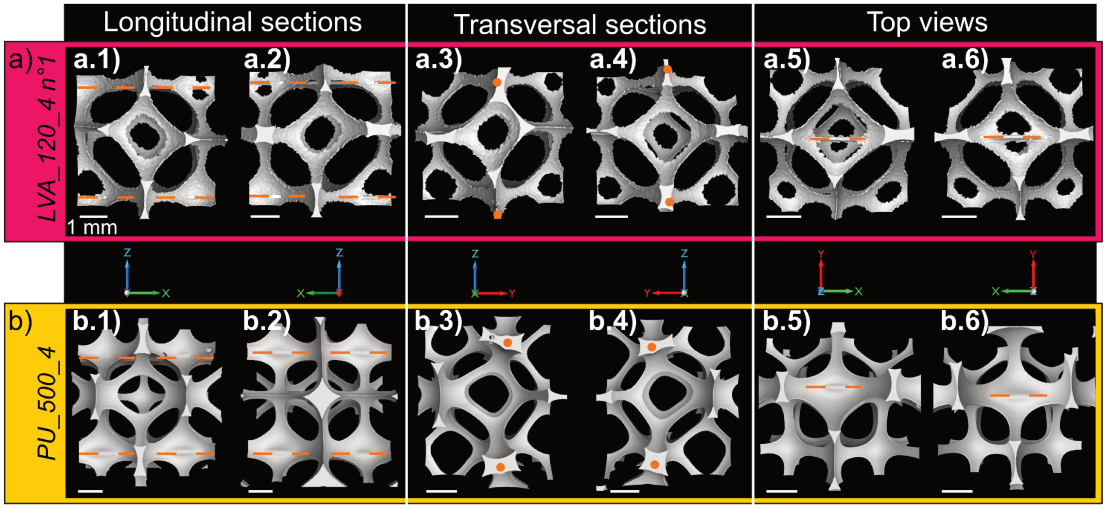


Figure 5.18 – 3D reconstruction of Kelvin-like cells in all directions. a) Kelvin cell from the `LVA_120_4 n°1` sample. b) Kelvin-like cell from the `PU_500_4` sample. Only the struts and vertices are visible due to the resolution chosen (Chapter 1). Resolution: 25 μm. Scale bars: 1 mm.

In Figure 5.18b.1, we can see in the foreground a square face, while in the background we see a material aggregate on which four struts are attached, which is also represented in Figure 5.18b.2 (in the foreground). To be more precise, in these figures we only see four struts attached, but in reality this aggregate is an 8 order vertex (Fig. 5.19a), which has been artificially cut for the figure. There is no fibre inside this aggregate: The 8 order vertex has formed spontaneously next to the fibre.

Kelvin-like cells with 11 faces are often found in our foam-fibre samples. They seem to be a signature of the presence of fibres. Moreover, at some places in our samples, we can observe a tendency for these 11-face cells to alternate, i.e. there is a layer of bubbles where we can see 8 order vertices and a layer of bubbles where we can see the 'open' square faces, as shown in Figure 5.19b (from the `PU_500_4` sample, same sample as the one from which Figure 5.18b close-up view is extracted). We can also imagine that if the foam had more time to drain, i.e. if solidification were delayed, the aggregates located on the fibres or these 8th order vertices would disappear, resulting in a "perfect" Kelvin structure.

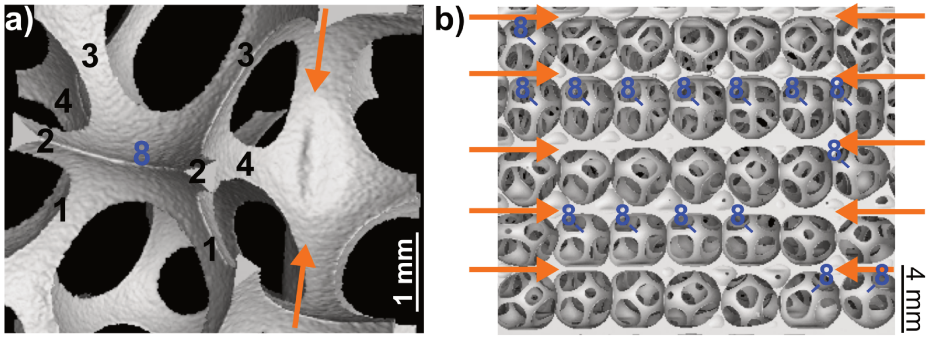


Figure 5.19 – 3D reconstruction of the `PU_500_4` sample. The fibres are highlighted by orange arrows. a) Enlargement of the 8 order vertex presented in Figure 5.18b.2. b) Longitudinal section. Five layers of Kelvin-like structure are visible. Resolution: 25 μm.

Another observation is that the arrangement in ordered structure seems to depend strongly on the diameters of the bubbles and more precisely on their dispersity (Chapter 1). Taking the example of the samples `LVA_120_4 n°1` and `LVA_120_4 n°2` (Fig. 5.16), we can see that the first sample is much more ordered than the second. Although the protocol of fabrication was identical (Section 5.2.2), the images show a dispersity in the bubble size. This is also highlighted by the measurement of the average diameter of the bubbles (Table 5.3 and Section 5.3.2.3 below). Indeed, it seems that if the dispersity of the bubbles increases (i.e. becoming more polydisperse) the Kelvin structure is no longer obtained.

We have succeeded in generating such an ordered structure on several layers for two different types of foam (LVA and PU) and two fibre diameters (120 and 500 μm). The number of Kelvin-like cells and the number of layers are evaluated manually by a visual inspection of the tomographic images directly in the VG Studio software (Table 5.3). If the cells are grouped together in the same location, the number of layers is specified with the number of cells along the x, y and z axis. Otherwise, it is indicated that they are dispersed throughout the system.

Name	**Diameter**	**Dispersity**	**Number of Kelvin-like cells**	**Layers (x x y x z)**
`PU_120_4`	3.7 ± 0.4 mm	11 %	150	dispersed
`PU_500_4`	3.7 ± 0.4 mm	11 %	240	7 x 5 x 5
`LVA_120_4 n°1`	3.7 ± 0.6 mm	16 %	240	5 x 7 x 6
`LVA_120_4 n°2`	3.4 ± 0.8 mm	23 %	100	dispersed
`LVA_500_4 n°1`	3.6 ± 0.6 mm	17 %	190	4 x 9 x 5
`LVA_500_4 n°2`	3.5 ± 0.2 mm	6 %	250	7 x 6 x 6

Table 5.3 – Bubble diameters, their dispersity, the number of Kelvin-like cells and their organisation in layers for each foam sample (with nylon fibres parallel to the y-axis and spaced with 4 mm), taken from the foam characteristic study presented in Section 5.3.2.3 below.

The importance of the dispersity of bubble diameters is even more apparent in the different fibre configurations (6 or 8 mm square array and honeycomb array, as described in Figure 5.6). In Figure 5.20, several foam-fibre systems are presented with 2D tomographic images and 3D reconstructions. As the representation is difficult with the common 3D reconstructions already used in this study, we use here a visualisation of the bubble volumes only (i.e. without the struts and the vertices) where a same colour corresponds to a same volume. The fibres are highlighted with red dashed line.

We can see in Figure 5.20, at first sight, that the bubbles align between the fibres, but also that the presence of smaller or larger bubbles disturbs the order. Indeed, Figure 5.206.a shows 2D tomographic image of the sample `PU_120_6`. The bubbles are arranged locally in a staggered pattern between the fibres spaced 6 mm apart. An example of ordered bubbles is highlighted by blue hatching, but if we observe bubbles of different diameters, such as the bubbles highlighted by grey hatching, they insert defects in the ordering behaviour. Figure 5.206.b and 6.c show the 3D reconstruction of the volumes

of the samples, respectively, `LVA_120_6` and `PU_500_6`. We can clearly see the impact of the bubble diameter: while sample `LVA_120_6` is ordered because it appears to have the same bubble size (Fig. 5.206.b), sample `PU_500_6` is disordered due to the presence of small bubbles, in blue (Fig. 5.206.c).

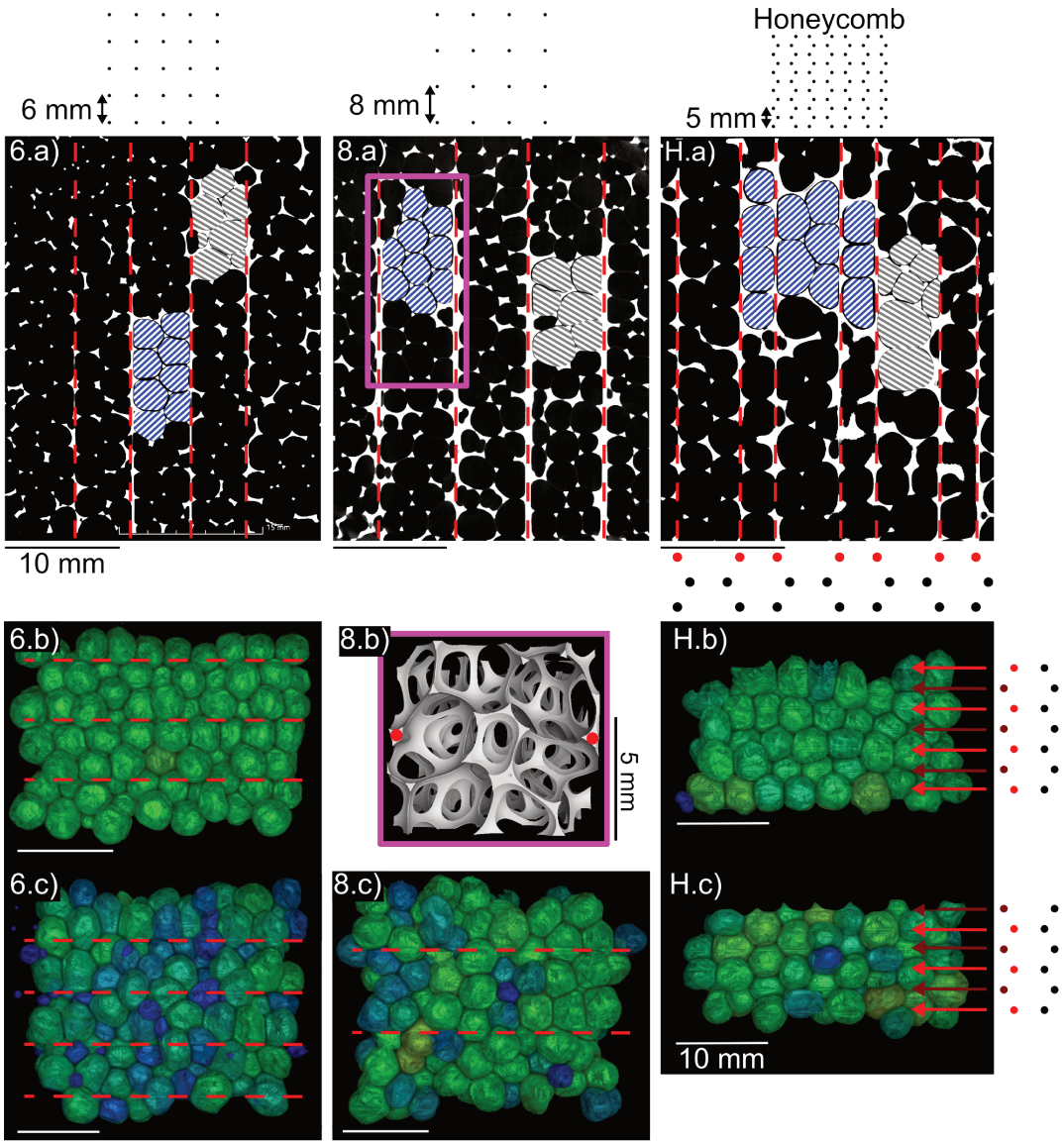


Figure 5.20 – Impact on the foam structure of the presence of FC nylon fibres in a square array with 6 and 8 mm spacing and in a honeycomb array: 2D longitudinal sections from tomographic images of the samples: 6.a) `PU_120_6`, 8.a) `PU_500_8` and H.a) `LVA_120_Honeycomb`. Examples of ordered bubbles are highlighted by blue hatching and disordered bubbles by grey hatching. Longitudinal sections of the 3D reconstruction of the volumes of the samples: 6.b) `LVA_120_6`, 6.c) `PU_500_6`, 8.c) `LVA_500_8`, H.b) and H.c) `LVA_120_Honeycomb`. The fibres are highlighted in red dashed lines. 8.b) Transversal section from a common 3D reconstruction of the sample `PU_500_8`, corresponding to the pink box drawn around the ordered bubbles in 8.a). The fibres are highlighted in red circles.
Sample names: `Foam Type_Fibre Diameter` (in μm)`_Spacing` (in mm). Resolution: 25 μm. Scale bar: 10 mm

Figure 5.208.a shows a 2D longitudinal section from tomographic images of the sample `PU_500_8`. We can see here that, on average, there is the place for 3 bubbles between the fibres spaced 8 mm apart. A set of ordered bubbles is highlighted by blue hatching and, here again, if bubbles are polydisperse in size, they are no longer aligned (grey hatching in Figure 5.208.a). Figure 5.208.b is a transversal section from an usual representation 3D reconstruction of the sample `PU_500_8`. The transversal section shown here corresponds to the pink box drawn around the ordered bubbles in Figure 5.208.a. The fibres are highlighted with red circles. We observe that the bubbles in the middle are perfectly aligned as we can see the black background through the bubbles. Figure 5.208.c shows the 3D reconstruction of the volumes of the sample `LVA_500_8`. It highlights again that in the presence of smaller (in blue) or bigger (in orange-green) bubbles, the ordering behaviour is no longer obtained.

Figure 5.20H.a shows a 2D longitudinal section from tomographic images of the sample `LVA_120_Honeycomb` (top view). We can see FC nylon fibres alternately spaced at 6 and 3 mm. Here again, we can see that bubbles are aligned between the fibres (blue hatching): one after the other between fibres spaced 3 mm apart and in a staggered pattern of two bubbles between the bubbles spaced 6 mm apart. Figures 5.20H.b and H.c are longitudinal sections of the 3D reconstruction of the volumes of two different parts of the sample `LVA_120_Honeycomb` (side views). Here, the direction and location of the fibres are highlighted with arrows to avoid overloading the images. The light red arrows are one layer above the dark red arrows (the cross-section of the fibre configuration is drawn next to the image). The sample in Figure 5.20H.b seems to be slightly more ordered than in Figure 5.20H.c due to the presence of different bubble size in the latter.

5.3.2.3 Foam-fibre system analysis from VG-Studio software

We now focus on bubble size and structure thickness analyses performed on those samples with VG Studio software. Figures 5.21a and b show the average equivalent bubble diameter for the PU and LVA systems respectively. Comparing the results for foams with fibres to those without fibres, we can see that fibres have no impact on bubble diameter for both systems, showing that the frictional interaction of the bubble with the fibres preserves volume constant of individual bubbles. However, there is a slight decrease of the bubble diameters for the PU foam with 500 μm diameter fibres and 6 mm spacing. This can be explained either by an experimental deviation or by the limitation of the software, which can artificially divide the bubbles into smaller ones (Chapter 1).

Figures 5.21c and d show the strut and vertex thicknesses. For each sample with fibres, we also obtained histograms of the distribution of strut thickness normalised by the mean strut thickness. As a reminder, the histograms are arbitrarily divided in two to distinguish both strut and vertex thicknesses (the method is illustrated in Figure 5.9). This arbitrary choice can lead to small errors in the measurement of averages. Nevertheless, for both LVA and PU foams, the addition of fibres to the foams appears to have a noticeable impact on thicknesses.

For PU foams, incorporating 120 μm diameter fibres seems to slightly decrease the average thicknesses. Indeed, as shown in Figure 5.15d and e, the fibres can pass through bubbles and are then considered as struts. In addition, the VG Studio software does not differentiate between fibres and actual struts, so it counts fibres in its thickness analysis. This may explain why average thicknesses are decreasing.

For LVA foam, as reference LVA foams initially have lower thicknesses than reference PU foams, adding fibres increases the average thickness. For 500 μm diameter fibres, the more they are, the thicker the struts and vertices. For 120 μm diameter fibres, the opposite happens: the further apart they are, the thicker the struts and vertices. This is a bit non-intuitive, as we might expect the same trend as for 500 μm diameter fibres. The explanation may be the presence of defects inside the LVA foams without fibres, i.e. thicker vertices which may have an order of 8 due to a cluster of poorly mixed $CaHPO_4$ or GDL.

As the two peaks corresponding to strut and vertex thicknesses cannot be distinguished for all samples, Figures 5.21e and f show the average of the structure thickness of the entire foam of each sample. The trends are the same as in the previous figures: 120 μm diameter fibres seem to have a very limited impact on structure thickness of PU foams, but increase thickness of LVA foams. In both systems, the more 500 μm diameter fibres, the thicker the structures.

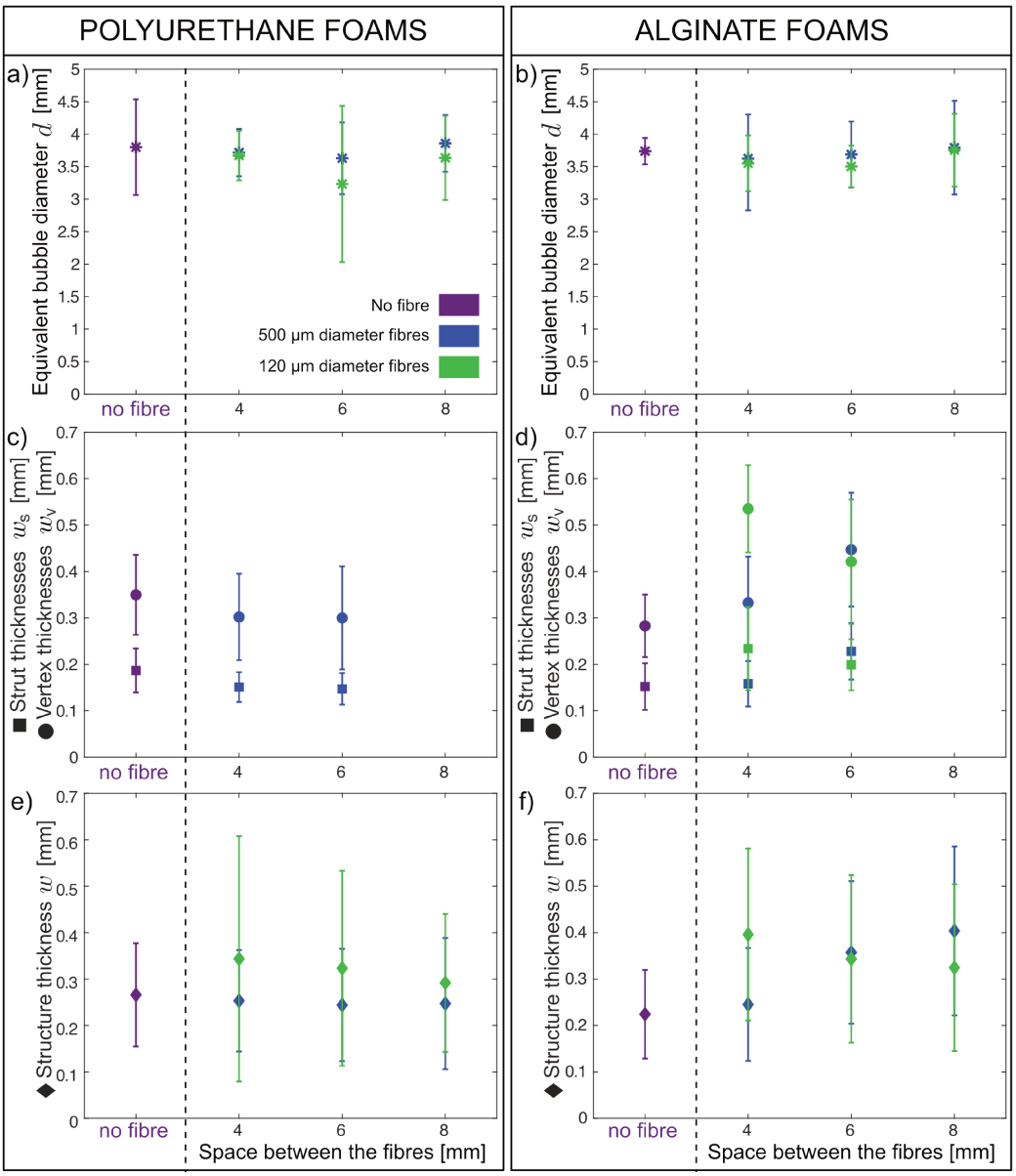


Figure 5.21 – Comparison of foams with and without fibres in terms of bubble diameters and structure thicknesses for respectively, PU and LVA foams: a)-b) Equivalent bubble diameters d; c)-d) Strut thickness w_s and vertex thickness w_v (for the cases where the strut and vertex peaks are distinguishable); e)-f) Global structure thickness w as a function of the space between fibres of 120 and 500 μm diameter. The first violet points (left of each graph) correspond to the average for three reference foams without fibre, (owing that these three samples are identical, the error bars correspond to the average of the three standard deviation from the reference samples). For the PU foam-fibre systems, only one foam-fibre sample is produced per configuration. The error bars correspond to standard deviations of bubble diameter or thicknesses of each sample. For the LVA foam-fibre systems, results and standard deviation are the average of two samples per configuration, except in figure d): the results for 500 μm fibres are obtained with only one foam-fibre sample.

5.3.2.4 Dual "scaffold" analysis

This Section will only discuss the results for the LVA foam-fibre systems due to time constraints, but the protocol that we are developing with those samples could also be applied to polyurethane foams. As shown in Section 5.3.2.2 and Table 5.3, the foam structure is locally ordered between the fibres. For a best representation of what could happen in the `LVA_120_4 n°1` sample, we virtually cut it closer in order to focus on a central zone (i.e around the ordered zone), the cutting protocol is described in Chapter 1. In what follows, we will specify whether we are focusing on this central zone or on a larger portion of the sample.e will specify the case where we are focusing on this central zone.

Orders of the vertices

As explained in Section 5.3.1.2, the programme extracts the proportion of vertices of order n. In the presence of fibres, the number of vertices of order different than 4 increases, showing that the number of material aggregates and then of 8 vertex orders increases. Note that the fibres are not distinguished from the struts during the extraction process. As an example, for the `LVA_120_4 n°1` sample there is 80 % of $O(4)$ vertices.

Strut angle distribution

Figure 5.22a compares the strut angle distribution between LVA samples with and without fibres.

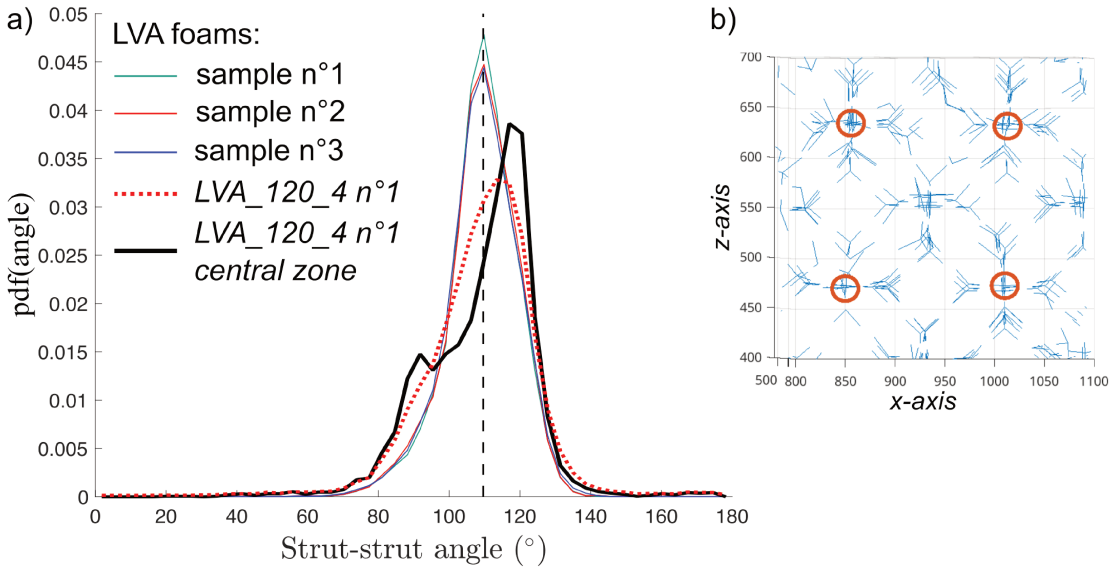


Figure 5.22 – a) Strut angle distribution for three reference LVA samples and for one foam-fibre sample, with two analysis zones: the `LVA_120_4 n°1` sample (highlighted by red dotted line) and the `LVA_120_4 n°1 (central zone)` sample (highlighted by solid black line). The vertical dashed line highlights an angle at 109.5 °. Extraction with $G = 20$ voxels following the procedure explained in Chapter 1, from tomographic images with a resolution of 25 μm. b) Representation of the pair of extracted struts with an angle of less than 100 °. Note that these are angles between extracted struts, it does not mean that there is no local adaptation to Plateau's rules. Struts are drawn with blue lines and fibre location are highlighted with red circles.

We can first see for the `LVA_120_4 n°1` sample, that the major peek is shifted around 120 ° instead of 109.5 ° for the cases without fibres. We can also see a "shoulder" at around 90°, which is even more pronounced when we look only at the central zone of the sample. To visualise where these 90 ° angles lie, we have drawn all the pairs of struts (in blue) with angles smaller than 100 ° on the Figure 5.22b. We can thus see that these angles (< 100 °) are not only located on the fibres (highlighted by red circles) but also next to them. This is the result of a self-reorganisation of the bubbles induced by the presence of the fibres. Note that these are angles between extracted struts, i.e. a "straight line" network, it does not mean that there is no local adaptation to Plateau's rules due to the natural curvature of the films and struts [1].

Steinhardt's analysis

From the extracted strut networks, we can then analyse the orientational order in the samples. To do that, we consider the bond orientational order parameters developed by Steinhardt et al. [55]. A detailed description of those parameters is presented in Appendix 8. The method consists in defining a set of coefficients Q_ℓ (which are non zero only for ℓ even), that do not depend on the choice of the coordinate system and are invariant by any global rotation of the structure.

Those Q_ℓ probe the orientational order and are all equal to zero in the case of a perfectly isotropic material. For an anisotropic material, the values of Q_ℓ are different from zero and can be seen as a signature of the global orientational order.

Of course, the dependence of Q_ℓ on ℓ does not give univocally the nature of the (orientationally) ordered structure, but as can be seen with the comparison with the simple cubic structure in Figure 5.23, the graphs may be significantly different and are definitely helpful to track the emergence of a long-range orientational order within the foam.

In the context of foams, these parameters have been rarely used. To our knowledge, this parameter is used in [121] in the context of the crystallisation of a monodisperse foam, but with a slightly different definition, using the bubble centers network instead of the strut network. Their analysis is performed for each bubble environment and not wholesale, as a result, Q_ℓ is a random variable characterised by a pdf. The Steinhardt decomposition is used in [121] more to characterise the local environment than to highlight the possible pervading of a local order throughout the foam sample. The Steinhardt parameter is thus used for the first time in this thesis to characterise the long distance ordering of a foam and defined on the network of struts, a definition not prone to difficulties coming with defining the center of bubbles [122].

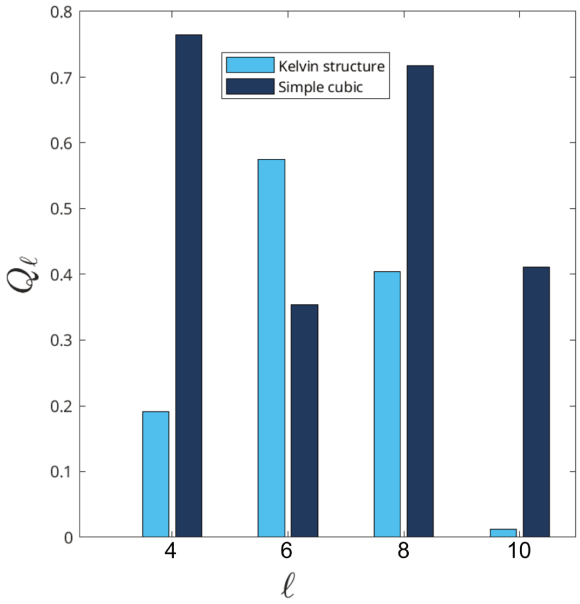


Figure 5.23 – Light blue: Steinhardt's parameter Q_ℓ for the perfect Kelvin structure (space-filling network of Truncated Octahedra). For sake of comparison, the corresponding Q_ℓ for the simple cubic network is shown in dark blue.

Figure 5.24a shows the values of Q_ℓ for several 120 μm fibre configurations in LVA foams. First, the fibre-less case (highlighted in black) exhibit very low value of Q_ℓ compared to the sample with fibres and to the Kelvin structure (in light blue), as its structure is almost isotropic. We can then observe that for the central zone of the 4 mm spacing square array (in hatched purple), the Q_ℓ distribution is the closest to that of a Kelvin structure. In the case of the honeycomb array (in yellow), we observe relatively high values of Q_ℓ but with a shape of distribution different than that of the Kelvin structure: The sample exhibit some orientational order, but different from the Kelvin structure.

Figure 5.24b shows the values of Q_ℓ for the 500 μm fibre configurations in LVA foams. The reference without fibre is given in Figure 5.24a. Two samples are represented for the case of 500 μm fibre with a spacing of 4 and 6 mm. We can see that the Q_ℓ distribution shape for each sample pair are quite similar. Moreover, Figure 5.24b compares the Q_ℓ distributions for the 4, 6 and 8 mm spacing and we can observe that the closer the fibres are together, the more the Q_ℓ distribution resembles that for a Kelvin structure.

These results come from work in progress and the analyses are still being carried out.

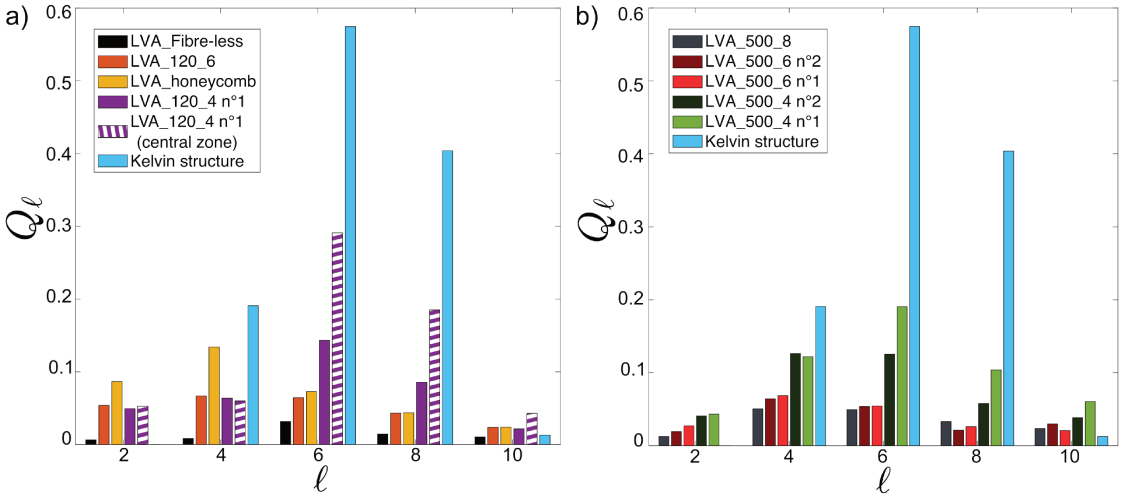


Figure 5.24 – Values of Q_ℓ for multiple fibre configurations for LVA foams with a) 120 μm fibres and b) 500 μm fibres, compared to the fibre-less case (highlighted in black only in a) and to the Kelvin Structure (highlighted in blue light). The foam-fibre samples are highlighted with the following color code: `LVA_120_6` in orange, `LVA_honeycomb` in yellow, `LVA_120_4 n°1` in purple, `LVA_120_4 n°1 (central zone)` in hatched purple, `LVA_500_8` in grey, `LVA_500_6 n°2` in dark red, `LVA_500_6 n°1` in light red, `LVA_500_4 n°2` in dark green and `LVA_500_4 n°1` in light green.

5.3.3 In-situ compression

This section presents the first results of in-situ compression tests on PU foams containing FC nylon fibres with either 120 μm or 500 μm diameter, spaced with 4, 6 or 8 mm. The foam samples are imaged at 4 levels of compressive strain (0, 10, 20 and 30 %). For comparison, a PU foam without fibre is tested in compression, perpendicular to the z-axis (corresponding to the height of the container in which the foam was produced). The foam-fibre samples are compressed perpendicular to the fibres.

Figure 5.25 shows 3D reconstructions of each compressive strain level, first, on a PU sample without fibre: We can see deformations that are typical for foams (without fibre), as described in Chapter 1. From 0 to 20 %, the bending of the struts becomes increasingly severe until a layer of bubbles collapses and the densification regime begins at 30 %.

Then, for PU samples with fibres, the tomographic images come in pairs: for each level of compression deformation, there is a 3D reconstruction of the whole sample and, below, a visualisation of the fibres only.

First observation is that the fibre deformations seem to start from the bottom of the samples (regardless the spacing between the fibres). This can be explained by the fact that force is applied from the bottom plate (the upper plate remains fixed). Similar phenomena are observed in the work of Brangwynne et al. [123] in which they studied the buckling of a plastic rod embedded in elastic gelatin (in bulk) to mimic the compressive deformation of microtubules. They explained that the buckling was localised in a region close to the site of force application and that the amplitude of the short wavelength decreased with distance from this site due to the longitudinal mechanical coupling of the rod to the bulk network. Moreover, it seems that the fibre deformation stays localised at the bottom of the `PU_120_6` and `PU_120_8` samples. The two foams appear to be linearly compressed with a pronounced buckling of the lower bubble layers only, while the top of the fibres remain straight (with the exception of a few fibres).

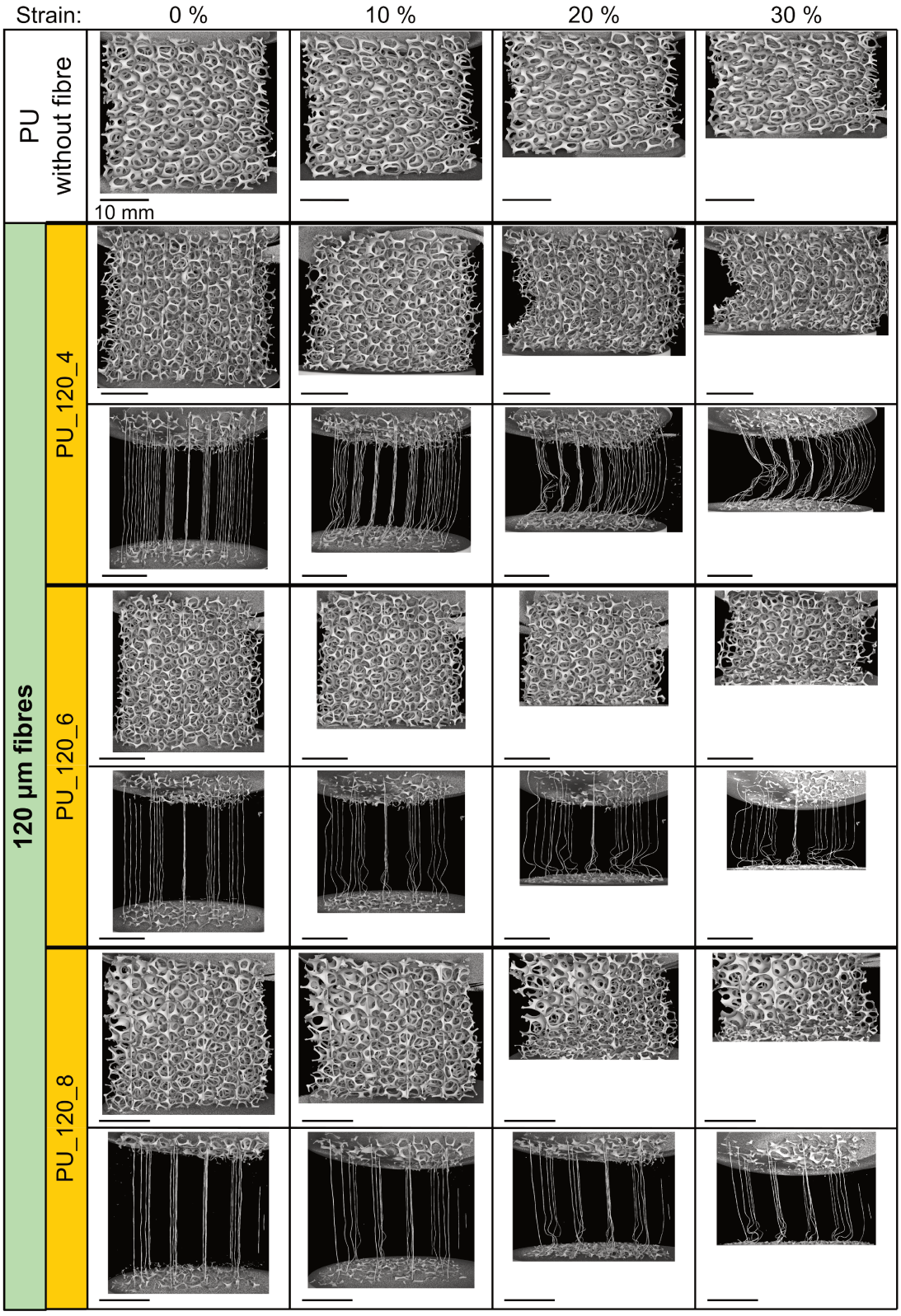


Figure 5.25 – X-ray tomographic 3D reconstruction of the deformed PU foams (without and with 120 μm fibres) for compressive strains of 0, 10, 20 and 30 %. The upper plate is fixed, while the bottom plate is controlled in displacement. Resolution: 25 μm. Scale bar: 10 mm.

On the contrary, in the PU_120_4 sample, we can clearly see the buckling of the entire sample with a very sharp fold of the fibres on the left of the tomographic images. The fibres seem to buckle all in the same direction. This can be explained by the fact that the PU_120_4 sample was initially placed slightly tilted: This may have constrained the sample more inhomogeneously than the other two samples. In our system, the presence of the foam between the fibres brings an additional level of complexity. Collective buckling of elastic beams has already been observed in the work of Guerra et al. [124]. They showed that thin slender structures can buckle, bend and push against each other when confined in a box and that the resulting ordered pattern changes as a function of the number and thickness of the beams, the spacing between them, the width of the box and the applied deformation.

With the examination of the top view image of the PU_120_4 sample (Fig. 5.26), we can see that the fibres seem to buckle in 3D configurations. Su et al. [125] show in their experiments that an elastic rod embedded within an elastomeric bulk matrix can buckle into a 3D coiled configuration for large matrix stiffness and in an alternation between 2D planar and 3D coiled buckling configurations in case of a softer matrix.

At this stage of our study, it is difficult to go beyond these preliminary remarks because, as also explained Su et al. [125] this type of compression testing to highlight such a buckling pattern is very sensitive to the boundary conditions imposed at the site of the applied force. Some improvements to the protocol will surely be required in order to improve the boundary conditions.

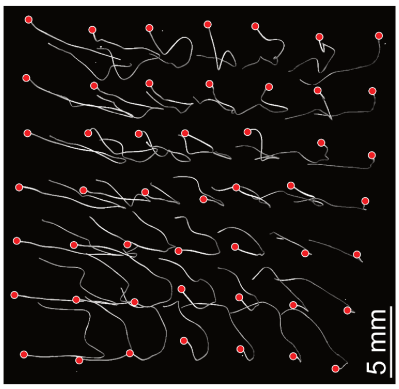


Figure 5.26 – Top view of X-ray tomographic 3D reconstruction of the deformed PU_120_4 sample for a compressive strain of 30 %. Only the fibres are represented. The upper plate is fixed, while the bottom plate is controlled by displacement. Resolution: 25 μm.

Figure 5.27 shows results for the compression deformation of PU samples with 500 μm fibres. All fibres seem to buckle in a same direction with a global buckling of the whole sample, no matter the spacing between the fibres. A more detailed study of fibre deformation is complicated here because segmentation of the foam and fibres is not possible due to the low contrast on the tomographic images, compared to the 120 μm fibres (probably due to the difference in supplier: 120 μm fibres from Flashmer MagixFluoro and 500 μm fibres from Savage Gear Regenerator).

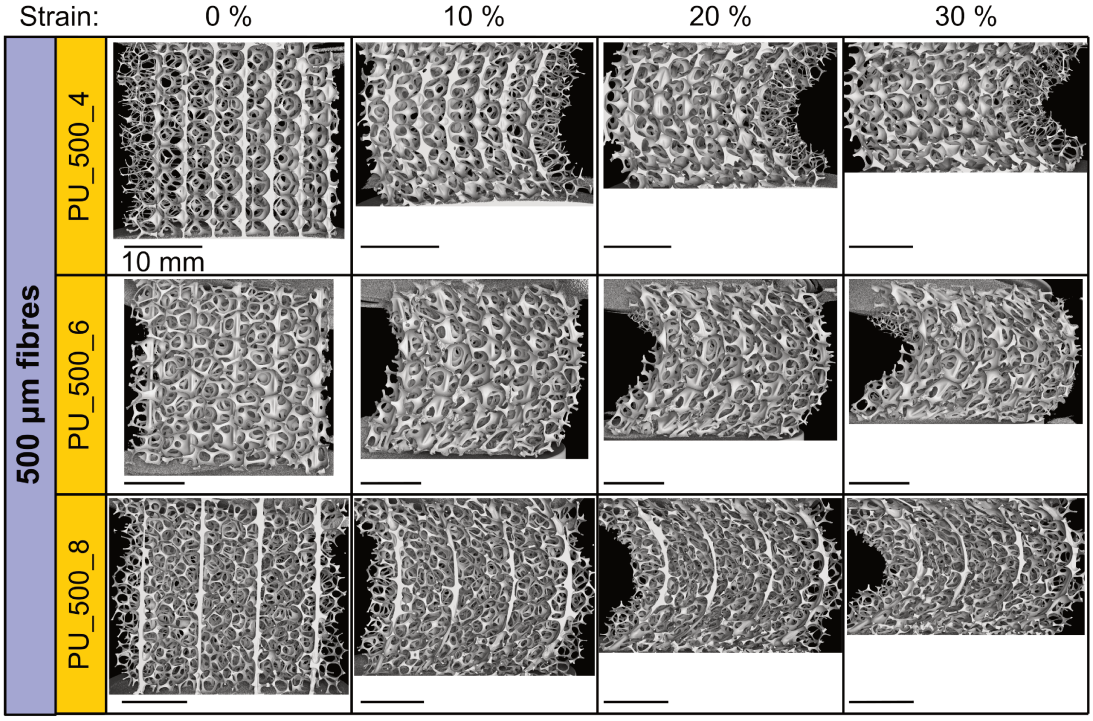


Figure 5.27 – X-ray tomographic 3D reconstruction of the deformed PU foams with 500 μm fibres for compressive strains of 0, 10, 20 and 30 %. The upper plate is fixed, while the bottom plate is controlled in displacement. Resolution: 25 μm. For comparison, a sample without fibre is shown in Figure 5.25. Scale bar: 10 mm.

5.4 Conclusion

To conclude, we focus here on the rigidity-dominated case of 3D solid foam - ordered fibre systems. Using our protocol, we are able to manufacture LVA and PU foams in a homogeneous and reproducible manner. We have shown that the foams have the ability to mechanically self-assemble between arrays of ordered fibres. When the spacing between the fibres is close to the average bubble diameter, the bubbles arrange themselves to form a Kelvin-like cell structure. To characterise them, statistical foam analyses are performed with both methods described in Chapter 1, using the VG Studio Software and the home-made extractor of strut network in Matlab. The use of Steinhardt parameters has enabled us to highlight the increase in orientational order in our foams when fibres are present. Finally, first results of in-situ compression tests on PU-fibre foams are presented, showing different deformations which depend on the fibre diameter and the spacing between them.

Conclusion and Outlook

Conclusion

In this manuscript, we explored the problematics of introducing fibres into foams solidified from liquid precursors. During this work, we proposed several experimental set-ups in order to understand and highlight the parameters that enable the controlled modification of foam structures.

In particular, in Chapter 2, we highlighted the importance of the geometrical and mechanical parameters of the fibres used in ordered liquid foams. In Chapters 3 and 4, we described the physical and experimental parameters that enable the manufacture of foams with a controllable structure, through the initial viscosity of the foam material, the foaming process and the solidification kinetics. These preliminary studies were used to select the appropriate formulation for producing the foam-fibre systems described in Chapter 5. The techniques used during this PhD work include the rheology of bulk materials, liquid foam templating, tomographic image processing using VG Studio software and an in-house Matlab program, and in-situ compression inside the X-ray tomograph.

We chose to work on two liquid foam templating systems based on alginate hydrogel foams and polyurethane foams. The alginate foam system has the advantage of being able to dissolve and be cleaned in water, enabling a statistical study to be carried out on several samples, while the polyurethane foam system enables to produce samples that can be removed from their containers, do not collapse under their own weight, and can thus be used for mechanical characterisations.

After a general introduction (Chapter 1) on liquid foams, liquid foam templating, mechanical and structural foam characterisation, we divided this PhD work in three main parts.

The first part (Chapter 2) was dedicated to the quasi-2D model experiment of a ribbon introduced into a liquid ordered foam. Confining bubbles into tubes to form foam columns leads to periodically ordered foam structures which are controlled by the ratio of tube width to bubble diameter [18]. We demonstrated that the equilibrium geometry of these bubble columns may be modified by the addition of elastic ribbons, resulting in geometries that differ from traditional foam structures prescribed by Plateau's laws [1]. Using X-ray micro-tomography, we quantified the equilibrium shapes of the quasi-2D foam-ribbon systems. The excellent agreement between our experiments and theory for both the amplitude and the full profile of the structures demonstrated that the resulting geometry of the ribbon-foam system is controlled by the competition between the bending energy of the ribbon and the interfacial energies of the bubble surfaces. Pre-analyses were carried out to integrate gravity into the theory illustrating the flattening of long ribbons

in columns of bubbles. Finally, we discussed proof-of-concept experiments showing that such setup can be used as a method to mold materials with characteristic shapes and curves imprinted by the foam structure.

In the second part (Chapters 3 and 4), we developed foams using the liquid foam templating technique, that offers a high degree of control over the foam structure. In Chapter 3, we proposed a method for generating and controlling the structure of solid foams from liquid foam templates, using the example of Alginate-$CaHPO_4$-based hydrogel foams. Using rheological characterisation, we showed how the formulation, the initial solution viscosity and gelation kinetics influence the foam structure. We provided a highly controllable foaming process by bubbling nitrogen through nozzles inside the solution. We demonstrated here that by adding control over the initial properties of the liquid (such as viscosity), solidification kinetics and drainage, we can finely tune the foam structure (bubble size, structure thickness, homogeneity of the samples). The tomography results showed that by decoupling the foam generation and solidification while accounting for foam drainage, it is possible to modify the density of solid foams.

In Chapter 4, we presented two protocols to obtain flexible polyurethane foams. The first protocol studied provided a lot of information on the introduction and choice of fibres, using a chemical foaming process. We have showed that limiting the length of the fibres is important to preserve the stability of the bubbles, but also that to produce X-ray tomography images, the contrast between the fibres and the foam is important to segment them. Chemical foaming is interesting to study the random dispersion of fibres inside foams, but its main drawback is that there is no control over the solidification kinetics. As two chemical reactions take place in parallel, bubbles are created at the same time as the polymer matrix solidifies, sometimes causing the bubbles to deform and no longer respect the Plateau's laws. Mechanically, the foam showed an increasing brittleness when more water was added. We then decided to switch to another, more controllable system, using mechanical foaming and removing water to reduce the chemical formation of bubbles.

This second protocol used the bubbling through a nozzle technique (as used for alginate foams in Chapter 3), but a major improvement has been made to this technique to adapt it to produce homogeneous polyurethane foams. Indeed, to solve the problems of homogeneity and density gradient, we based our approach on the idea of triggering solidification of the foam by introducing the catalyst in a second step, by superimposing a foam with catalyst on a foam without catalyst. By adjusting the catalyst concentration, the second foam was able to drain more or less inside the first one and we thus controlled the density of the latter. We also demonstrated that the mechanical properties of the foam can be adjusted with the formulation. Despite the fact that this method is very sensitive to environmental conditions in the laboratory (particularly humidity), the optimised formulation and protocol allowed us to obtain reproducible model foams.

The protocols developed and the formulations optimised in Chapters 3 and 4 were used in the final part, dedicated to foam-fibre systems (described in Chapter 5).

We demonstrated that the foams are able to self-assemble mechanically within arrays of organised fibres. We showed that bubbles align themselves to create a Kelvin-like cell structure when the distance between fibres is almost equal to the average bubble diameter. Statistical foam analysis were carried out to characterise the samples, using

the VG Studio software and a custom Matlab strut network extractor programme. We were able to demonstrate how the presence of fibres increased the orientational order in our foams by using Steinhardt parameters. Finally, preliminary results from in-situ compression testing on PU-fibre foams were obtained, displaying various deformations that depend on the fibre diameter and the spacing between them.

Outlook

Outlook for liquid foam-fibre systems

With the quasi-2D foam-fibre system, the consideration of gravity needs to be studied in more depth to understand why the experimental points sometimes do not agree with theory. An experimental improvement can be undertaken to obtain perfectly regular foams and improve the overall measurements.

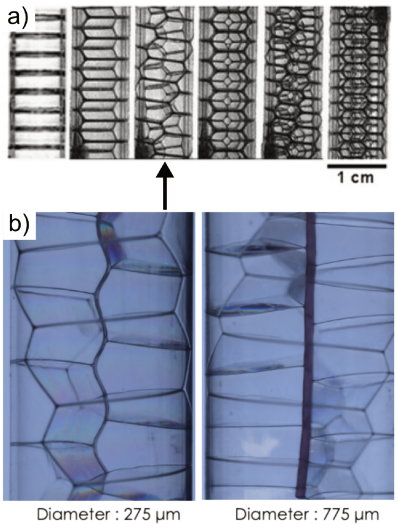


Figure 5.28 – a) Ordered foam structures in cylindrical tubes (from [22]). b) Pictures of two different flexible fibres (of 275 and 775 μm diameter) in helical aqueous foams.

Another interesting axis of research could focus on the influence of the presence of a fibre on other ordered structures. By modifying the ratio between the bubble diameter and the cylindrical tube width, we can obtain a helical bubble configuration as shown by the arrow in Figure 5.29a. Preliminary tests were carried out by inserting silicone fibres (Zhermack - Elite Double 8 - Polyvinylsiloxane with 8 Shore A hardness) of different diameters (275 and 775 μm) in this helical structure. Identical results to those presented in Chapter 2 can be seen in Figure 5.29b: if the fibre is small, its bending rigidity is low and it will therefore deform to follow the structure of the foam, whereas if it is thick, its bending rigidity increases and the shape of the foam is modified. As the theoretical study was more complex and we wanted to move forward towards solidifying systems, we chose not to continue with experiments on this system in the context of this PhD work.

Outlook for solid foam-fibre systems

With alginate foams, an interesting idea could be to also to test the superimposition of two foams as we saw in Chapters 3 and 5 that there is a density gradient due to gravity in such systems.

For polyurethane foams, it would probably be interesting to change the components of the formulation to try to reduce chemical foaming. For example, we saw in Chapter 3 that there are catalysts that facilitate the blowing reaction (which is the case with the catalyst we were using, as we adapted the formulation from Testouri et al. [97]) while there are others that facilitate the gelling reaction. Moreover, by testing different types of surfactant we might be able to reduce the presence of microbubbles. Indeed, we can see in Figure 5.29a the presence of microbubbles (highlighted by pink arrows) in the foam struts. In terms of mechanics, this introduces weaknesses that will become starting points for buckling of the foam. In addition, chemical foaming (in particular of the bulk material at the bottom of the pot resulting from the drainage of material in the foam, as shown in Figure 4.14) pushes the foam upwards. In the presence of fibres, the bubbles can be

deformed as shown in Figures 5.29 b and c where the orange bubble is strongly deformed by a fibre (highlighted by a red circle).

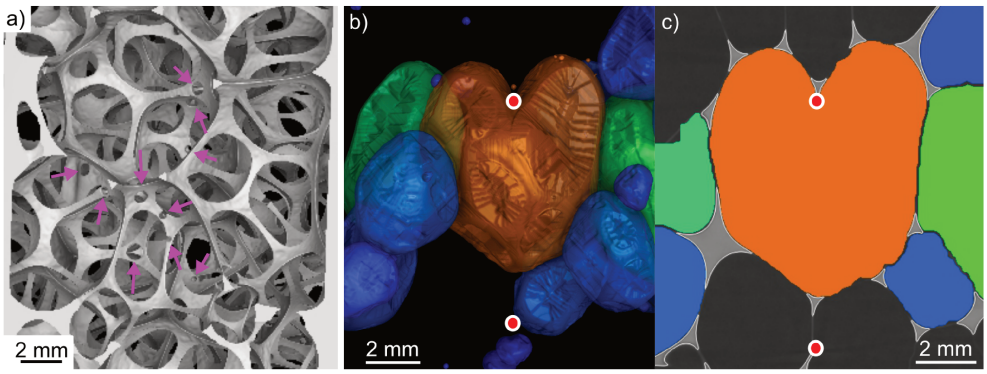


Figure 5.29 – Polyurethane foams produced with the protocol described in Chapter 4: a) Microbubbles trapped in the struts highlighted with pink arrows. b) Heart-shape bubble formed due to chemical foaming that pushes the bubble against a fibre.

For both alginate and polyurethane systems, in Chapter 5, we demonstrated the importance of the bubble size dispersity on the ability of bubbles to order themselves between the fibres. An improvement in the foaming method can therefore be important here. For example, a micro- or millifluidic protocol could be considered to obtain perfectly monodisperse foams.

In terms of fibre configurations, many possibilities can be tested with the system presented in Chapter 5. For example, instead of making a square network of fibres with 6 and 8 mm spacing, it might be interesting to test a 4x6 or 4x8 mm rectangular network so that in one direction the bubbles are always in contact with a fibre. Indeed, we saw in Chapter 5 that the bubbles arranged themselves spontaneously in ordered structures that differ from regular disordered foams when they were in contact with the fibres.

We formed a honeycomb network in Chapter 5 but forming a hexagonal network (i.e. put an additional fibre in the centre of the hexagon), seems to be interesting in terms of mechanics. Indeed, Jiang et al. [126] showed that with such a configuration of ABS tubes in a polyurethane foam it was possible to obtain auxetic behaviour. Auxetic materials are materials with a negative Poisson's ratio. This means that when such materials are compressed, they retract in the direction perpendicular to the force applied [127]. As shown in the image taken from their work (Fig. 5.30a), we can see that the sample retracts when a force compresses it. On the same subject, Zorzetto et al. [128] have shown that the presence of re-entrant inclusions (Fig. 5.30b left) in 3D-printed solid cellular materials confers auxetic properties to these materials, notably through the integration of "heart-shaped" cells as shown in Figure 5.30b right. Finally, the use of chemical foaming in our polyurethane foams could be useful to create a structure with heart-shaped bubbles as shown in Figure 5.29b.

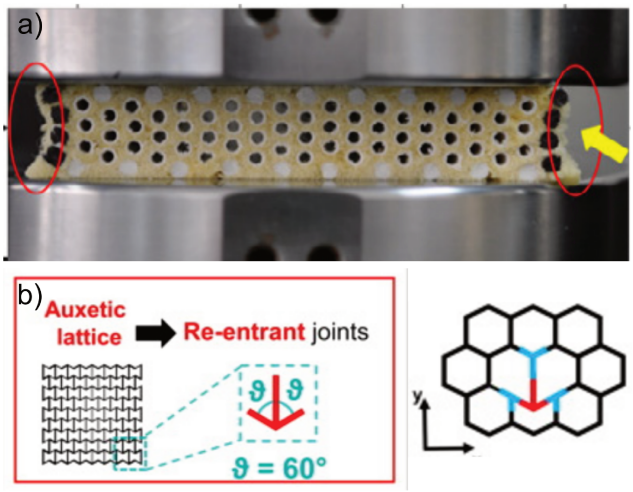


Figure 5.30 – a) Auxetic behaviour of a polyurethane foams containing ABS tubes. Taken from [126]. b) Diagram of auxetic lattices showing the re-entrant joints. Taken from [128].

In terms of flexible fibres, pre-tests were carried out as shown in Figure 5.31. During the fabrication of a polyurethane foam (following the protocol described in Chapter 3, we deposited silicone fibres (Zhermack - Elite Double 8 - Polyvinylsiloxane with 8 Shore A hardness), with rectangular cross-sectional dimensions of 300x400 μm, on the bubbles in transition on the PVC sheet from the first tube to the container. Figure 5.31 left shows the whole sample, whereas Figure 5.31 right shows only the fibres. We can see that the fibres are all bundled together and bent on themselves. The way they are positioned is a result of the way they were introduced. Work will need to be done on how the fibres are introduced: if they are dispersed so that they don't lie against each other, but also if flexible fibres are attached into the container. Particular attention will need to be paid to the tension put on the fibres (whether we want them to be very taut or very loose between the walls of the container). This could have an impact on the final structure of the foam. An experimental challenge that we faced concerns the production of silicone fibres. For our experiments, we moulded fibres one by one in tubes of different diameters or, in the case of fibres with a rectangular cross-section, they were moulded in a plate of Plexiglas etched with a micro-milling machine to the chosen size. A more robust fibre manufacturing protocol thus has to be developed for future work with multiple flexible fibres.

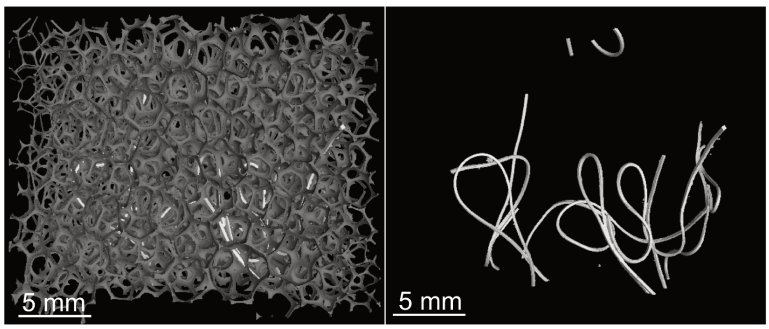


Figure 5.31 – Elastic silicone fibres (in white) with rectangular cross-sectional dimensions of 300x400 μm, surrounded by polyurethane foam (in grey).

Résumé de thèse : Architectures d'assemblages mousse-fibres : des systèmes liquides aux matériaux polymères hiérarchiques

Introduction

Une mousse est un ensemble de bulles de gaz emprisonnées dans un matériau liquide ou solide. De nouvelles techniques ont récemment été développées pour produire des mousses solides à partir de mousses liquides [2]. Leurs architectures sont alors liées aux structures de ces précurseurs liquides, elles-mêmes dictées par les lois de Plateau : trois films se rejoignent à 120° formant un canal de liquide appelé bord de Plateau et quatre bords de Plateau se rejoignent dans une géométrie tétraédrique [1]. Malgré les innovations récentes sur ces nouvelles techniques de fabrication de mousses solides [20, 40, 77], nous manquons toujours de méthodes pour contrôler et personnaliser la géométrie et la topologie des mousses (forme, taille et connexion des bulles). L'idée de cette thèse est d'utiliser des fibres afin de modifier la structure des mousses de manière auto-assemblée à l'état liquide, c'est-à-dire en permettant aux bulles et aux fibres de s'organiser spontanément avant l'étape de solidification. La modification des structures pourrait, par exemple, améliorer les propriétés mécaniques des mousses au-delà du simple renforcement mécanique fourni par les fibres.

La préparation de ces systèmes mousse-fibres soulève des questions fondamentales importantes : comment modifier les structures de mousses par l'introduction de fibres et quels sont les paramètres importants des fibres permettant de contrôler ces modifications ? Pour répondre à ces questions, la première étape de ces travaux a été d'étudier un modèle aqueux composé d'une colonne de bulles (Fig. 1a) dans laquelle une lamelle en silicone a été introduite (Fig. 1b). Ce modèle permet de simplifier le problème et de comprendre ce qu'il peut se passer dans le deuxième système étudié : une mousse solide fabriquée à partir d'un précurseur liquide (Fig. 1c et d) et renforcée de fibres (Fig. 1e).

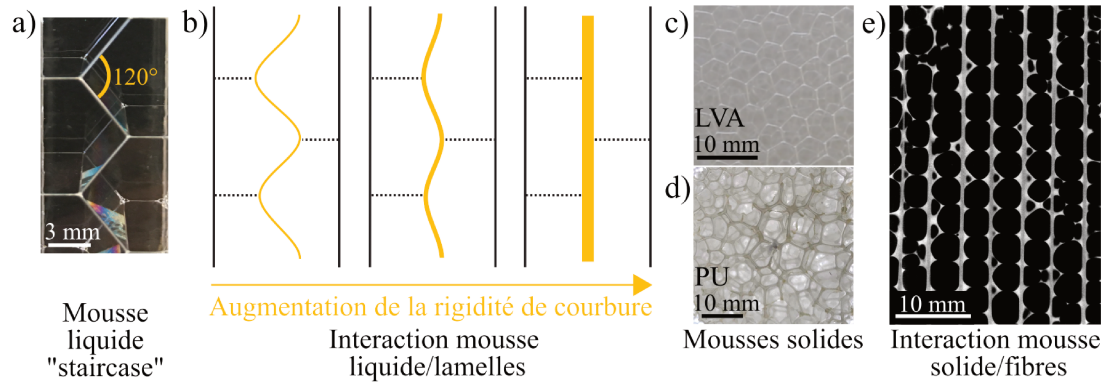


Figure 1 – **a)** Structure de bulles quasi-2D dite « en escalier » qui possède des films centraux connectés les uns aux autres avec un angle de 120°. **b)** Aperçu de l'expérience modèle. **c)** Mousse hydrogel d'alginate (LVA). **d)** Mousse polyuréthane (PU). **e)** Système mousse polyuréthane - fibres de nylon tendues et ordonnées.

1 Modèle aqueux quasi-2D

Le premier défi de ces travaux a été de trouver les paramètres clés impliqués dans les mousses enrichies de fibres. Les mousses sont des structures complexes avec des architectures précises dictées par les lois de Plateau [1] : nous avions besoin d'une expérience modèle quasi-2D qui illustre de manière simplifiée ce qui pourrait se passer dans une mousse enrichie de fibres. Nous avons donc remplacé les fibres par des lamelles en élastomère et la mousse liquide 3D par une colonne de mousse 2D composée d'un assemblage ordonné de bulles de savon monodisperses (Chapitre 2). En effet, confiner des bulles dans des tubes permet d'obtenir des structures ordonnées, respectant toujours les lois de Plateau et qui dépendent du ratio entre les dimensions du tube et le volume des bulles [18]. La structure d'intérêt s'appelle structure « en escalier », elle est invariante par translation dans la direction transverse au tube et a l'avantage de posséder des films centraux qui zigzaguent avec un angle de 120° entre chaque film (Fig. 1a). C'est dans ces films centraux que les lamelles élastiques de différentes épaisseurs sont introduites.

Les formes d'équilibre du système colonne de bulles/lamelle (Fig. 1b) sont dictées par la compétition entre élasticité et capillarité, c'est-à-dire entre l'aptitude de la lamelle à se déformer sous la contrainte de la mousse et le comportement de la phase liquide des bulles lorsqu'elle rencontre la lamelle. L'imagerie 3D par tomographie aux rayons X (RX) nécessite un système stable dans le temps, or une mousse aqueuse évolue sous l'effet de la gravité, une attention particulière a donc été portée au fait de limiter autant que possibles les dérives temporelles. Après optimisation du protocole et du dispositif expérimental, nous avons extrait les profils des lamelles d'épaisseurs différentes et donc de rigidités de courbure différentes. La rigidité de courbure est un paramètre important dans cette étude, il définit la façon dont la lamelle plie selon son élasticité et son épaisseur. Deux cas limites ont été mis en avant aussi bien théoriquement qu'expérimentalement : si la lamelle est fine, sa rigidité de courbure est petite, alors elle se déformera sous l'effet de la capillarité ; et inversement, si la lamelle est épaisse, sa déformation est faible, la forme d'équilibre sera alors dictée par la rigidité de la lamelle (Fig. 2) [56].

En résumé, nous avons mis en évidence que la géométrie d'équilibre des colonnes de bulles peut être modifié par l'introduction de lamelles élastiques, ce qui donne des

formes qui diffèrent des structures classiques de la mousse, telles qu'elles sont décrites par les lois de Plateau. Nous avons montré que la géométrie résultante du système lamelle-mousse est contrôlée par la compétition entre l'énergie de flexion de la lamelle et l'énergie interfaciale des surfaces de bulles, comme l'illustre l'excellent accord entre nos expériences et la théorie. Les interactions entre les mousses et les structures flexibles se produisent également dans des techniques de fabrication largement utilisées, telles que dans l'industrie du papier [46, 107, 108]. Enfin, à l'aide d'un système réticulable sous UV, nous avons proposé des matériaux présentant des formes et des courbes caractéristiques résultant de la compétition elasto-capillaire. Toutefois, certaines questions restent encore à explorer comme l'impact de la gravité sur un système identique ou le passage du système quasi-2D à un système 3D.

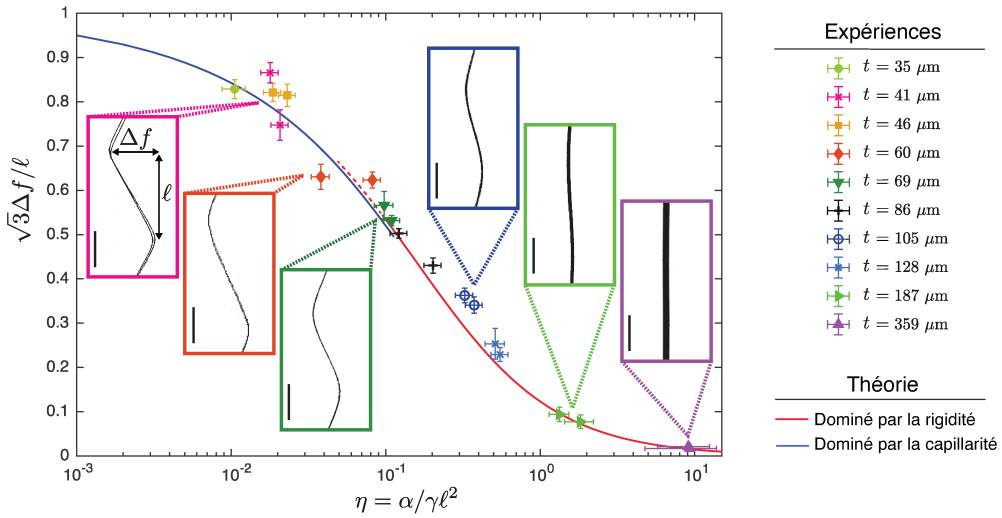


Figure 2 – Amplitude adimensionnée $\sqrt{3}\Delta f/\ell$ en fonction de la rigidité de courbure adimensionnée $\eta = \alpha/(\gamma\ell^2)$ avec ℓ la longueur d'une demi période, α la rigidité de courbure par unité de largeur de la lamelle et γ la tension de surface. Les prédictions théoriques, pour le cas dominé par la rigidité (à droite du graphique, correspondant aux lamelles rigides) et pour le cas dominé par la capillarité (à gauche du graphique, correspondant aux lamelles flexibles), sont représentées par des lignes pleines, respectivement en rouge et en bleu. Les expériences correspondent à la deuxième demi-période en partant du bas de la lamelle de polydiméthylsiloxane (PDMS) avec 10 épaisseurs différentes, ce qui donne des rigidités de courbure différentes. Les images montrent les tomographies à rayons X des systèmes correspondants (barres d'échelle : 2 mm).

2 Fabrication de mousses solides à partir d'un précurseur liquide

L'étape suivante de ces travaux consiste à s'orienter vers des mousses complexes 3D avec des fibres, avec des formulations permettant la solidification, afin de construire des matériaux hiérarchiques solides polymères. Cette stratégie repose sur le fait que l'incorporation de fibres à l'état liquide vise à modifier la structure des mousses de manière à ce qu'elles s'assemblent d'elles-mêmes, c'est-à-dire en permettant aux bulles et aux fibres de s'organiser spontanément avant la solidification. Nous nous sommes donc concentrés sur la fabrication de mousses solides à partir de précurseurs liquides afin de modifier la

topologie de la mousse à l'état liquide par l'introduction de fibres et la solidification de ce nouveau système.

La fabrication de mousses solides à partir d'un précurseur liquide commence dans un premier temps par la fabrication d'une mousse liquide [2]. Dans ce cas-là, le procédé est souvent mécanique (agitateur, bullage au travers d'une canule [37, 32], microfluidique [40, 97]) à partir d'une solution de monomère ou polymère. Dans un second temps, vient la solidification afin d'obtenir une mousse polymère solide. La solidification peut se contrôler par relargage progressif de l'agent réticulant ou en ajustant la concentration de catalyseur [74]. Elle peut également être déclenchée par un stimulus extérieur (UV [129] ou changement de température par exemple [130]). En d'autres termes, la mousse liquide possède suffisamment de temps pour trouver un équilibre métastable avant solidification. Il faut néanmoins faire attention à ce que ce temps ne soit pas trop long pour éviter la déstabilisation de la mousse.

Durant cette thèse, nous avons travaillé sur la fabrication de mousses solides en bullant au travers de canules dans un liquide stationnaire. Contrôler le temps de solidification a permis de contrôler les paramètres de la mousse solide, notamment sa densité finale, en solidifiant la mousse à différents temps de drainage.

Deux systèmes ont été étudiés, les mousses hydrogel d'alginate et les mousses de polyuréthane.

- Les **mousses d'alginate** (polymère extrait de l'algue brune *Phacophyceae*) possèdent une phase continue en hydrogel. Elles sont facilement utilisables et solubles dans l'eau, ce qui a permis de réaliser de nombreux échantillons rapidement, en particulier pour les systèmes mousse - fibres, où une configuration de fibres tendues et ordonnées peut être réutilisée pour plusieurs mousses (Fig. 1e et Section 3.2) et ainsi mener une étude statistique.

- Les **mousses de polyuréthane** permettent d'obtenir des mousses solides démoulables et utilisables pour différentes caractérisations. Avec ce système, il est également possible de contrôler la taille des pores par différentes techniques de moussage (chimique ou mécanique), la cinétique de solidification ainsi que la flexibilité de la mousse solide finale, modifiable par la formulation du polyuréthane.

Il a fallu porter une attention particulière pour que les deux systèmes soient identiques, c'est-à-dire que les mousses aient les mêmes caractéristiques (quantité de mousse, tailles de bulles, densité, etc.), afin de permettre une étude comparative. Toute la caractérisation structurelle a été réalisée à partir de tomographie RX, à l'aide du logiciel VG Studio MAX 2023.1 et de Matlab.

2.1 Protocole de moussage

Nous utilisons ici une des techniques les plus classiques de bullage : du gaz est soufflé à travers une ou plusieurs canules dans un liquide stationnaire moussant (Fig. 3a). Cette méthode a déjà largement été étudiée théoriquement afin d'obtenir une prédiction adéquate de la taille des bulles [36], puis développée à l'échelle industrielle par exemple en métallurgie pour la fabrication de mousses d'aluminium [131]. De nombreux paramètres permettent de contrôler et ajuster la taille des bulles afin d'obtenir une mousse personnalisée : la pression du gaz, la tension de surface et la viscosité du liquide, les

dimensions et la forme de la canule, les conditions de mouillage, la densité du gaz et du liquide ainsi que le régime de bullage (quasi-statique, dynamique ou turbulent) [37, 36].

Nous avons notamment étudié l'impact de la pression du gaz, de la viscosité du liquide et du temps de solidification (Sections 2.3 et 2.2), à l'aide de deux systèmes différents : les mousses hydrogel d'alginate et les mousses de polyuréthane (PU).

Les mousses d'alginate sont générées en soufflant de l'azote par quatre buses à pression constante dans une solution d'alginate. La mousse s'écoule d'un premier tube sur une feuille en PVC et est ensuite recueillie dans un récipient à section carrée (Fig. 3a).

Les mousses de polyuréthane sont également fabriquées avec cinq canules qui soufflent de l'azote directement dans le mélange de PU. Toutefois, pour pallier à des problèmes d'homogénéité des échantillons, deux mousses de PU sont superposées. La première étape consiste à fabriquer une mousse PU sans catalyseur (temps de solidification supérieur à 24h). Une seconde mousse est ensuite fabriquée de la même manière mais cette fois-ci avec du catalyseur (temps de solidification de quelques heures). Par superposition et sous l'effet du drainage, elle figera ainsi la première mousse (Fig. 3b).

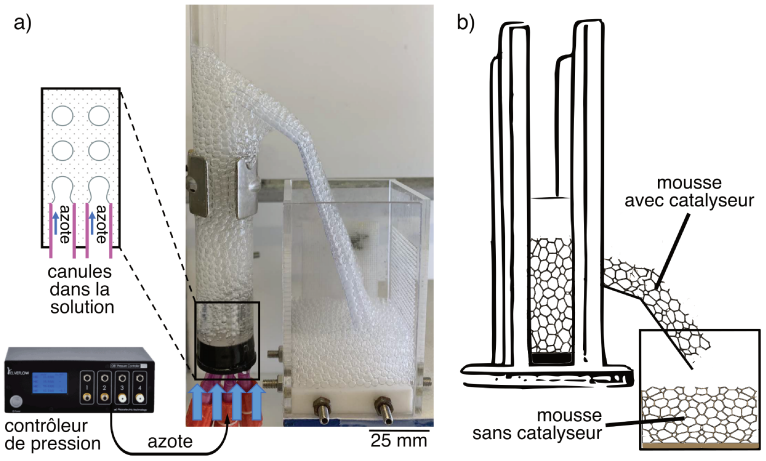


Figure 3 – Dispositifs expérimentaux pour fabriquer a) les mousses hydrogel d'alginate ; b) les mousses de polyuréthane.

2.2 Résultats : mousses d'alginate

Pour cette partie, nous avons montré qu'il est possible de personnaliser la structure des mousses (taille de bulles, épaisseurs des bords de Plateau, densité) en contrôlant différents paramètres à différentes étapes de fabrication de la mousse (Section 2.1):

- les **propriétés initiales de la solution** notamment la viscosité qui a un impact important sur la taille des bulles lors du bullage au travers d'une canule [36]. En effet, la Figure 4a montre que le diamètre des bulles augmente avec l'augmentation de la viscosité de la solution. Ce paramètre est d'autant plus important dans le cas de la fabrication des mousses dont la solution solidifie au cours du temps, entraînant ainsi une augmentation de la viscosité et donc une augmentation de la taille des bulles.

- le **temps de solidification.** Il est important de choisir le bon système au départ afin d'éviter une modification de la structure de la mousse au cours du temps.

Pour cette étude, nous avons besoin d'un système où la gélification des solutions d'alginate commence au plus tôt 2 min après le mélange des réactifs (2 min est le temps nécessaire pour mélanger et buller) (Fig. 4b). Cela permet de fabriquer la mousse avant que les propriétés physiques de la solution ne soient modifiées par le début de la solidification. Il faut aussi un temps de gélification pas trop long pour éviter la déstabilisation de la mousse mais suffisant pour permettre son drainage.

- le **drainage** de la mousse. Sous l'effet de la gravité, le liquide contenu majoritairement à l'intérieur des bords de Plateau s'écoule du haut vers le bas de la mousse. A l'état initial, la mousse est très dense et les bords de Plateau très épais mais en drainant ils s'amincissent au fur et à mesure [11]. Ainsi, en contrôlant le temps de gélification, il est possible de stopper le drainage et donc de figer la mousse à une densité donnée (Fig. 4c).

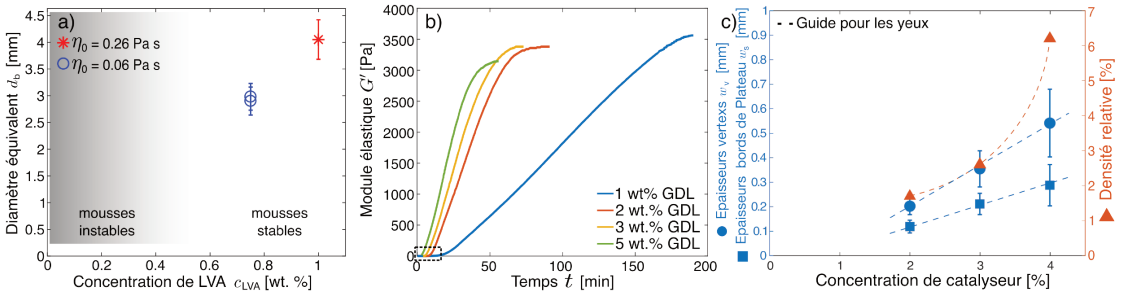


Figure 4 – **a)** Diamètre de bulle équivalent en fonction de la concentration d'alginate, c_{LVA}. Noter que la viscosité initiale η_0 étant une fonction croissante de c_{LVA}, le diamètre des bulles augmente donc lorsque la viscosité de la solution augmente. **b)** Module élastique G' en fonction du temps, mesuré en rhéologie sur des échantillons d'hydrogel d'alginate non moussés. **c)** Impact de la concentration en GDL c_{GDL}. Axe gauche en bleu : épaisseurs des bords de Plateau w_s et des vertex w_v. Tous les résultats sont mesurés avec le logiciel VG Studios. Axe droit en rouge : Densité relative de la mousse correspondante.

Cette méthode de production de mousses d'alginate offre un degré élevé de contrôle de la structure de la mousse. Cette étude montre que la concentration de GDL a un impact sur la viscosité des solutions, mais aussi sur le diamètre des bulles et l'épaisseur de la structure de la mousse. Le GDL est un acide qui déclenche la gélification dès qu'il est en contact avec les solutions d'alginate (par diminution du pH). Plus la concentration en acide augmente, plus la gélification est rapide. Noter que cette modification du pH n'est pas immédiate, il y a un laps de temps au début (encadré en pointillé - Fig. 4b) qui permet le bullage de la solution avant solidification. La viscosité initiale des solutions et la cinétique de gélification, associés au phénomène de drainage, ont un impact sur l'épaisseur de la structure en mousse. Nous avons déjà vu que le bullage à travers des canules permet de contrôler dans une large mesure la taille des bulles, mais nous démontrons ici qu'en contrôlant les propriétés initiales du liquide (telles que la viscosité), la cinétique de solidification et le drainage, nous pouvons ajuster avec précision la structure de la mousse (taille des bulles, densité, dispersité).

2.3 Résultats : mousses de polyuréthane

Le protocole de fabrication des mousses de polyuréthane (PU) était initialement le même que celui mentionné dans la Section 2.1 et décrit sur la Figure 3 mais le mélange de PU étant plus visqueux et les temps de solidification plus difficiles à contrôler, il a fallu ajuster le protocole. Plusieurs améliorations ont été réalisées concernant :

- la **quantité** de produit ou la **pression du gaz** requises en fonction du volume de l'échantillon et de la taille de bulles souhaitée
- le **récipient** de réception afin d'améliorer le démoulage de la mousse
- le **séchage et dégazage des produits** pour éviter la présence d'eau qui réagit chimiquement en dégageant du CO_2 et donc crée des microbulles parasites
- l'**homogénéité** des échantillons afin d'éviter un gradient d'épaisseur des bords de Plateau causé par le drainage
- la **formulation**
- le **protocole de fabrication**

L'utilisation de la méthode de superposition de deux mousses (Fig. 3b) pour la fabrication de mousses PU, permet de contrôler la densité de la mousse résultante. En effet, en modifiant la concentration de catalyseur dans la seconde mousse (Section 2.1), cette dernière va drainer plus ou moins profondément dans la première mousse et ainsi modifier l'épaisseur de ses bords de Plateau et donc modifier la densité finale de la mousse (Fig. 5).

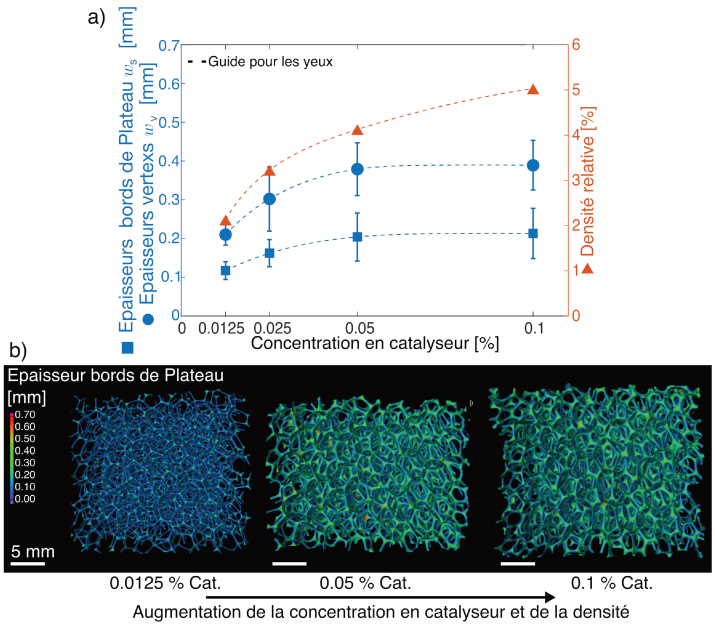


Figure 5 – Impact de la concentration du catalyseur dans la deuxième mousse sur la structure de la première mousse : **a)** Axe gauche en bleu : épaisseur de la structure ; Axe droit en rouge : densité relative de l'échantillon en fonction de la concentration du catalyseur. Les lignes pointillées sont des guides pour l'œil. **b)** Reconstruction en 3D à partir de la tomographie à rayons X de mousses de polyuréthane avec différentes concentrations de catalyseur.

Cette nouvelle méthode de production de mousse, basée sur la superposition de deux mousses, offre un degré élevé de contrôle sur la structure de la mousse solide obtenue. En ajustant la concentration du catalyseur, nous pouvons faire en sorte que la seconde mousse coule plus ou moins à l'intérieur de la première et contrôler ainsi la densité de cette dernière. Les propriétés mécaniques de la mousse peuvent également être ajustées en fonction de la formulation. De plus, lors du bullage dans une canule, la taille des bulles est définie par la pression du gaz, la tension superficielle et la viscosité du mélange liquide, la taille et la forme des buses, les conditions de mouillage, la densité du liquide et le régime de bullage, de sorte qu'en contrôlant un ou plusieurs de ces paramètres, nous pouvons déjà contrôler la taille des bulles et la densité de la mousse.

3 Système mousse - fibres

Dans ce chapitre, nous avons étudié l'impact de fibres sur une mousse. L'idée est d'intégrer des fibres dans une mousse à l'état liquide afin que le système puisse trouver un équilibre avant la solidification. Dès le protocole de fabrication des mousses validé, différentes configurations ont été testées sur des mousses d'alginate et/ou de polyuréthane : fibres rigides ou flexibles, dispersées ou ordonnées dans la mousse.

3.1 Dispersion aléatoire de fibres

Ces pré-tests ont été réalisés sur des mousses de polyuréthane.

- **Fibres rigides**. Cette partie a été explorée par Le Quan Ngo (4eme année de l'UTC), stagiaire dans notre équipe. Il s'est penché sur la dispersion aléatoire de fibres dans une mousse polyuréthane par moussage chimique. Après amélioration de la formulation et du protocole pour l'introduction des fibres, il a pu mettre en avant l'importance du contraste nécessaire entre les fibres et la mousse de PU, ainsi que la difficulté de contrôle sur la technique de moussage chimique du PU. C'est pour cette raison que nous sommes passés à un moussage mécanique présenté dans la section 2.1. A l'aide de ses résultats, nous avons également validé les hypothèses émises dans notre article [56] : une fibre possédant une grande rigidité de courbure (telle que la fibre de nylon) ne se déforme pas. C'est l'agencement des bulles qui est modifié (angles de 90° entre les bulles et la fibre, alors que les connections entre les films de polyuréthane se font habituellement à 120°).

- **Fibres flexibles** (Fig. 6(i)). Les fibres de silicone ont été déposées dans un flux de bulles sur la feuille PVC (Fig. 3a) afin de permettre un auto assemblage mousse - fibres. Les fibres se retournent et se plient les unes contre les autres. Nous avons pu remarquer que les fibres de silicone que nous possédions au laboratoire ne possédaient pas des rigidités de courbure suffisamment basses pour atteindre le cas limite où les fibres se déforment pour suivre les structures des mousses.

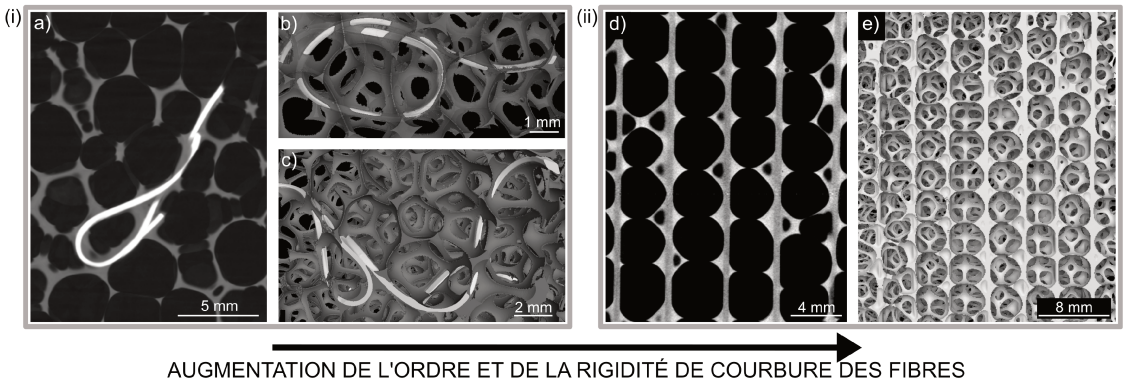


Figure 6 – Systèmes mousse-fibres avec : (i) Fibres élastiques en silicone, en blanc, avec une section transversale rectangulaire de 300x400 μm, entourées de mousse de polyuréthane, en gris, produit en suivant le protocol décrit dans le Chapitre 4). (ii) Fibres de nylon ordonnées de 500 μm de diamètre, espacées de 4 mm. d) Image 2D d'un système mousse d'alginate - fibres de nylon (Chapitre 5). e) Reconstruction 3D d'un système de mousse polyurethane - fibres de nylon (Chapitre 5). Résolution de la tomographie : 25 μm.

3.2 Fibres rigides ordonnées

Pour cette dernière partie, le récipient recueillant la mousse (Fig. 3a) a été modifié pour y intégrer des parois trouées de manière régulière. C'est par ces trous que sont tendues et ordonnées des fibres de nylon de diamètre 120 ou 500 μm avec des espacements entre chaque fibre de 4, 6 ou 8 mm (Fig. 6(ii)). Le protocole est ensuite le même que présenté dans la Section 2.1, avec soit la superposition de deux mousses de PU ou alors une mousse simple d'alginate déposée délicatement entre les fibres. Grâce à un temps de solidification contrôlé et suffisamment long, la mousse liquide peut trouver un équilibre, drainer et se réarranger entre les fibres. Les mousses sont ensuite tomographiées puis les images analysées. Nous procédons d'abord à une étude globale, c'est-à-dire à l'échelle d'une bulle (distribution des tailles de bulles, porosité, densité, drainage) puis à une étude locale, à l'échelle d'un noeud ou d'un bord de Plateau (nombre de voisins, distribution des angles, drainage, modification structurelle par les fibres).

Nous avons remarqué que :

- les bulles sont **alignées** entre les fibres
- les **angles sont modifiés** entre les bords de Plateau ou les films
- la **distribution des tailles de bulles** reste inchangée quel que soit le diamètre ou l'espacement des fibres
- les fibres semblent agir comme un **réservoir de liquide** rendant la mousse plus dense dans la zone des fibres
- le **ratio espacement des fibres / taille des bulles** est important dans le réarrangement des bulles

Un des points remarquables de cette étude est l'apparition d'une **structure de Kelvin** lorsque l'espacement des fibres s'approche de la taille des bulles (Fig. 7a). Une cellule

de Kelvin contient 8 faces hexagonales et 6 faces carrées. La structure de Kelvin est un empilement de ces cellules suivant un réseau cubique centré avec le respect des lois de Plateau. Toutes les cellules sont identiques et de surface minimale (Fig. 7b) [13]. Cette structure n'est réalisable que si la taille des bulles est similaire sur plusieurs rangées de fibres.

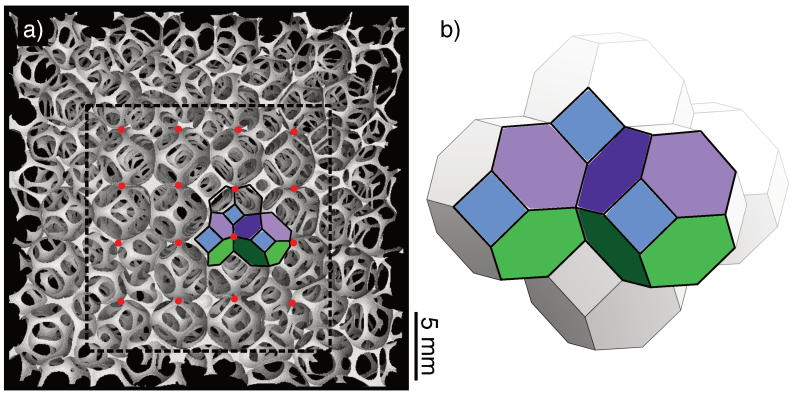


Figure 7 – a) Reconstruction 3D à partir d'une tomographie RX d'un système mousse d'alginate - fibres de nylon ordonnées. Les fibres, ici représentées par des points rouges, sont espacées de 4 mm pour un diamètre de bulles identique. Les bulles sont alignées entre les fibres et s'empilent pour former une structure de Kelvin. b) Structure de Kelvin [13]. Pour aider à la visualisation, les faces identiques ont été coloriées dans la même couleur.

Nous nous sommes concentrés ici sur le cas dominé par la rigidité avec des systèmes de fibres ordonnées dans une mousse solide 3D. En utilisant notre protocole, nous sommes en mesure de fabriquer des mousses d'alginate et de polyurethane de manière homogène et reproductible. Nous avons montré que les mousses ont la capacité de s'auto-assembler mécaniquement entre des réseaux de fibres ordonnées. Lorsque l'espace entre les fibres se rapproche du diamètre moyen des bulles, les bulles s'organisent pour former une structure cellulaire de type Kelvin. Pour les caractériser, des analyses statistiques des fibres sont effectuées avec les deux méthodes décrites au Chapitre 1 en utilisant le logiciel VGStudio et l'extraction de réseau de bords de Plateau à l'aide d'un script Matlab. L'utilisation des paramètres de Steinhardt (Chapitre 5) nous a permis de mettre en évidence l'augmentation de l'ordre d'orientation de nos mousses lorsque les fibres sont introduites. Enfin, les premiers résultats des tests de compression sur les mousses polyurethane enrichies de fibres sont présentés, montrant différentes déformations qui dépendent du diamètre des fibres et de l'espace entre elles.

Conclusion

Ces travaux ont été divisés en plusieurs parties comprenant (i) une expérience modèle permettant la quantification des formes d'équilibre de systèmes mousse/lamelle élastique, (ii) l'élaboration de deux protocoles de fabrication de mousses solides personnalisables à partir d'un précurseur liquide (l'un pour des mousses hydrogel d'alginate, l'autre pour des mousses de polyuréthane) et (iii) l'étude de la modification des structures de mousses solides par l'introduction de fibres. À terme, la sélection des fibres, de la technique de moussage et de la formulation du matériau constitutif permettront de réaliser des

matériaux composites possédant des structures et des propriétés mécaniques uniques. Durant cette thèse et d'après les résultats de l'expérience modèle, nous avons étudié de manière plus détaillée le cas dominé par la rigidité de la fibre, c'est-à-dire que la mousse est déformée et organisée autour des fibres. Bien que des pré-tests ont été réalisées avec une gamme de fibres plus souples, le cas dominée par la capillarité n'a pas pu être étudié et reste encore à explorer. Toutefois, avec ces résultats et les futurs à venir, couplés avec les techniques de moussage présentées ici, nous pourrons créer des matériaux mousse/fibres aux propriétés différentes et personnalisables. La mise à l'échelle industrielle de tels systèmes a un grand intérêt dans divers domaines (médecine, aéronautique, mécanique, thermique) et permettrait ainsi d'augmenter la gamme actuelle d'applications des mousses.

Appendices

1 Impact of the threshold on the bubble size measurement via VG Studio software

As explained in Section 1.4.2.4, compromises have to be made on the choice of sensibility threshold because if it is too small, the software can divide bubbles (Fig. 1.14b) whereas if it is too large, it can merge others (Fig. 1.14c)

To find the best sensibility threshold, systematic pre-tests were carried out for each system. Here is an example of a treatment made on polyurethane foam. Figure 1.1 shows the histogram of the bubble volume distribution of one and unique sample, for two threshold sensibilities (20 and 50 %).

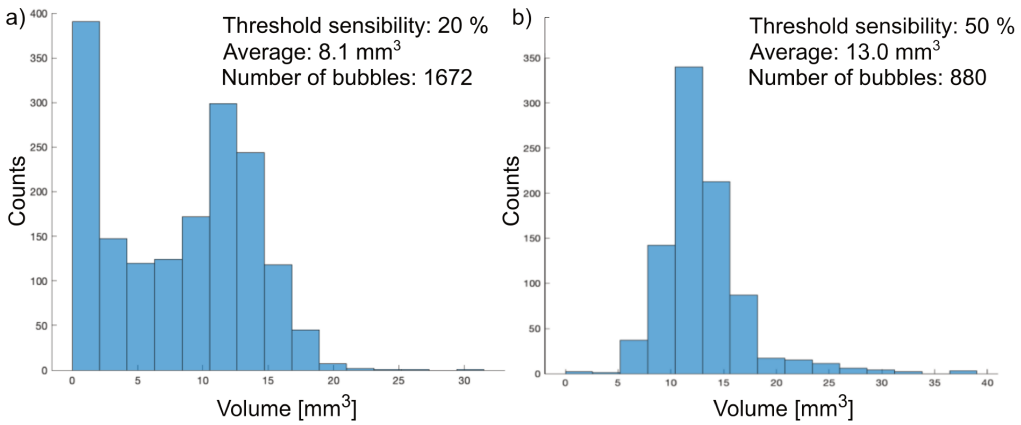


Figure 1.1 – Bubble volume distribution of a polyurethane foam, for threshold sensibilities of 20 and 50 %.

We can see in Figure 1.1a a first bar corresponding to the presence of microbubbles trapped in the vertices. From 0 to 10 mm^3, the number of bubbles measured is high due to the division of certain bubbles by the software. On the other hand, for a sensibility threshold of 50 %, the peak of small bubbles has disappeared but the number of bubbles over 20 mm^3 has increased.

Table A.4 summarises the average volume of bubbles and their number for the different threshold sensibilities tested. We can see that the threshold sensitivity has a real impact on the size and number of bubbles measured. The greater the threshold, the smaller the number of bubbles and the greater their average volume. Note that 100 % sensitivity corresponds to all bubbles merging. A compromise must be made depending on the sample and the system (polyurethane or alginate foam) in order to eliminate as many

small parasite bubbles as possible (which have no impact on the foam structure) without merging the "real" bubbles.

Threshold sensibilities	5 %	20 %	35 %	40 %	45 %	50 %
Average volume	8.1	8.1	9.5	10.9	12.0	13.0
Bubble number	1672	1672	1397	1189	1051	880

Table A.4 – Summary of the average volume of bubbles and their number for different threshold sensibilities.

2 Additional information on the strut network extraction

To illustrate the strut network extraction procedure described in Section 1.4.2.5, graphs corresponding to some examples of intermediate results are given here. We present in this appendix results of an alginate foam without fibres, but we proceeded in the same way for all samples.

Figure 2.2 shows the probability density function (PDF) of the strut lengths l that is used to help to define the gluing parameter G, i.e. the distance in voxel between two vertices below which the two vertices are merged by the programme.

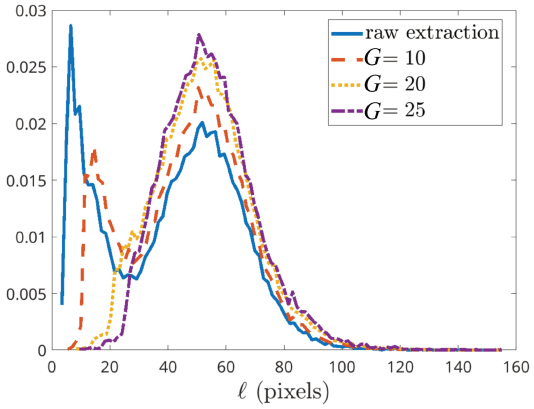


Figure 2.2 – PDF of the strut lengths l of an alginate foam without fibres. Solid blue line: bare distribution after step 5 (Fig. 1.16); Dashed lines: after step 7 but before step 8: Dashed red line: $G = 10$ px; Dotted yellow line: $G = 20$ px; Dash-dotted purple line: $G = 25$ px.

After step 5 (Fig. 1.16), the number of struts and vertices are 38861 and 24572 respectively. This order of magnitude is found by estimating that the sample is a 5cm×5cm×5cm cube housing bubbles of volume $(5\text{mm})^3$, each bubble having approximately 13 faces of 6 edges. One finds $\sim 10^3 \times (13 * 6/3) \sim 2.10^4$ struts. The ratio struts/vertices should be 2 (because $2N_{\text{struts}} = 4N_{\text{vertices}}$ for pure $O(4)$ vertices), we have 1.6, which indicates some defects in the network structure and may be due to non negligible $O(3)$ spurious vertices.

The strut length distribution just after step 5 is shown in Figure 2.2. The spurious vertices are responsible for the unphysical excess of very small strut lengths, cleary visible as a sharp peak at $\ell = 6.5$. These bunches of vertices can be explained by the presence of microbubbles trapped in the vertices and preserved by the numerical skeletonisation, as illustrated in Figure 2.3. On the other hand, the second peak at $\ell = 55$ is physical,

and witnesses the monodispersity of the bubbles. The correct value for G is roughly a value which would remove as much as possible of the small-G peak and keep as much as possible of the large-G peak. With this criterion $G = 25$ is the best choice for this sample, since the remaining main curve has no shoulder anymore on the left.

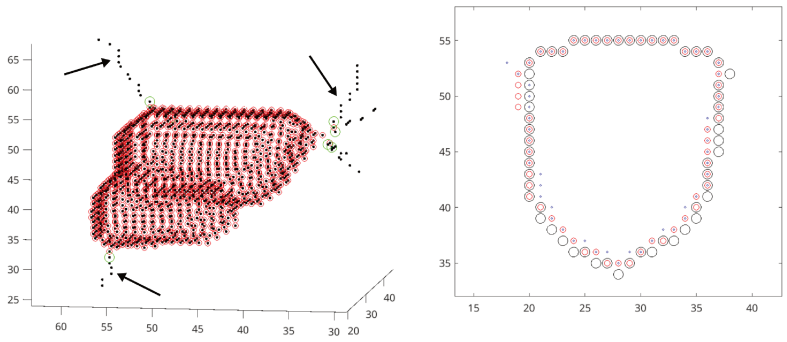


Figure 2.3 – Typical example of spurious vertex bunches produced by the skeletonisation procedure after step 5. Left : 3D perspective of two bubbles trapped in a vertex. At least three struts (highlighted with arrows) meet on this vertex. The red circled pixels are so-called "branch points", i.e. skeleton pixels with more than two neighbours (with a neighbourhood definition of 26 neighbours per pixel) of some struts. The green circled pixels corresponds to strut end points once the branch points have been removed. Right : Sectional view of the left graph highlighting the microbubble structures. Small (blue), intermediate (red) and large (black) circles correspond to skeleton pixels located at $z = 47$, 48, 49 px respectively. It can be remarked that not one $z = 48$ px is rounded by its 26 neighbours, as required by the skeleton definition.

After G has been chosen, the programme repeats a series of steps 7-8-7-8-... (Fig. 1.16) until no more cleaning or gluing $O(3)$ vertices remain. To understand the change, Figure 2.4 shows for $G = 25$ (the most relevant choice) the prior distribution (purple circle line, as seen in purple in Figure 2.2) as well as the final distribution (solid green line) after programme exit.

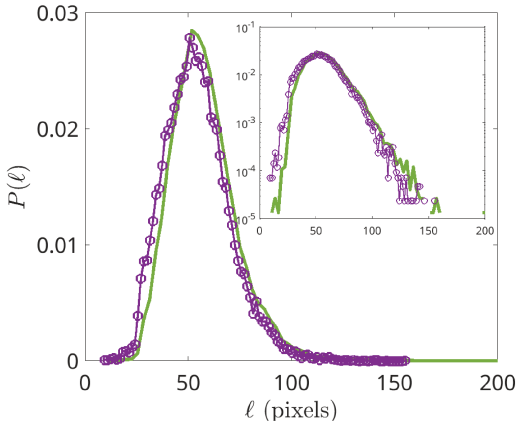


Figure 2.4 – PDF of the strut lengths l of an alginate foam without fibres. Purple circle line: Same curve as the purple of Figure 2.2 ($G = 25$); Solid green line: After letting the cycles 7-8-7-... pass ($G = 25$). Inset : same curves in semilog.

Actually after just one step 7 (a "cleaning"), the PDF(l) is indistinguishable from the

final one. The most noticeable feature is a smoothing of the visible noise in the curve, and an expected modest depletion of the small ℓ probability. The number of struts during the reduction process is shown in Table A.5, it shows that the very first cleaning disposes of 10% of the struts, but the successive steps 8-7-8-... removes only 4‰ of the rest : The quantitative impact of the step 8 is relatively modest.

	End of step 5	End of step 6	End of step 7 (1^{st} visit)	(2^{nd} visit)	(3^{d} visit)
# of remaining struts	38861	28759	25794	25687	25678

Table A.5 – Evolution of the number of struts during the whole extraction process for the stack of an alginate foam without fibre and the choice $G = 25$.

To remove spurious $O(3)$ vertices located at the borders of the samples and thus to identify a relevant subset, two graphs are produced (Fig. 2.5), showing the repartition of $O(3)$ vertices layer by layer, vertically and radially. The subsequent analyses consider always such cylindrical subsets of samples, chosen so as to remove the external layers fraught with spurious $O(3)$ vertices. We stress the fact that this notion is relative to each sublayer, in particular the horizontal layer barycenters may not be vertically superposed. However, for reasonably vertically aligned cuboidal samples, all local layer barycenter should be approximately aligned on the same vertical axis containing the total barycenter.

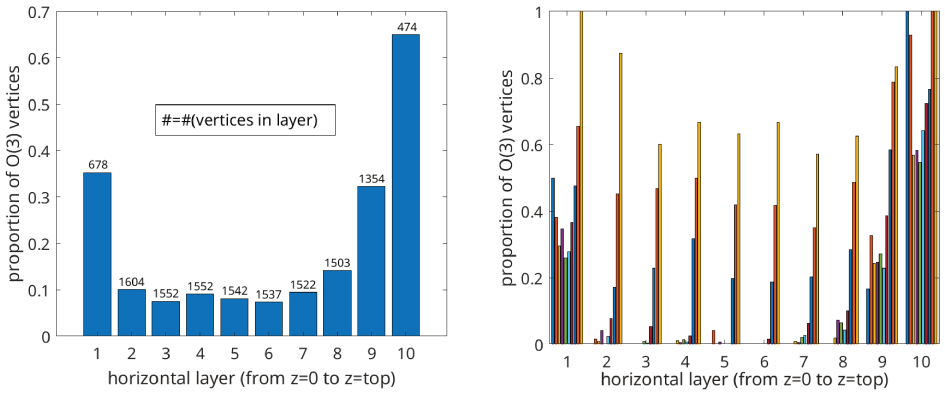


Figure 2.5 – Repartition of $O(3)$ vertices. Left : number of $O(3)$ vertices in each horizontal layer. Right : Each horizontal layer is virtually cut in concentric rings of fixed radial width, and the proportion of $O(3)$ vertices is shown for each radial sublayer. In the multiple bar plot shown, one sees that the 3 most external layers have an anomalously large number of $O(3)$ vertices, as well as the bottommost layer (numbered 1) and the three topmost layers (8,9 and 10). The numbers of horizontal and radial layers have been chosen to 10 in this example, and can be tuned differently.

3 Fitting parameters of the Cross model used on the rheological results

Table 3 lists the parameters of the Cross model for the four viscosity as a function of shear rate curves shown in Figure 3.5a.

Solutions	Zero-shear viscosity [Pa s]	Infinite-shear viscosity [Pa s]	Consistency [s]	Rate index
1 wt% LVA	0.257798	0.005709	0.002711	0.729422
1 wt% LVA + 0.02 M $CaHPO_4$	0.213389	0.040743	0.003244	0.946030
1 wt% LVA + 0.02 M $CaHPO_4$ + 2 wt% Disponil	0.200118	0.042249	0.003252	0.983405
0.5 wt% LVA	0.058271	0.136711	0.000023	0.547729

4 Simulation of the plateau storage moduli for different GDL concentration

Simulations to explain the slight difference in plateau values of Figure 3.7, using the Hyperquad Simulation and Speciation programme (HySS) are presented in this Appendix. This work has been performed by Imene Ben Djemaa.

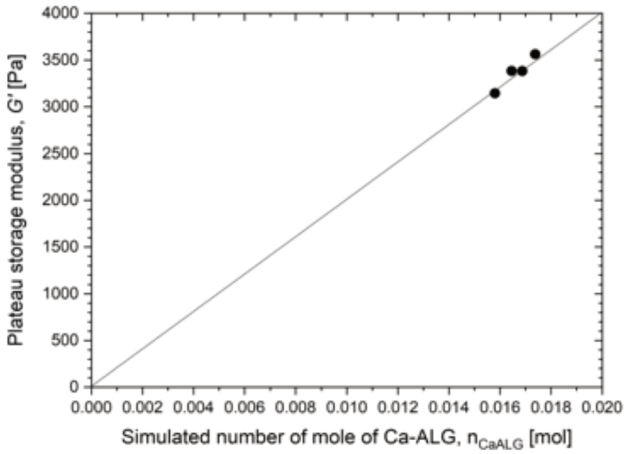


Figure 4.6 – Plateau storage moduli from Figure 3.7 as a function of the number of mole of cross-linked alginate with calcium (HySS simulation).

We can see an agreement between experimental values and simulation. As expected G' = f(CaALG): Since Gluconate (Gluc) from GDL chelates calcium ions and compete with alginate in bonding with the released calcium from $CaHPO_4$ particles, increasing its concentration at a constant alginate concentration results in increased % CaGluc and decreased % CaALG.

5 Struts position in the alginate foams using sequential tomography scans

Dimensions of the sample: x: 44.97 y: 44.97 z: 31.97 mm
Coordinates of the sample center: 0 0 0
Coordinates of the ROI centers:

Struts n	Time [min]	x	y	z
1	20	1.44	-6.19	-2.36
	95	1.51	-6.19	-2.23
2	20	-7.06	-3.86	5.34
	95	-6.91	-3.91	5.66
3	20	13.29	-9.86	-3.91
	95	13.29	-9.86	-3.59
4	20	-17.41	2.31	6.46
	95	-17.41	2.31	6.56

6 Limit of the foam superimposition method for high catalyst concentration in polyurethan foams

Pre-tests were carried out on polyurethane foams with 0.1 % catalyst to understand how the superimposed foam drained into the first foam, in Chapters 4 and 5. To visualise the drainage front, black dye was added to the second foam before being deposited on the first foam. At the bottom of the foam, we can see areas that have remained white. This reflects inhomogeneous drainage and explains why we choose 0.025 % of catalyst in Chapter 5.

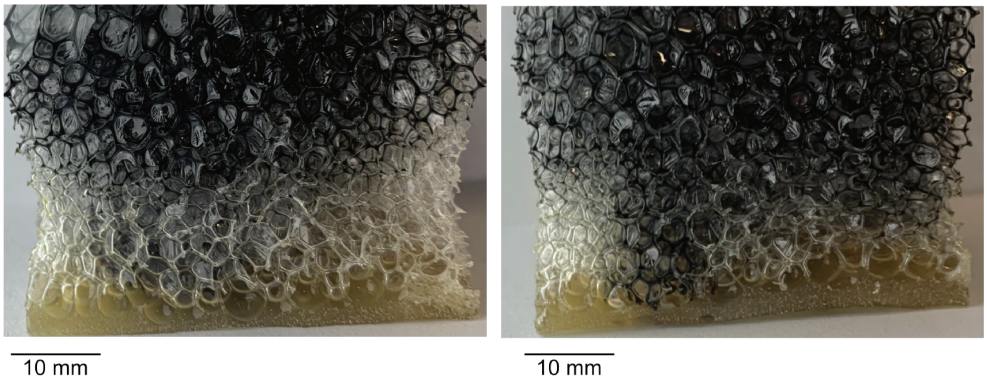


Figure 6.7 – Visualisation of the drainage front in the foam superimposition protocol using black dye on PU foam with 0.1 % catalyst.

7 Dual scaffold analysis: Orders of the vertices

Figure 7.8 shows the proportion of vertex order within the reference samples of LVA and PU without fibres, produced with the protocole described, respectively, in Chapter 3 and Chapter 4. In Chapter 1, we saw that the vertices of order other than 4 are the signatures of materials aggregates that the programme is trying to represent. We could consider them as a pair of O(4) vertices or a O(8) vertex and as representative of the real defects present in foams. We can see that the LVA protocol is reproducible with an identical proportion of vertex orders (Fig. 7.8a)

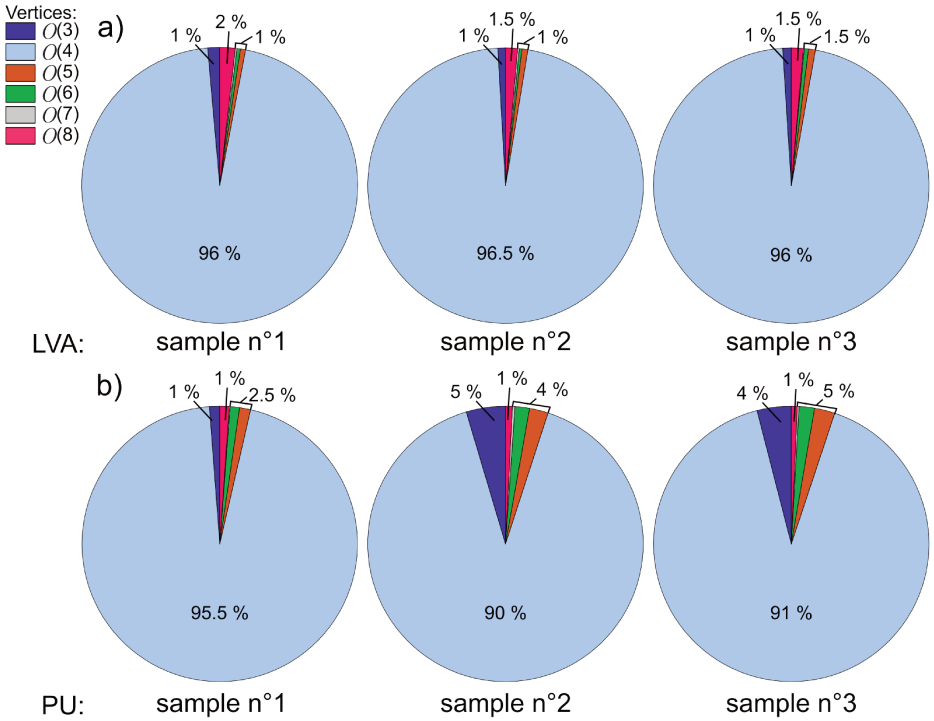


Figure 7.8 – Proportion of vertex orders over a) the reference LVA samples produced with the protocol described in Chapter 3 and b) the reference PU samples produced with the protocol described in Chapter 4. Extraction with $G = 20$ voxels following the procedure explained in Chapter 1, from tomographic images with a resolution of 25 μm.

8 Steinhardt analysis

In 1981, few years after the prediction of the hexatic phase of 2D liquids [132, 133], namely a liquid-like phase with no translational order yet a long range orientational order, Steinhardt, Nelson and Ronchetti inquired the extension of the correlation of rotational order to 3D liquid systems [54, 55]. Their method consists in looking at the global orientational density function over the unit radius 3D sphere

$$\rho(\boldsymbol{n}) = \frac{1}{2N_b} \sum_{\langle i,j \rangle} [\delta(\boldsymbol{n} - \widehat{\boldsymbol{r}}_{\boldsymbol{ij}}) + \delta(\boldsymbol{n} + \widehat{\boldsymbol{r}}_{\boldsymbol{ij}})] \tag{8.1}$$

This function is defined for any unit vector $\boldsymbol{n}$ and each configuration of the fluid : N_b is the total number of nearest-neighbour pairs (i, j) within the fluid (defined via a cutoff criterion or a Voronoi cell decomposition, or any other convenient mean), the sum operates once on all pairs of nearest neighbors $\langle i, j \rangle$, and $\widehat{\boldsymbol{r}}_{\boldsymbol{ij}} = (\boldsymbol{r_j} - \boldsymbol{r_i})/|\boldsymbol{r_j} - \boldsymbol{r_i}|$ is the "bond unit vector" going from i to j. The presence of two delta functions for each pair $\langle i, j \rangle$ is necessary because the bonds are not physically oriented, and this symmetry $i \leftrightarrow j$ must be preserved (in other words, $\widehat{\boldsymbol{r}}_{\boldsymbol{ij}}$ represents equally well the bond than its opposite).

A fonction $\rho(\boldsymbol{n})$ defined on the unit sphere can be represented by its expansion on the spherical harmonics $Y_\ell^m(\boldsymbol{n}) = Y_\ell^m(\theta, \phi)$, once an external coordinate system $(O, \boldsymbol{e_x}, \boldsymbol{e_y}, \boldsymbol{e_z})$ (centered at the center of the sphere) has been given ; (θ, ϕ) represents here the polar and azimuthal angles of the spherical coordinates of $\boldsymbol{n}$. This expansion is the spherical

equivalent of the Fourier series expansion of the periodic functions which can be also viewed as functions over the unit circle :

$$\rho(\boldsymbol{n}) = \sum_{\ell=0}^{\infty} \sum_{m=-\ell}^{\ell} \rho_{\ell m} Y_\ell^m(\theta, \phi) \tag{8.2}$$

$$\rho_{\ell,m} = \int_0^\pi \mathrm{d}\theta \sin\theta \int_0^{2\pi} \mathrm{d}\phi \rho(\boldsymbol{n}) (Y_\ell^m)^\star(\theta, \phi) = \frac{1 + (-1)^\ell}{2N_b} \sum_{\langle i,j \rangle} (Y_\ell^m)^\star(\theta_{ij}, \phi_{ij}) \tag{8.3}$$

Notice that $\rho_{\ell,m} = 0$ if ℓ is odd, as a consequence of the $\boldsymbol{n} \longleftrightarrow -\boldsymbol{n}$ symmetry.

If no bond orientational order is present in the fluid (and in our case, in the strut network of the foam), the bond vector $\widehat{\boldsymbol{r}}_{\boldsymbol{ij}}$ are expected to uniformly populate the unit sphere, up to tiny fluctuations for finite N_b. As a result, for such an isotropic case, one expects that all coefficients but the first ρ_{00} be zero ($Y_0^0(\boldsymbol{n}) = \frac{1}{2\sqrt{\pi}}$ =const.). Conversely, if an orientational order develops, this isotropy is broken, and the set of mode amplitudes $\rho_{\ell,m}$ will account for this order. Unfortunately, two difficulties arises, beyond the a priori infinite size of this set. On the one hand, it depends on the choice of the coordinate system $(\boldsymbol{e}_x, \boldsymbol{e}_y, \boldsymbol{e}_z)$, on the other hand any orientational order sets in by breaking the global isotropy of space in a particular, randomly chosen, direction, and this direction selection will also give rise to different signatures in the set $\{\rho_{\ell,m}\}_{\ell,m}$. To overcome this, Steinhardt *et al.* proposed to use only combinations of modes which are naturally rotationnally invariants.

This restriction solves at once both difficulties : Such a rotationnally invariant quantity would give the same result for any other choice of coordinate system and any global rotation of the transited structure. Several rotationnally invariant combination of $\rho_{\ell,m}$ can be constructed, for lack of time we considered only the first of the Steinhardt indicators,

$$Q_\ell = \left[\frac{4\pi}{2\ell + 1} \sum_{m=-\ell}^{\ell} |\rho_{\ell,m}|^2 \right]^{1/2} \tag{8.4}$$

(we can assume ℓ even, since $Q_{\mathrm{odd}} = 0$). In this definition, only the sum over m of $|\rho_{\ell,m}|^2$ matters to obtain a rotationally invariant quantity, the other coefficients and square root are kept for sake of consistency with the original Steinhardt's definition (the factor $2\ell + 1$ makes an average of the sum, and 4π is also $|\rho_{0,0}|^2$ for an isotropic fluid).

Example : the Steinhardt parameters of a Kelvin Structure

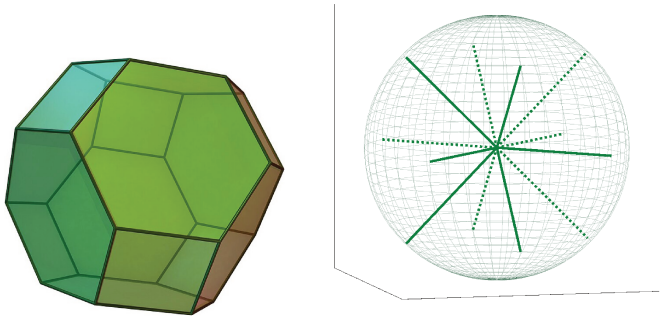


Figure 8.9 – (left) Truncated Octahedron (right) Bond orientation density $\rho(\boldsymbol{n})$ for the ideal Kelvin Structure.

Let us consider an ideal Kelvin structure, namely a regular space-filling network of truncated octahedron. The truncated octahedron (see fig. 8.9) has edge unit vectors $\boldsymbol{u}_j \in \{(0, \pm 1, \pm 1)/\sqrt{2}$ and circular permutations$\}$, i.e. 12 different equal vectors, but only 6 different directions. This can be checked in the figure, by focusing on the hexagons : The two front hexagons provide 5 of these vectors, and the top hexagon only one. The bottom and rear hexagons are parallel to the front and top ones, and the square edges belong all to hexagons as well. The multiplicity of each of the 6 directions is 6 because they all play equivalent role (in particular any hexagon-hexagon edge is parallel to a hexagon-square edge). As a result, for the Kelvin structure, one can write

$$\rho(\boldsymbol{n}) = \frac{1}{12} \sum_j \delta(\boldsymbol{n} - \boldsymbol{u}_j) \tag{8.5}$$

Figure 8.9 (right) shows the disposition of the 12 vectors $\boldsymbol{u}_j$ defining $\rho(\boldsymbol{n})$. In spherical coordinates it corresponds to $\theta \in \{45°, 90°, 135°\}$, and for each of these θ, the angle ϕ is $\in \{0, \frac{\pi}{2}, \pi, \frac{3\pi}{2}\}, \{\frac{\pi}{4}, \frac{3\pi}{4}, \frac{5\pi}{4}, \frac{7\pi}{4}\}, \{0, \frac{\pi}{2}, \pi, \frac{3\pi}{2}\}$ respectively.

The Steinhardt's coefficients for the Kelvin structure are shown in Figure 5.23 and compared with the simple cubic structure and with our foam structures.

Bibliography

[1] J. Plateau, Statique expérimentale et théorique des liquides soumis aux seules forces moléculaires (Gauthier-Villard, 1873). 3, 4, 5, 27, 37, 45, 67, 100, 112, 119, 125, 126

[2] C. Stubenrauch, A. Menner, A. Bismarck, and W. Drenckhan, Emulsion and Foam Templating - Promising Routes to Tailor-Made Porous Polymers, Angew. Chem. Int. Ed. **57**, 10024–10032 (2018). 3, 6, 47, 125, 128

[3] Industrial Foam Market by Foam Type, Resin Type, End-Use Industry and Region, https://www.marketsandmarkets.com/Market-Reports/industrial-foam-market-179125646.html. Accessed: 2023-11-03. 3

[4] P. Laurain, Mathématiques savonneuses, En ligne (2011). URL: http://images.math.cnrs.fr/Mathematiques-savonneuses.html. 1

[5] D. Everett, Basic principles of colloid science, RSC Publishing (1988). 2

[6] S. Dukhin, G. Kretzschmar, and R. Miller, Dynamics of absorption at liquid interfaces: theory, experiment, application, Elsevier (1995). 2

[7] V. Bergeron, Forces and structure in thin liquid soap films, Journal of Physics: Condensed Matter **11**, R215 (1999). 2

[8] R. Höhler, Y. Yip Cheung Sang, E. Lorenceau, and S. Cohen-Addad, Osmotic Pressure and Structures of Monodisperse Ordered Foam, Langmuir **24**, 418–425 (2008). 2

[9] D. Weaire and S. Hutzler, The physics of foams (Clarendon Press, 1999). 2, 7, 15

[10] W. Drenckhan and S. Hutzler, Structure and energy of liquid foams, Advances in colloid and interface science **224**, 1–16 (2015). 3, 5

[11] A. Saint-Jalmes, Physical chemistry in foam drainage and coarsening, Soft Matter **2**, 836–849 (2006). 3, 7, 130

[12] I. Cantat, F. Cohen-Addad, S. anf Elias, F. Graner, R. Hölhler, O. Pitois, F. Rouyer, and A. Saint-Jalmes, Foams Structure and Dynamics (Oxford, 2013). 3, 7, 8, 15

[13] W. L. K. Thomson, On the division of space with minimum partitional area, Philos. Mag. **2**, 503–514 (1887). 4, 102, 104, 134

[14] D. Weaire and R. Phelan, A counter-example to Kelvin's conjecture on minimal surfaces, Philosophical Magazine Letters **69**, 107–110 (1994). 4

[15] M. E. Rosa, M. A. Fortes, and M. F. Vaz, Deformation of three-dimensional monodisperse liquid foams, The European Physical Journal E **7**, 129–140 (2002). 4

[16] A. Meagher, D. McAteer, S. Hutzler, and D. Weaire, Building the pyramids: perfect bubble crystals, Philosophical Magazine **93**, 4138–4150 (2013). 5

[17] R. Höhler, Y. Yip Cheung Sang, E. Lorenceau, and S. Cohen-Addad, Osmotic Pressure and Structures of Monodisperse Ordered Foam, Langmuir **24**, 418–425 (2008). 5

[18] S. Hutzler, J. Barry, P. Grasland-Mongrain, D. Smyth, and D. Weaire, Ordered packings of bubbles in columns of square cross-section, Colloids and Surfaces A: Physicochemical and Engineering Aspects **344**, 37–41 (2009). 5, 6, 31, 119, 126

[19] A. Skrypnik, L. Knüpfer, P. Trtik, V. Tholan, S. Parkes, and S. Heitkam, Neutron radiography of liquid foam structure near a vertical wall, Soft Matter (2023). 5

[20] A. van der Net, G. W. Delaney, W. Drenckhan, D. Weaire, and S. Hutzler, Crystalline arrangements of microbubbles in monodisperse foams, Colloids and Surfaces A: Physicochemical and Engineering Aspects **309**, 117–124 (2007). 5, 125

[21] A. Kraynik, Foam Structure: From Soap Froth to Solid Foams., MRS Bulletin **28**, 275–278 (2003). 5

[22] W. Drenckhan and D. Langevin, Monodisperse foams in one to three dimensions, Current Opinion in Colloid & Interface Science **15**, 341–358 (2010). 5, 6, 122

[23] M. Saadatfar, J. Barry, D. Weaire, and S. Hutzler, Monodisperse foams in one to three dimensions, Philos Mag Lett **88**, 661–8 (2008). 5

[24] D. Weaire, S. Hutzler, and N. Pittet, Cylindrical packings of foam cells, Forma **7**, 259 (1992). 5

[25] N. Rivier, N. Pittet, and D. Weaire, Cylindrical packings of foam cells, Forma **10**, 65–73 (1995). 5

[26] D. Reinelt, P. Boltenhagen, and N. Rivier, Deformed foam structure and transitions in a tube, The European Physical Journal E **4**, 299–304 (2001). 6, 31

[27] D. Weaire, N. Pitter, and S. Hutzler, Steady-State drainage of an aqueous foam, PRL **71**, 2670–2673 (1993). 7

[28] N. Vandewalle, H. Caps, D. Delon, A. Saint-Jalmes, E. Rio, L. Saulnier, M. Adler, A. Biance, O. Pitois, S. Cohen-Addad, R. Höhler, D. Weaire, S. Hutzler, and D. Langevin, Foam stability in microgravity., Journal of Physics: Conference Series **327**, 012024 (2011). 7

[29] D. Barrett, E. Daly, M. Dolan, S. Kelly, W. Drenckhan, D. Weaire, and S. Hutzler, Taking Plateau into micro-gravity: the formation of an eight-fold vertex in a system of soap films, Microgravity - Science and Technology (2008). 7

[30] A. Meagher, The structure of monodisperse foam, PhD thesis (2012). 7

[31] W. Drenckhan and S.-J. A., The science of foaming., Adv Colloid Interface Sci. (2015). 9

[32] F. Scargiali, A. Busciglio, F. Grisafi, and A. Brucato, Bubble Formation at Variously Inclined Nozzles, Chem. Eng. Techol. **37**, 1507–1514 (2014). 9, 128

[33] E. Kosari, J. Eshrgahi, W. Ahmed, and P. Hanafizadeh, Experimental investigation of bubble growth and detachment in stagnant liquid column using image – based analysis, Energy Equipment and Systems **7**, 353–375 (2019). 9

[34] A. Sattari and P. Hanafizadeh, Bubble formation on submerged micrometer-sized nozzles in polymer solutions: An experimental investigation, Colloids and Surfaces A: Physicochemical and Engineering Aspects **564**, 10–22 (2019). 9

[35] H. Xiao, S. Geng, A. Chen, C. Yang, F. Gao, T. He, and Q. Huang, Bubble formation in continuous liquid phase under industrial jetting conditions, Chemical Engineering Science **200**, 214–224 (2019). 9

[36] M. Jamialahmadi, M. Zehtaban, H. Müller-Steinhagen, A. Sarrafi, and J. Smith, Study of Bubble Formation under Constant Flow Conditions, Trans. IChemE **79A**, 523–532 (2001). 9, 128, 129

[37] A. Kulkarni and J. Joshi, Bubble Formation and Bubble Rise Velocity in Gas-Liquid Systems: A Review, Ind. Eng. Chem. Res. **44**, 5873–5931 (2005). 9, 128, 129

[38] N. A. Fleck, V. S. Deshpande, and M. F. Ashby, Micro-architectured materials: past, present and future, Proc. R. Soc. A. **466**, 2495–2516 (2010). 10, 14

[39] L. Gibson and M. Ashby, Cellular Solids: Structure and Properties (Cambridge University Press, 1997), 2nd ed. 10, 11, 12, 13, 14, 91, 92

[40] S. Andrieux, Monodisperse highly ordered and polydisperse biobased solid foams, PhD thesis (2018). 12, 125, 128

[41] M. Dabo, Analyse du comportement mécanique des mousses polymères: apport de la tomographie X et de la simulation numérique, PhD thesis (2015). 13, 14

[42] J. Berger, H. Wadley, and R. McMeeking, Mechanical metamaterials at the theoretical limit of isotropic elastic stiffness, Nature **543**, 533–537 (2017). 14, 15

[43] E. Matzke, The three-dimensional shape of bubbles in foam - an analysis of the role of surface forces in three-dimensional cell shape determination, American Journal of Botany **33**, 58–80 (1945). 15, 99

[44] T. Cotgreave and J. Shortall, The mechanism of reinforcement of polyurethane foam by high-modulus chopped fibres, Journal of materials science **12**, 708–717 (1977). 16, 90, 91

[45] F. Schott, B. Dollet, S. Santucci, C. Claudet, M. Argentina, C. Raufaste, and R. Mokso, Three-dimensional liquid foam flow through a hopper resolved by fast X-ray microtomography, Soft Matter **19**, 1300–1311 (2023). 16

[46] S. Burke, M. Möbius, T. Hjelt, J. Ketoja, and S. Hutzler, Analysis of the foam-forming of non-woven lightweight fibrous materials using X-ray tomography, SN Applied Sciences (2021). 16, 89, 90, 101, 127

[47] K. Mader, R. Mokso, R. Raufaste, B. Dollet, S. Santucci, J. Lambert, and M. Stampanoni, Quantitative 3D characterization of cellular materials: Segmentation and morphology of foam, Colloids and Surfaces A: Physicochemical and Engineering Aspects **415**, 230–238 (2012). 16

[48] S. Pardo-Alonso, E. Solórzano, L. Brabant, P. Vanderniepen, M. Dierick, L. Van Hoorebeke, and M. Rodríguez-Pérez, 3D Analysis of the progressive modification of the cellular architecture in polyurethane nanocomposite foams via X-ray microtomography, European Polymer Journal **49**, 999–1006 (2013). 16

[49] M. Montminy, A. Tannenbaum, and C. Macosko, New Algorithms for 3-D Imaging and Analysis of Open-Celled Foams, Journal of Cellular Plastics **37**, 501–515 (2001). 16, 21

[50] M. Montminy, M. Tannenbaum, and C. Macosko, The 3D structure of real polymer foams, Journal of Colloid and Interface Science **280**, 202–211 (2004). 16, 21, 100

[51] W. Röntgen, Über eine neue Art von Strahlent [Concerning a new type of radiation], Ann. Phys. Chem. New Series **64**, 1–37 (1898). 16

[52] S. Stock, Microcomputed Tomography - Methodology and Applications (CRC Press Taylor & Francis Group, 2020). 16

[53] VGStudio, Foam/powder analysis module. 19

[54] P. Steinhardt, D. Nelson, and M. Ronchetti, Icosahedral Bond Orientational Order in Supercooled Liquids, Phys. Rev. Lett. pp. 1297–1300 (1981). 25, 143

[55] P. Steinhardt, D. Nelson, and M. Ronchetti, Bond-orientational order in liquids and glasses, Phys. Rev. B **28**, 784–805 (1983). 25, 112, 143

[56] M. Jouanlanne, A. Egelé, D. Favier, W. Drenckhan, J. Farago, and A. Hourlier-Fargette, Elastocapillary deformation of thin elastic ribbons in 2D foam columns, Soft Matter **18**, 2325–2331 (2022). 28, 126, 132

[57] J. Bico, É. Reyssat, and B. Roman, Elastocapillarity: when surface tension deforms elastic solids, Annual Review of Fluid Mechanics **50**, 629–659 (2018). 28

[58] B. Roman and J. Bico, Elasto-capillarity: deforming an elastic structure with a liquid droplet, Journal of Physics: Condensed Matter **22**, 493101 (2010). 28

[59] R. W. Style, R. Tutika, J. Y. Kim, and M. D. Bartlett, Solid–Liquid Composites for Soft Multifunctional Materials, Advanced Functional Materials p. 2005804 (2020). 28

[60] D. P. Holmes, Elasticity and stability of shape-shifting structures, Current Opinion in Colloid & Interface Science **40**, 118 – 137 (2019). 28

[61] R. R. A. Syms, E. M. Yeatman, V. M. Bright, and G. M. Whitesides, Surface tension-powered self-assembly of microstructures - the state-of-the-art, Journal of Microelectromechanical Systems **12**, 387–417 (2003). 28

[62] M. De-Volder and A. J. Hart, Engineering Hierarchical Nanostructures by Elastocapillary Self-Assembly, Angewandte Chemie International Edition **52**, 2412–2425 (2013). 28

[63] L. Hines, K. Petersen, G. Z. Lum, and M. Sitti, Soft Actuators for Small-Scale Robotics, Advanced Materials pp. 1603483–n/a (2016). 28

[64] K. S. Kwok, Q. Huang, M. Mastrangeli, and D. H. Gracias, Self-Folding Using Capillary Forces, Advanced Materials Interfaces **7**, 1901677 (2020). 28

[65] M. Saint-Jean, Cellular structures for shape morphing, Thesis (2023). 28

[66] S. Frazier, X. Jiang, and J. Burton, How to make a giant bubble, Physical Review Fluids **5**, 013304 (2020). 29

[67] M. Pasquet, L. Wallon, P. Fusier, F. Restagno, and E. Rio, An optimized recipe for making giant bubbles, The European Physical Journal E volume **45** (2022). 29

[68] I. Johnston, D. McCluskey, C. Tan, and M. Tracey, Mechanical characterization of bulk Sylgard 184 for microfluidics and microengineering, Journal of Micromechanics and Microengineering **24** (2014). 29, 30

[69] F. Elias, S. Hutzler, and M. Ferreira, Visualization of sound waves using regularly spaced soap films, European Journal of Physics **28**, 755–765 (2007). 31

[70] H. Goldstein, Classical Mechanics (Addison-Wesley, 1980). 37

[71] C. Lanczos, The Variational Principles of Mechanics (Dover, 1986). 37

[72] M. A. Eddings, M. A. Johnson, and B. Gale, Determining the optimal PDMS–PDMS bonding technique for microfluidic devices, Journal of Micromechanics and Microengineering **18**, 067001 (2008). 38

[73] J. Miller, A. Lazarus, B. Audoly, and P. M. Reis, Shapes of a suspended curly hair, Physical review letters **112**, 068103 (2014). 39

[74] I. Ben Djemaa, F. Boulmedais, S. Auguste, M. Tarnowska, S. Andrieux, and W. Drenckhan-Andreatta, Glucono-δ-lactone induced alginate gelation: new insights into the effect of the crosslinker carrier type on the hydrogel mechanics, Submitted . 46, 48, 49, 128

[75] K. Draget, Alginates, Handbook of Hydrocolloids: Second Edition pp. 807–828 (2009). 48

[76] E. Ahmed, Hydrogel: Preparation, characterization, and applications: A review, J. Adv. Research **6**, 105–121 (2015). 48

[77] I. Ben Djemaa, S. Auguste, W. Drenckhan-Andreatta, and S. Andrieux, Hydrogel foams from liquid foam templates: Properties and optimisation, Advances in Colloid and Interface Science **294**, 102478 (2021). 48, 49, 125

[78] K. Chung, N. Mishra, C. Wang, F. Lin, and K. Lin, Fabricating scaffolds by microfluidics, Biomicrofluidics **3**, 022403 (2009). 48

[79] T. Andersen, J. Melvik, O. Gåserød, E. Alsberg, and B. Christensen, Ionically gelled alginate foams: Physical properties controlled by type, amount and source of gelling ions, Carbohydrate Polymers **99**, 249–256 (2014). 48

[80] X. Liu, L. Qian, T. Shu, and Z. Tong, Rheology characterization of sol–gel transition in aqueous alginate solutions induced by calcium cations through in situ release, Polymer **44**, 407–412 (2003). 48

[81] V. Jost and M. Reinelt, Effect of Ca^{2+} induced crosslinking on the mechanical and barrier properties of cast alginate films., Applied Polymer Science **135** (2017). 48

[82] S. Andrieux, M. Patil, L. Jacomine, A. Hourlier-Fargette, S. Heitkam, and W. Drenckhan, Investigating Pore-Opening of Hydrogel Foams at the Scale of Freestanding Thin Films, Macromol. Rapid Commun. **43**, 2200189 (2022). 50, 53, 54

[83] M. Cross, Relation between viscoelasticity and shear-thinning behaviour in liquids, Rheologica Acta **18**, 608–614 (1979). 50, 53

[84] H. Winter and F. Chambon, Analysis of linear viscoelasticity of a crosslinking polymer at gel point, Journal of Rheology **30**, 367–382 (1986). 50

[85] A. Franck, Understanding rheology of thermosets, TA Instrument (2004). 50

[86] O. Smidsrød, Solution properties of alginate, Carbohydrate Research **13**, 359–372 (1969). 53

[87] C. Kuo and P. Ma, Ionically Crosslinked Alginate Hydrogels as Scaffolds for Tissue Engineering: Part 1. Structure, Gelation Rate and Mechanical Properties, Biomaterials **22**, 511–521 (2001). 54

[88] K. Draget, K. Østgaard, and O. Smidsrød, Homogeneous alginate gels: a technical approach, Carbohydrate polymers **14**, 157–178 (1991). 54

[89] O. Bayer, Das di-isocyanat-polyadditionsverfahren-(polyurethane), Angew. Chem. **59**, 257–272 (1947). 66

[90] K. Zia, S. Anjum, M. Zuber, M. Mujahid, and . Jamil, Synthesis and molecular characterization of chitosan based polurethane elastomers using aromatic diisocyanate, Int. J. Biol. Macromol **66**, 26–32 (2014). 66

[91] J. Akindoyo, M. Beg, S. Ghazali, M. Islam, N. Jeyaratnam, and A. Yuvaraj, Polyurethane types, synthesis and applications - a review, RSC Adv. **6**, 114453–114482 (2016). 66, 67

[92] M. Ionescu, Chemistry and technology of polyols fo polyurethanes (Rapra Technology, 2007). 66, 67, 76

[93] D. Randall and S. Lee, The Polyurethanes Book (Wiley Ltd., 2002). 66, 67, 76

[94] M. Hamann, Morphology control of polyurethane foams, Thesis (2023). 67

[95] M. Hamann, G. Cotte-Carluer, S. Andrieux, D. Telkemeyer, M. Ranft, M. Schütte, and W. Drenckhan, Fluorocarbon-driven pore size reduction in polyurethane foams: an effect of improved bubble entrainment, Colloid and Polymer Science (2023). 67, 68, 69, 70, 74

[96] A. Testouri, Highly structured polymer foams from liquid foam templates using millifluidic lab-on-a-chip techniques, Thesis (2012). 67

[97] A. Testouri, M. Ranft, C. Honorez, N. Kaabeche, J. Ferbitz, D. Freidank, and W. Drenckhan, Generation of Crystalline Polyurethane Foams Using Millifluic Lab-on-a-Chip Technologies, Adv. Eng. Mat. **15**, 1086–1098 (2013). 67, 68, 70, 74, 75, 122, 128

[98] B. Zhmud, Viscosity Blending Equations, Lube Magazine **121**, 22–27 (2014). 75

[99] J. Miller, S. Lin, K. Hwang, K. Wu, P. Gibson, and S. Cooper, Properties of Polyether-Polyurethane Block Copolymers: Effects of Hard Segment Length Distribution, Macromolecules **18**, 32–44 (1985). 76, 78

[100] H. Jeong, J. Park, S. Kim, J. Lee, and N. Ahn, Compressive viscoelastic properties of softwood kraft lignin-based flexible polyurethane foams, Fibers and polymers **8**, 1301–1310 (2013). 78

[101] C. Boys, Soap-bubbles and the forces which mould them. Being a course of three lectures delivered in the theatre of the London institution on the afternoons of Dec. 30, 1889, Jan. 1 and 3, 1890, before a juvenile audience (Reprinted by T.Y. Crowell Company, 1962). 88

[102] J. Bico, B. Roman, L. Moulin, and A. Boudaoud, Elastocapillary coalescence in wet hair, Nature **432**, 690 (2004). 88

[103] Y. Hu, Z. Lao, B. Cumming, D. Wu, J. Li, H. Liang, J. Chu, W. Huang, and M. Gu, Laser printing hierarchical structures with the aid of controlled capillary-driven self-assembly, PNAS **112**, 6876–6881 (2015). 88

[104] S. Tawfick, J. Bico, and S. Barcelo, Three-dimensional lithography by elasto-capillary engineering of filamentary materials, MRS Bulletin **41**, 108–114 (2016). 88

[105] J. Ha, Y. Kim, R. Siu, and S. Tawfick, Dynamic pattern selection in polymorphic elastocapillarity, Soft Matter **18**, 262–271 (2022). 88, 89

[106] S. Li, D. Bolei, A. Grinthal, A. Schneider-Yamamura, J. Kang, R. Martens, C. Zhang, J. Li, S. Yu, K. Bertoldi, and J. Aizenberg, Liquid-induced topological transformations of cellular microstructures, Nature **592**, 386–391 (2021). 88, 89

[107] M. Smith, V. Punton, and A. Rixson, The structure and properties of paper formed by a foaming process, Tappi **57**, 107–101 (1974). 89, 127

[108] A. Al-Quararah, T. Hjelt, A. Koponen, A. Harlin, and J. Ketoja, Response of wet foam to fibre mixing, Colloids and Surfaces A: Physicochem. Eng. Aspects **467**, 97–106 (2015). 89, 90, 101, 127

[109] D. Whyte, B. Haffner, A. Tanaka, T. Hjelt, and S. Hutzler, Interactions of fibres with simple arrangements of soap films, Colloids and Surfaces A: Physicochem. Eng. Aspects **534**, 112–119 (2017). 89, 90, 101

[110] L. Berreur., B. de Maillard, and S. Nösperger, L'industrie française des matériaux composites, (2001). 90

[111] N. Abu Hassan, S. Ahmad, R. Chen, and V. Natarajan, Synergistically enhanced mechanical, combustion and acoustic properties of biopolymer composite foams reinforcement by kenaf fibre, Composites Part A: Applied Science and Manufacturing **155**, 106826 (2022). 90

[112] D.-A. Serban, O. Weissenborn, S. Geller, L. Marsavina, and M. Gude, Evaluation of the mechanical and morphological properties of long fibre reinforced polyurethane rigid foams, Polymer Testing **49**, 121–127 (2016). 90, 91

[113] M. Ardanuy, M. Antunes, and J. Velasco, Vegetable fibres from agricultural residues as thermo-mechanical reinforcement in recycled polypropylene-based green foams, Waste Management **32**, 256–263 (2012). 90

[114] A. Desai and S. Nutt, Modeling of fiber-reinforced phenolic foam, Journal of cellular plastics **44**, 391–413 (2008). 90

[115] D. Askeland, The science and engineering of materials, Springer New York **1** (2013). 91

[116] S. Hussain and M. Kortschot, Polyurethane foam mechanical reinforcement by low-aspect ratio micro-crystalline cellulose and glass fibres., Journal of cellular plastics **51**, 59–73 (2015). 91, 92

[117] S. Hussain and M. Kortschot, Understanding the effects of high aspect ratio fibers on the mechanical reinforcement of soybean based polyurethane foam., Cellular Polymer **33** (2014). 91

[118] L. Le Barbenchon, J. Kopp, J. Girardot, and P. Viot, Reinforcement of cellular materials with short fibres: Application to a bio-based cork multi-scale foam, Mechanics of Materials **142**, 103271 (2020). 91

[119] S. Murmu, Alternatives derived from renewable natural fibre to replace conventional polyurethane rigid foam insulation, Cleaner Engineering and Technology **8**, 100513 (2022). 91

[120] A. Kraynik, D. Reinelt, and F. van Swol, Structure of random monodisperse foam, Phys. Rev. E **67**, 031403 (2003). 99

[121] A. J. Meagher, D. Whyte, J. Banhart, S. Hutzler, D. Weaire, and F. García-Moreno, Slow crystallisation of a monodisperse foam stabilised against coarsening, Soft Matter pp. 4710–4716 (2015). 112

[122] W. Mickel, S. Kapfer, G. Schröder-Turk, and K. Mecke, Shortcomings of the bond orientational order parameters for the analysis of disordered particulate matter, J. Chem. Phys. **138**, 0445015 (2013). 112

[123] C. Brangwynne, F. MacKintosh, S. Kumar, N. Geisse, J. Talbot, L. Mahadevan, K. Parker, D. Ingber, and D. Weitz, Microtubules can bear enhanced compressive loads in living cells because of lateral reinforcement, Journal of cell biology **175**, 733–741 (2006). 114

[124] A. Guerra, A. Slim, D. Holmes, and O. Kodio, Self-Ordering of Buckling, Bending, and Bumping Beams, PRL **130**, 148201 (2023). 116

[125] T. Su, J. Liu, D. Terwagne, P. Reis, and B. Katia, Buckling of an elastic rod embedded on an elastomeric matrix: planar vs. non-planar configurations, Soft Matter **10**, 6294–6302 (2014). 116

[126] L. Jiang and H. Hu, Low-velocity impact response of multilayer orthogonal structural composite with auxetic effect, Composite Structures **169**, 62–68 (2017). 123, 124

[127] S. Hoguin, Stocker de l'énergie mécanique grâce aux matériaux auxétiques, https://www.techniques-ingenieur.fr/actualite/articles/stocker-de-lenergie-mecanique-grace-aux-materiaux-auxetiques-58784/. Accessed: 2023-11-04. 123

[128] L. Zorzetto and D. Ruffoni, Re-entrant inclusions in cellular solids: From defects to reinforcements, Composite Structures **176**, 195–204 (2017). 123, 124

[129] F. Schüler, D. Schamel, A. Salonen, W. Drenckhan, D. Gilchrist, and C. Stubenrauch, Synthesis of macroporous polystyren by polymerization of foamed emulsions, Angew. Chem. Int. Ed. **51**, 2213–2217 (2012). 128

[130] O. Skurtys, P. Bouchon, and J. Aguilera, Formation of bubbles and foams in gelatine solutions within a vertical glass tube, Food Hydrocolloids **22**, 706–714 (2008). 128

[131] X. Fan, X. Chen, X. Liu, H. Zhang, and Y. Li, Bubble Formation at a Submerged Orifice for Aluminum Foams Produces by Gas Injection Method, Metal. Mat. Trans. A **44A**, 729–737 (2013). 128

[132] J. Kosterlitz and D. Thouless, Ordering, metastability and phase transitions in two-dimensional systems, Journal of Physics C: Solid State Physics **6**, 1181 (1973). 143

[133] D. Nelson and B. Halperin, Dislocation-mediated melting in two dimensions, Phys. Rev. B pp. 2457–2484 (1979). 143

[134] P. Jahangiri, R. Korehei, S. Zeinoddini, A. Madani, Y. Sharma, A. Phillion, D. Martinez, and J. Olson, On filtration and heat insulation properties of foam formed cellulose based materials, Nord Pulp. Pap. Res. J. **29**, 584–591 (2014).

[135] T. Pöhler, P. Jetsu, and H. Isomoisio, Benchmarking new woodfibre based sound absorbing material made with a foamforming technique, Build Acoust. **23**, 131–143 (2016).

[136] Y. Luo, S. Xiao, and S. Li, Effect of initial water content on foaming quality and mechanical properties of plant fibre porous cushioning materials, BioResources **12**, 4259–4269 (2017).

Manon JOUANLANNE

Architectures d'assemblages mousse-fibres : des systèmes liquides aux matériaux polymères hiérarchiques

Résumé

L'objectif de cette thèse est de créer de nouveaux matériaux en modifiant la géométrie et la topologie des mousses (forme, taille et connexion des bulles) par l'introduction de fibres. La première partie de la thèse s'intéresse à une expérience modèle permettant la quantification des formes d'équilibre de systèmes mousse liquide/lamelle élastique, avec un excellent accord entre théorie et expériences, et mettant en lumière la compétition entre élasticité et capillarité. La deuxième partie de la thèse développe l'élaboration de mousses solides à partir d'un précurseur liquide, formées grâce à une méthode de bullage au travers de canules. Les fibres sont ensuite introduites dans les mousses à l'état liquide, c'est-à-dire en permettant aux bulles et aux fibres de s'organiser spontanément avant l'étape de solidification. Différentes formulations ont été étudiées, en se focalisant sur des mousses d'hydrogel d'alginate et des mousses de polyuréthane. Enfin, la troisième partie de la thèse analyse l'impact des fibres rigides et ordonnées sur la modification structurelle des mousses. Un protocole de caractérisation a été développé à partir d'images tomographiques à rayon X. L'ensemble de ces travaux montre qu'en sélectionnant la technique de moussage, la formulation du matériau constitutif de la mousse et la géométrie des fibres, il est possible de réaliser des matériaux composites qui possèdent des structures uniques, considérablement modifiées par l'inclusion de fibres et prometteuses en termes de propriétés mécaniques.

Mots Clés : Mousse, Alginate, Polyuréthane, Elastocapillarité, Composite, Tomographie RX

Abstract

The aim of this thesis is to create new materials by modifying the geometry and topology of foams (shape, size and connection of bubbles) through the introduction of fibres. The first part of the thesis focuses on a model experiment enabling the quantification of the equilibrium forms of foam/elastic ribbon systems, with excellent agreement between theory and experiment, and highlighting the competition between elasticity and capillarity. The second part of the thesis develops the elaboration of solid foams from a liquid precursor, formed using a bubbling through nozzles. The fibres are then introduced into the foams in the liquid state, i.e., allowing the bubbles and fibres to organise themselves spontaneously before the solidification stage. Different formulations were studied, focusing on alginate hydrogel and polyurethane foams. Finally, the third part of the thesis analyses the impact of rigid and ordered fibres on the structural modification of foams. A characterisation protocol was developed using X-ray tomographic images. All this work shows that by selecting the foaming technique, the formulation of the foam constitutive material and the geometry of the fibres, it is possible to produce composite materials with unique structures, considerably modified by the inclusion of fibres and promising in terms of mechanical properties.

Keywords: Foam, Alginate, Polyurethane, Elastocapillarity, Composite, X-ray tomography